NTNU
Norwegian University of
Science and Technology

Investigation of Wave-Induced ULS and ALS Characteristic Loads and Responses on a Pile Structure in the Ekofisk Area

Importance of Breaking Waves

Ida Haftun Overn
Ida Fredsvik Waage

Marine Technology
Submission date: June 2016
Supervisor: Sverre Kristian Haver, IMT

Norwegian University of Science and Technology
Department of Marine Technology

NTNU

Norwegian University of
Science and Technology

Investigation of wave-induced ULS and ALS characteristic loads and responses on a pile structure in the Ekofisk area

Ida H. Overn and Ida F. Waage

Department of Marine Technology
NTNU
Spring 2016

Preface

This thesis completes a Master of Science degree in Marine Technology at the Norwegian University of Science and Technology in Trondheim, Norway. It represents the workload of a collaboration between two students specializing within marine structures. We were engaged in researching, performing and writing this thesis in the period from January to June 2016. The outline of this thesis was formulated together with our supervisor, Sverre Kristian Haver.

Model test experiments require a large amount of preparatory and supplementary work, in addition to the conduction itself, which has resulted in an evenly distributed workload throughout the entire period. The collaboration has worked out well and both participants have contributed equally. It has been a challenging and timeconsuming process, but at the same time rewarded us with valuable knowledge and experience.

A number of people have assisted this master's thesis, both academically and practically. We would firstly like to express our deepest gratitude to our supervisor Sverre Kristian Haver for his time, help and valuable guidance throughout the entire project. Furthermore, we would like to sincerely thank Torgeir Wahl and Terje Rosten for all their practical assistance during the model test experiments in Lilletanken.

We would also like to thank the NTNU Professors Trygve Kristiansen, Sverre Steen and Svein Sævik for their time and academical assistance. Finally, we would like to thank Ole David Økland from MARINTEK for his professional expertise and assistance during certain parts of the model tests.

Trondheim, June 10, 2016

Ida Haftun Overn

Ida Fredsvik Waage

Contents

List of Symbols

α_F	Scale parameter in the Forristall distribution.
α_f	Percentile levels for the ULS and ALS extremes.
α_W	Scale parameter in the Weibull distribution.
α_G	Location parameter in the Gumbel distribution.
$\bar{\beta}$	Relation between ω_1 and ω_0
$\bar{c}$	Generalized damping.
$\bar{k}$	Generalized stiffness.
$\bar{M}$	Generalized moment.
$\bar{m}$	Generalized mass.
$\bar{p}$	Generalized force.
β_b	Reduction factor for breaking wave amplitude.
β_D	Parameter in the Donelan spectrum.
β_F	Shape parameter in the Forristall distribution.
β_W	Shape parameter in the Weibull distribution.
β_G	Scale parameter in the Gumbel distribution.
$\ddot{\theta}$	Rotational acceleration.
$\Delta\omega$	Nyquist frequency resolution.
Δ_R	Roughness parameter.
ΔH_S	Variation between measured tests of a sea state.
$\dot{\theta}$	Rotational velocity.
$\dot{u}$	Horizontal water particle acceleration.
η_{wm}	Signal sent to wave maker.
Γ	Gamma distribution.
γ_b	Breaking wave index.
γ_D	Parameter in the Donelan spectrum.
γ_J	Peak shape parameter of the JONSWAP wave spectrum.
γ_m	Material factor.
γ_S	Peakedness parameter of a wave spectrum.
γ_{1,H_S}	Third statistical moment of Weibull distribution.
γ_f	Load factor.
λ	Wave length.
λ_B	Breaking wave length.
λ_P	Wave length corresponding to T_P
λ_W	Location parameter in the Weibull distribution.
λ_{scale}	Scaling ratio.
$\mu_{\ln(T_P)}(h_S)$	Mean value of $\ln(T_P)$ given H_S.
μ_{H_S}	First statistical moment of Weibull distribution.
μ_X	Mean value of data sample.
ν	Parameter used in the Donelan spectrum.
ω_P	Wave freqency corresponding to T_P.
ω_0	Eigenfrequency.

ω_1	Frequency corresponding to t_1.
ω_d	Damped eigenfrequency.
Φ	Standard Gaussian distribution.
Ψ	Wake amplification factor.
$\psi(z)$	Assumed shape function.
ρ_{alu}	Material density of aluminium.
ρ_f	Full scale water density (1025 [kg/m^3]).
ρ_m	Model scale water density (1000 [kg/m^3]).
$\sigma^2_{H_S}$	Second statistical moment of Weibull distribution.
σ_D	Parameter in the Donelan spectrum.
σ_J	Spectral width parameter of the JONSWAP spectrum.
$\sigma_{\ln(T_P)}(h_S)$	Standard deviation of $\ln(T_P)$ given H_S.
$\sigma^2_{\zeta\zeta}$	Variance of wave spectrum.
σ^2_{out}	Averaged measured variance from the model tests.
σ_X	Standard deviation of data sample.
θ	Rotation.
θ_h	Homogenous solution of the equation of motion.
θ_p	Particular solution of the equation of motion.
ε	Wave steepness.
ε_D	Parameter used in the Donelan spectrum.
ε_{cr}	Critical wave steepness with respect to breaking.
ε_{ss}	Sea state steepness.
φ	Phase shift.
ξ	Damping ratio.
ζ	Surface elevation.
ζ_a	Linear wave amplitude.
a_0	Curvefitting constant for $\mu_{\ln(T_P)}(h_S)$
a_1	Curvefitting constant for $\mu_{\ln(T_P)}(h_S)$.
a_2	Curvefitting constant for $\mu_{\ln(T_P)}(h_S)$.
a_f	Full scale acceleration.
a_m	Model scale acceleration.
b_0	Curvefitting constant for $\sigma_{\ln(T_P)}(h_S)$.
b_1	Curvefitting constant for $\sigma_{\ln(T_P)}(h_S)$.
b_2	Curvefitting constant for $\sigma_{\ln(T_P)}(h_S)$.
C	Crest height.
c	Damping.
C_D	Drag coefficient.
C_g	Group velocity.
C_P	Measured crest height of a plunging breaker.
C_p	Phase velocity.
C_q	Crest height corresponding to the annual q probability of exceedance.
C_{1h}	Characteristic largest extreme crest height in a sea state of 1 [h] duration.
C_π	Parameter used in calculation of Ψ
C_A	Added mass coefficient.
c_{cr}	Critical damping.
C_{DS}	Roughness dependency of C_D.
C_M	Mass coefficient.
C_{Th}	Characteristic largest extreme crest height within a sea state of T [h] duration.
D	Pile diameter.
D_C	Deviation between compared wave crest heights.
D_F	Deviation between compared base shear forces.
D_M	Deviation between compared overturning moments.
D_i	Inner pile diameter.

D_o Outer pile diameter.

E_{alu} Young's modulus for aluminium.

EI Bending stiffness.

f Wave induced in-line loads on an unit length of the pile.

F_P Measured base shear force exerted by a plunging breaker.

F_q Annual q-probability of exceedance base shear force.

F_α Base shear force estimated from percentiles.

$F_{C|H_S,T_P}(c \mid H_S, T_P)$ Distribution of individual crest height for a given sea state.

$F_{C_{Th}|H_S,T_P}(c_{Th} \mid H_S, T_P)$ T-hour distribution of maximum crest heights for a given sea state.

f_D Drag term in f.

F_f Full scale force.

f_{H_S,T_P} Joint probability density function of H_S and T_P.

$F_{H_S}(h)$ Marginal distribution of H_S.

$f_{H_S}(h_S)$ Marginal probability density function for H_S.

F_{max} Largest base shear force from measurements.

F_m Model scale force.

f_M Mass term in f.

$f_{T_P|H_S}(t_P \mid h_S)$ Conditional probability density function for T_P given H_S.

g Gravitational acceleration.

g_{1,H_S} Third statistical moment of data sample, skewness.

H Wave height.

h Water depth.

h_0 Distance from flume bottom to flap hinge.

H_i Incident wave height.

H_r Reflected wave height.

H_S Significant wave height.

H_S^* H_S value of the most unfavourable sea state.

H_f Full scale wave height.

H_m Model scale wave height.

$H_{S,D}$ H_S value provided by the theoretical Donelan spectrum.

$H_{S,in}$ Input H_S value for a sea state.

$H_{S,max}$ Maximum measured H_S value from model tests of a sea state.

$H_{S,out}$ Averaged measured H_S value from model tests.

$H_{S,pile}$ Averaged measured H_S value from model tests when the pile is present.

h_{sq} H_S value corresponding to the annual q probability of exceedance.

I Impulse.

I_θ Rotational moment of inertia.

I_{xy} Second moment of inertia.

k Wave number.

k_1 Wave number corresponding to T_1.

k_n Wave number of the last wave in a wavetrain.

k_P Wave number corresponding to T_P

k_θ Rotational stiffness.

K_C Keulegan-Carpenter number.

L Length of pile.

M Total mass of the pile.

m_0 Zeroth spectral moment.

M_C Predicted moment by assuming constant impulsive load form.

M_H Measured moment from hammer test.

M_L Predicted moment by assuming linearly decreasing impulsive load form.

M_P	Measured overturning moment exerted by a plunging breaker.
M_q	Annual q-probability of exceedance overturning moment.
M_S	Predicted moment by assuming sinusoidal impulsive load form.
M_α	Overturning moment estimated from percentiles.
m_{H_S}	First statistical moment of data sample, mean value.
M_{max}	Largest overturning moment from measurements.
m_{Th}	Annual number of T-hour sea states.
n_{Th}	Number of crest heights during T [h].
$p(t)$	Time history of impulsive load.
P_0	Impulsive load magnitude.
q	Annual probability level.
R	Reflection coefficient.
R_c	Characteristic response.
R_d	Design resistance.
S	Flap motion at the top of the flap.
$S^2_{H_S}$	Second statistical moment of data sample, variance.
S_0	Flap motion at water surface level.
S_1	Mean steepness parameter.
S_d	Design load.
S_r	Real flap motion.
$S_{\zeta\zeta}(\omega)$	Wave spectrum.
S_c	Characteristic load.
T	Wave period.
T_1	Mean wave period in a sea state.
t_1	Impact duration.
T_P	Spectral peak period.
T^*_P	T_P value of the most unfavourable sea state.
T_0	Eigenperiod.
T_d	Damped eigenperiod.
t_f	Focus time of breaking wave.
t_{pq}	T_P value corresponding to the annual q probability of exceedance.
u	Horizontal water particle velocity.
u_1	First variable in standard Gaussian space.
u_2	Second variable in standard Gaussian space.
U_0	Surface roughness.
U_{10}	Mean wind speed 10 [m] above mean surface level.
U_f	Full scale velocity.
U_m	Model scale velocity.
U_r	Ursell number.
x_f	Focus point of breaking wave.
X_{Th}	Characteristic largest extreme response within a sea state of T [h] duration.
y_0	Displacement of the pile's top.
z_b	Distance from flume bottom to impact location.

List of Abbreviations

ALS	Accidental Limit State
API	American Petroleum Institute
DAF	Dynamic Amplification Factor
DNV	Det Norske Veritas
DOF	Degree of Freedom
NORSOK	Norsk Sokkels Konkuranseposisjon
FORM	First Order Reliability Method
IFORM	Inverse First Order Reliability Method
ISO	International Organisation for Standardization
JONSWAP	Joint North Sea Wave Project
LRFD	Load and Resistance Factor Design
METOCEAN	Meteorologic and Oceanographic
MOM	Method of Moments
OGP	International Assiciation of Oil and Gas Producers
PDF	Probability Density Function
PM	Pierson Moskowitz
STD	Standard Deviation
ULS	Ultimate Limit State

List of Figures

List of Tables

Sammendrag

Metocean konturlinjer tilsvarende årlig overskridelsessannsynlighet på 10^{-2} og 10^{-4} for værforholdene i Ekofisk området genereres basert på hindcast data. Den gjennomsnittlige bølgeretningen for de forskjellige sjøtilstandene brukes til å etablere konturlinjer for både nord, sør, vest og total sjø. Valgte kritiske sjøtilstander fra disse konturlinjene modelltestes for å måle ekstreme responser for en smal pel. I tillegg modelltestes spesielle bølgetog konstruert for å bryte på pelens plassering slik at brytende bølgers viktighet kan vurderes i forhold til andre ekstreme laster. For å oppnå pålitelige resultater fra modelltestingen utføres også en omfattende undersøkelse av forholdene i bølgetanken.

De fleste kritiske sjøtilstandene er basert på JONSWAP bølgespekter, mens noen sammenliknes med tilsvarende sjøtilstander basert på et Donelan bølgespekter. Modelltestene basert på Donelan spekteret fører til høyere bølgetopper og kraftigere målte responser i bunnen av pelen enn de som er basert på JONSWAP spekteret for steile sjøtilstander. Det motsatte skjer med de mindre steile sjøtilstandene, der JONSWAP spekteret fører til de verste forholdene. Derfor antas Donelan spekteret å være mest passende for de steile sjøtilstandene, mens JONSWAP bør brukes for de minst steile sjøtilstandene dersom man ønsker å oppnå de mest kritiske responsene.

Modelltesting av de valgte sjøtilstandene bestod av lavere bølger enn først antatt, noe som delvis kan forklares av mekaniske tap i bølgemaskinen. Dette kan videre ha ført til noe underestimerte karakteristiske responser. Dette bør tas hensyn til i en videreføring av dette prosjektet ved å innføre en korreksjon i signalet til bølgemaskinen slik at bevegelsen økes.

De bølge-induserte lastene fra brytende bølger anses som viktige for det globale designet av den smale pelen relativt til de karakteristiske responsene. I tillegg må store slagkraftige lokale krefter påberegnes fra mulige styrtbrytende bølger, noe som kan føre til lokal skade av strukturen eller i verste fall redusere dens totale kapasitet.

Abstract

A set of metocean contour lines corresponding to annual exceedance probabilities of 10^{-2} and 10^{-4} describing the environmental conditions at the Ekofisk area are established based on hindcast data. These are divided into different propagation directions as the total sea is composed of considerable waves from north, south and west. For the sake of measuring extreme responses of a slender pile structure, critical sea states selected from these contour lines are subjected for model testing. Wavetrains designed to break at the exact location of the pile are generated in order to investigate the importance of breaking waves relative to the extreme pile responses. A comprehensive investigation of the experimental setup is performed to ensure reliable model test results.

Model tests of critical sea states based on both the JONSWAP wave spectrum and the Donelan wave spectrum are performed for comparable reasons. The Donelan spectrum provides larger crest heights and more severe pile responses than the JONSWAP spectrum for steep sea states. For less steep sea states the opposite trend is seen. Hence, the Donelan spectrum is concluded to be most suitable for steep sea states and the JONSWAP spectrum for less steep sea states in order to obtain the most severe responses.

The critical sea states subjected for model testing are found to consist of smaller wave heights than desired partly due to mechanical losses in the wave maker. This may have led to an underprediction of the characteristic pile responses. In order to account for this in a future extension of this experiment, a correction term amplifying the wave maker motion should be introduced.

Based on the findings from this model test experiment, breaking waves are considered important for global design of the slender pile structure located south in the North Sea. In addition, tremendous impact forces exerted by plunging breakers may lead to local damage of the pile, which in worst case can harm its overall structural strength.

Chapter 1

Introduction

Introduction and problem definition

Various types of load conditions must be investigated in the design process of an offshore structure in order to ensure structural and operational safety. This thesis will concern wave-induced loads on a slender pile structure located at the Ekofisk area. The extreme environmental conditions at this location will be recreated based on the Norwegian hindcast data base, NORA10, giving weather characteristics every 3 [h] from 1957 - 2014.

The recreated environmental conditions will be subjected for model testing in the laboratory flume "Lilletanken" located at Marinteknisk Senter in Trondheim, Norway. Wave-induced pile responses under these conditions will be obtained through the model tests. As the extreme waves are presumed to be rather steep, breaking waves are expected to occur. Are breaking waves important relative to other extreme waves acting on a slender structure under the extreme environmental conditions?

Rules and regulations

Extreme events are defined by annual exceedance probability levels corresponding to the commonly used limit states: Ultimate Limit State (ULS) and Accidental Limit State (ALS). The objective of these limit states is to find environmental conditions, loads and responses with an annual exceedance probability of 10^{-2} and 10^{-4} for ULS and ALS, respectively.

A structure or a structural element is considered satisfactory designed if the design load effect S_d does not exceed the design resistance R_d. A limit state is defined when the design load is equal to the design resistance, i.e. when $S_d = R_d$ [1]. The formula for the design load effect is given in equation 1.1, where γ_{fi} represents the different load factors corresponding to the characteristic load effects S_{ci}. The design resistance can be found as shown in equation 1.2, where γ_m is the material factor and R_c is the characteristic response.

$$S_d = \sum_{i=1}^{n} \gamma_{fi} S_{ci} \tag{1.1}$$

$$R_d = \frac{1}{\gamma_m} R_c \tag{1.2}$$

Load factors γ_{fi} are meant to account for deviations from the characteristic loads, uncertainties in the model and possible load enhancement if several types of loading act simultaneously. The material factor γ_m is meant to account for deviations from the characteristic resistance in the material. This factor is generally set to 1.15 for steel and 1.2 for aluminium structures [2].

The procedure of defining the characteristic load effects and the design resistance for ULS and ALS will be explained in the following.

Ultimate Limit State (ULS)

The ULS annual probability level of exceedance is taken as the 100 year value. Two sets of load combinations applicable for all kinds of structures exist for this limit state, as given in table 1.1 [1].

Table 1.1: Load factors for the two load combinations for ULS [1].

Combination	Permanent loads	Variable loads	Environmental loads	Deformation loads
a	1.3	1.3	0.7	1.0
b	1.0	1.0	1.3	1.0

The environmental conditions are of main interest in this thesis. Different types of environmental loads can be hydrodynamic loads induced by waves and current, wind, earthquake, tidal effects or snow and ice to mention some. It should be pointed out that the environmental safety factor in combination b can be set to 1.15 if the strucutre is unmanned.

Accidental Limit State (ALS)

The ALS annual probability of exceedance is taken as the 10 000 year value. This check shall ensure that the structure does not loose the overall structural strength [3]. Both resistance to accidental actions and resistance in damaged condition are carried out in the ALS check [2]. This means that the structure shall be able to resist the 10 000 year event, as well as the environmental loads in damaged condition without any danger or failure. Minor damage is hence accepted in the ALS.

The load factors and material factor for the ALS check are generally set to 1.0 [2].

Objective

The main objective of this thesis is to find the extreme base shear responses and overturning moments of the pile when it is subjected to regular ULS and ALS annual q-probability waves, irregular waves within the critical sea states as well as plunging breaking waves. The latter also includes local impact force from the wave-structure interaction.

Intermediate objectives are:

- Establish a metocean design basis for the Ekofisk area.
- Find a selection of critical ULS and ALS sea states.
- Estimate the ULS and ALS annual q-probability waves.
- Generate regular, irregular and breaking waves in the flume.
- Measure pile responses for all the generated waves.
- Theoretical and statistical predictions of the respective wave-induced loads.

Scope

Metocean Contour Line Approach

Extreme loads and responses may be found based on the most unfavorable environmental conditions. These are estimated by a combination of statistical and probabilistic models through the metocean contour line approach. Metocean contour lines give the combinations of sea state parameters like significant wave height H_S and spectral peak period T_P that correspond to given annual exceedance probabilities [4]. The annual exceedance probabilities q are normally taken as the ULS and ALS values given in the regulations.

Waves propagating from north, south and west are expected to be significant at the Ekofisk area, such that contour lines for total sea as well as for sea states with these mean directions are established. Two dimensional waves representing the sea from one direction only may then be tested in the flume.

The contour lines do not include short term variability, which must be accounted for in the prediction of extreme wave crests and pile responses in the critical sea states found from this method. The most unfavorable sea states along the ULS and ALS contour lines provide the characteristic loads and responses of the pile. Short term variability is accounted for by introducing fractile levels for the probabilities or predetermined factors for the characteristic values [5] [6].

Model Test Experiments

Large non linear effects are expected to become important in the extreme wave conditions, which may be hard to describe theoretically. The measured pile responses from the model

tests include all relevant non-linearities as well as complex wave-structure interaction. A detailed investigation of different limitations and uncertaintes related to the experimental setup in the flume should be performed in order to ensure useful and reliable results from the model testing.

A proper scaling factor shall be chosen in order to describe the real problem as precise as possible. It is important to choose the scaling factor carefully as the different physical properties related to the geometrical model, the measurements and the load predictions must be scaled. The relation between the water depth in the flume and at the location of interest may be a limiting factor for the choice of scaling ratio if shallow water effects are of importance. In addition, the limited flume length will introduce flowfields and wave reflections not present in the full scale problem.

The tests are carried out during 4 weeks only, which means that the investigation and the tests themselves must be limited.

Critical Sea States

The objective of model testing the selected sea states is to investigate non linear behaviour, complex wave-body interaction and statistical properties within the critical ULS and ALS sea states. Time series of the irregular waves within the different sea states may be simulated by means of superposition of many regular harmonic wave components. Wave amplitudes for the different wave components may be randomly selected by use of a suitable wave spectrum.

A wave spectrum is defined in terms of the sea state parameters H_S and T_P, and often a mean propagation direction and a spreading function. The waves within a sea state may be divided into wind seas or swells, but the most severe events within the critical sea states are assumed to be composed of wind waves. Several types of wave spectrums exist in the literature, where the JONSWAP and the Donelan spectrum can be shown to be applicable for wind seas in the North Sea. A combination of wind seas and swells may be described by a Torsethaugen spectrum, which is based on the JONSWAP spectrum.

The model tests limit to investigate wind seas using the JONSWAP wave spectrum. The Donelan spectrum will be used and compared to the results when using the JONSWAP spectrum for some sea states, whereas a small theoretical study regarding the Torsethaugen spectrum will be performed.

The largest measured responses from the model tests of the critical sea states will be determined in order to predict the most severe wave-induced overturning moments and base shear responses. Probabilistic description of these measurements will be used to find the characteristic ULS and ALS pile responses by use of predetermined fractiles accounting for the short term variability [7].

The crest heights corresponding to the ULS and ALS annual q-probabilities of exceedance will be determined for waves propagating from north, south and west as well as for total sea. A theoretical approach describing the wave-induced loads from these waves by means of Morison's equation will be suggested.

Plunging Breakers

As the selected critical sea states are rather steep, some of the extreme wave crests are likely to break. Breaking waves will be studied in detail by generating a wavetrain designed to break at the location of the pile by use of wave focusing. The objective is to predict the wave-induced loads exerted by such waves on the structure as they are hard to predict theoretically and may impact with an enormous impulsive force over a limited structural area of the pile. This prediction will be calculated by recreating the measured pile responses with a dynamic response program. The importance of breaking waves compared to the regular non-breaking extreme waves may then be assessed.

Outline of the thesis

The following chapters are included in this thesis:

Metocean

Metocean contour lines for waves propagating from north, south, west and total sea are established from the NORA10 hindcast data. A selection of critical ULS and ALS sea states and annual q-probability waves will be determined.

Model test experiments

Limitations and uncertainties related to the experimental setup in the flume will be investigated in order to plan and analyze the following model tests and results as correct as possible.

Generation of critical sea states

Irregular waves within the critical sea states are generated by means of superposition of many regular wave components. A proper wave spectrum is used in order to model the different wave amplitudes. Individual and extreme crest heights will be assessed together with other measurements from the critical sea states.

Generation of a plunging breaker

A plunging breaker is generated by means of wave focusing in order to ensure a breaking wave at the location of the pile. Measured wave properties will be analyzed.

Wave-induced loads on the pile

Measured base shear responses and overturning moments exerted by regular q-probability waves, irregular waves within the critical sea states and plunging breakers will be given and compared to theoretical approaches. Morison's equation is used for the annual q-probability waves, whereas statistical description of the extreme pile responses is used for the critical sea states. The magnitude of the local impact impulsive forces from the plunging breakers are predicted by means of a simplified dynamic response model.

Chapter 2

Literature Study

Metocean

The metocean approach is a combination of meteorological and oceanographic descriptions originated by oil and gas engineers in the late 1970's. Further developments, improvements and applications of the method have been proposed by various researchers in the literature, resulting in the extensive method used today [4] [8]. The method is often combined with criterions given in different rules and regulations, for example by DNV GL [9], Norsk Sokkels konkuranseposisjon (NORSOK) [7], International Assiciation of Oil and Gas (OGP) [10], International Organisation for Standardization (ISO) [3] and American Petroleum Institute (API).

Establishment of the conotur lines based on a joint distribution of sea state parameters like significant wave height H_S and peak period T_P was proposed in 1986 [11]. The IFORM approach was proposed in order to deal with the correlation between the two parameters [6] [4]. This method was proved not to include the short term variability leading to an underprediction of about 10 - 15 % of the estimated characteristic loads and responses. Different methods accounting for the short term variability have been proposed [5], for example by introducing commonly used and highly investigated percentile levels for the estimated values [12] [13] [14].

Model Testing

Breaking waves on a Pile

The well-known Morison equation has been proven by comprehensive laboratory and field studies to provide satisfactory estimates of the forces exerted on a pile exposed to continous surface waves [15]. This equation is not suitable for a breaking wave, as it does not fulfill the assumed conditions of the equation.

The first studies of forces exerted by breaking waves were concentrated around forces on a wall rather than a pile [16] [17]. Already in the years of 1937 - 1938 a rapid pressure rise of about 50 times the hydrostatic pressure was observed in both laboratory and field studies of this phenomena [17] [18], and further development of this knowledge was of interest. The large impact load was explained by compression of entrapped air between the wall and the breaking wave [19].

An extensive laboratory study in 1958 investigated breaking waves on, prior to and after the location of a pile, concluding that the exact point of breaking is extremely important for the maximum force on the pile [20]. In these studies the total force exerted by a breaking wave was assumed to be estimated by Morison's equation with the drag coefficient being 2.5 times the original value, resulting in large impact forces [20] [21] [22]. The famous Morison equation was then expanded to include another term accounting for the impulsive force, but laboratory studies provided an underprediction of the values by this equation [23].

In 1984 the equation of the total force from a breaking wave was expanded further. In addition to the impulsive force and the force from Morison's equation, a third force representing the static pressure caused by the different water levels between leeward and seaward sides of the pile was included [24]. The forces calculated by this method were found to have triangular force intensities and slightly larger magnitudes than the forces of uniform force intensity calculated by previously proposed methods [24].

A new method for calculating impact forces of breaking waves due to random ocean waves based on experimental results and previous theoretical considerations [25] [26] was proposed in 1986. This method assumed a force acting on the upper half of the pile, a triangular force distribution along the pile and a time history of the impact force given as a linearly decreasing impulse [27]. It was shown to provide results in good agreement with the experimental results [27].

Several effects with regard to the impact force were observed under large-scaled model tests carried out in 2005. A large influence on the impact force magnitude was seen due to distance between wave breaking and pile, curling factor and pile-up effect [28].

Model test experiments of wave slamming forces on a pile by measuring local force responses at different surface elevations were carried out in 2011, assuming a triangular impulse load [29] [30]. This resulted in slightly lower force values than presented by earlier studies. In 2013 a study of wave slamming forces on truss structures for wind turbines was performed. The analysed results of that study showed that the calculated slamming forces based on previous models [28] [31], as well as the response force calculated by the duhamel integral were larger than the measured slamming force [32].

Plunging breakers

Laboratory tests at NRC indicated that not all extreme events will occur sooner or later when performing long sequence model tests of irregular waves [33]. Generation of a special wavetrain including the extreme event should be performed in order to measure the corresponding pile responses. The sweep frequency method was established in order to obtain a breaking wave at a predefined point by a set of successive waves utilizing the properties of wave groups [34] [35].

Sea state descriptions

Various wave spectrums suitable for different locations and environmental conditions have been proposed in the literature. The most severe sea states are often dominated by wind seas, whereas moderate and low sea states are often composed of both wind seas and swells [9]. The Pierson Moskowitz (PM) wave spectrum is a one-peaked wave spectrum frequently applied for describing wave conditions for fully developed wind seas [36]. The JONSWAP wave spectrum is a corrected PM spectrum that describes a growing sea state rather than a fully developed sea state [37]. The Donelan wave spectrum is a proposed correction of the JONSWAP spectrum [38]. It is shown to decrease proportional to ω^{-4} contrary to ω^{-5} which is originally used [39].

Torsethaugen wave spectrum is a two peaked wave spectrum describing both wind seas and swells [40]. This wave spectrum is based upon two JONSWAP spectrums where the parameters are empirically fitted to the Norwegian continental shelf with measurements from Haltenbanken and Statfjord [40] [41].

Chapter 3

Metocean

3.1 Introduction

The objective of this chapter is to find the sea states providing extreme loads and responses for an offshore pile structure located at the Ekofisk area. It is important to ensure a proper design under these conditions both from a safety point of view and an economical perspective. The most unfavourable environmental conditions may be found from the metocean contour lines, which are established by a combination of statistical models and probabilistic approaches.

The rules and regulations give annual probability levels of exceedance corresponding to different limit states [7]. A limit state is a design criterion ensuring that the response, with a specified probability, will not exceed a certain value. This thesis limits to the Ultimate Limit State (ULS) and the Accidental Limit State (ALS), which corresponds to annual q-probability levels of exceedance given as 10^{-2} and 10^{-4}, respectively. This means that the events most probably will occur only once every 100 years for ULS and every 10 000 years for ALS.

Statistical models describing environmental and oceanographic conditions must be established in order to estimate the events corresponding to the different limit states. This will be explained in detail in this chapter, using the approach of metocean contour lines corresponding to the two defined limit states. Then, proper estimates of long term extremes can be obtained utilizing short term methods.

3.2 Methodology

3.2.1 Establishment of metocean contour lines

Metocean contour lines are curves showing the sea states corresponding to given annual probabilities of exceedance [4]. These sea states are usually defined in terms of significant wave height H_S and spectral peak period T_P. The annual probabilities of exceedance are often taken as the ULS and ALS values as previously defined, and the goal is to determine a design sea state. The method of establishing such metocean contour lines will be explained in the following.

Joint Probability Density Function (PDF)

A scatter diagram generated from hindcasted data forms the basis of the joint probability density function for the H_S and T_P values. This function provides the long term variability, and is established by means of the marginal distribution of H_S and the conditional distribution of T_P given H_S, as shown in equation 3.1.

$$f_{H_S,T_P}(h_S, t_P) = f_{H_S}(h_S) f_{T_P|H_S}(t_P \mid h_S) \tag{3.1}$$

Marginal distribution of H_S

The distribution of H_S can be modeled as the 3-parameter Weibull distribution shown in equation 3.2 [42], where the parameters can be directly obtained from the hindcast data by the method of moments (MOM) [43] [44].

$$F_{H_S}(h_S) = 1 - \exp\left[-\left(\frac{h_S - \lambda_W}{\alpha_W}\right)^{\beta_W}\right] \tag{3.2}$$

MOM utilizes the first, second and third statistical moment of a data sample containing k datapoints. These moments are given in equation 3.3, 3.4 and 3.5, respectively.

$$m_{H_S} = \frac{1}{k}\sum_{i=1}^{k} H_{S,i} \tag{3.3}$$

$$S^2_{H_S} = \frac{1}{k-1}\sum_{i=1}^{k} (H_{S,i} - m_{H_S})^2 \tag{3.4}$$

$$g_{1,H_S} = \frac{\frac{1}{k}\sum\limits_{i=1}^{k} (H_{S,i} - m_{H_S})^3}{\left[S^2_{H_S}\right]^{3/2}} \tag{3.5}$$

Corresponding moments for the Weibull distribution can be calculated according to equation 3.6, 3.7 and 3.8 below [44]. The three distribution parameters λ_W, α_W and β_W can then be found by requiring $\gamma_{1,H_S} = g_{1,H_S}$, $\sigma^2_{H_S} = S^2_{H_S}$ and $\mu_{H_S} = m_{H_S}$.

$$\mu_{H_S} = \lambda_W + \alpha_W \Gamma\left(1 + \frac{1}{\beta_W}\right) \tag{3.6}$$

$$\sigma^2_{H_S} = \alpha^2_W \left[\Gamma\left(1 + \frac{2}{\beta_W}\right) - \Gamma^2\left(1 + \frac{1}{\beta_W}\right)\right] \tag{3.7}$$

$$\gamma_{1,H_S} = \frac{\Gamma\left(1 + \frac{3}{\beta_W}\right) - 3\Gamma\left(1 + \frac{1}{\beta_W}\right)\Gamma\left(1 + \frac{2}{\beta_W}\right) + 2\Gamma^3\left(1 + \frac{1}{\beta_W}\right)}{\left[\Gamma\left(1 + \frac{2}{\beta_W}\right) - \Gamma^2\left(1 + \frac{1}{\beta_W}\right)\right]^{3/2}} \tag{3.8}$$

Conditional distribution of T_P given H_S

The distribution of T_P given H_S can be modeled as the lognormal distribution shown in equation 3.9, where the H_S-dependent parameters $\mu_{\ln(T_P)}(h_S)$ and $\sigma_{\ln(T_P)}(h_S)$ must be estimated by curvefitting [45]. These parameters can by experience be fitted to functions of the form shown in equation 3.10 and 3.11.

$$f_{T_P|H_S}(t_P \mid h_S) = \frac{1}{\sqrt{2\pi}\sigma_{\ln(T_P)}(h_S)t_P} \exp\left[-\frac{1}{2}\left(\frac{\ln(t_P) - \mu_{\ln(T_P)}(h_S)}{\sigma_{\ln(T_P)}(h_S)}\right)^2\right] \tag{3.9}$$

$$\mu_{\ln(T_P)}(h_S) = E[\ln(T_P)] = a_0 + a_1 h_S^{a_2} \tag{3.10}$$

$$\sigma_{\ln(T_P)}(h_S) = STD[\ln(T_P)] = b_0 + b_1 \exp\left[b_2 h_S\right] \tag{3.11}$$

.

Rosenblatt transformation

The established distributions of H_S and T_P are transformed through a Rosenblatt transformation into the standard Gaussian space, as shown in equation 3.12 and 3.13. This is done in order to remove the correlation between H_S and T_P. The two new variables, u_1 and u_2, are then forming circles in the standard Gaussian space defined by the given annual q-probabilities of exceedance. Contour lines in the physical space are obtained by an inverse Rosenblatt transformation of the obtained circles. This method is often referred to as the Inverse First Order Reliability Method (IFORM) and the procedure is shown in figure 3.1. In physical space the contour lines are defined in terms of H_S and T_P, and the correlation between these two variables is then reintroduced. Rosenblatt transformation preserve probabilities, such that the contour lines in physical space also correspond to the required annual q-probabilities of exceedance.

$$\Phi(u_1) = F_{H_S}(h_S) \tag{3.12}$$

$$\Phi(u_2) = F_{T_P|H_S}(t_P \mid h_S) \tag{3.13}$$

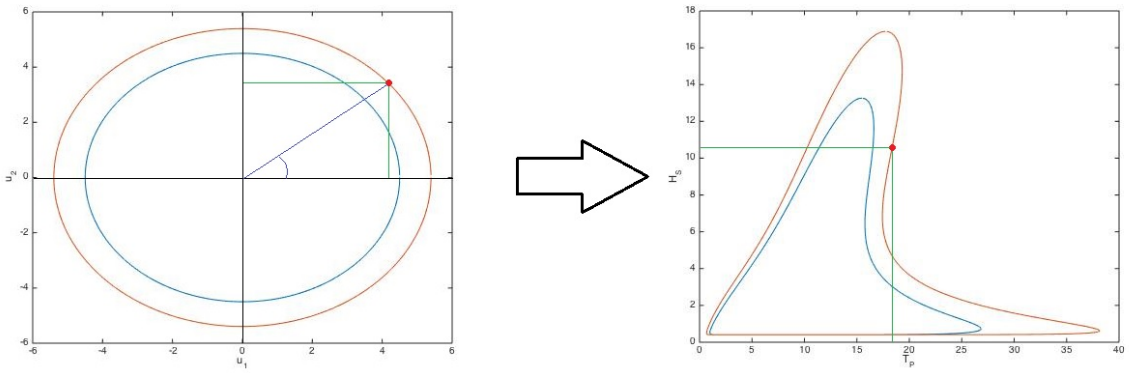

Figure 3.1: Transformation of the contour lines from standard Gaussian space to physical space.

q-probability sea state parameters

The H_S value with an annual q-probability of being exceeded, termed h_{sq}, can be estimated by use of the marginal distribution of H_S. It is found by solving equation 3.14 with respect to h_{sq}, where m_{Th} is the number of T-hour sea states during one year.

$$F_{H_S}(h_{sq}) = 1 - \frac{1}{m_{Th}} \tag{3.14}$$

The corresponding T_P value, termed t_{pq}, may be given as a 90 percent band. That is, the range of T_P values that with a probability of 0.9 will belong to the estimated h_{sq} value. These bounds, termed t_θ, can be calculated according to equation 3.15, where z_θ are the probability values taken as 0.05 and 0.95.

$$t_\theta = \exp\left[\mu_{\ln(T_P)}(h_{sq})\right] + z_\theta \sigma_{\ln(T_P)}(h_{sq})\Big] \tag{3.15}$$

3.2.2 Short term description of long term extremes

The extreme crest heights are of main interest as the offshore pile structure shall be designed to resist these in a satisfactory manner. Prediction methods of the extreme crest heights and pile responses will be presented in the following.

T-hour distribution of extreme crest heights

If the surface elevation within a sea state is assumed to be a realization of a Gaussian process, the Forristall distribution will provide proper estimates for the individual crest heights C influenced by second order effects [46]. This distribution is based on the 2-parameter Weibull distribution shown in equation 3.16, where the parameters can be determined by the empirical formulas given in equation 3.17 and 3.18. These parameters characterize the degree of non linearity in the waves [46] and the distribution can hence be said to depend on H_S and T_P as they are central in these formulas.

$$F_{C|H_S,T_P}(c \mid H_S, T_P) = 1 - \exp\left[-\left(\frac{c}{\alpha_F H_S}\right)^{\beta_F}\right] \tag{3.16}$$

$$\alpha_F = 0.3536 + 0.2892 S_1 + 0.1060 U_r \tag{3.17}$$

$$\beta_F = 2 - 2.1597 S_1 + 0.0968 U_r^2 \tag{3.18}$$

The Ursell number U_r and the steepness parameter S_1 are given in equation 3.19 and 3.20, respectively. Here k_1 is the wave number corresponding to the mean wave period T_1 and h is the water depth [9].

$$U_r = \frac{H_S}{k_1^2 h^3} \tag{3.19}$$

$$S_1 = \frac{2\pi}{g}\frac{H_S}{T_1^2} \tag{3.20}$$

The mean wave period T_1 can be calculated by equation 3.21 when the peak shape parameter γ_S of the wave spectrum is known [9]. This parameter can be calculated according to equation 3.22 by use of H_S and T_P.

$$\frac{T_1}{T_P} = 0.7303 + 0.04936\gamma_S - 0.006556\gamma_S^2 + 0.0003610\gamma_S^3 \tag{3.21}$$

$$\gamma_S = \begin{cases} 5 & \text{if } \frac{T_P}{\sqrt{H_S}} \leqslant 3.6 \\ \exp\left(5.75 - 1.15\frac{T_P}{\sqrt{H_S}}\right) & \text{if } 3.6 < \frac{T_P}{\sqrt{H_S}} < 5.0 \\ 1 & \text{if } \frac{T_P}{\sqrt{H_S}} \geqslant 5 \end{cases} \tag{3.22}$$

Assuming identical distribution and independency of the individual crest heights, the T-hour distribution can be expressed as shown in equation 3.23. Here n_{Th} is the number of crest heights during T [h], as given in equation 3.24.

$$F_{C_{Th}|H_S,T_P}(c_{Th} \mid H_S, T_P) = \left[F_{C|H_S,T_P}(c \mid H_S, T_P)\right]^{n_{Th}} \tag{3.23}$$

$$n_{Th} = \frac{Th \cdot 60 \cdot 60}{T_1} \tag{3.24}$$

T-hour distribution of extreme pile responses

The largest maximum responses X_{Th} during a given sea state of T-hour duration may be modeled by the Gumbel distribution shown in equation 3.25. This distribution of extreme values is a good description of the upper tail of exponentially shaped distributions [47] [48].

$$F_{X_{Th}|H_S T_P}(x_{Th} \mid H_S, T_P) = \exp\left[-\exp\left[-\frac{x_{Th} - \alpha_G}{\beta_G}\right]\right] \tag{3.25}$$

The distribution parameters α_G and β_G can be estimated from a response data sample using MOM, as shown in equation 3.26 and 3.27, respectively [44]. Here μ_X is the mean value and σ_X the standard deviation of the response data sample.

$$\alpha_G = \mu_X - 0.57722\beta_G \tag{3.26}$$

$$\beta_G = 0.7797\sigma_X \tag{3.27}$$

Short term description of long term response

The most unfavourable sea states along the ULS and ALS contour lines are taken as those providing the most extreme responses in both limit states [7]. Responses estimated from the metocean contour lines will be underpredicted by about 10 - 15 % for linear response problems, and even more for non linear response problems, as the short term variability is neglected in this method [4]. The literature suggests several methods on how to account for the short term variability due to different short term sea state realizations. One suggestion is to multiply the mean value with a predetermined factor [6], another one is to introduce the fractile levels [5] given in table 3.1 [7]. Using these fractiles, the extreme crest heights and responses corresponding to the different limit states, termed C_{Th} and X_{Th}, can be found by equation 3.28 and 3.29, respectively. Here H_S^* and T_P^* represent sea state parameters for the most unfavourable sea state along the contour line. Estimates of the characteristic largest crest height and response are then obtained based on a short term analysis of this sea state. Such simplified results should be verified by a long term analysis or model testing [7].

Table 3.1: Fractile levels for ULS and ALS given in NORSOK [7].

Limit State	Lower α_f	Upper α_f
ULS	85 %	90 %
ALS	90 %	95 %

$$F_{C_{Th}|H_S,T_P}\left(C_{Th} \mid H_S^*, T_P^*\right) = \alpha_f \tag{3.28}$$

$$F_{X_{Th}|H_S,T_P}(X_{Th}|H_S^*, T_P^*) = \alpha_f \tag{3.29}$$

Full long term analysis

The full long term analysis accounts for the short term variability as well as the long term variability of the different sea states [11]. Integrating these two as shown in equation 3.30 and 3.31, the long term distribution of crest height and response is obtained, respectively.

$$F_{C_{Th}}(c) = \int_{h_S} \int_{t_P} F_{C_{Th}|H_S,T_P}(c \mid h_s, t_p) f_{H_S T_P}(h_s, t_p) dt_p dh_s \tag{3.30}$$

$$F_{X_{Th}}(x) = \int_{h_S} \int_{t_P} F_{X_{Th}|H_S,T_P}(x \mid h_s, t_p) f_{H_S T_P}(h_s, t_p) dt_p dh_s \tag{3.31}$$

The characteristic largest crest heights and responses corresponding to an annual exceedance probability q are then determined by solving equation 3.32 and 3.33 with respect to C_{Th} and X_{Th}, respectively. Here m_{Th} is the annual number of T-hour sea states.

$$F_{C_{Th}}(C_{Th}) = 1 - \frac{q}{m_{Th}} \tag{3.32}$$

$$F_{X_{Th}}(X_{Th}) = 1 - \frac{q}{m_{Th}} \tag{3.33}$$

3.3 Processing the hindcast data

The hindcast data are related to the Ekofisk area south in the North Sea, as shown in figure 3.2. Spectral parameters like H_S and T_P have been estimated for sea states with a 3 [h] duration throughout 57 years. These data form the basis for the investigation of the environmental conditions at the desired location.

Figure 3.2: Location of the hindcasted data: Latitude: 56.31, Longitude: 3.41.

The hindcasted $T_{P,hind}$ values are discrete variables with logarithmic spacing including only one decimal. This combination leads to an increasing difference between cohesive values of $T_{P,hind}$, as shown in figure 3.3. To prevent the scatter diagram to include zero-columns, a randomized correction to the hindcasted $T_{P,hind}$ values are performed as shown in equation 3.34 below, where i is calculated according to equation 3.35 and rnd is a random uniformly distributed number between 0 and 1. The effect of such a randomizing of the T_P values are shown in figure 3.4.

$$T_P = 3.244 \exp\left[0.09525(i - 0.5 - rnd)\right] \tag{3.34}$$

$$i = ROUND\left[1 + \frac{\ln(T_{P,hind}/3.244)}{0.09525}\right] \tag{3.35}$$

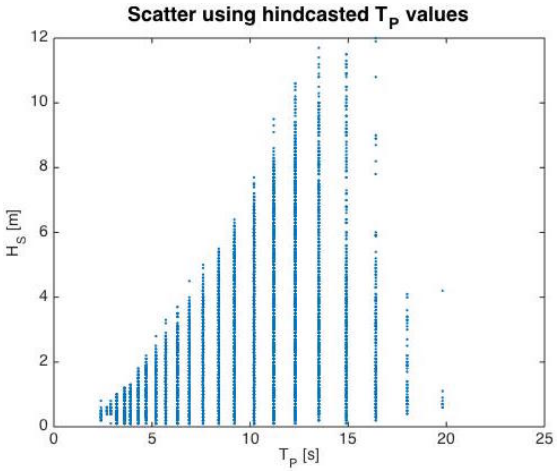

Figure 3.3: Scatter using the original $T_{P,hind}$ values.

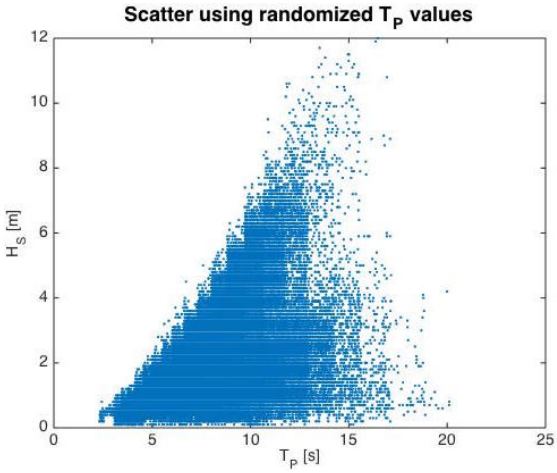

Figure 3.4: Scatter using the randomized T_P values.

Using the randomized T_P values, the sea states are grouped into classes for both H_S and T_P in a scatter diagram. A step of 0.5 [m] is used for H_S and a step of 1 [s] is used for T_P. The joint PDF for H_S and T_P is based on this diagram, as a marginal distribution of H_S and a conditional distribution of T_P given H_S are estimated. This is further used to establish the contour lines.

There will most likely be sea of significance from both north, south and west, while the sea from east may be of minor interest at this location. The mean direction of the sea within the different sea states is therefore subjected for further investigation. Four sectors are used for division of the total sea as shown in figure 3.5. Then the environmental conditions can be investigated based on which direction the seas are propagating from.

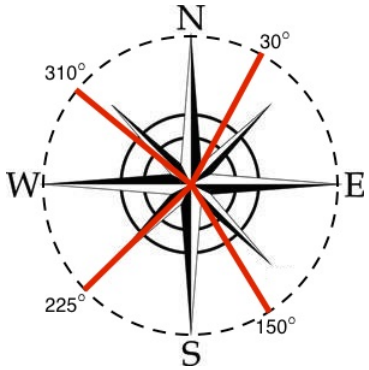

Figure 3.5: Sectors used for division of the total sea.

3.4 Results

3.4.1 Annual number of sea states

When dividing the sea states from the hindcast data into different directions, the annual number of sea states m_{3h} becomes as shown in table 3.2 below. The annual exceedance probabilities q will hence be divided by these values in order to establish the respective contour lines.

Table 3.2: Total- and annual number of sea states.

Direction	Total number of sea states	Annual number of sea states, m_{3h}
North	57 445	1010
South	31 359	551
West	44 382	780
Total	166 051	2920

3.4.2 Scatter diagram

The scatter diagram for the total sea is shown in figure 3.6 below. Scatter diagrams regarding waves from north, south and west can be found in appendix B.1.

Hs \ Tp		0	1	2	3	4	5	6	7	8	9	10	11	12	13	14	15	16	17	18	19	20	sum
		1	2	3	4	5	6	7	8	9	10	11	12	13	14	15	16	17	18	19	20	21	
0.0	0.5	0	6	87	362	36	48	66	50	39	50	17	8	5	8	5	1	1	0	0	0	0	789
0.5	1.0	0	23	539	4591	5828	2625	1417	1103	824	540	334	195	115	67	42	38	19	8	5	1	1	18315
1.0	1.5	0	1	77	2384	8775	9944	5337	3078	2398	1555	813	432	217	105	68	42	25	12	3	2	1	35269
1.5	2.0	0	0	0	124	3345	10004	7865	4106	2421	2122	1334	673	293	132	76	32	16	4	1	0	0	32548
2.0	2.5	0	0	0	2	335	4531	8661	5002	2221	1413	1264	732	361	147	57	22	20	3	4	0	0	24775
2.5	3.0	0	0	0	0	10	839	5526	5772	2336	948	652	611	345	146	60	13	7	1	0	0	0	17266
3.0	3.5	0	0	0	0	1	71	1960	5043	2777	936	441	330	236	131	51	24	8	2	1	0	0	12012
3.5	4.0	0	0	0	0	0	6	408	2984	2984	1132	336	204	149	86	39	17	8	3	1	0	0	8357
4.0	4.5	0	0	0	0	0	0	49	1201	2701	1256	416	164	79	38	46	11	7	2	1	0	0	5971
4.5	5.0	0	0	0	0	0	0	4	260	1814	1264	421	137	49	25	29	6	3	0	0	0	0	4012
5.0	5.5	0	0	0	0	0	0	0	37	758	1070	496	151	38	16	15	7	3	0	0	0	0	2591
5.5	6.0	0	0	0	0	0	0	0	5	171	868	474	152	58	11	7	0	1	0	0	0	0	1747
6.0	6.5	0	0	0	0	0	0	0	0	21	367	327	173	63	10	5	6	2	0	0	0	0	974
6.5	7.0	0	0	0	0	0	0	0	0	2	119	231	157	82	17	4	0	0	0	0	0	0	612
7.0	7.5	0	0	0	0	0	0	0	0	0	26	135	81	53	17	5	1	0	0	0	0	0	318
7.5	8.0	0	0	0	0	0	0	0	0	0	6	47	62	35	16	3	0	0	0	0	0	0	169
8.0	8.5	0	0	0	0	0	0	0	0	0	0	26	42	28	17	8	1	1	0	0	0	0	123
8.5	9.0	0	0	0	0	0	0	0	0	0	0	4	21	21	17	4	1	0	0	0	0	0	68
9.0	9.5	0	0	0	0	0	0	0	0	0	0	0	15	8	9	7	5	0	0	0	0	0	44
9.5	10.0	0	0	0	0	0	0	0	0	0	0	2	8	11	8	5	0	0	0	0	0	0	34
10.0	10.5	0	0	0	0	0	0	0	0	0	0	0	3	10	9	5	1	0	0	0	0	0	28
10.5	11.0	0	0	0	0	0	0	0	0	0	0	0	1	4	2	2	0	0	0	0	0	0	9
11.0	11.5	0	0	0	0	0	0	0	0	0	0	0	0	3	2	9	1	0	0	0	0	0	15
11.5	12.0	0	0	0	0	0	0	0	0	0	0	0	0	0	3	2	0	0	0	0	0	0	5
sum		0	30	703	7463	18330	28068	31293	28641	21467	13672	7770	4352	2263	1039	554	229	121	35	16	3	2	166051

Figure 3.6: Scatter diagram for total sea.

3.4.3 Marginal distribution of H_S

The estimated marginal distribution of H_S for the total sea is shown in figure 3.7, and the three parameters in this Weibull distribution are found in table 3.3. Distributions together with their corresponding parameters for waves propagating from the other directions can be found in appendix B.2.

Table 3.3: Estimated parameters for the three parameter Weibull distribution for total sea.

Parameter	Estimated value
α_W	1.7078
β_W	1.2548
λ_W	0.4104

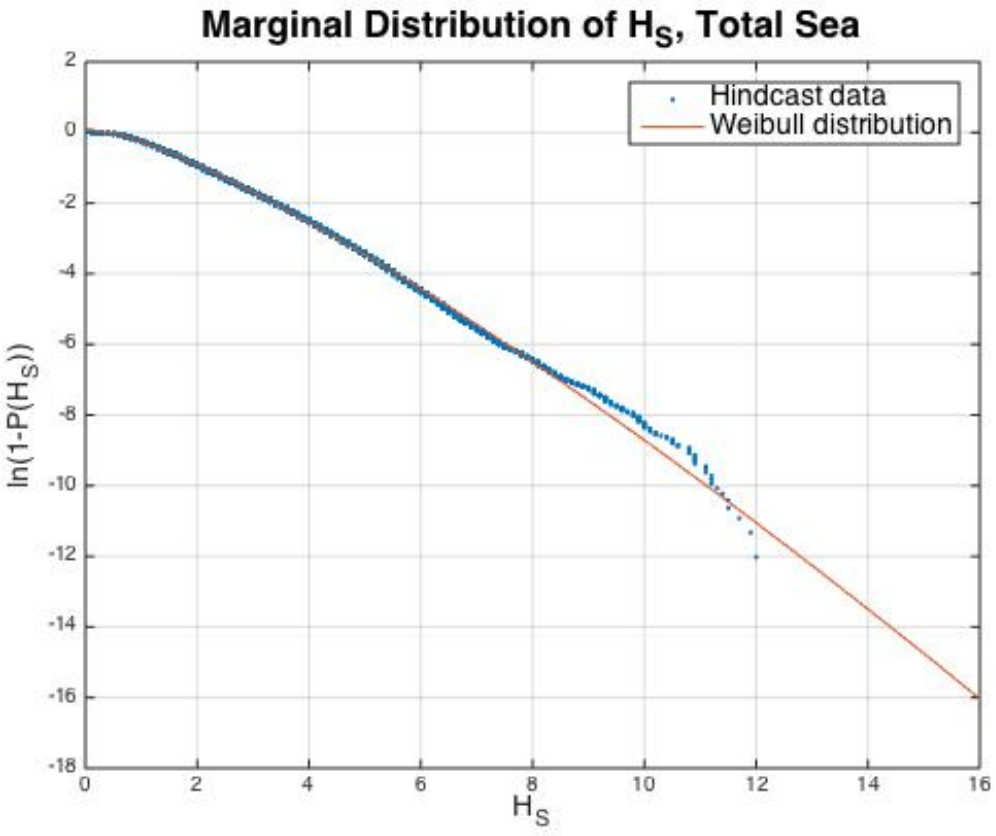

Figure 3.7: Marginal distribution of H_S for total sea.

3.4.4 Conditional distribution of T_P given H_S

The conditional distribution of T_P given H_S for the total sea is established based on the scatter diagram in figure 3.6. The curvefitting for the expected value is based upon equation 3.10. Using the coefficients shown in table 3.4 the function in figure 3.8 is obtained.

Table 3.4: Estimated coefficients for the expected value of $\ln(T_P)$ given H_S for total sea.

Coefficient	Estimated value
a_0	0.9344
a_1	0.8256
a_2	0.3024

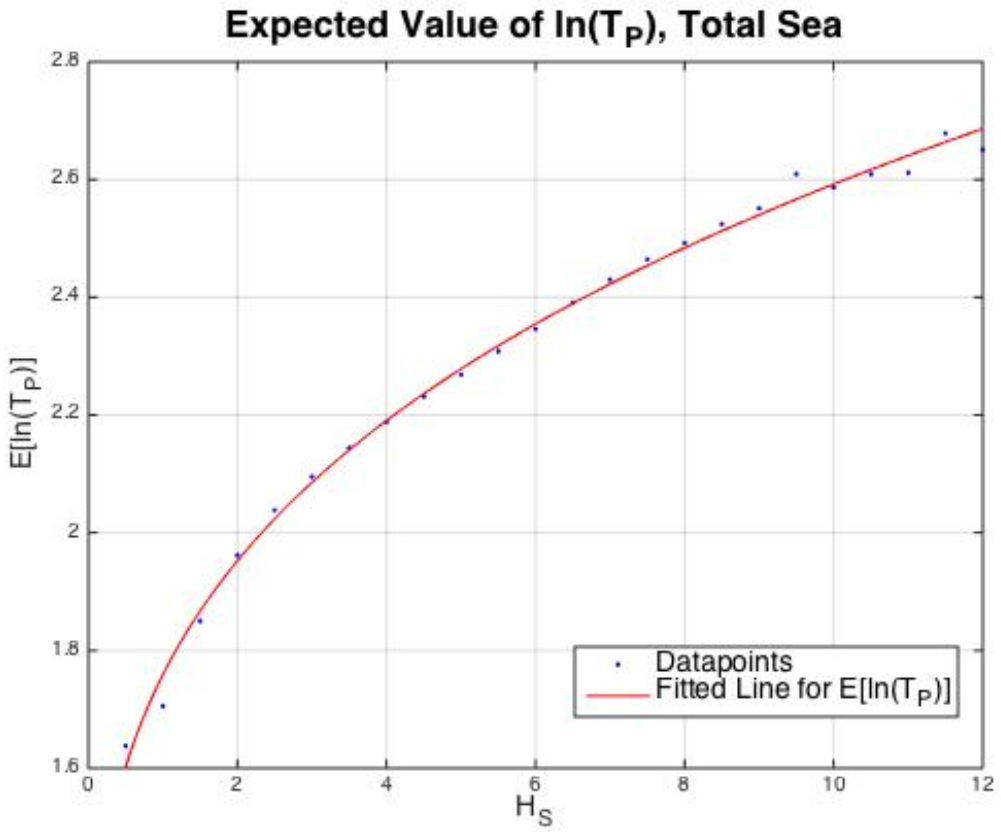

Figure 3.8: Curvefitting for the expected value for T_P given H_S for total sea.

The curvefitting for the standard deviation is based upon equation 3.11. Using the coefficients in table 3.5, the H_S-dependent function shown in figure 3.9 is obtained.

Table 3.5: Estimated coefficients for the standard deviation of $\ln(T_P)$ given H_S for total sea.

Coefficient	Estimated value
b_0	0.0765
b_1	0.4214
b_2	0.4741

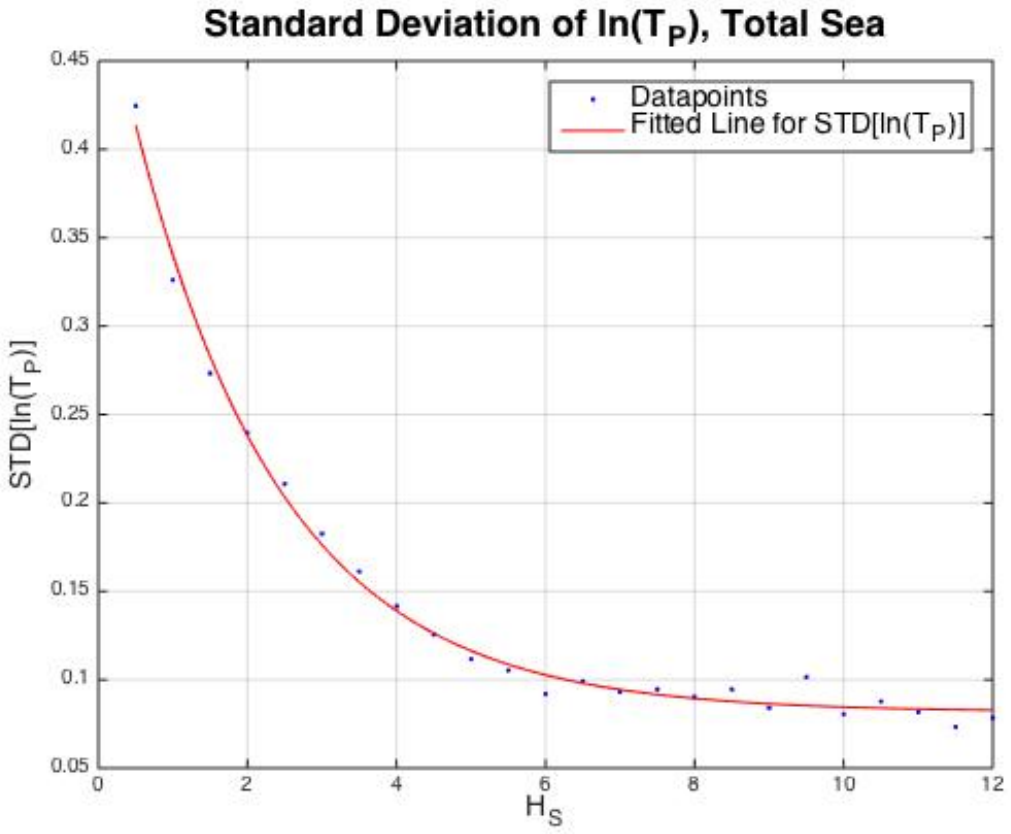

Figure 3.9: Curvefitting for the standard deviation of T_P given H_S for total sea.

Functions and coefficients from curvefitting for the waves propagating from north, south and west can be found in appendix B.3.

3.4.5 Contour lines

Contour lines for both ULS and ALS for the total sea are shown in figure 3.10 together with the hindcast data. The contour lines for waves propagating from north, south and west can be found in appendix B.4.

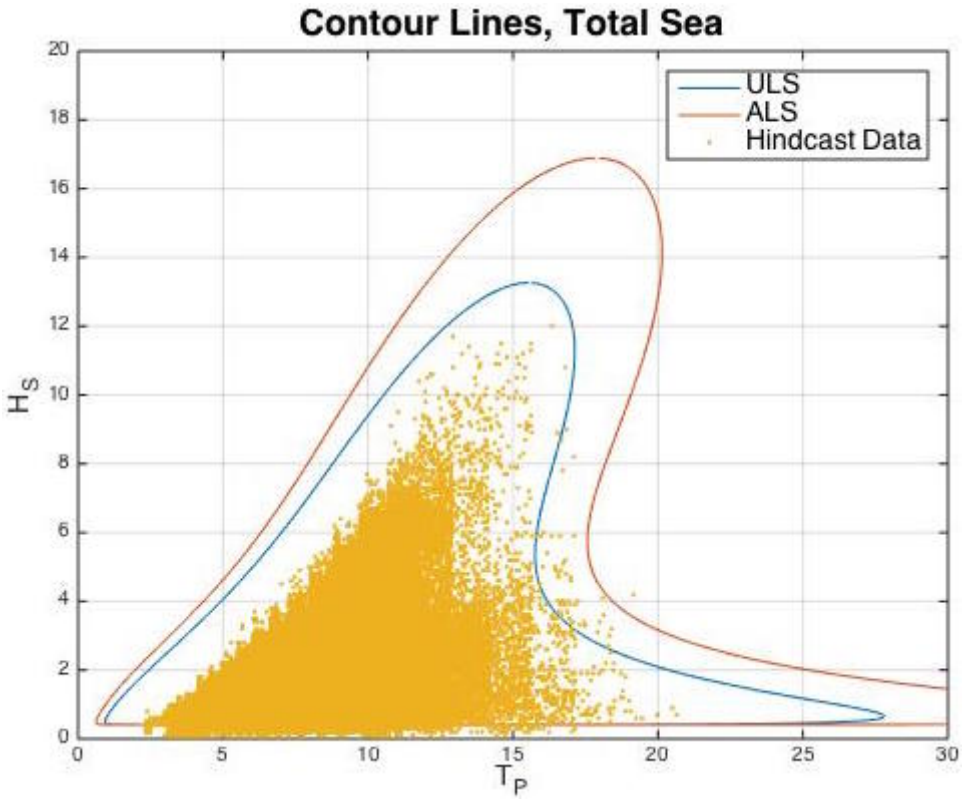

Figure 3.10: ULS and ALS contour lines for total sea.

3.4.6 q-probability values

The h_{sq} values for the total sea with corresponding 90 percent bands for t_{pq} are given in table 3.6 for ULS and ALS. Corresponding extreme crest heights are found by using the T-hour distribution from equation 3.28 with T = 3 [h] and suitable percentile levels from table 3.1. Tables for waves propagating from north, south and west can be found in appendix C.

Table 3.6: h_{sq} values with 90 percent bands for t_{pq} and the corresponding largest C_q for both ULS and ALS regarding total sea.

	h_{sq} [m]	t_{pq} [s]	C_q [m]
ULS	13.26	15.51 - 16.67	15.69
ALS	16.89	17.78 - 19.10	20.79

3.5 Discussion and Recommendations

It is recommended to have at least 10, preferably up to 20 years of data available in order to obtain reliable extreme value predictions. The hindcast data are based upon 57 years, which is well within the preferable number of years.

3.5.1 Accuracy of the marginal distribution of H_S

The marginal distributions of H_S for total sea and waves propagating from north are found to be good estimates as the measured hindcast data follow these distributions without any large deviations. The estimated distributions regarding waves from south and west are found to be somewhat poorer as the measurements deviate for H_S values above 6 [m] and 8 [m], respectively. Bootstrapping by use of 100 Monte Carlo simulations is performed in order to evaluate the estimated distributions in detail, assuming independency between the different H_S values. The bootstappings are shown in appendix B.5, and is exemplified by figure 3.11 below which shows the distribution of waves propagating from south.

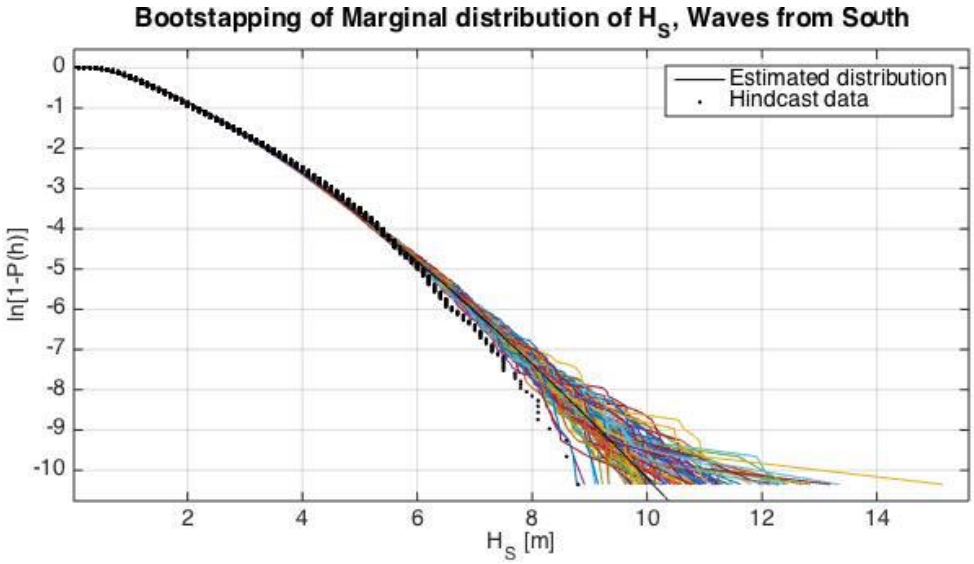

Figure 3.11: Bootstrapping by means of Monte Carlo simulation for the marginal distribution of H_S for waves propagating from south.

It can be seen that the hindcasted datapoints fall somewhat below the range given by 100 Monte Carlo simulations regarding the waves propagating from south. If the assumption of completely independent H_S values holds, the established distribution may not predict satisfactory values for higher H_S. A further improvement of this distribution, for example by introducing a hybrid distribution [11], may hence be of interest in further work.

The estimated h_{sq} values for waves propagating from all directions with corresponding 90 % bands based on the 100 Monte Carlo simulations are given in table 3.7. All the estimated h_{sq} values are seen to lie within the 90 % bands. These uncertainty bands are quite narrow, as the distributions assumes independent H_S values.

Table 3.7: Annual q-probability values for waves propagating from north, south and west as well as for the total sea with 90 % bands.

	ULS		**ALS**	
	h_{sq} [m]	90 % band [m]	h_{sq} [m]	90 % band [m]
North	13.79	13.47 - 14.10	18.57	18.06 - 19.09
South	10.48	10.29 - 10.67	13.36	13.06 - 13.66
West	12.52	12.33 - 12.76	16.01	15.71 - 16.36
Total	13.26	13.09 - 13.40	16.89	16.64 - 17.11

In reality there will be a certain dependency of succeeding sea states, which means that the Monte Carlo simulations may not provide realistic data samples. Table 3.8 gives the 90 % bands of the annual largest H_S values from the hindcast data and the corresponding 90 % bands by means of Monte Carlo simulation. The latter assumes independent H_S values and are shown to provide somewhat narrower bands than the hindcast values. This implies a significant dependency of succeeding H_S values in reality, such that the bootstrappings of the H_S-distributions give a much narrower scatter than they should have based on the real conditions. Hence, the uncertainty bands given for the h_{sq} values in table 3.7 are too small.

Table 3.8: 90 % bands of the annual largest H_S values for waves propagating from north, south and west as well as for the total sea from hindcast data and Monte Carlo simulation.

	Annual largest H_S [m]	
	Hindcast	Monte Carlo
North	6.00 - 11.20	7.50 - 11.37
South	4.50 - 8.10	6.17 - 9.42
West	6.20 - 11.20	8.09 - 10.74
Total	6.60 - 11.50	8.18 - 11.00

3.5.2 Standard deviation of $\ln(T_P)$

The limiting values of $\sigma_{\ln(T_P)}(h)$, as well as the variance $\sigma^2_{\ln(T_P)}(h)$, for increasing wave heights are given in table 3.9. They are found from figure B.8, B.10 and B.12 in appendix B.3 for the directional sea and in figure 3.9 for the total sea. By experience the variance

for $\ln(T_P)$ normally approaches 0.002 [s^2] in the North Sea [49], where the main part of the waves propagate from one direction only. The variance for the total sea at the Ekofisk area is found to be 3.6 times larger than normal. Here the waves are propagating from several directions, and the variance for $\ln(T_P)$ is found to be closer to 0.002 [s^2] for the directional sea, especially from north. For waves propagating from west, the variance is found to be somewhat larger again.

Table 3.9: Limiting values for the standard deviation of $\ln(T_P)$.

	$\sigma_{\ln(T_P)}(h)$ [s]	$\sigma^2_{\ln(T_P)}(h)$ [s^2]
North	0.050	0.0025
South	0.055	0.0030
West	0.070	0.0049
Total	0.085	0.0072

3.5.3 ULS and ALS contour lines

A range of critical sea states will be selected both from the ULS and ALS contour lines. The waves within these sea states are expected to be generally steep, and large non linear effects are assumed to become important. Model testing of these are hence recommended in order to ensure that no non linear behaviour is overseen.

As the contour lines for total sea are composed of waves propagating from several directions, the ULS and ALS contour lines for the directional sea will be used in the selection of these sea states. The most severe sea states are then assumed to propagate in one direction only, which is highly appropriate as two dimensional waves is the only test option in the flume.

The ULS and ALS contour lines obtained for waves propagating from north, south and west are compared in figure 3.12 and 3.13, respectively. It is clear that the sea states with highest H_S values are found among those propagating from north, whereas some of the steepest sea states can be found among those propagating from west.

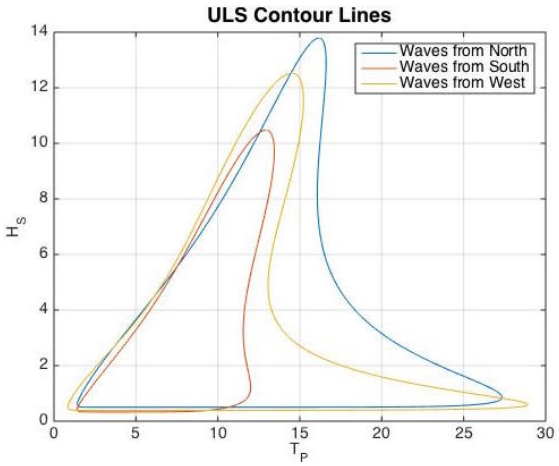

Figure 3.12: Comparison of the ULS contour lines for waves propagating from north, south and west.

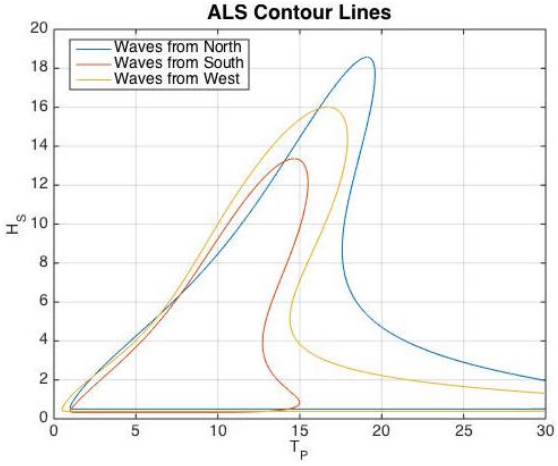

Figure 3.13: Comparison of the ALS contour lines for waves propagating from north, south and west.

Critical sea states

The m_{3h} values in table 3.2 were wrongly calculated in an early phase of this project, leading to improper contour lines. The sea states found based on these contours are the ones subjected for model testing, which means that the contour lines presented in this chapter are not used in the selection of the critical sea states.

The critcal ULS and ALS sea states subjected for model testing are given in table 3.10. They are based on the wrongly established contour lines in figure 3.14 and 3.15, and selected such that the most unfavourable sea state for both limit states are included. The H_S values are chosen such that they are equally distributed along the range, and the corresponding lowest T_P values are selected. This is done in order to ensure that the sea states with the steepest waves are selected.

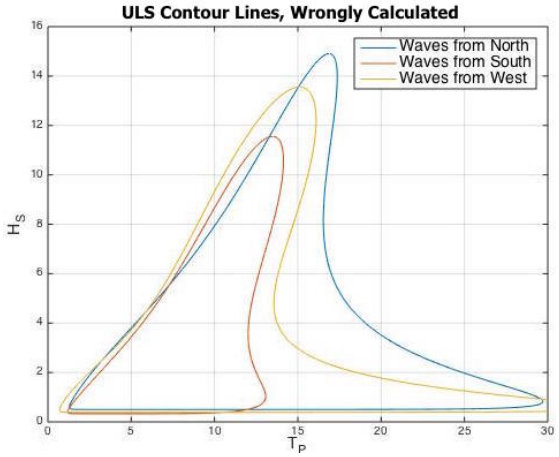

Figure 3.14: Wrongly established ULS contour lines.

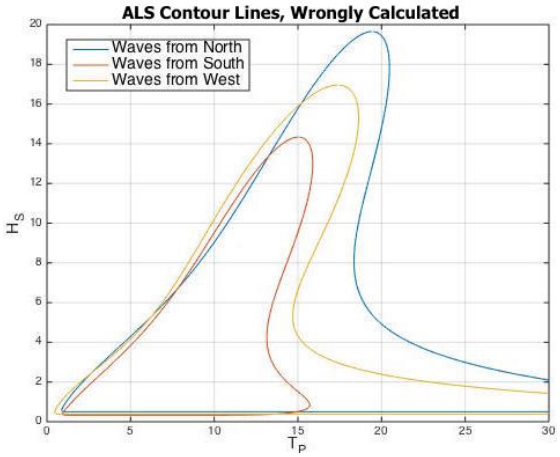

Figure 3.15: Wrongly established ALS contour lines.

Correct sea states based on the contour lines established in this chapter as presented in figure 3.12 and 3.13 are also given in table 3.10. These are chosen to have the same T_P values as the wrongly selected sea states as the H_S values are expected to be somewhat reduced in the model tesing. A comparison between these sea states and the obtained sea states from model testing will therefore be possible.

The sea state steepness ε_{SS} is given in equation 3.36 and used to compare the correct sea states to the wrongly established sea states subjected for model testing. Here k_P is the wave number corresponding to the T_P values.

$$\varepsilon_{SS} = \frac{H_S}{\lambda_P} = \frac{H_S k_P}{2\pi} \tag{3.36}$$

Table 3.10: Critical sea states.

Limit	**Wrong Contour Lines**			**Correct Contour Lines**		
State	H_S [m]	T_P [s]	ε_{SS} [-]	H_S [m]	T_P [s]	ε_{SS} [-]
ULS	10.00	10.55	0.0576	9.40	10.55	0.0542
	11.00	11.48	0.0537	10.40	11.48	0.0508
	12.00	12.38	0.0507	11.40	12.38	0.0482
	13.00	13.71	0.0456	12.20	13.71	0.0427
	14.00	15.40	0.0402	13.42	15.40	0.0385
	14.91	16.76	0.0374	-	-	-
ALS	12.00	11.30	0.0605	11.70	11.30	0.0589
	13.00	12.00	0.0583	12.58	12.00	0.0564
	14.00	13.00	0.0540	13.74	13.00	0.0530
	15.00	14.00	0.0506	14.60	14.00	0.0493
	16.00	15.20	0.0469	15.50	15.20	0.0454
	17.00	16.00	0.0458	15.88	16.00	0.0428
	18.00	16.90	0.0445	16.88	16.90	0.0418
	19.00	18.00	0.0427	17.95	18.00	0.0404
	19.60	19.40	0.0408	18.48	19.40	0.0373

The sea states subjected for model testing are seen to have larger H_S values than the correct ones, leading to a somewhat higher sea state steepness for the wrongly selected sea states. These differences are rather small, especially for ALS, and can hence be assumed to be complemented by the expected uncertainties related to model testing. The differences between the correctly and wrongly selected sea states for ULS and ALS are shown in figure 3.16 and 3.17, respectively

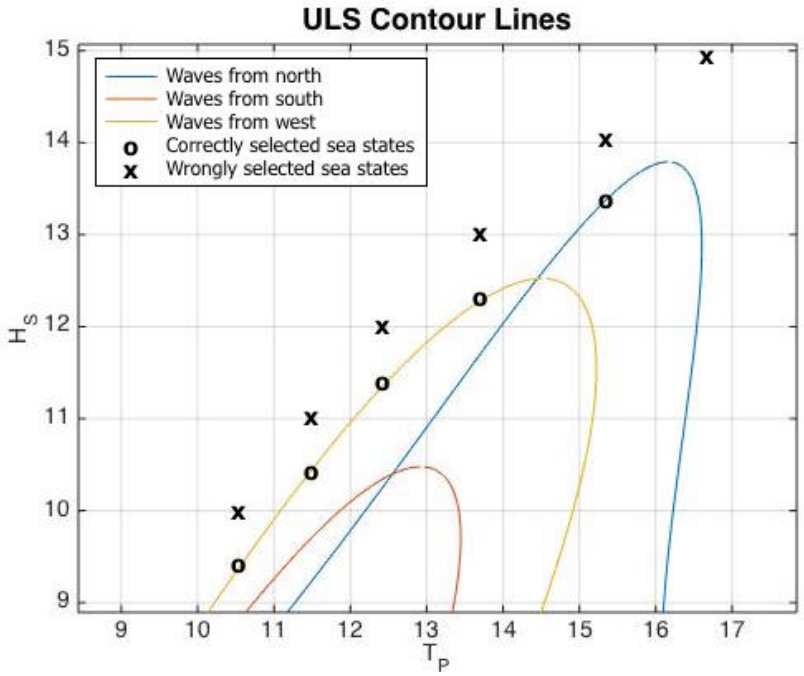

Figure 3.16: Differences between correctly and wrongly selected critical ULS sea states.

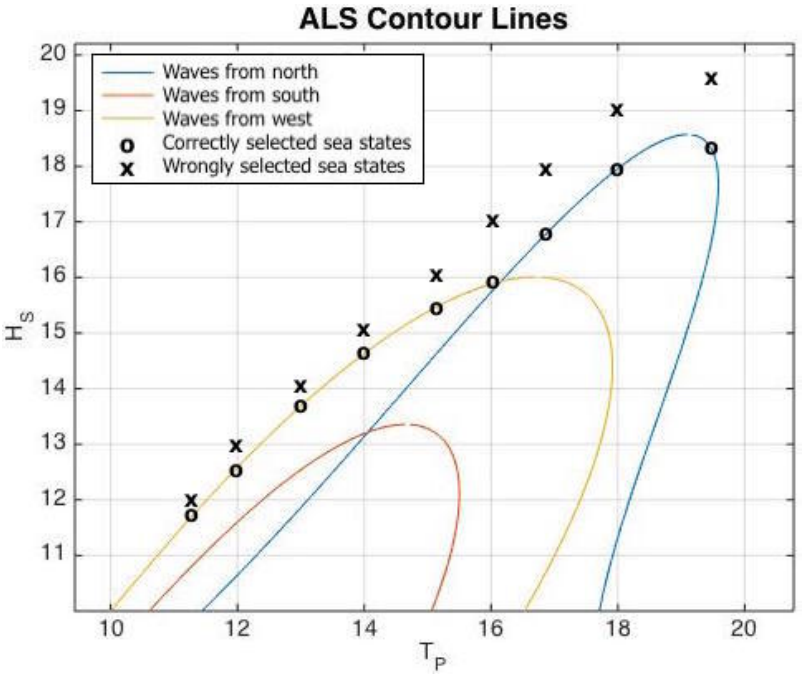

Figure 3.17: Differences between correctly and wrongly selected critical ALS sea states.

Chapter 4

Model Test Experiments

4.1 Introduction

4.1.1 Model testing

Engineering problems in relation to non linear hydrodynamic behaviour may be hard to describe theoretically. Non-linearity is often seen for extreme wave conditions and theoretical estimates of wave-body interactions under such conditions shall hence be supported by model tests [1]. The objective of model testing is to investigate features not supported in the literature. The tests should cover uncertainties related to the experimental setup and ensure that no hydrodynamic features have been overlooked.

Note that all the values in this chapter will be given in model scale.

4.1.2 Experimental setup

The model tests are conducted in one of the flumes at MARINTEK's hydrodynamic laboratories in Trondheim, Norway. The geometrical dimensions of the flume are given in table 4.1.

Table 4.1: Geometrical dimensions of the flume.

Dimension	[m]
Length	27.3
Width	2.8
Water depth	0.97

The flume is equipped with a wave maker of flap type hinged 8 [cm] above the bottom in one of the ends, while a wave absorbing beach is found at the opposite end. The pile is installed together with waveprobes unequally distributed over the flume's length, as shown in figure

4.1. This figure also shows the distances from the wave maker to the different elements installed. A waveprobe is placed beside the pile when the pile is present, whereas it is placed at the location of the pile when the pile is absent. Pile information and dimensions are given in table 4.2.

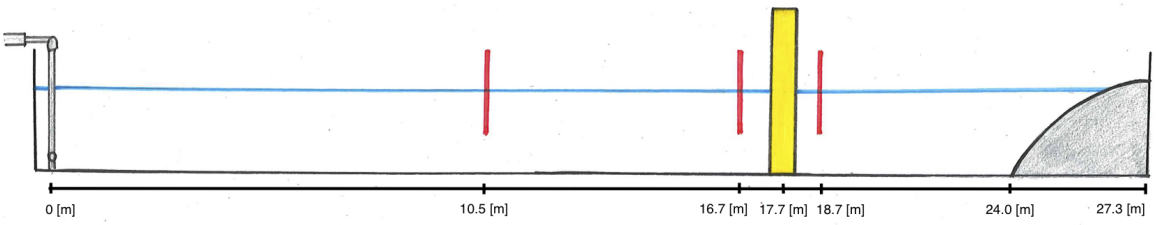

Figure 4.1: The experimental setup in the flume.

Table 4.2: Pile dimensions and information.

Outer diameter	D_o	0.16	[m]
Inner diameter	D_i	0.15	[m]
Length	L	1.53	[m]
Density	ρ_{alu}	2700	$\left[\frac{kg}{m^3}\right]$
Youngs modulus	E_{alu}	70	[GPa]

4.1.3 Uncertainties and limitations

A large number of uncertainties and limitations are introduced when performing model tests of a full scale problem. These are important to investigate as they may influence the results. To describe the location of interest as precise as possible a proper scaling factor must be determined, and the water depth in the flume may then be a limiting factor. In addition, the limited flume length may lead to wave reflections and flow fields that will not occur in the real world. An investigation of the wave absorbing beach design would therefore be of interest. As the actual wave heights in the flume may not coincide with the theoretical wave heights, the accuracy of the wave maker should also be studied. Furthermore the accuracy of the measuring devices should be examined in order to ensure correct measurements.

The above mentioned limitations, features and uncertainties will be investigated in this chapter.

4.2 Theory

4.2.1 Convertion from full scale to model scale

The experimental setup should represent the full scale problem as exact as possible to obtain useful test results. This is achieved by fulfilling kinematic, dynamic and geometric similarity, most commonly through a method called Froude scaling [50]. The scaling ratio given in equation 4.1 is then used to achieve geometrical similarity [50].

$$\lambda_{scale} = \frac{L_{fullscale}}{L_{model}} \tag{4.1}$$

Depending on the modeled problem, L may represent wave length, water depth or a structural dimension. Applying this scaling ratio the following full scale to model scale relations are obtained [50]:

Wave height:	$H_f = \lambda_{scale} H_m$
Velocity:	$U_f = \sqrt{\lambda_{scale}} U_m$
Time:	$t_f = \sqrt{\lambda_{scale}} t_m$
Acceleration:	$a_f = a_m$
Force:	$F_f = \frac{\rho_f}{\rho_m} \lambda_{scale}^3 F_m$
Moment:	$M_f = \frac{\rho_f}{\rho_m} \lambda_{scale}^4 M_m$

Here the subscript f represents full scale, while m represents model scale.

4.2.2 Biésel transfer function

The transfer function for a flap hinged a certain distance h_0 above the flume bottom is shown in equation 4.2 [51]. Here the relation between total linear wave height H and total flap motion S_0 is given in terms of the wave number k. Figure 4.2 shows how this function depends on the wave period T. The different parameters involved in equation 4.2 are shown in an illustration of the wave maker in figure 4.3.

$$\frac{H}{S_0} = \frac{2}{k(h-h_0)} \left[\frac{\sinh(kh)\left((h-h_0)k\sinh(kh) - \cosh(kh) + \cosh(kh_0)\right)}{\sinh(kh)\cosh(kh) + kh} \right] \tag{4.2}$$

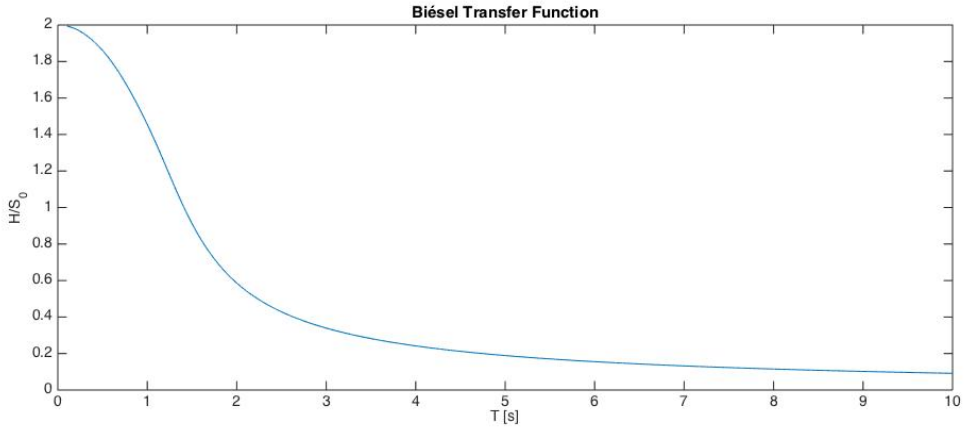

Figure 4.2: Biésel transfer function vs. wave period.

It should be noted that equation 4.2 relates the wave height to the flap motion at water surface level, as shown in figure 4.3. From this figure it is easily seen that the flap is connected to a moving brace at the top, and the signal sent to the wave maker should hence be calculated at this position. A linear increase of the signal must then be performed as shown in equation 4.3.

$$S(z) = S_0 \frac{h + z - h_0}{h - h_0} \tag{4.3}$$

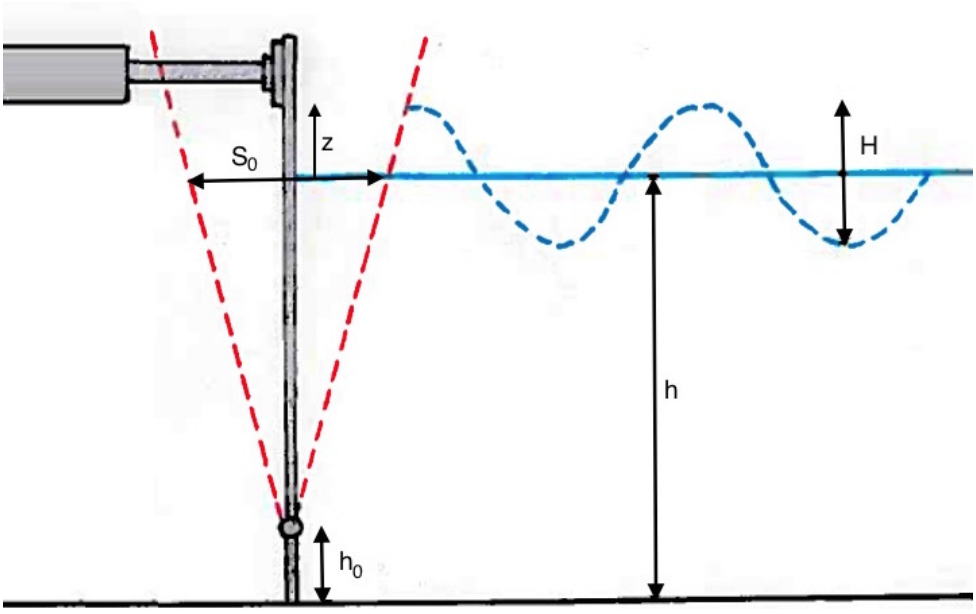

Figure 4.3: Sketch of the wave maker

4.2.3 Wave reflections

Wave reflections due to limited flume length may influence the generated waves in model testing in a way not present for a full scale problem. The wave absorbing beach at the end of the flume should therefore be designed to reduce this effect as much as possible. Relating the reflected wave heights H_r to the incident wave heights H_i the coefficient of wave reflections R is obtained as shown in equation 4.4 [9]. The most common wave beach design targets a reflected wave height less than 5 - 10 % of the incident wave height [50].

$$R = \frac{H_r}{H_i} \tag{4.4}$$

4.2.4 Pile properties

Eigenperiod and eigenfrequency

An undamped system will oscillate with the eigenperiod T_0 as given in equation 4.5.

$$T_0 = \frac{2\pi}{\omega_0} \tag{4.5}$$

The eigenfrequency, ω_0, can be found as a relation between the rotational stiffness of the system, k_θ, and the rotational moment of inertia, I_θ, as given in equation 4.6.

$$\omega_0 = \sqrt{\frac{k_\theta}{I_\theta}} \tag{4.6}$$

Second moment of inertia

The second moment of inertia for the cross section of the pile used in the calculation of bending stiffness is shown in equation 4.7.

$$I_x = I_y = I_{xy} = \frac{\pi}{64}(D_i^4 - D_o^4) \tag{4.7}$$

Damping

Damping is most commonly specified by the damping ratio, ξ, as given in equation 4.8, where c_{cr} is the critical damping [52].

$$\xi = \frac{c}{c_{cr}} \tag{4.8}$$

An approximation of the damping ratio can be found using the logarithmic decrement when the oscillation path is measurable, as shown in equation 4.9 [52]. The damped eigenperiod T_d can then be calculated according to equation 4.10.

$$\xi = \frac{1}{2\pi n} \ln\left(\frac{y_i}{y_{i+n}}\right) \tag{4.9}$$

$$T_d = \frac{2\pi}{\omega_d} = \frac{2\pi}{\omega_0\sqrt{1-\xi^2}} \tag{4.10}$$

When the damping ratio, eigenfrequency and damped eigenperiod are known, the importance of damping for the freely oscillating system can be anticipated by means of equation 4.11 [52]. Here y_0 is the initial pile displacement and $y(t)$ gives the damped oscillation path as a function of time.

$$y(t) = e^{-\xi\omega_0 t} y_0 \cos(\omega_d t) \tag{4.11}$$

4.3 Flume investigation

4.3.1 Choice of proper scaling ratio

The water depth at the location of interest is about 100 [m] in full scale. Since the water depth in the flume is 1 [m], a proper scaling ratio is found to be 1:100. During the model tests the actual water depth was found to range between 0.96 - 0.98 [m], which is taken into account in the generation of the input files.

4.3.2 Wave generation

Waves in the flume are generated by the wave maker. The motion of the wave maker can be calculated by combining the desired time history of the surface elevation and the transfer function given in equation 4.2 and 4.3. MATLAB is used for generation of such an input file, and the scripts can be found on the external memory stick. The sampling frequency of the signal sent to the wave maker is set to 50 [Hz].

A set of regular waves are conducted in the flume. They are tested both with and without the pile installed, such that the uncertainties and limitations related to the experimental setup can be investigated.

4.3.3 Measuring devices

The waveprobes measure the instantaneous surface elevations in the flume. Strain gauges in the foundation of the pile are used to measure base shear responses and overturning moments. These measurements are stored as a binary file, and a MATLAB script which can be found at the external memory stick is used to import the data for further analyzing.

A hammer with a load cell in the tip is used for comparison between applied loads and measured responses in order to examine the goodness of the strain gauges. In addition a comprehensive calibration of the waveprobes are performed, as well as regular inspections.

4.3.4 Pile behaviour

The pile's eigenperiod and damping ratio are estimated by oscillating the pile in calm water under video surveillance. In order to find the rotational stiffness, a relation between overturning moments and pile rotations is established by displacing the pile a certain distance under video monitoring.

4.4 Results and observations

4.4.1 The wave maker

Uncertainties related to the wave maker should be investigated in order to ensure that the desired wave heights are obtained in the flume. In a preparatory model test experiment a piston type wave maker was used, and the accuracy of both wave makers will be presented in the following. The two wave makers are shown in figure 4.4.

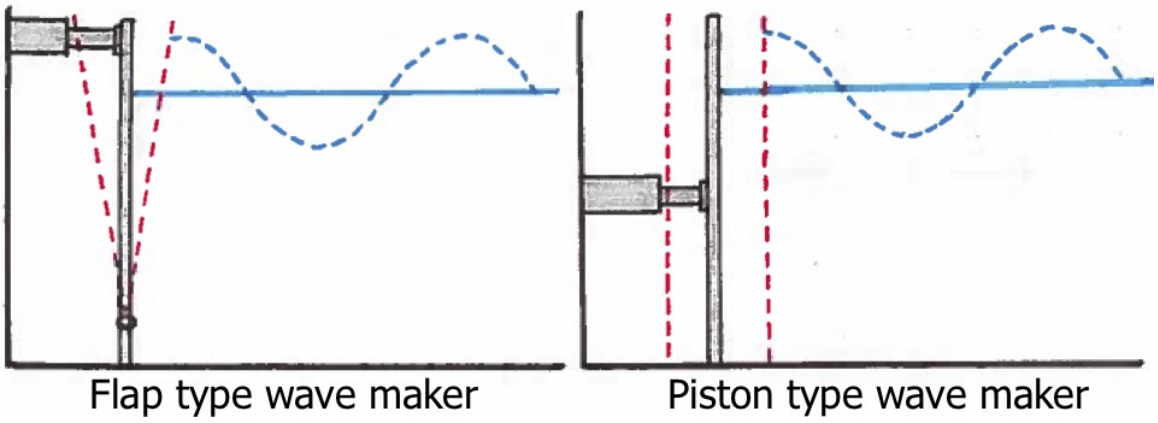

Figure 4.4: Wave maker of flap and piston type.

Biésel transfer function

Figure 4.5 and 4.6 show the Biésel transfer function plotted together with measured values of H/S_0 in model scale for flap and piston type wave maker, respectively. The deviations are found to be large for the piston, whereas the accuracy of the flap is very good. It is important to mention that the water depth was 0.6 [m] when the piston was used, contrary to the 1 [m] water depth when using the flap. Still, the effect of different water depths should be taken care of in the transfer functions.

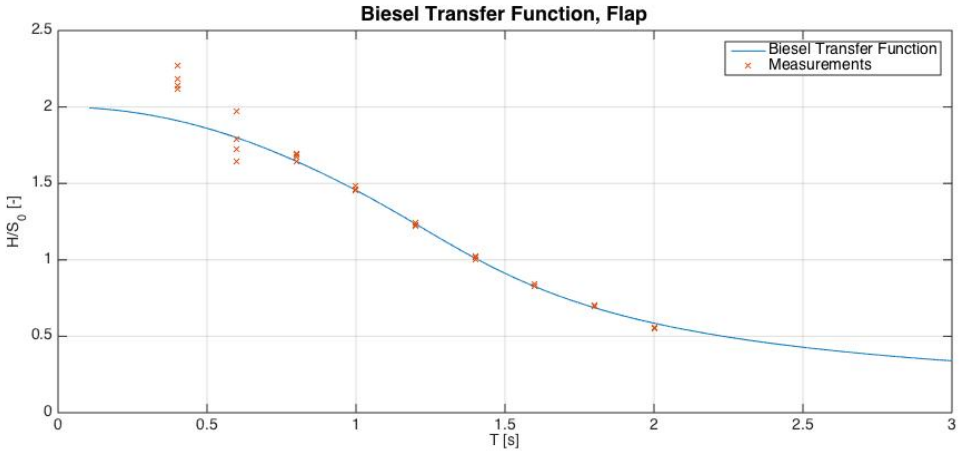

Figure 4.5: Theoretical Biésel transfer function vs. wave period plotted together with measured values in model scale for the flap type wave maker.

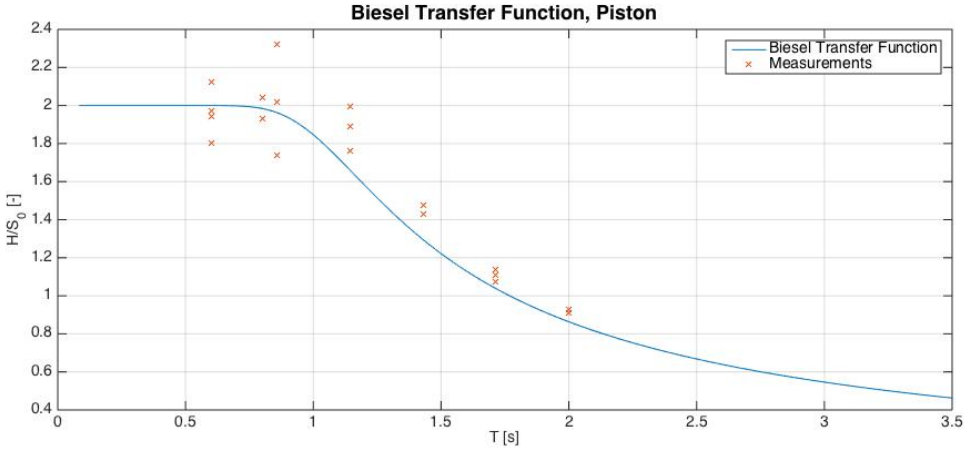

Figure 4.6: Theoretical Biésel transfer function vs. wave period plotted together with measured values in model scale for the piston type wave maker.

Mechanical losses in the flap

Figure 4.7 shows the error Δ between the calculated flap displacement S_0 and the real flap displacement S_r for different wave periods, as given in equation 4.12. It is easily seen that the mechanical losses become significant for smaller periods, i.e. higher angular wave frequencies.

$$\Delta = \frac{S_r - S_0}{S_0} \tag{4.12}$$

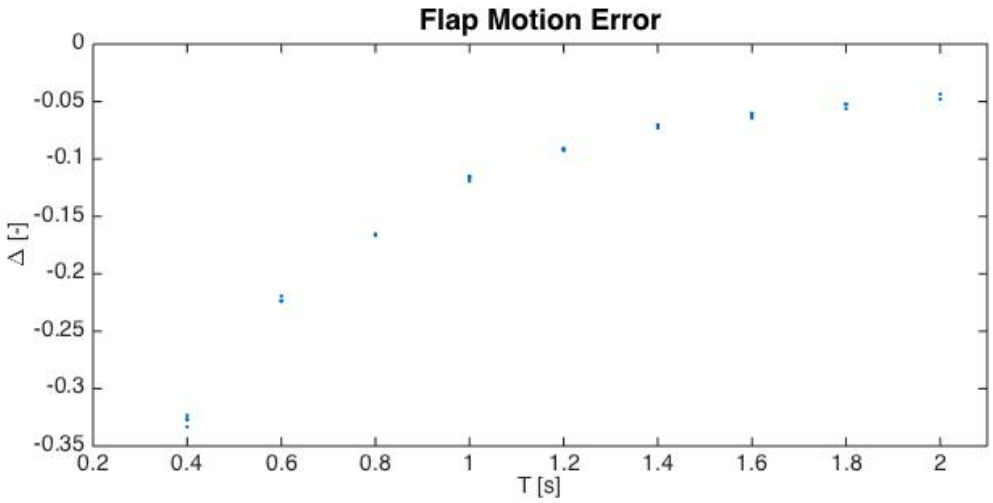

Figure 4.7: Error between theoretical flap displacement and real flap displacement for different periods in model scale.

Wave height correction

Due to the mechanical losses in the flap, the measured wave heights are expected to be smaller than the theoretical wave heights. Hence, a H-dependent correction term may be introduced in the time series of the desired flap motion. Relations between the theoretical and measured wave heights are shown in figure 4.8, where a proposed trendline has been estimated by means of the least square's method. A fourth degree polynom is used to calculate a coefficient that should be included in the wave maker signal in order to obtain the desired wave heights in the flume.

Such a correction term can also be established based on the measured and theoretical flap displacement as shown in figure 4.7. Still, there may be some other error sources than mechanical losses in the flap reducing the wave heights. This proposed correction takes all possible error sources related to the wave heights into account.

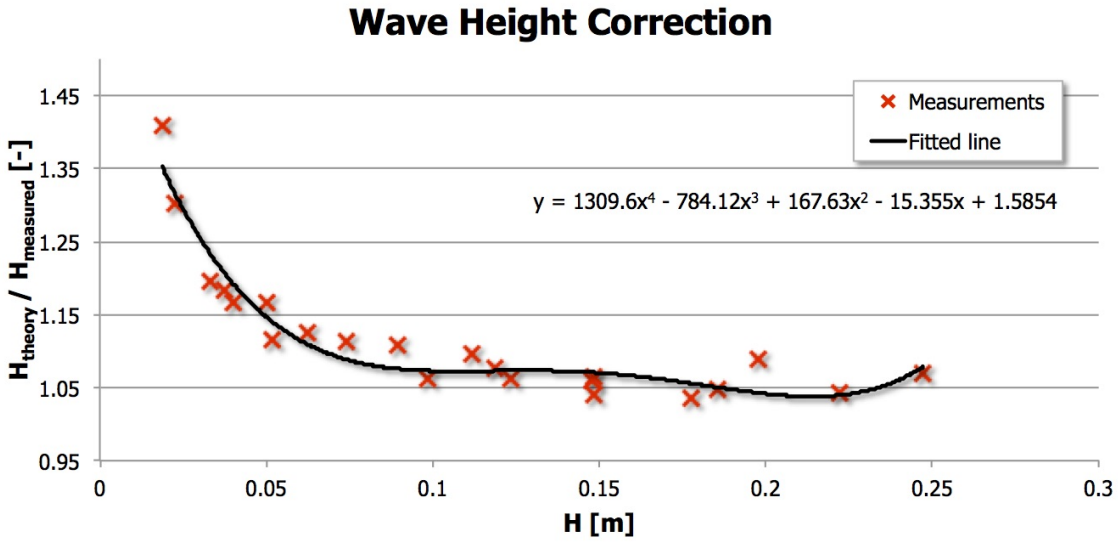

Figure 4.8: Relations between theoretical and measured wave heights in model scale with an estimated trendline.

4.4.2 Beach design

Reflection coefficients are measured in order to investigate beach design A as shown in figure 4.9. Beach design B was used in the preparatory model test experiment and the two designs will be compared in the following. The reflections for beach design A are measured both with and without the pile installed in the flume in order to examine the importance of the pile's presence.

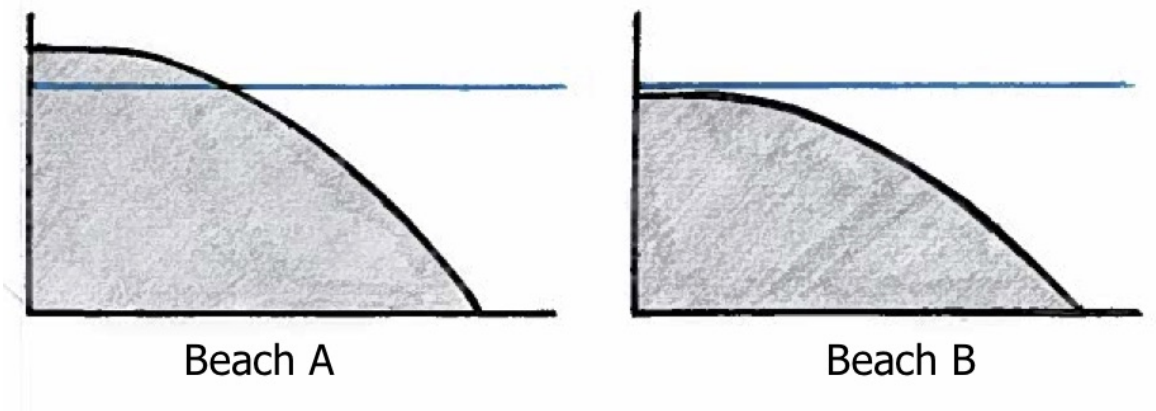

Figure 4.9: Beach design A and B.

Beach design A without pile

Figure 4.10 shows the measured reflection coefficients R in the flume without the pile installed. Generally larger reflections seem to occur for the highest steepness. The reflections are about 3 - 4 % of the incident wave height for the lowest period, increasing gradually for higher periods. Note the somewhat rapid increase from 0.8 [s] to 1 [s] for the largest steepness and from 1.6 [s] to 1.8 [s] for the lowest steepness. Still, all the reflections seem to stabilize around values under 10 % which is the design target.

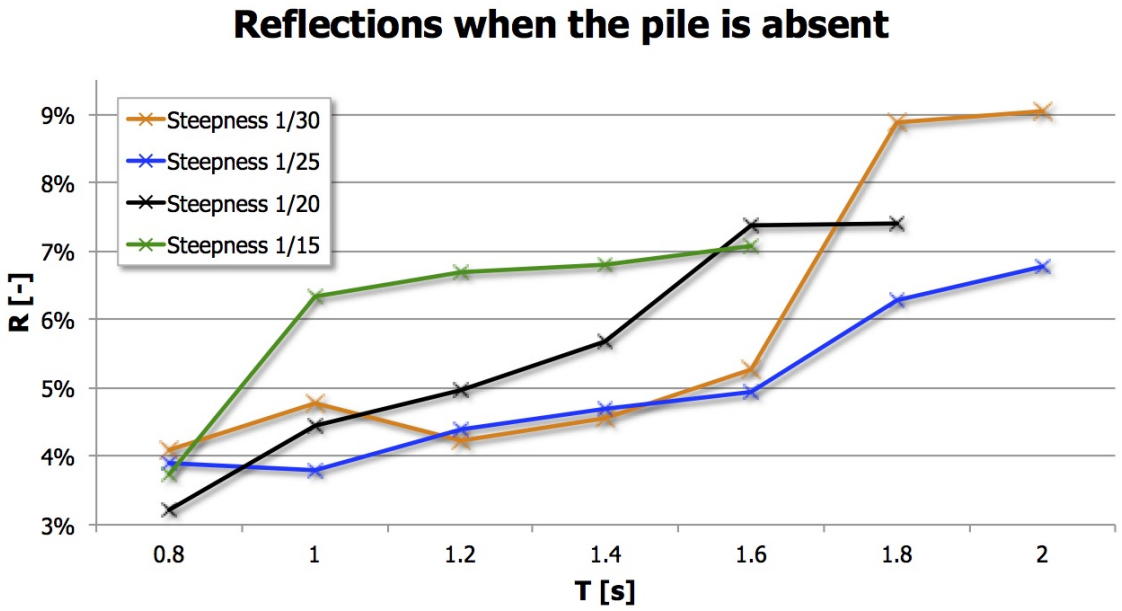

Figure 4.10: Reflection coefficients for beach design A for different steepnesses and periods in model scale without the pile installed.

Beach design A with pile

Measured reflections with the pile installed are shown in figure 4.11. Also here the largest reflections tend to occur for the highest steepness. For the lowest period the reflections are found to be 3.5 - 4.5 %, which is slightly larger than the reflections when the pile is absent. Then a gradual increase takes place until 1.2 [s] where a small downtrend can be seen, independent of steepness. It is woth noting that 1.2 [s] is twice the pile's eigenperiod, such that oscillations of the pile may amplify the surface elevations leading to somewhat higher reflections for this period. The reflections do not seem to stabilize for the largest periods as they did in figure 4.10. Instead a further, somewhat larger, gradual increase is seen for these periods. Hence, the reflections are expected to exceed the design target of 10 % for periods above 2 [s].

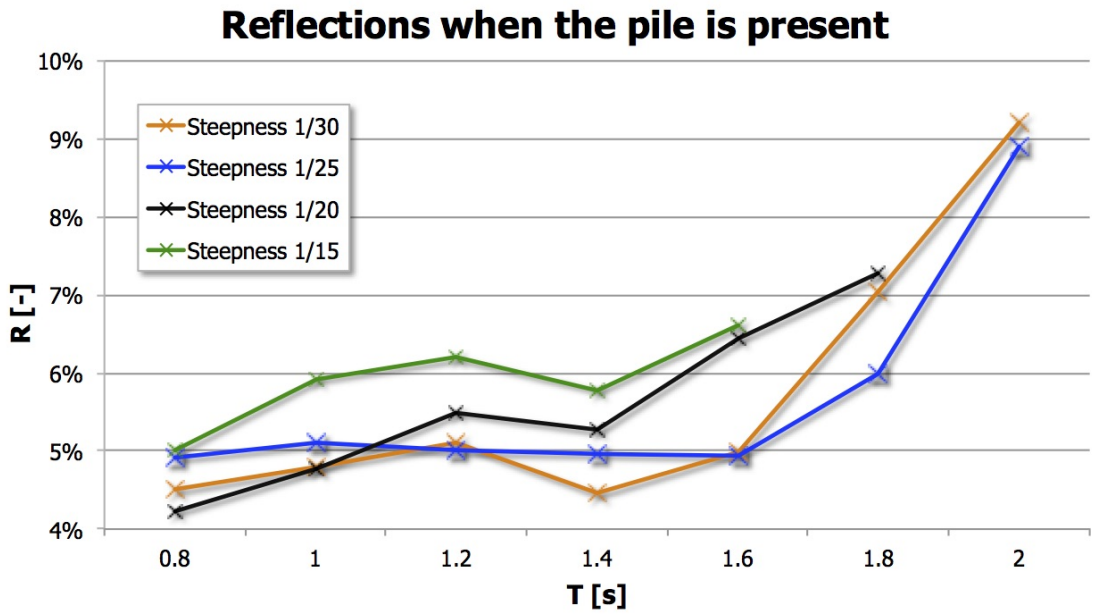

Figure 4.11: Reflection coefficients for beach design A for different steepnesses and periods in model scale with the pile installed.

Beach design B

The results from the preparatory model test experiment with beach design B are shown in figure 4.12. Generally the reflections are found to be larger and more spread for this beach design than for beach design A. For the lowest period the reflections are about 2 - 5 %, while they seem to stabilize around 10 - 13 % for the largest period which is above the design target. Note that there seem to be a sudden drop at T = 1 [s] for steepness $\frac{1}{20}$, which may be explained by measurement errors or other more complex properties in the flume.

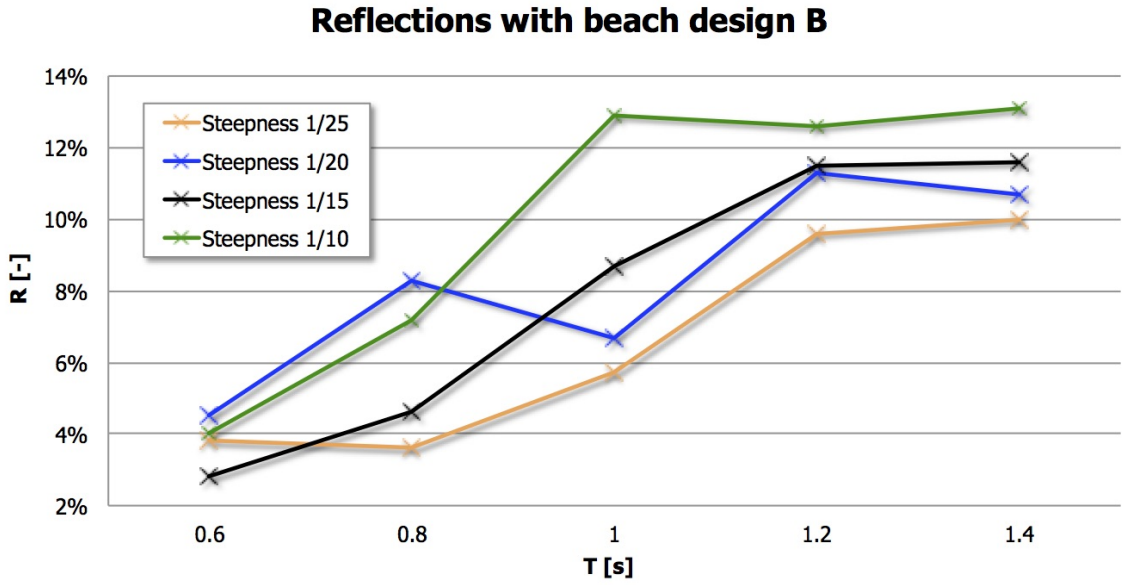

Figure 4.12: Reflection coefficients for beach design B for different steepnesses and periods in model scale 1:100.

4.4.3 Pile properties and behaviour

The necessary measurements and calculations in order to establish the equation of motion for the pile will be presented in the following. In addition, the effect of the pile's presence in the flume is investigated.

Eigenperiod

The eigenperiod of the pile is measured to be 0.6 [s] by means of video surveillance.

Damping

An average damping ratio ξ of 0.0529 [-] is obtained by freely oscillating the pile in calm water from an initial displacement y_0. Figure 4.13 shows the oscillation path of the damped pile system, where the dotted lines represent the amplitude boundaries given as $\pm y_0 e^{-\xi\omega_0 t}$.

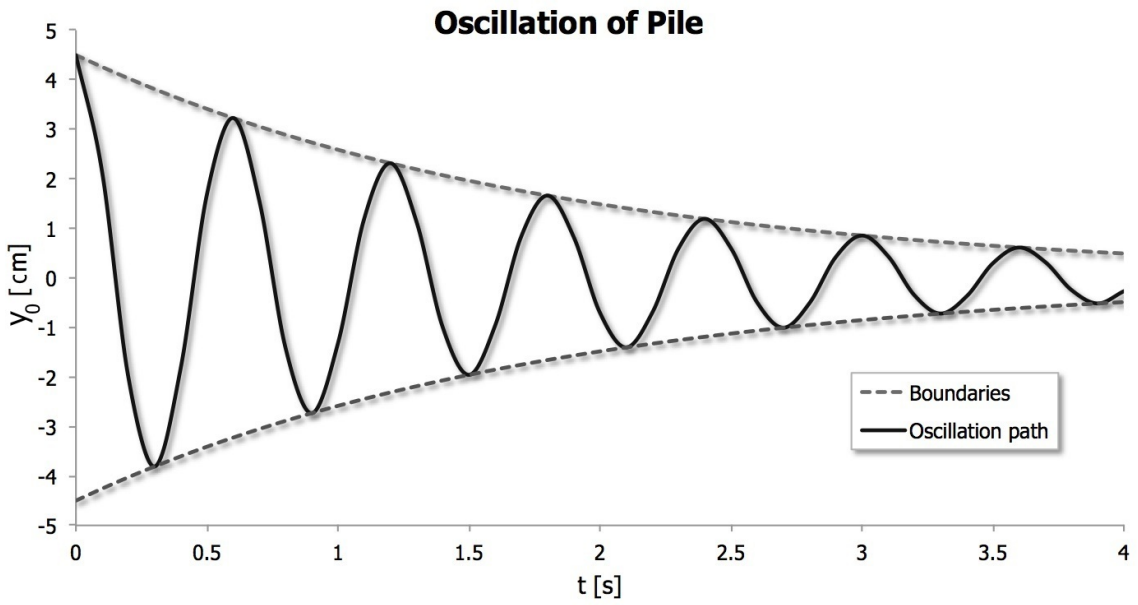

Figure 4.13: Oscillation of the damped pile system.

Mass and stiffness

The structural mass of the pile is measured to be 11.58 [kg]. An increase of 17.14 [kg] must be accounted for because the pile is filled with water up to mean water surface level. In addition, there is a concentrated mass of 5.08 [kg] placed on top of the pile. Hence, the total mass M of the pile is 33.80 [kg].

A rotational stiffness k_θ of 3788 [Nm/rad] is obtained by fitting a linear trendline to the relation between measured moment and corresponding rotation, as shown in figure 4.14.

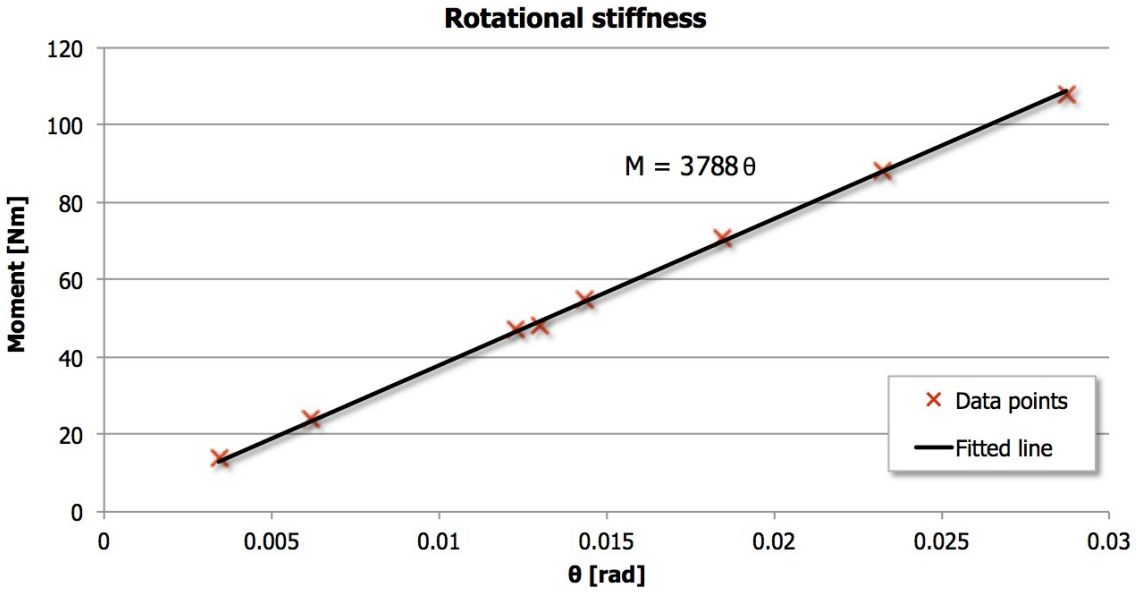

Figure 4.14: Relation between moment and rotation with an estimated trendline.

Using the pile dimensions given in table 4.2 the second moment of inertia I_{xy} is calculated to be $7.319 \cdot 10^6$ [mm^4] by equatin 4.7. The bending stiffness, EI, of the pile then becomes $5.124 \cdot 10^5$ [Nm^2].

An overview of all the pile properties calculated in this section can be found in table 4.3.

Table 4.3: Pile properties.

Eigenperiod	T_0	0.6	[s]
Damping ratio	ξ	0.0529	[-]
Total mass	M	33.80	[kg]
Rotational stiffness	k_θ	3788	$\left[\frac{Nm}{rad}\right]$
Bending stiffness	EI	0.512	[MNm^2]

Diffractions from the pile

Figure 4.15 shows the surface elevation with and without the pile present in the flume for small wave heights of approximately 0.014 [m]. Wave packets occuring after the wave train are seen when the pile is present. The incident wave heights are rather small compared to the diameter of the pile, such that these wave packets are seen due to diffractions from the pile.

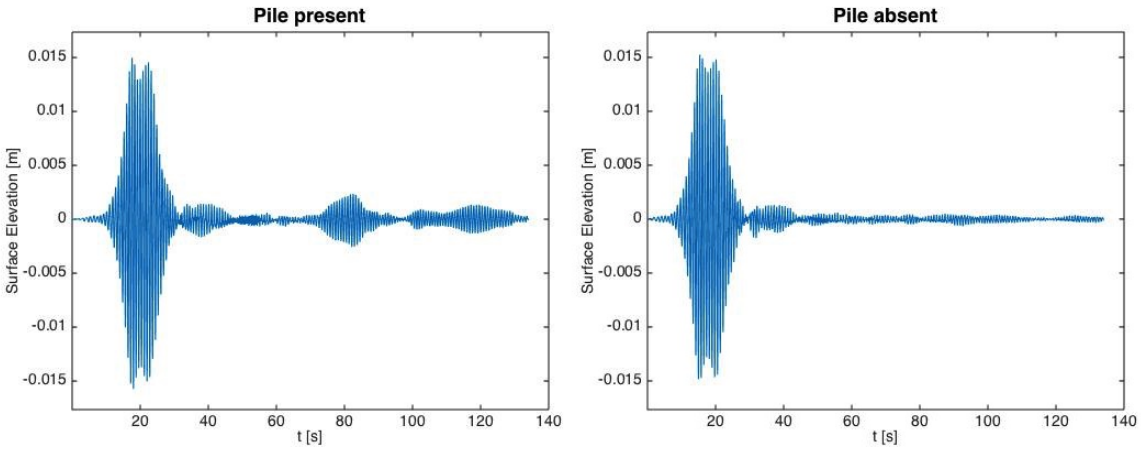

Figure 4.15: Comparison of the surface elevation with and without the pile installed for T = 0.8 [s].

4.4.4 Measuring devices

Waveprobes

A calibration of the waveprobes is performed in order to ensure precise measurements of the surface elevation. The accuracy of the waveprobes is also inspected on a regular basis throughout the whole experiment.

Strain gauges

The hammer shown in picture 4.16 is used to apply known static loads on the pile. Resulting measurements from the strain gauges are shown in table 4.4. Good accordance is found between applied and measured loads on the pile and the strain gauges can hence be assumed to provide satisfactory measurements.

Figure 4.16: Hammer with a load cell in the tip used for static tests.

Table 4.4: Applied and measured loads from the static hammer tests.

	Force [N]		**Moment [Nm]**	
Test	Applied	Measured	Applied	Measured
1	39.26	38.30	54.57	55.78
2	36.66	35.83	50.96	52.52
3	28.72	30.48	39.92	43.01

4.5 Discussion and recommendations

4.5.1 Accuracy of the wave maker

The flap type wave maker is found to provide more accurate results than the piston, as better accordance to the respective Biésel transfer function is seen. Some deviations between the motion of the flap and measured wave heights are seen for T = 0.4 [s], which is much lower than the periods of main interest in this experiment. Hence, these deviations are not considered to be relevant. From chapter 3 the relevant periods are found to range from 1 [s] to 1.9 [s] in model scale.

The real motion of the flap is measured to be smaller than required due to mechanical losses. This loss is about 14 % for T = 1 [s], while it reduces to 5 % for increasing periods. Lower wave heights than desired are therefore expected from this wave maker. A H-dependent correction model to the wave maker signal is proposed in order to account for this. The goodness of this model is left for further work due to time limitations, and it is hence not included in the rest of this thesis.

4.5.2 Goodness of the beach design

Beach design A provides smaller reflection coefficients than beach design B and can hence be considered a better wave absorber. All the reflection coefficients for this beach are found to be less than 10 %, which is given as the design target [50]. They may still be of significant importance and the model tests should hence be of limited duration followed by a certain waiting period for the water to calm down.

4.5.3 Presence of the pile

Larger reflection coefficients are measured when the pile is present in the flume. This has nothing to do with beach reflections, rather the pile's interaction with the waves. It is especially worth noting that the reflections for T = 1.2 [s] stand out as they are somewhat higher than for the neighboring periods. As this period is twice the eigenperiod of the pile, the surface elevation may be amplified due to resonance. Oscillatory pile behaviour are hence expected to influence the model tests and all tests should be conducted both with and without the pile present in the flume.

For waves of sufficiently low wave heights compared to the pile's diameter, diffractions are seen to be of significant magnitudes. This effect is not as clearly seen for the surface elevations as the wave height increases. Still, diffractions from the pile may be of importance for wave heights of significant magnitude compared to the pile's diameter as well. As a comparable study in the future the pile should therefore be restrained towards oscillations in order to determine the effect of diffractions.

The pile can be modelled as an undercritically damped and infinitely stiff body with a

rotational spring in the bottom, as the bending stiffness is 135 times larger than the rotational stiffness.

Chapter 5

Generation of the Critical Sea States

5.1 Introduction

Irregular wave conditions corresponding to the critical sea states selected in chapter 3 will be subjected for model testing in this chapter. These sea states are selected along the wrongly established ULS and ALS contour lines due to a calculation error early in this project. Still, the sea states subjected for model testing are only slightly larger than the correct ones which are based on 3 [h] weather characteristics from the Ekofisk area. The objective of this model testing is to measure the responses of the pile structure in extreme wave conditions, as large non linear effects and complex wave-body interactions are expected to become important.

Extreme loads and responses of the pile according to ULS and ALS design will be further investigated in chapter 7, while this chapter will focus on the model tests. The method of irregular wave generation by use of a proper wave spectrum will be explained, and a study of different wave spectrums are therefore of interest. Measurements, observations and analyzes of the model tests, wave conditions and statistical properties will be presented in the results.

5.1.1 Wave Spectrums

Assuming the surface elevation within a sea state to be a random stationary Gaussian process, a wave spectrum can be used as a short term description of the sea state conditions. Stationarity means that environmental parameters like H_S and T_P can be assumed constant throughout the duration, which is commonly assumed to be from 20 [min] up to 6 [h] [9]. The wave spectrum, also referred to as power spectrum, describes the energy density for a given sea state within a limited geographical area and time interval.

The variance $\sigma^2_{\zeta\zeta}$ of the surface elevation ζ within a sea state can be calculated accord-

ing to equation 5.1 where $\bar{\zeta}$ is the mean value. It can also be calculated by means of the zeroth spectral moment, m_0, as shown in equation 5.2. The value of the 1/3 largest waves in the sea state corresponds to H_S and can then be calculated by means of equation 5.3.

$$\sigma_{\zeta\zeta}^2 = \frac{1}{n}\sum_{i=1}^{n}\left(\bar{\zeta} - \zeta_i\right)^2 \tag{5.1}$$

$$\sigma_{\zeta\zeta}^2 = m_0 = \int_{-\infty}^{\infty} S_{\zeta\zeta}(\omega)d\omega \tag{5.2}$$

$$H_S = 4\sqrt{m_0} \tag{5.3}$$

The three wave spectrums called the JONSWAP spectrum, Torsethaugen spectrum and Donelan spectrum will be presented in the following.

JONSWAP spectrum

The most severe sea states are often governed by wind seas [37]. Due to the geographical surroundings in the North Sea, it is common to assume that the sea states are not fully developed. The JONSWAP (Joint Sea North Sea Wave Project) spectrum is suitable for wind seas and describes growing sea states, which make it applicable for this experiment. Equation 5.4 gives the analytic formula for this wave spectrum, where ω_P is the wave frequency corresponding to the T_P value of the given sea state as shown in equation 5.5. The peak shape parameter γ_J is for simplicity set equal to 2, and the spectral width parameter σ_J is given in equation 5.6.

$$S_{\zeta\zeta}(\omega) = \frac{5}{32\pi}H_S^2 T_P \left(\frac{\omega_P}{\omega}\right)^5 \exp\left[-\frac{5}{4}\left(\frac{\omega_P}{\omega}\right)^4\right](1 - 0.287\ln\gamma_J)\,\gamma_J^{\exp\left[-\frac{\left(\frac{\omega}{\omega_P}-1\right)^2}{2\sigma_J^2}\right]} \tag{5.4}$$

$$\omega_P = \frac{2\pi}{T_P} \tag{5.5}$$

$$\sigma_J = \begin{cases} 0.07 & \text{if } \omega \leqslant \omega_P \\ 0.09 & \text{if } \omega > \omega_P \end{cases} \tag{5.6}$$

Torsethaugen spectrum

Less severe sea states are often composed of both wind seas and swells, especially in open sea areas [9]. Such sea states may be expressed as a combination of two fitted JONSWAP spectrums from the Norwegian continental shelf as shown in equation 5.7; one for wind seas and one for swells. It will hence be a two-peaked wave spectrum. Details about the empirical parameters deduced from H_S and T_P can be found in the literature [40] [41].

$$S_{\zeta\zeta}(\omega) = S_{wind}(\omega) + S_{swell}(\omega) \tag{5.7}$$

Donelan spectrum

A correction to the high-frequency range of the JONSWAP spectrum was proposed by Toba [39]. The decay of the corrected spectrum, called the Toba form, is proportional to ω^{-4} contrary to the decay of the original JONSWAP spectrum which is proportional to ω^{-5}. An analytic formula based on field results for the corrected spectrum, called the Donelan wave spectrum, is given in equation 5.8 [38]. The parameters are functions of ν and given in equation 5.9, 5.10 and 5.11, whereas the expression for ν is given in equation 5.12 [38] in terms of U_{10}, which is the 10 [min] mean wind velocity 10 [m] above water surface level.

$$S_{\zeta\zeta}(\omega) = \beta_D g^2 \omega_P^{-1} \omega^{-4} \exp\left[-\left(\frac{\omega}{\omega_P}\right)^{-4}\right] \gamma_D^{\exp\left[-\frac{(\omega-\omega_P)^2}{2\sigma_D^2\omega_P}\right]} \tag{5.8}$$

$$\beta_D = 0.0165 \cdot 10^{-6} \nu^{-3.3} \tag{5.9}$$

$$\gamma_D = \begin{cases} 6.489 + 6\log\nu & \text{if } \nu \geqslant 0.159 \\ 1.7 & \text{if } \nu < 0.159 \end{cases} \tag{5.10}$$

$$\sigma_D = 0.08 + 1.29 \cdot 10^{-3} \nu^{-3} \tag{5.11}$$

$$\nu = \frac{U_{10}}{T_P g} \tag{5.12}$$

This proposed wave spectrum may be hard to apply for engineering purposes as the parameters do not include general sea state parameters like H_S and T_P. A convenient parameterization of the wave spectrum in terms of these is based on equation 5.13 and 5.14 [53]. The expressions given in equation 5.15, 5.16 and 5.17 are then obtained, and all the parameters in the Donelan spectrum are hence described in terms of H_S and T_P rather than U_{10}.

$$\varepsilon_D = 6.365 \nu^{0.55} \tag{5.13}$$

$$\varepsilon_D = \frac{g^2 m_0}{U_{10}^4} \tag{5.14}$$

$$\beta_D = 200 g^{-1.571} m_0^{0.786} T_P^{-3.143} \tag{5.15}$$

$$\gamma_D = 6.489 + 6\log\left[2.649 \cdot 10^7 g^{-2.857} m_0^{1.429} T_P^{-5.714}\right] \tag{5.16}$$

$$\sigma_D = 0.08 + 6.940 \cdot 10^{-26} g^{8.571} m_0^{-4.287} T_P^{17.142} \tag{5.17}$$

5.1.2 Distribution of wave crests

Assuming the surface elevation to be a standard Gaussian process and that only one crest height is found between succeeding positive zero crossings, the surface elevation process is said to be narrowbanded. The wave crests for such a process can be shown to follow the first order Rayleigh distribution in equation 5.18. Combined with equation 5.3, the distribution can be expressed in terms of the H_S value.

$$F_C(c) = 1 - \exp\left[-\frac{1}{2}\left(\frac{c}{\sigma_{\zeta\zeta}}\right)^2\right] \tag{5.18}$$

For a sea state consisting of steeper waves, the crest heights may follow a higher order distribution. The Forristall distribution describes wave crests influenced by second order effects and is previously given in equation 3.16 in chapter 3 [46].

The extreme wave crests may follow the second order T-hour distribution as given in equation 3.23 in chapter 3.

5.2 Simulation of irregular sea

Superposition of N different wave components may be used in order to obtain an irregular sea surface elevation if linear theory is assumed. This summation is shown in equation 5.19, where the surface elevation ζ is given as a function of space and time.

$$\zeta(x,t) = \sum_{i=1}^{N} \zeta_{a,i} \cos\left(\omega_i t - k_i x + \varphi_i\right) \tag{5.19}$$

The different wave components are given in terms of linear wave amplitude, $\zeta_{a,i}$, angular frequency, ω_i, corresponding wave number, k_i, and a given phase angle φ_i. How to obtain these parameters will be presented in the following.

Wave frequency ω_i

The angular frequencies ω_i for the different wave components in equation 5.19 are determined such that the frequency range in which the wave spectrum is non-zero is covered. The values of the wave frequencies can then be determined by linearly spacing N components in this frequency interval.

To avoid the time history to repeat during the simulation, the Nyquist frequency resolution $\Delta\omega$ in equation 5.20 should be used, where T_{tot} is the total duration of the simulation.

$$\Delta\omega = \frac{2\pi}{T_{tot}} \tag{5.20}$$

Wave number k_i

The wave numbers k_i corresponding to the different ω_i values are determined by the dispersion relation given in equation 5.21. This relation is valid for both deep and shallow water, as it approaches $\omega_i^2 = k_i g$ for increasing water depth h.

$$\omega_i^2 = k_i g \tanh(k_i h) \tag{5.21}$$

Wave amplitude $\zeta_{a,i}$

Assuming the individual maximum of the surface elevation process to follow the Rayleigh distribution in equation 5.18, the amplitude $\zeta_{a,i}$ can be found as shown in equation 5.22. As the Rayleigh distribution gives the probability of being less than or equal to the inserted value of C, the amplitude for wave component i can be generated by inserting a random number uniformly distributed between 0 and 1 for $F_C(c)$.

$$\zeta_{a,i} = \sqrt{-2 S_{\zeta\zeta}(\omega_i) \Delta\omega \log\left(1 - F_C(c)\right)} \tag{5.22}$$

Phase angle φ_i

The phase angle φ_i for the different wave components is determined by randomly picking a value uniformly distributed between 0 and 2π.

Signal sent to wave maker

A wave maker signal η_{wm} is generated by combining the transfer function in equation 4.2 in chapter 4 with the time history for the desired surface elevation at the wave maker position. This is shown in equation 5.23, where the position of the wave maker is taken as $x = 0$ [m].

$$\eta_{wm}(t) = \sum_{i=1}^{N} \frac{\sqrt{-2S_{\zeta\zeta}(\omega_i)\Delta\omega \log\left(1 - F_C(c)\right)}}{\frac{H}{S}(k_i)} \cos\left(\omega_i t + \varphi_i\right) \tag{5.23}$$

5.3 Description of the experiment

The sea states subjected for model testing were determined by the contour line approach for both ULS and ALS in chapter 3. These are given in table 5.1, where every sea state is assigned an ID number such that they can be distinguished from each other.

Table 5.1: Sea states subjected for model testing.

ULS			**ALS**		
ID	H_S [m]	T_P [s]	ID	H_S [m]	T_P [s]
1	10.00	10.55	7	12.00	11.30
2	11.00	11.48	8	13.00	12.00
3	12.00	12.38	9	14.00	13.00
4	13.00	13.71	10	15.00	14.00
5	14.00	15.40	11	16.00	15.20
6	14.91	16.76	12	17.00	16.00
			13	18.00	16.90
			14	19.00	18.00
			15	19.60	19.00

Each sea state is conducted ten times using different random seeds in order to obtain a more correct representation of the statistical properties. They are tested both with and without the pile present in the flume, such that exact measurements from the location of the pile are obtained additional to wave conditions without influence from the pile's presence. In order to restrict the reflections from running wild, the duration of each run is limited to 6 [min] in model scale which corresponds to 1 [h] in full scale. The waiting time between each run is set to 15 [min] for the water to calm down.

Measurements of all the ten tests including the waiting time are stored in one binary file, as exemplified in figure 5.1. The file must be manually divided into ten individual parts in order to obtain the measurements of each test.

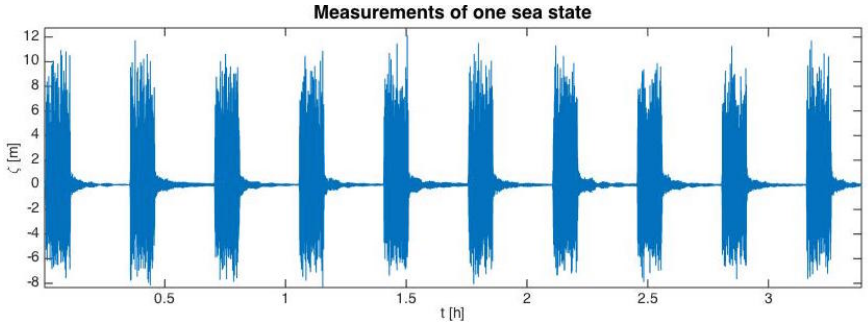

Figure 5.1: Example of measurements from model testing of one sea state

5.4 Results and observations

Results and observations from the model tests of the critical sea states will be presented in the rest of this chapter. Appendix D is built up such that each sea state is given a separate section, including information, measurements and plots. Some of the sea states will be used to exemplify and illustrate the results in the following.

5.4.1 Wave spectrums

A theoretical study of the JONSWAP spectrum, Torsethaugen spectrum and Donelan spectrum in order to determine the most suitable wave spectrum that should be used in the wave generation will be presented. Estimated wave spectrums from the measurements will be investigated in order to determine the real wave conditions obtained in the flume. To distinguish the different significant wave heights from one another, the following terms will be used in the rest of this chapter:

- $H_{S,in}$ Original H_S value the sea state is based upon.
- $H_{S,out}$ Averaged H_S calculated from measurements when the pile is absent.
- $H_{S,pile}$ Averaged H_S calculated from measurements when the pile is present.
- $H_{S,D}$ The H_S value provided by the theoretical Donelan wave spectrum.

Theoretical study of the input wave spectrums

The JONSWAP, Torsethaugen and Donelan wave spectrums are plotted together for sea state 1 in figure 5.2, which is the sea state of lowest $H_{S,in}$ value in the experiment. Two peaks for the Torsethaugen spectrum are seen for this sea state and for several sea states of lower $H_{S,in}$ values, indicating that both wind seas and swells are significant. The resemblance between the Donelan and JONSWAP spetrums shown in figure 5.2 is also seen for the other sea states of lower $H_{S,in}$ values.

Figure 5.3 compares the three wave spectrums for sea state 15, which is the sea state of highest $H_{S,in}$ value in the experiment. The two peaks for the Torsethaugen spectrum are seen to develop into one with magnitude approaching the JONSWAP peak for increasing $H_{S,in}$ values. Generally, the swell-peak decreases whereas the peak for the wind sea increases, implying that swells become less important in the description of the most severe sea states. On the other hand, the Donelan peak decreases compared to the JONSWAP peak for increasing $H_{S,in}$ values as shown in figure 5.3. This behaviour of the Donelan spectrum will be investigated further in section 5.4.3.

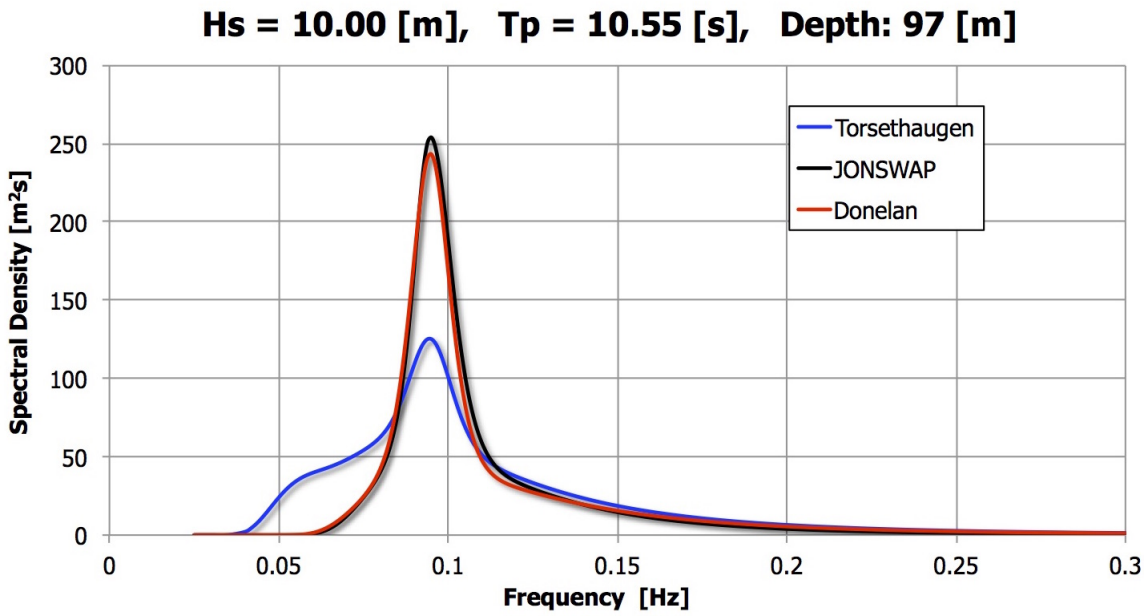

Figure 5.2: Comparison of the JONSWAP, Torsethaugen and Donelan spectrum for sea state 1.

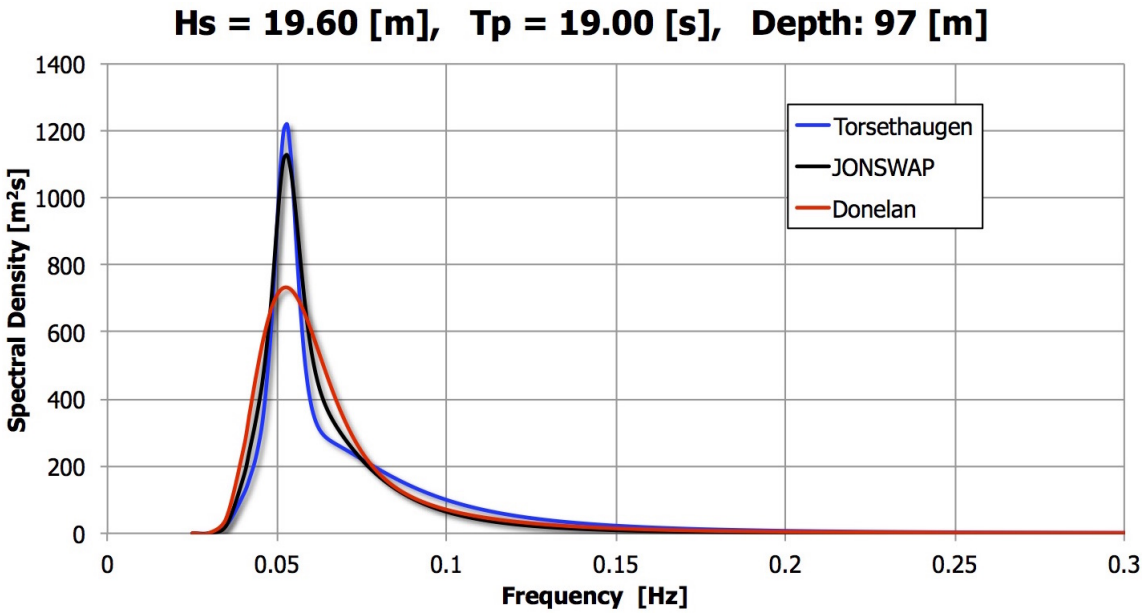

Figure 5.3: Comparison of the JONSWAP, Torsethaugen and Donelan spectrum for sea state 15.

The sea states of main interest in this experiment are those on the top of the ULS and ALS contour lines. Hence, a pure wind sea spectrum is sufficient. Due to the somewhat strange behaviour of the Donelan spectrum for the most severe sea states, the JONSWAP spectrum will be used in this experiment. Still, the sea states of largest and smallest $H_{S,in}$ values for both ULS and ALS are tested using both JONSWAP and the Donelan spectrum for comparable purpose.

Investigation of the ten tests of each sea state

The variance $\sigma^2_{\zeta\zeta}$ of every test may be calculated from the time series according to equation 5.1 or by integration of the wave spectrum estimated from measurements. When $\sigma^2_{\zeta\zeta}$ is known, equation 5.3 can be used to calculate the corresponding significant wave height H_S. To exemplify this, the variances calculated by both methods for all ten tests of sea state 1 are given in table 5.2 together with corresponding H_S values. This sea state is generated by use of the JONSWAP spectrum with $H_{S,in} = 10.00$ [m] and $T_P = 10.55$ [s].

The two methods of calculating $\sigma^2_{\zeta\zeta}$ and H_S are shown to provide similar results. If the numbers in table 5.2 are extended to include more than four decimals, a small deviation between the two methods can be seen. It can hence be concluded that both methods provide satisfactory estimates of variance and significant wave height. The averaged values of the tests, called σ^2_{out} and $H_{S,out}$ are good descriptions of the sea states obtained in the flume and will be further used in the rest of this chapter.

Table 5.2: Estimated $\sigma^2_{\zeta\zeta}$ and H_S values calculated according to the time series and the wave spectrum for sea state 1.

	Time series		**Spectrum**	
Test	$\sigma^2_{\zeta\zeta}$ [m^2]	H_S [m]	$\sigma^2_{\zeta\zeta}$ [m^2]	H_S [m]
1	5.38	9.28	5.38	9.28
2	5.35	9.25	5.35	9.25
3	5.15	9.07	5.15	9.07
4	4.68	8.66	4.68	8.66
5	5.12	9.05	5.12	9.05
6	5.23	9.15	5.23	9.15
7	4.76	8.73	4.76	8.73
8	5.17	9.09	5.17	9.09
9	5.21	9.13	5.21	9.13
10	5.47	9.35	5.47	9.35
avg	$\sigma^2_{out} = 5.15$	$H_{S,out} = 9.08$	$\sigma^2_{out} = 5.15$	$H_{S,out} = 9.08$

From table 5.2 the $H_{S,out}$ value is found to be 9.08 [m], which is 90.80 % of the $H_{S,in}$ value

for this sea state. This implies that deviations of significance between $H_{S,in}$ and $H_{S,out}$ are related to the model tests, which will be further investigated later in this section.

The smallest and largest H_S value from the ten tests in table 5.2 are 8.66 [m] and 9.35 [m], respectively. This gives a difference between the tests of 0.69 [m], which corresponds to 7.60 % of the average $H_{S,out}$ value. The variability ΔH_S given in equation 5.24 describes the variation of the ten tests and gives an impression of the uncertainties related to the averaged $H_{S,out}$ value.

$$\Delta H_S = \frac{H_{S,max} - H_{S,min}}{H_{S,out}} \tag{5.24}$$

The variability of the ten tests for each sea state is given in table 5.3, where the largest ΔH_S is found to be 18.91 % for sea state 13 when the pile is present. It is therefore likely to believe that there are either one test with a very large or a very small H_S value, or both. Figure 5.4 shows the measured H_S values for all the ten tests of this sea state together with the mean $H_{S,out}$ and $H_{S,pile}$ values.

From figure 5.4 it is seen that the measured H_S value for test 7 when the pile is present is extremely low compared to the other tests in sea state 13. The time history of this test does not indicate any measuring error, such that it can be assumed reliable. Test 7 provides a small H_S value when the pile is absent as well, but the difference is not as big in this case. It is also worth noting that there is a rather large difference between the two averaged $H_{S,out}$ and $H_{S,pile}$ values for this sea state where the measurements when the pile is absent provide very low values compared to when the pile i present.

Table 5.3: Variability of the measured H_S values from the ten tests for each sea state.

ID	$H_{S,in}$ [m]	$\Delta H_{S,out}$ [%]	$\Delta H_{S,pile}$ [%]
1	10.00	7.60	6.34
2	11.00	11.02	9.85
3	12.00	7.66	6.76
4	13.00	13.00	12.16
5	14.00	9.40	9.06
6	14.91	9.76	10.80
7	12.00	7.65	6.09
8	13.00	8.86	9.64
9	14.00	8.88	10.84
10	15.00	10.24	8.73
11	16.00	12.44	13.58
12	17.00	9.09	9.87
13	18.00	10.25	18.91
14	19.00	8.25	11.35
15	19.60	11.48	10.53

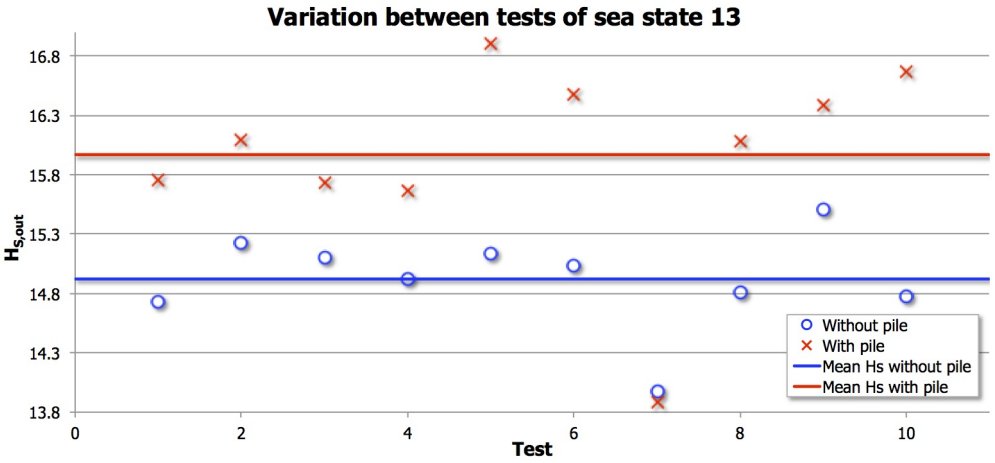

Figure 5.4: Graphical representation of the variation between the tests of sea state 13 when the pile is present and when it is absent.

Deviation between $H_{S,in}$ and $H_{S,out}$

The $H_{S,in}$ values and averaged measured $H_{S,out}$ and $H_{S,pile}$ values for all sea states are given in table 5.4. It is easily seen that the $H_{S,out}$ values are smaller than the input $H_{S,in}$ values for all sea states, and that the values are found to be higher when the pile is present than when it is absent.

Table 5.4: Input- and measured H_S values when the pile is absent and present.

ID	$H_{S,in}$ [m]	$H_{S,out}$ [m]	$\frac{H_{S,out}}{H_{S,in}}$	$H_{S,pile}$ [m]	$\frac{H_{S,pile}}{H_{S,in}}$	$\frac{H_{S,pile}}{H_{S,out}}$
1	10.00	9.08	0.9080	9.31	0.9310	1.0253
2	11.00	10.07	0.9155	10.25	0.9318	1.0179
3	12.00	10.97	0.9142	11.09	0.9242	1.0109
4	13.00	11.92	0.9169	12.01	0.9238	1.0076
5	14.00	12.55	0.8964	12.81	0.9150	1.0207
6	14.91	12.99	0.8712	13.24	0.8880	1.0192
7	12.00	10.72	0.8933	11.01	0.9175	1.0271
8	13.00	11.29	0.8685	11.52	0.8862	1.0204
9	14.00	12.39	0.8850	12.73	0.9093	1.0274
10	15.00	13.28	0.8853	13.63	0.9087	1.0264
11	16.00	13.75	0.8594	14.14	0.8838	1.0284
12	17.00	14.96	0.8800	15.40	0.9059	1.0294
13	18.00	14.92	0.8289	15.97	0.8872	1.0704
14	19.00	15.63	0.8226	16.13	0.8489	1.0320
15	19.60	15.94	0.8133	16.43	0.8383	1.0307

The measurements for the different sea states with and without the pile present are graphically presented in figure 5.5 together with the ideal relation, i.e. when $H_{S,in} = H_{S,out} = H_{S,pile}$.

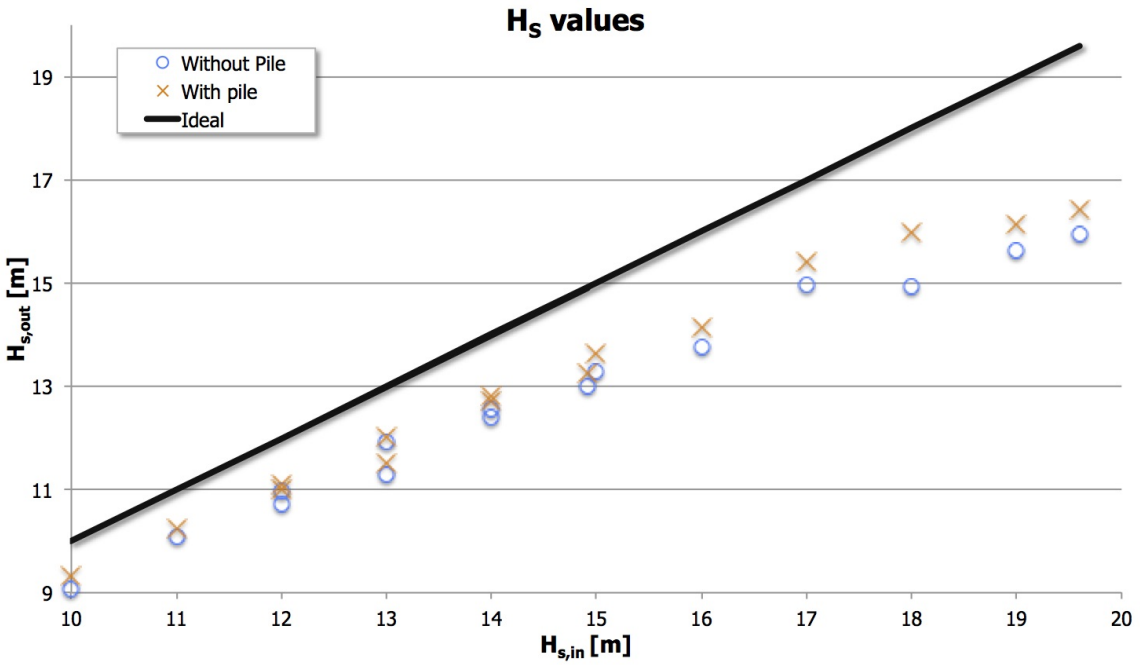

Figure 5.5: The measured H_S values for all the sea states showing the deviation from input value.

It should be noted from table 5.4 that sea state 13 has an unexpectedly low $H_{S,out}$ value as it is of smaller magnitude than for sea state 12. The $H_{S,out}$ value is in addition very low compared to the $H_{S,pile}$ value for sea state 13, as shown in figure 5.5 for $H_{S,in} = 18.00$ [m]. Recalling from figure 5.4 that the measured $H_{S,out}$ value was significantly smaller than the $H_{S,pile}$ value, this large deviation is not unexpected.

Due to the deviations between input and output wave spectrums, all the sea state steepnesses will be different than first assumed. Table 5.5 gives the steepnesses of both the input sea states and the sea states using $H_{S,out}$, termed $\varepsilon_{ss,in}$ and $\varepsilon_{ss,out}$, respectively. It is seen that the deviation between $\varepsilon_{ss,in}$ and $\varepsilon_{ss,out}$ increases for sea states located higher up on the contour lines, where the H_S values are generally large.

Table 5.5: Sea state steepnesses of input and output sea states.

ID	$\varepsilon_{ss,in}$ [-]	$\varepsilon_{ss,out}$ [-]	$\frac{\varepsilon_{ss,out}}{\varepsilon_{ss,in}}$ [-]
1	0.0576	0.0523	0.9080
2	0.0537	0.0492	0.9162
3	0.0507	0.0464	0.9152
4	0.0456	0.0418	0.9167
5	0.0402	0.0360	0.8955
6	0.0374	0.0326	0.8717
7	0.0605	0.0540	0.8926
8	0.0583	0.0506	0.8679
9	0.0540	0.0478	0.8852
10	0.0506	0.0448	0.8854
11	0.0469	0.0403	0.8593
12	0.0458	0.0404	0.8821
13	0.0445	0.0369	0.8292
14	0.0427	0.0352	0.8244
15	0.0408	0.0332	0.8137

Averaged wave spectrums

A representative wave spectrum for the tested sea states may be found by averaging the measured wave spectrums for all the ten tests. This is exemplified in figure 5.6 and 5.7 for sea state 1 and 15, respectively. Recall that sea state 1 has the lowest $H_{S,in}$ value and is among the steepest sea states, while sea state 15 has the largest $H_{S,in}$ value and is among the least steep sea states in this experiment. The averaged measured wave spectrums are plotted together with the JONSWAP spectrum for both $H_{S,in}$ and $H_{S,out}$.

As expected the deviation between the JONSWAP spectrum based on $H_{S,in}$ and the JONSWAP spectrum based on $H_{S,out}$ is much larger for sea state 15 than for sea state 1. The average spectrum from the measurements and the JONSWAP spectrum based on $H_{S,out}$ are shown to be in good accordance for sea state 15, whereas the high frequency range of sea state 1 seem to follow a higher order decrease than the JONSWAP spectrum.

The measured average wave spectrum is seen to consist of much noise. If even more tests are conducted for each sea state, say around 100, this effect may become smaller such that the graph will be smoothed out.

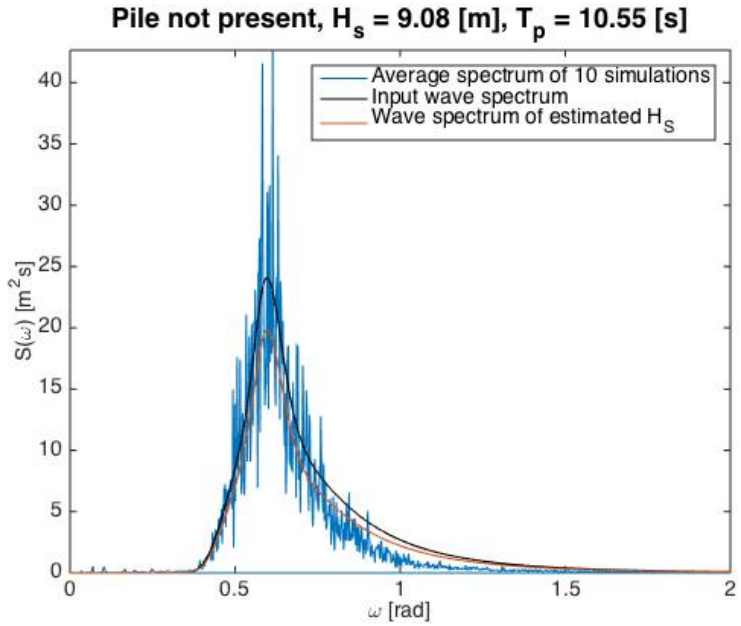

Figure 5.6: Averaged wave spectrum for sea state 1 with $H_S = 10.00$ [m] and $T_P = 10.55$ [s].

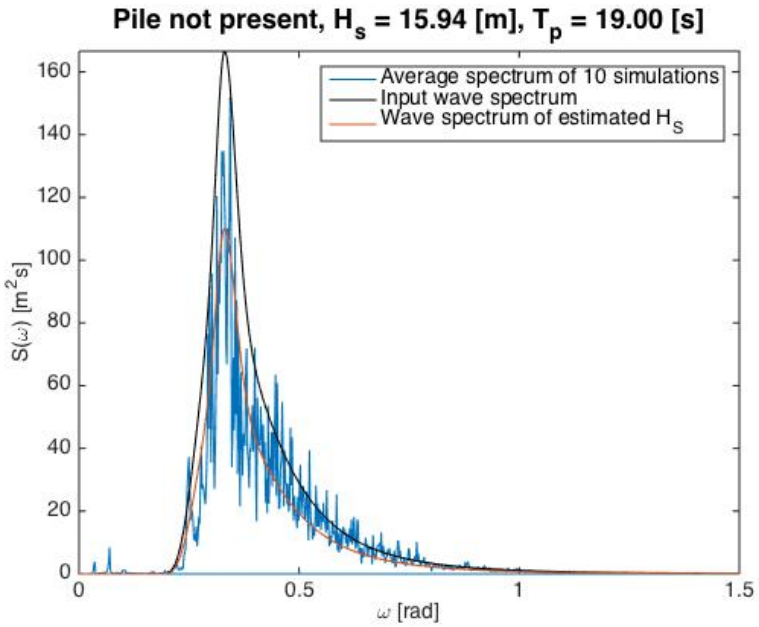

Figure 5.7: Averaged wave spectrum for sea state 15 with $H_S = 19.60$ [m] and $T_P = 19.00$ [s].

5.4.2 Statistical descriptions of the sea states

The distribution of wave crests within ten 1 [h] sea states and within an assembly of all the ten tests as well as the extreme value distribution are determined for all the sea states. Distributions of the individual crest heights are plotted together with the first order Rayleigh distribution and the second order Forristall distribution, while the extreme crest heights are plotted together with the T-hour distribution. The largest crest heights for all the tests are given in appendix D together with plots of the different distributions.

Distribution of the ten tests

The probabilities of the different wave crests for each of the ten tests for sea state 15 are seen in figure 5.8 together with the Forristall distribution and Rayleigh distribution for the respective $H_{S,out}$ value. In such a plot the scatter between the probabilities of the crest heights for the different tests can be seen. Still, it may be hard to determine by bare eye observations which distribution the wave crests tend to follow.

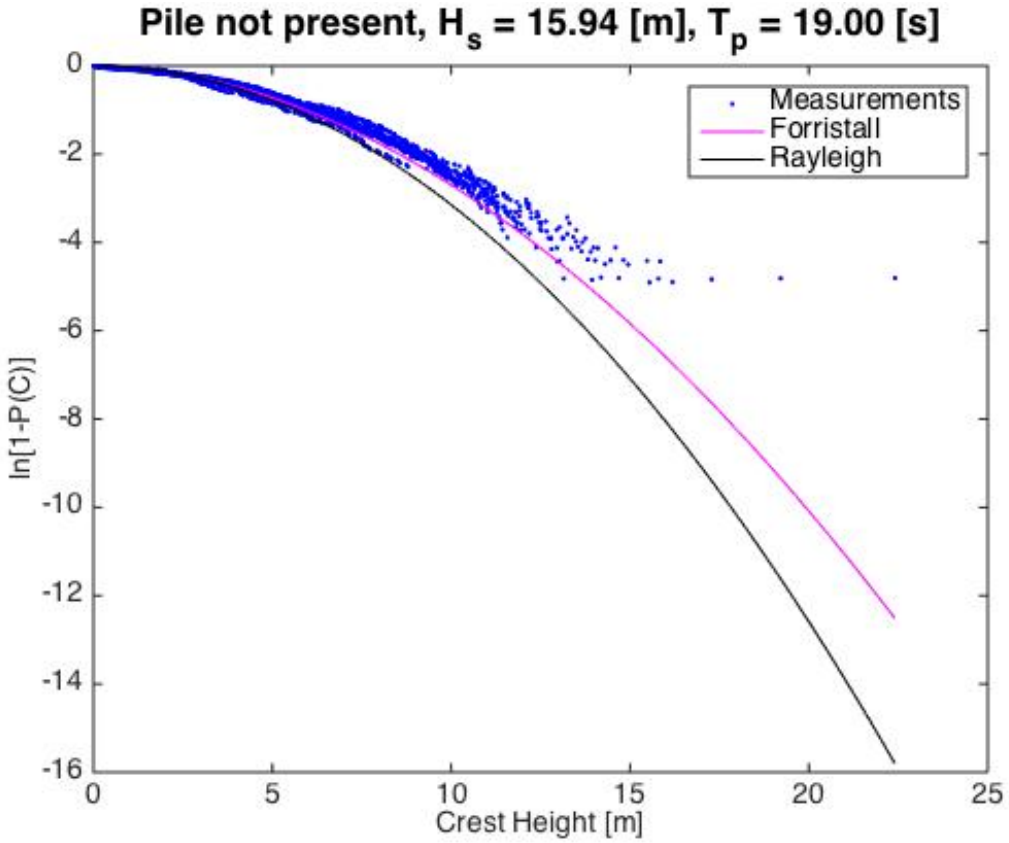

Figure 5.8: Distribution of the different wave crests plotted together with measurements from the ten tests for sea state 15.

Distribution of an assembly of the ten tests

The distribution of an assembly of all the ten tests can be used to get a better idea of the distribution trend of the wave crests in the sea state. Figure 5.9 shows an assembly of all the ten tests for the same sea state as shown in figure 5.8. From this figure it seen more clearly that the wave crests tend to follow the second order Forristall distribution, while a few of the largest crest heights seem to be influenced by higher order effects.

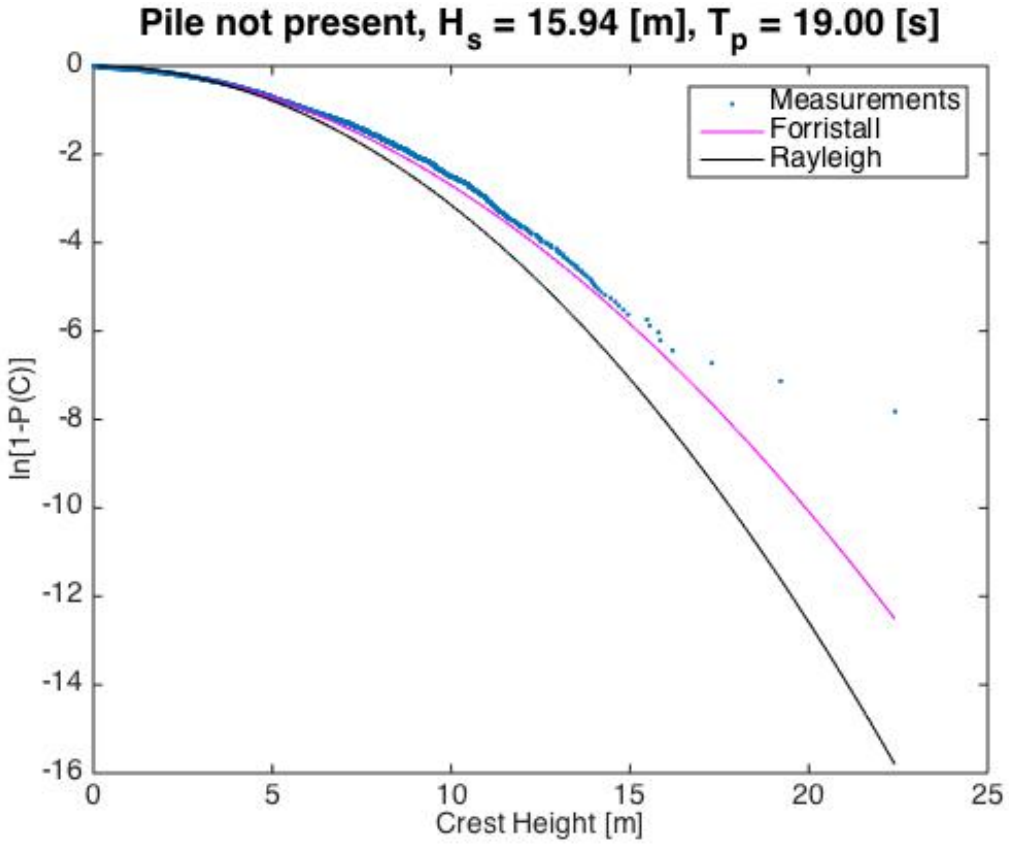

Figure 5.9: Distribution of the different wave crests plotted together with measurements for sea state 15.

A corresponding plot for sea state 1 is shown in figure 5.10. It can be seen that the probabilities for the wave crests up to about 7 [m] tend to follow the second order Forristall distribution, while an even higher order distribution seem to govern for wave crests up to about 9 [m]. Then the distribution tend to bend down below Forristall again.

The sea states subjected for model testing in this experiment are found to be generally

steep, where sea state 1 is among the steepest. Sea state 15 is the least steep sea state, and higher order than second order effects is therefore not seen in figure 5.9.

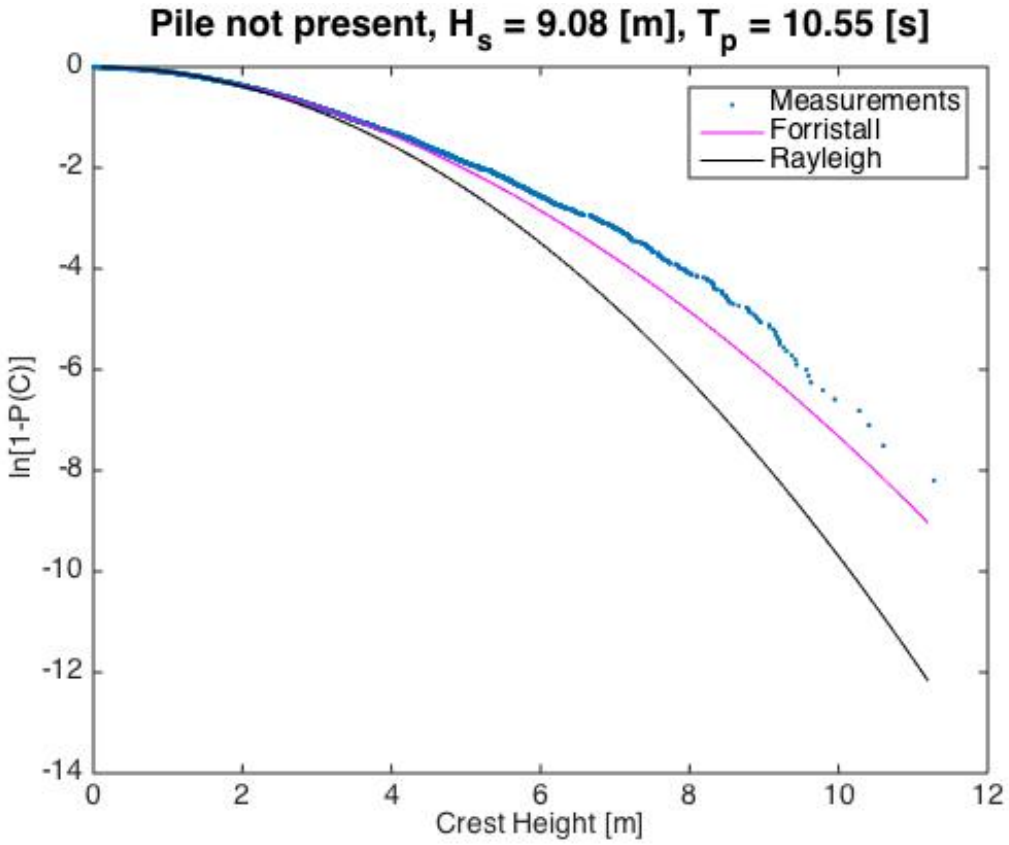

Figure 5.10: Distribution of the different wave crests plotted together with measurements for sea state 1.

Breaking

Waves are influenced by strongly non linear effects just prior to breaking leading to increased crest heights, whereas a decrease is introduced when breaking occur. This is exemplified in figure 5.10 where a higher order distribution of wave crests is seen above 7 [m] due to the growth of pre-breaking waves, while breaking is seen for crest heights above 9 [m].

The measured H_S values for the sea states are seen from table 5.4 to become larger when the pile is present than when it is absent, and steeper waves are hence expected when the pile is present in the flume. Distributions of wave crests for the steepest sea state in the experiment both with and without the pile installed are shown in figure 5.11, indicating wave breaking in both cases. Still, there seem to occur more breaking when the pile is

present as the measurements bend down far below the Forristall distribution earlier than when the pile is absent.

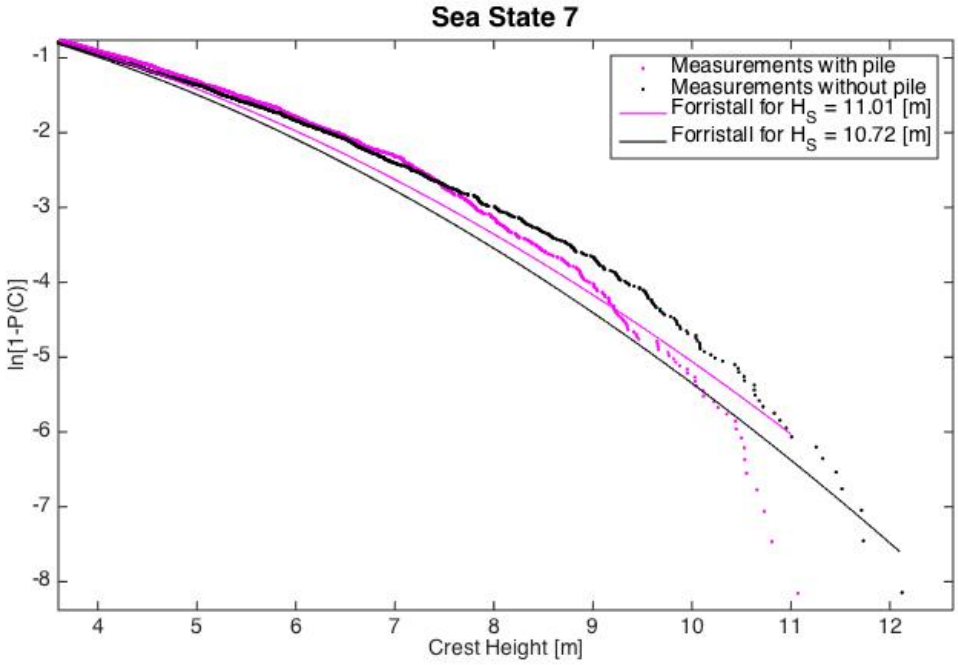

Figure 5.11: Distribution of wave crests in sea state 7 both when the pile is present and when the pile is absent.

Distribution of extreme crest heights

The T-hour distribution given in equation 3.23 in chapter 3 is the distribution of the extreme crest heights within a given sea state of T [h] duration. The largest crest height in each test for every sea state is found and plotted together with the distribution of extreme crest heights, using $T = 1$ [h]. This is exemplified in figure 5.12 and 5.13 for sea state 1 and 15, respectively. The measured extremes are located a considerable distance above the 1-hour distribution for both sea states, such that these distributions are assumed to underpredict the extreme crest heights. The same tendency is seen for the rest of the sea states given in appendix D.

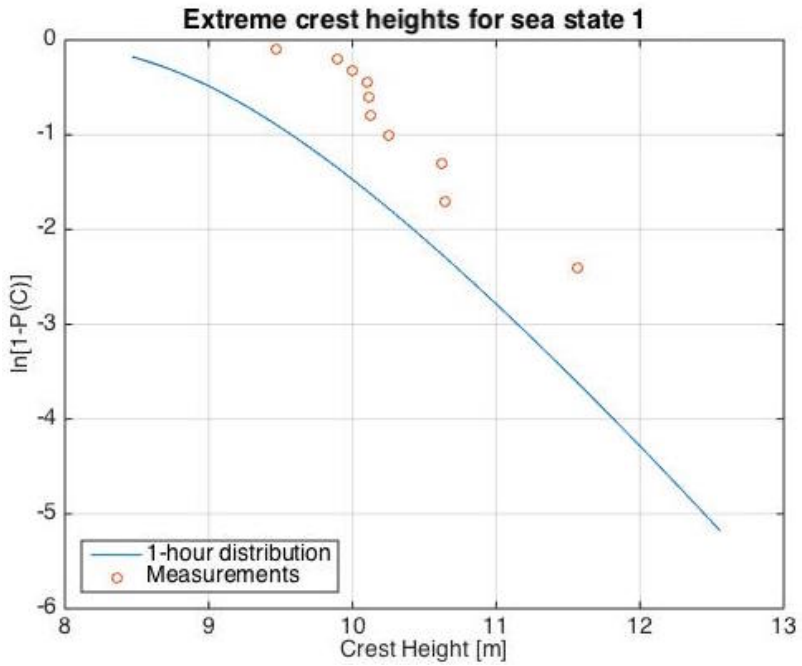

Figure 5.12: Distribution of extreme wave crests in sea state 1.

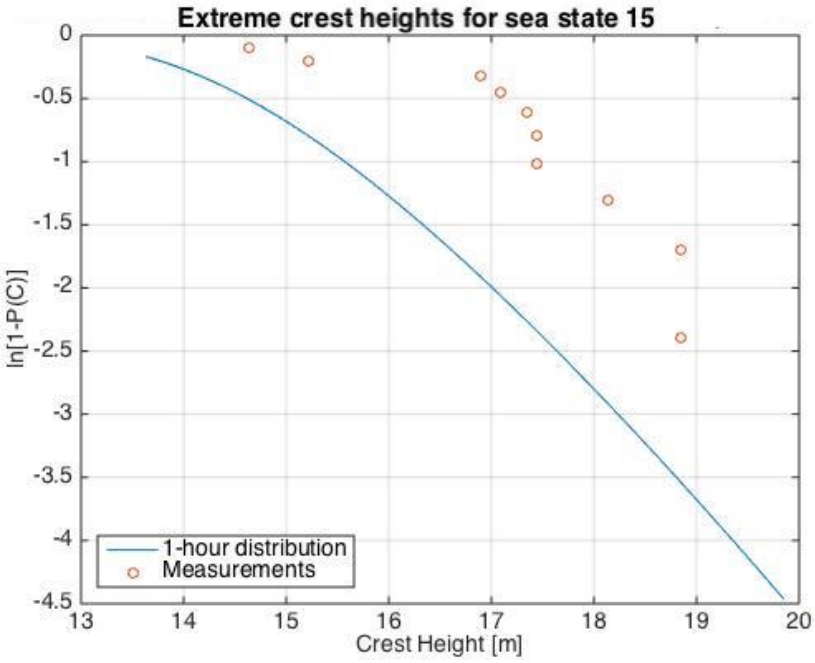

Figure 5.13: Distribution of extreme wave crests in sea state 15.

A range of crest heights covering the characteristic largest ULS or ALS value may be found by means of the 1-hour distribution and the predetermined fractiles given in table 3.1 in chapter 3. These ranges are given in table 5.6 for both the input sea states and the sea states obtained in the flume, termed $C_{1h,in}$ and $C_{1h,out}$, respectively. The largest measured crest heights C_{max} at the position of the pile are found above the corresponding percentile-ranges, which agrees well with the differences between the measured extreme crests and the 1-hour distribution. The ranges given by the 1-hour distribution may hence underpredict the characteristic values. It is worth noting that the largest crest height of 21.25 [m] is found for sea state 13.

Table 5.6: Crest heights corresponding to given fractile levels.

ID	T_P [s]	$H_{S,in}$ [m]	$C_{1h,in}$ [m]	$H_{S,out}$ [m]	$C_{1h,out}$ [m]	C_{max} [m]
1	10.55	10.00	11.57 - 11.91	9.08	10.34 - 10.65	11.65
2	11.48	11.00	12.51 - 12.89	10.07	11.31 - 11.65	13.53
3	12.38	12.00	13.46 - 13.87	10.97	12.20 - 12.56	15.00
4	13.71	13.00	14.34 - 14.77	11.92	13.06 - 13.45	16.24
5	15.40	14.00	15.18 - 15.64	12.55	13.51 - 13.92	16.24
6	16.76	14.91	16.01 - 16.50	12.99	13.82 - 14.24	15.09
7	11.30	12.00	14.33 - 15.03	10.72	12.58 - 13.17	13.37
8	12.00	13.00	15.39 - 16.12	11.29	13.07 - 13.69	15.00
9	13.00	14.00	16.28 - 17.06	12.39	14.19 - 14.86	16.75
10	14.00	15.00	17.20 - 18.02	13.28	15.05 - 15.77	18.59
11	15.20	16.00	18.12 - 18.99	13.75	15.38 - 16.11	18.23
12	16.00	17.00	19.17 - 20.09	14.96	16.69 - 17.48	17.64
13	16.90	18.00	20.19 - 21.17	14.92	16.49 - 17.28	21.25
14	18.00	19.00	21.19 - 22.22	15.63	17.17 - 17.99	17.83
15	19.00	19.60	21.74 - 22.79	15.94	17.40 - 18.23	18.85

5.4.3 Using the Donelan wave spectrum

Sea state 1, 6, 7 and 15 are tested using both the JONSWAP wave spectrum and the corrected version called the Donelan wave spectrum. A strange behaviour of the Donelan spectrum is seen for some H_S values, leading to a smaller area than required under this spectrum. An investigation of the theoretical wave spectrum will be presented in the following together with a comparison between the measurements of the four sea states using both JONSWAP and Donelan wave spectrum.

Theoretical study of the Donelan wave spectrum

A basic requirement for a wave spectrum is to describe the energy density within a given sea state as precise as possible. It should hence provide a variance leading to the same significant wave height as the input $H_{S,in}$ value. Terming the significant wave height provided by the theoretical Donelan spectrum $H_{S,D}$, a comparison between $H_{S,in}$ and $H_{S,D}$ is given for the four sea states in table 5.7 below.

Table 5.7: Values for $H_{S,in}$ and $H_{S,D}$ from the Donelan spectrum for sea state 1, 6, 7 and 15.

ID	Donelan input $H_{S,in}$ [m]	Donelan output $H_{S,D}$ [m]
1	10.00	9.99
6	14.91	14.92
7	12.00	12.01
15	19.60	19.86

There are good accordance between $H_{S,in}$ and $H_{S,D}$ for sea state 1, 6 and 7, whereas a small deviation is seen for sea state 15. Donelan spectrums for different $H_{S,in}$ values when keeping T_P constant and equal to 19 [s], which is the peak period of sea state 15, are shown in figure 5.14. The corresponding $H_{S,D}$ values are given in table 5.8.

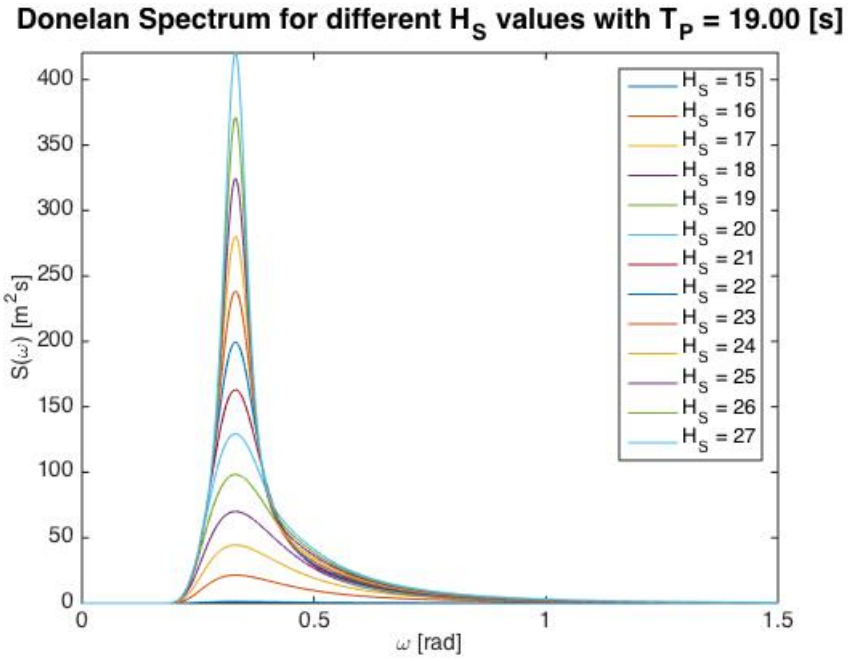

Figure 5.14: Theoretical Donelan wave spectrum for different H_S values with $T_P = 19.00$ [s].

Table 5.8: $H_{S,in}$ and corresponding $H_{S,D}$ values using Donelan wave spectrum for $T_P = 19.00$ [s].

$H_{S,in}$ [m]	$\varepsilon_{ss,in}$ [-]	$H_{S,D}$ [m]	$\frac{H_{S,D}}{H_{S,in}}$
15.00	0.0312	2.77	0.1847
16.00	0.0333	10.11	0.6319
17.00	0.0354	14.03	0.8253
18.00	0.0374	16.84	0.9356
19.00	0.0395	18.89	0.9942
20.00	0.0416	20.41	1.0205
21.00	0.0437	21.58	1.0276
22.00	0.0458	22.53	1.0241
23.00	0.0478	23.40	1.0174
24.00	0.0499	24.25	1.0104
25.00	0.0520	25.12	1.0048
26.00	0.0541	26.02	1.0008
27.00	0.0562	26.96	0.9985

It is clear that the Donelan spectrum does not provide satisfactory description for all $H_{S,in}$ values. The deviation is of significant magnitude for $H_{S,in}$ lower than 19 [m] when T_P is equal to 19 [s], as seen in table 5.8. An equal study for the T_P values corresponding to sea state 1, 6 and 7 can be found in appendix E.1, while a graphical representation of the results is given in figure 5.15 below. Better results are seen for lower T_P values, whereas for higher T_P values the $H_{S,in}$ must be larger in order to obtain a satisfactory wave spectrum. Generally, the Donelan spectrum seems to provide a good description for sea states steepnesses larger than 0.0370 [-].

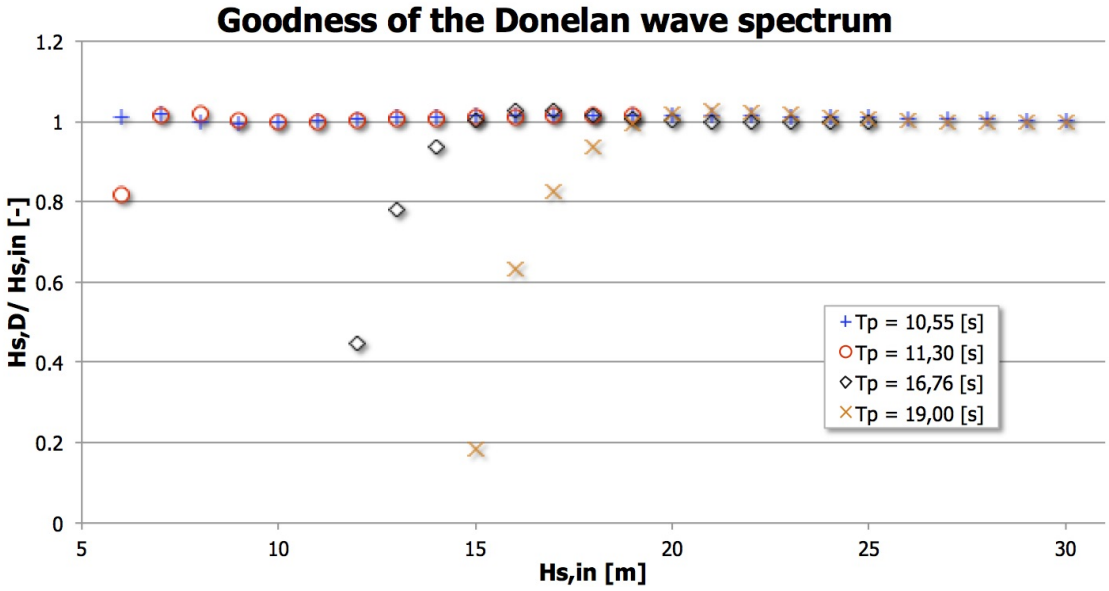

Figure 5.15: Relation between $H_{S,D}$ and $H_{S,in}$ for different $H_{S,in}$ values when keeping T_P constant.

Now that the Donelan spectrum is shown not to provide a good description for all sea states, the behaviour of the three parameters β_D, γ_D and σ_D in the analytic formula should be investigated when keeping T_P constant. Such an investigation is exemplified in the following for the T_P value of sea state 15, which is the sea state with largest deviation between the $H_{S,in}$ and the corresponding $H_{S,D}$ value as seen in figure 5.15.

Figure 5.16 shows the behaviour of the β_D parameter for H_S values up to 30 [m] for $T_P = 19$ [s]. The β_D parameter increases exponentially for increasing H_S values, but it is generally small in magnitude.

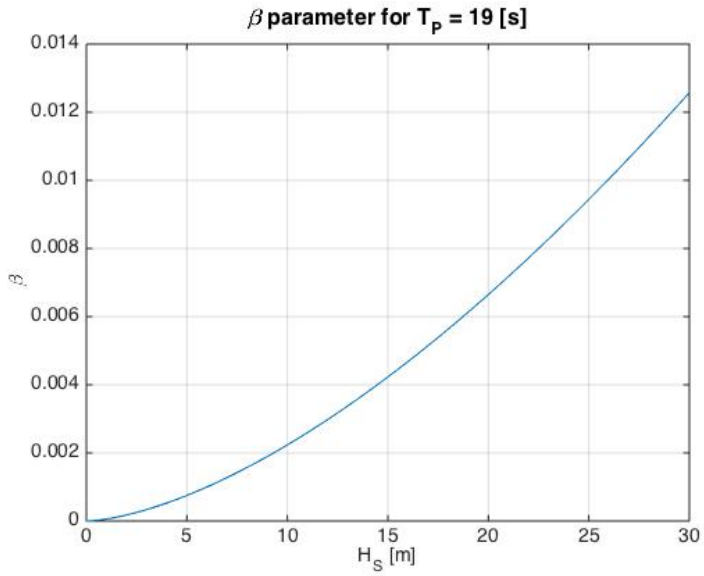

Figure 5.16: Behaviour of the β_D parameter for different H_S values when $T_P = 19.00$ [s].

The behaviour of the γ_D parameter for the same T_P value is shown for H_S values up to 30 [m] in figure 5.17. It has a negative value for H_S up to 15 [m], and approaches $-\infty$ when H_S approaches zero. For higher H_S values the parameter seems to stabilize and the values are somewhat larger in magnitude than for the β_D parameter.

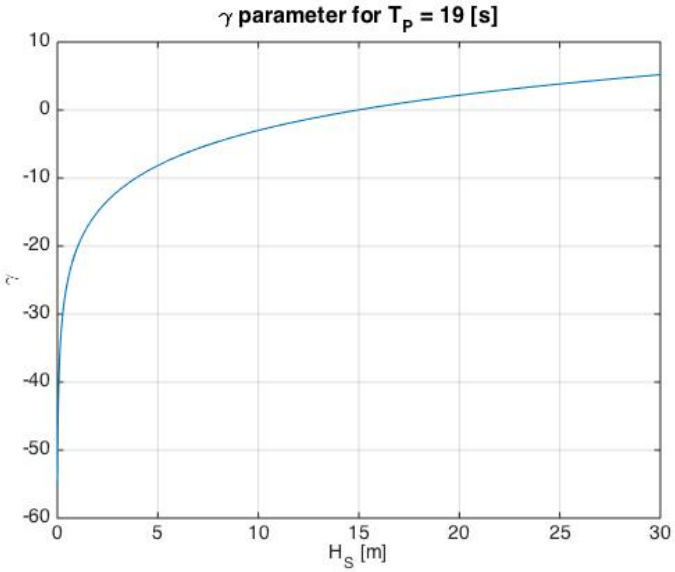

Figure 5.17: Behaviour of the γ_D parameter for different H_S values when $T_P = 19.00$ [s].

The σ_D parameter increases towards ∞ when H_S approaches zero, as seen in figure 5.18. Figure 5.19 gives a better picture of the behaviour of this parameter as the magnitude of the vertical axis is much smaller for H_S above 10 [m]. It can still be seen that the σ_D values are of relatively high magnitude for $H_S = 10$ [m], while they approach 0.08 for increasing H_S values.

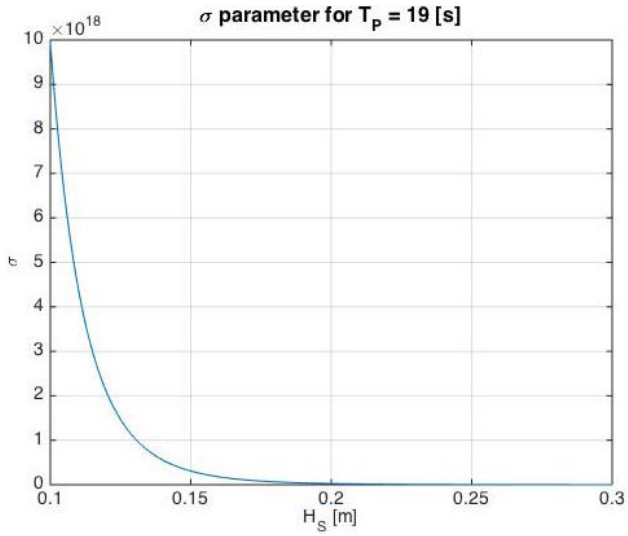

Figure 5.18: Behaviour of the σ_D parameter for the lowest H_S values when $T_P = 19.00$ [s].

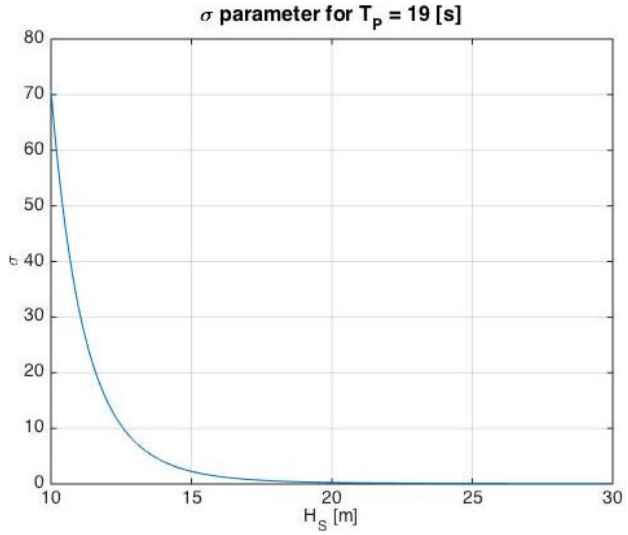

Figure 5.19: Behaviour of the σ_D parameter for H_S values between 10 [m] and 30 [m] when $T_P = 19.00$ [s].

Recalling the total expression for the Donelan wave spectrum in equation 5.8, the γ_D parameter will be raised to the power of one for decreasing H_S values as the σ_D parameter is found to increase rapidly in this case. The γ_D parameter is found to obtain negative values for decreasing H_S values, which means that the value of the total expression will be negative because the β_D parameter is always positive. A negative wave spectrum is unphysical, and the parameterization is hence way out of validation range for lower H_S values.

For larger H_S values the σ_D parameter approaches 0.08, which is between the two values commonly used for the normal JONSWAP spectrum, i.e. 0.07 and 0.09. The γ_D parameter is found to be positive for H_S values above 15 [m], and the resulting value of the wave spectrum will hence be positive for higher H_S values. From figure 5.15 the differences between $H_{S,in}$ and $H_{S,D}$ are found to be significant for $H_{S,in}$ values up to about 19 [m], which is where the σ_D parameter seems to approach 0.08.

Measurements

Sea state 1, 6, 7 and 15 have been tested in the flume by means of both the JONSWAP wave spectrum and the Donelan wave spectrum. The measured significant wave heights from these tests are given in table 5.9 both when the pile is present and when it is absent. There are no clear differences between the measurements using the different spectrums as the values are pretty close to one another. This means that there are significant deviations between $H_{S,in}$ and $H_{S,out}$ when using the Donelan spectrum as well. The measured values seem to be somewhat larger when using the Donelan wave spectrum for sea state 1 and 7, which are those located farthest down on the ULS and ALS contour lines. For sea state 6 and 15, which are those on top of the contour lines, the tests based on the Donelan spectrum seem to provide smaller values than those based on the JONSWAP spectrum. This trend is not clear, and even more sea states should be subjected for model testing and compared before drawing any conclusions.

Table 5.9: Measured H_S values for sea state 1, 6, 7 and 15 using JONSWAP wave spectrum and Donelan wave spectrum.

		JONSWAP		**Donelan**	
ID	$H_{S,in}$ [m]	$H_{S,out}$ [m]	$H_{S,pile}$ [m]	$H_{S,out}$ [m]	$H_{S,pile}$ [m]
1	10.00	9.08	9.31	9.13	9.17
6	14.91	12.99	13.25	12.67	12.75
7	12.00	10.72	11.01	11.15	11.21
15	19.60	15.94	16.43	15.74	16.36

The averaged wave spectrums of the ten tests when using the Donelan spectrum are shown in figure 5.20 and 5.21 for sea state 1 and 15, respectively. They are plotted together with the theoretical Donelan spectrums for both $H_{S,in}$ and $H_{S,out}$ as well as the corresponding JONSWAP spectrum for $H_{S,out}$. There is good accordance between the measured wave spectrum and the Donelan spectrum for $H_{S,out}$ regarding sea state 1, whereas there is a considerable deviation between the two spectrums for sea state 15. This deviation is so large that the theoretical Donelan spectrum using $H_{S,out}$ for sea state 15 is assumed invalid. A similar tendency is seen for sea state 6 and 7 as well, with large deviation for sea state 6 and good accordance for sea sate 7. These plots may be found in appendix E.2.

As seen in table 5.9 the $H_{S,out}$ values from the measurements are somewhat lower than the $H_{S,in}$ values. Sea state 6 and 15 have T_P values of 14.67 [s] and 19.00 [s], respectively. Recall from figure 5.15 that the theoretical Donelan spectrum for these T_P values is shown to provide poor description of sea states with significant wave heights below 14 [m] and 19 [m], respectively. These two sea states can therefore be concluded to have a sea state steepness out of the validation range for the parameterized Donelan spectrum, as the $H_{S,out}$ values are found to be 12.67 [m] for sea state 6 and 15.74 [m] for sea state 15. This is the reason for the large deviations between measured and theoretical Donelan spectrums for $H_{S,out}$ for these sea states. Still, the time series are based upon wave spectrums that are found within the validation range and can hence be assumed reliable.

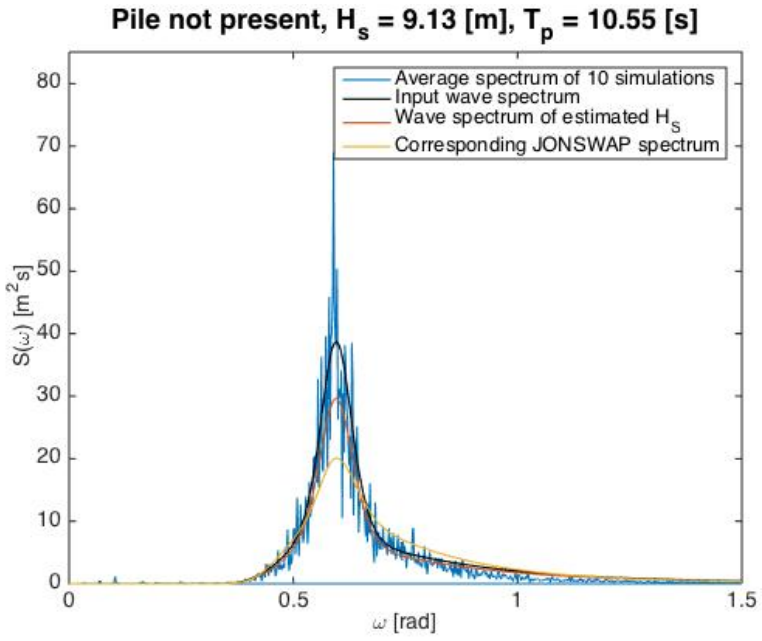

Figure 5.20: Measured wave spectrum plotted together with the Donelan wave spectrum for $H_{S,in}$ and $H_{S,out}$ compared to the JONSWAP spectrum for $H_{S,out}$ for sea state 1.

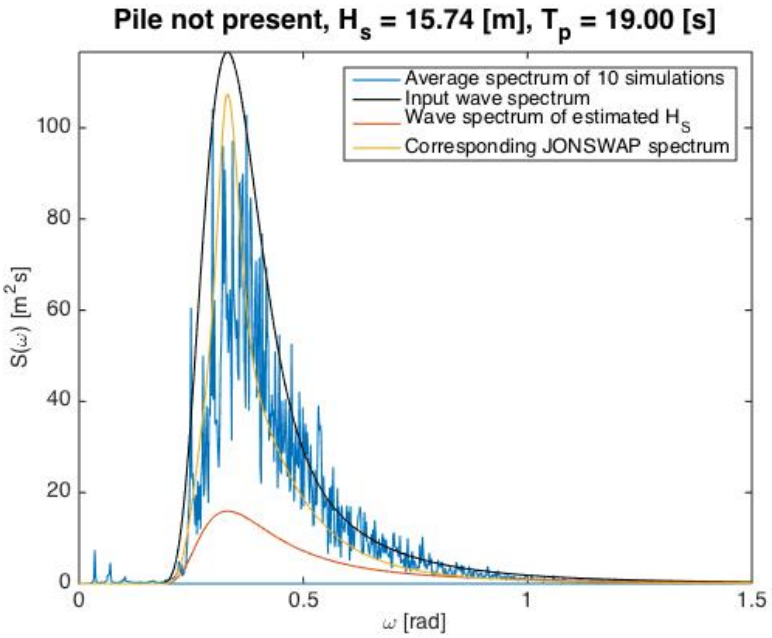

Figure 5.21: Measured wave spectrum plotted together with the Donelan wave spectrum for $H_{S,in}$ and $H_{S,out}$ compared to the JONSWAP spectrum for $H_{S,out}$ for sea state 15.

It is seen from figure 5.20 that the measured wave spectrum does fit the Toba form in a satisfactory manner for sea state 1, indicating that a decrease proportional to ω^{-4} has been obtained in the flume. Some deviations between the measurements and the tail of the theoretical Donelan spectrum are still seen for ω above 0.9 [rad]. Recalling from figure 5.6 that the decay of this sea state based on the JONSWAP spectrum seemed proportional to a higher order than ω^{-5}, the decays when using the two spectrums should be looked into. Figure 5.22 and 5.23 show the averaged measured wave spectrums for sea state 1 multiplied with both ω^4 and ω^5 using the JONSWAP spectrum and Donelan spectrum, respectively.

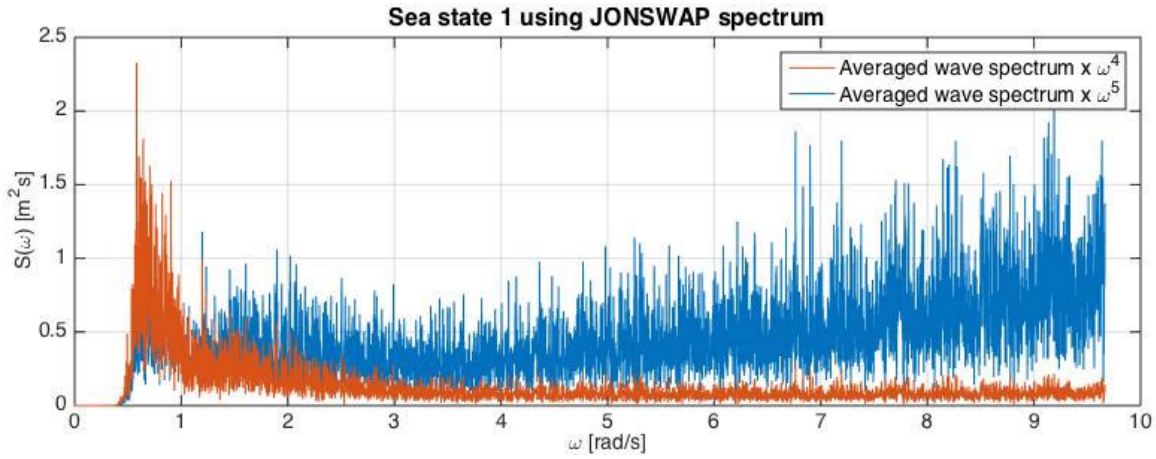

Figure 5.22: Measured wave spectrum of sea state 1 using the JONSWAP spectrum multiplied with ω^4 and ω^5.

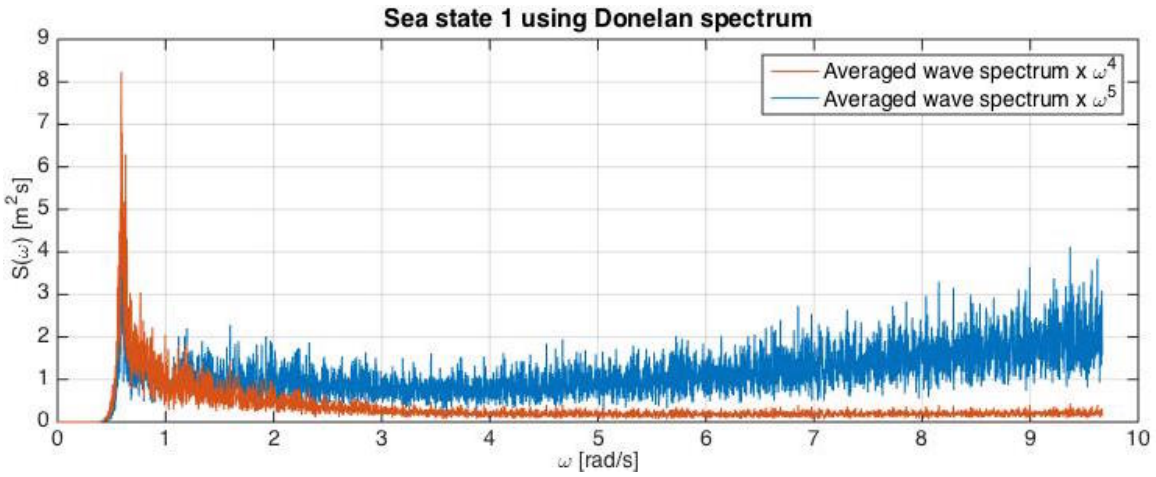

Figure 5.23: Measured wave spectrum of sea state 1 using the Donelan spectrum multiplied with ω^4 and ω^5.

It is clear that the measured wave spectrums multiplied with ω^5 increase with increasing frequencies in both cases. This implies that a decay proportional to ω^{-5} for frequencies above ω_P is not obtained using the JONSWAP spectrum. On the other hand, the measured wave spectrums proportional to ω^4 are decreasing somewhat using both wave spectrums. It is therefore likely to believe that a decay exactly proportional to ω^{-4} is not obtained using the Donelan wave spectrum, and that a decay between ω^{-4} and ω^{-5} is obtained using the JONSWAP spectrum. The same tendency is seen regarding sea state 15 in figure 5.24 and 5.25. An exact decay is hard to determine by bare eye observations due to the somewhat

noisy measured wave spectrums.

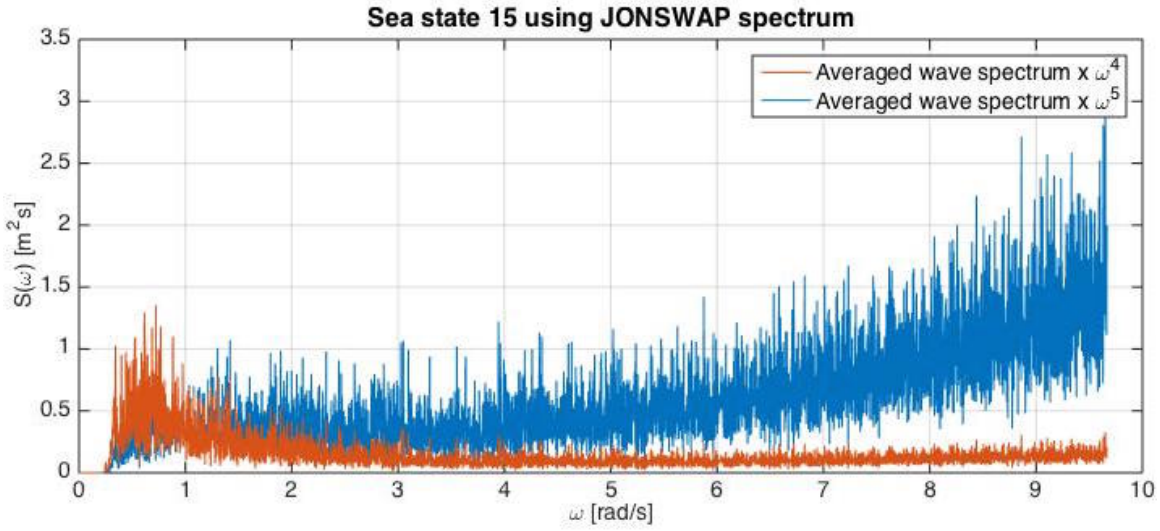

Figure 5.24: Measured wave spectrum of sea state 15 using the JONSWAP spectrum multiplied with ω^4 and ω^5.

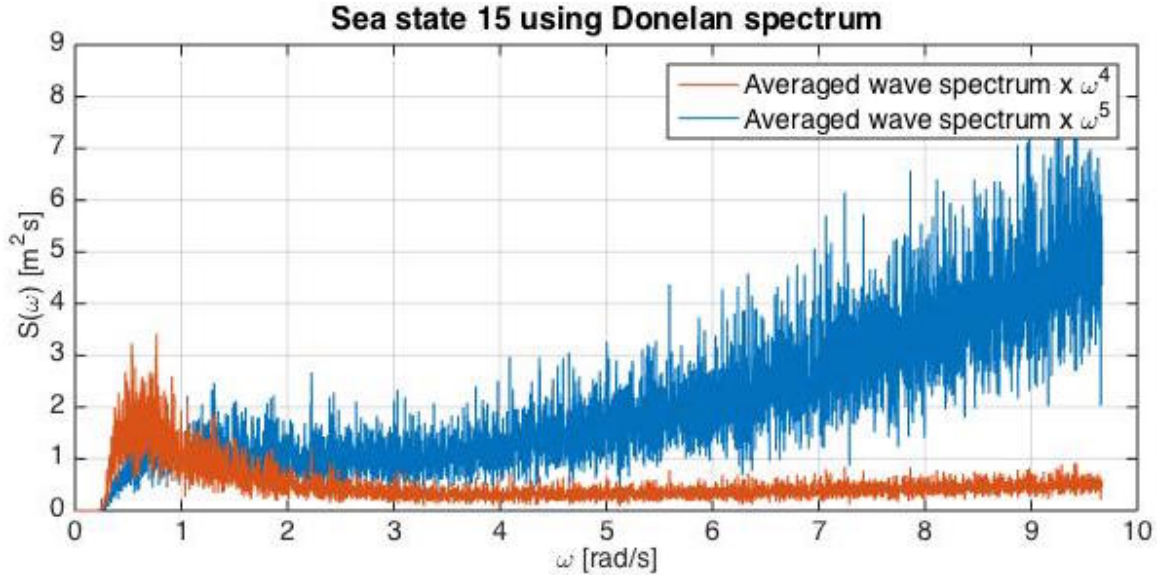

Figure 5.25: Measured wave spectrum of sea state 15 using the Donelan spectrum multiplied with ω^4 and ω^5.

Distribution of wave crests

The distribution of the measured wave crests using the Donelan wave spectrum and the JONSWAP wave spectrum are compared for all the sea states and can be found in appendix E.2. It is generally seen that the crest heights when the Donelan wave spectrum is used are somewhat higher than when the JONSWAP spectrum is used. This is exemplified for sea state 15 in figure 5.26 and may indicate that the sea state consists of steeper waves when the Donelan spectrum is used. A difference between the two spectrums is seen for the lowest crest heights in sea state 7 in figure E.10. As the largest crest heights are of main interest in this thesis, this phenomena is left for future investigation. There is no clear pattern between the two wave spectrums regarding wave breaking.

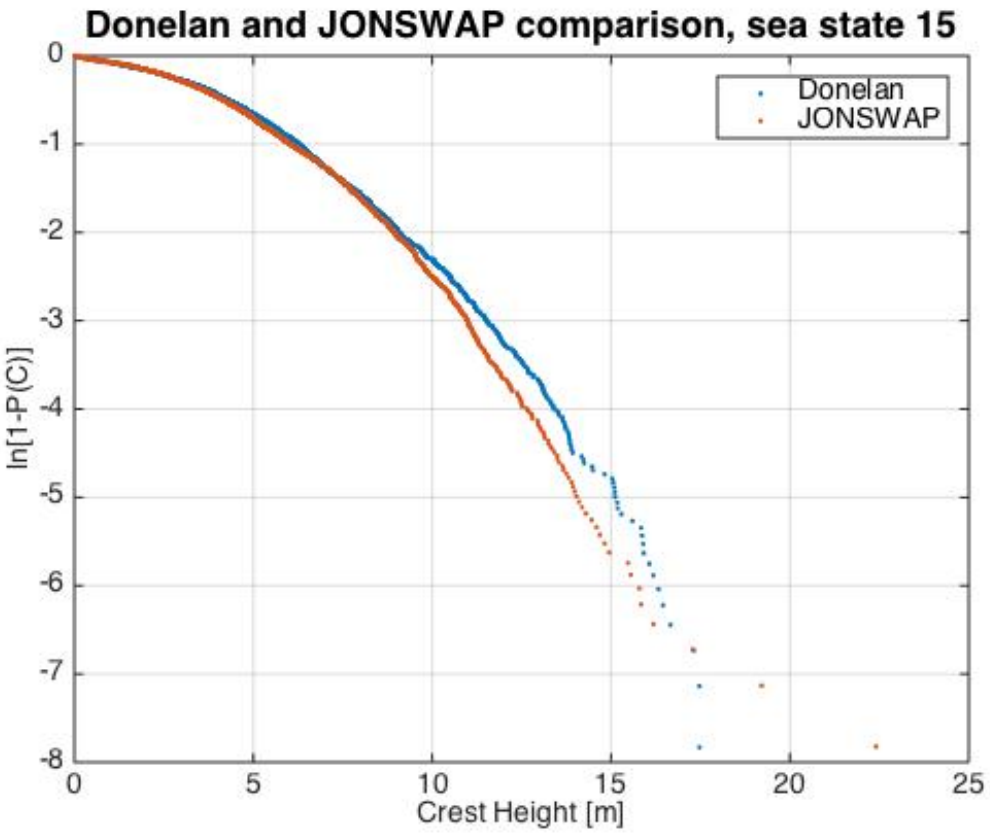

Figure 5.26: Distribution of wave crests for sea state 15 using both the JONSWAP wave spectrum and the Donelan wave spectrum.

The largest measured extreme crest heights are given in table 5.10 for sea state 1, 6, 7 and 15 using both JONSWAP and Donelan wave spectrum. Except from sea state 7, all the

largest extreme values are smaller when the Donelan spectrum is used. Figure 5.27, 5.28, 5.29 and 5.30 show the extreme value distributions for each sea state using both wave spectrums. It is clear that the measured extreme crest heights for sea state 1 and 7 are larger when the sea state is based on the Donelan wave spectrum, whereas the extremes for sea state 6 and 15 are larger when the JONSWAP spectrum is used. Note that a limiting factor for the crest heights seems to become important for sea state 1 and 6 using the Donelan spectrum as the measured values stagnate around 11.5 [m] and 15 [m], respectively. Such a stagnation is not seen for sea state 7, where the extreme crest heights seem to grow very high. The difference between the extremes is small for sea state 15.

Table 5.10: Largest measured crest heights C_{max} for sea state 1, 6, 7 and 15 using JONSWAP wave spectrum and Donelan wave spectrum.

ID	JONSWAP C_{max} [m]	Donelan C_{max} [m]
1	11.28	10.80
6	15.34	14.83
7	12.12	13.61
15	22.41	17.47

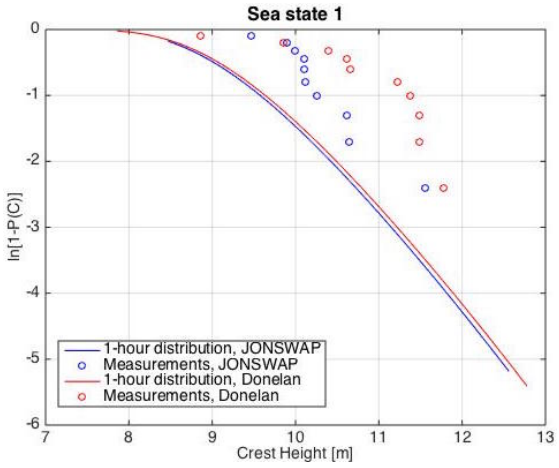

Figure 5.27: Extreme crest heights for sea state 1 using both JONSWAP and Donelan wave spectrum.

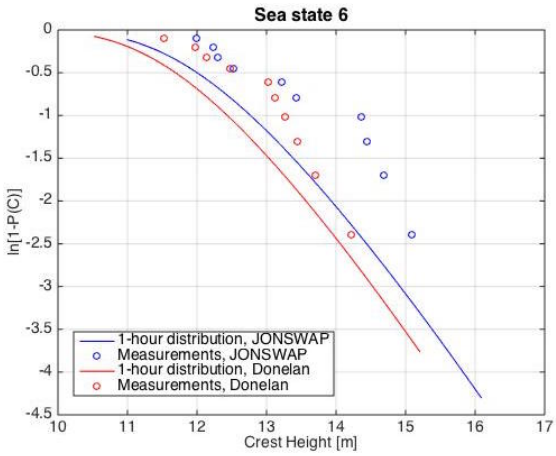

Figure 5.28: Extreme crest heights for sea state 6 using both JONSWAP and Donelan wave spectrum.

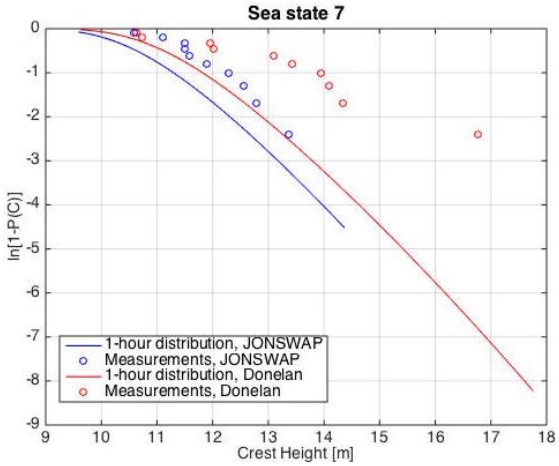

Figure 5.29: Extreme crest heights for sea state 7 using both JONSWAP and Donelan wave spectrum.

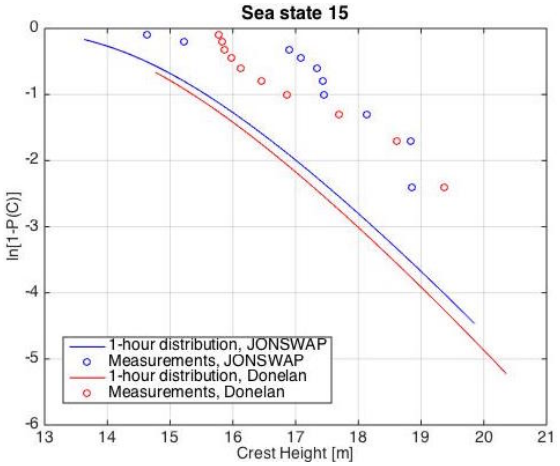

Figure 5.30: Extreme crest heights for sea state 15 using both JONSWAP and Donelan wave spectrum.

5.5 Discussion and recommendations

5.5.1 Input wave spectrums

The JONSWAP spectrum is used in the generation of the sea states in the model tests, as the Torsethaugen wave spectrum is found to coinside with the JONSWAP spectrum for the most severe ULS and ALS sea states. This means that swells are neglected in this experiment and that the sea states subjected for model testing are governed by wind seas. In addition, the Donelan spectrum is tested for the two sea states with the smallest and largest H_S value in the selected range for both ULS and ALS. These are also the steepest and the least steep sea states within the two limit states.

5.5.2 Deviations in measurements

Some deviations between $H_{S,in}$ and $H_{S,out}$ from the measurements are found, especially for sea states located high up on the contour lines. Generally the $H_{S,out}$ values are seen to be 82 % - 92 % of $H_{S,in}$, which may be explained by the mechanical losses in the flap as stated in chapter 4. The relation between the motion of the wave maker and the measured wave heights in the flume was then proven to fit the theoretical transfer function satisfactory, whereas the motion of the wave maker was seen not to fit the required motion as precise.

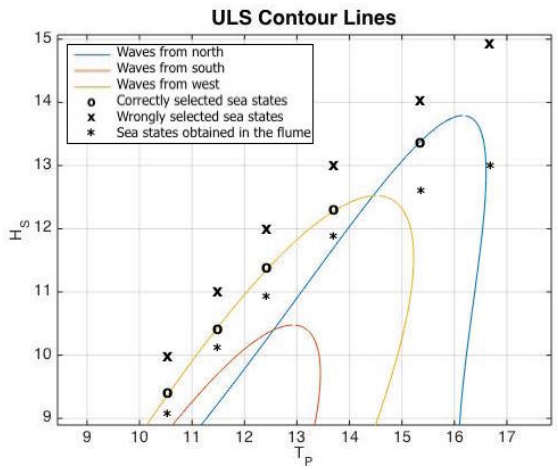

Figure 5.31: Wrongly and correctly selected ULS sea states and actual ULS sea states from model testing.

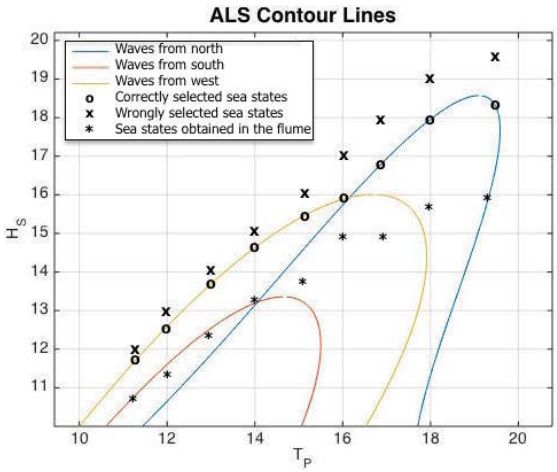

Figure 5.32: Wrongly and correctly selected ALS sea states and actual ALS sea states from model testing.

The somewhat low $H_{S,out}$ values result in model testing of other sea states than first assumed. Figure 5.31 and 5.32 show the top of the ULS and ALS contour lines including the wrongly and correctly selected critical sea states from chapter 3, as well as the sea states obtained in the flume. The deviations between input and output sea states are significant and

somewhat larger than between the output sea states and the correctly selected sea states. The error of wrongly selecting the critical sea states in chapter 3 is hence assumed not to be of relative significance as the losses related to the model testing are much larger. It is still important to have in mind that the results from the model testing do not completely correspond to the correctly selected sea states.

The presence of the pile in the flume leads to somewhat higher waves compared to when it is absent. The $H_{S,pile}$ values are 0.7 % - 7 % larger than the $H_{S,out}$ values, and the waves are generally steeper in these tests. From chapter 4 the oscillatory behaviour of the pile is found to be significant as it may amplify the incoming wave heights. The presence of the pile also leads to wave diffractions of significant magnitude as shown in figure 5.33, which may force the incoming waves upwards as they are oppositely directed.

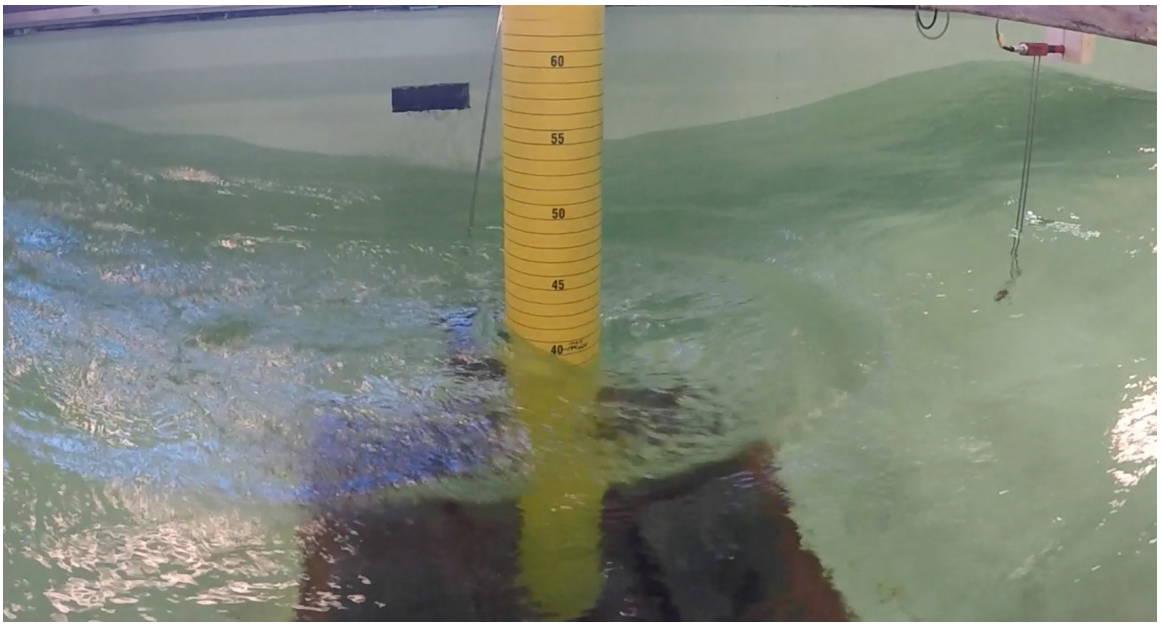

Figure 5.33: Diffraction from pile.

The deviation between measured and theoretical JONSWAP wave spectrum is found to be largest at the decreasing side, especially for the steepest sea states. This indicates that the energy density of the waves obtained in the flume seem to decrease more rapidly than proportional to ω^{-5}. The Donelan wave spectrum may be a better representation in such cases.

5.5.3 Statistical description

The steepness of the sea states is reduced as a result of the new, low $H_{S,out}$ values from the model tests. The crest heights of the least steep sea states still tend to follow the second order Forristall distribution, while the steepest sea states tend to follow an even higher order distribution. For the latter the distributions seem to bend down for increasing crest heights. A highly non linear behaviour is seen as waves get steep just prior to breaking, whereas breaking is seen as a drop in the crest height distributions for these sea states. The drop occurs when the waves start to break as this reduces the crest heights. Hence, breaking is still probable since the sea states consist of relatively steep waves despite the lower $H_{S,out}$ values. This feature should therefore be investigated further in order to predict loads and responses of the pile in the selected sea states. This will be done in chapter 6 and 7, where breaking waves are generated and studied in detail.

The range of extreme crest heights corresponding to the predefined percentiles given in chapter 3 will now become lower than first predicted. Still, the measured extreme crest heights are found above the 1-hour distributions for all sea states, such that the distribution can be assumed improper for the steep waves in this experiment. To investigate this further 1000 synthetic data samples may be generated based on the 1-hour distribution by means of Monte Carlo simulation. This is shown for sea state 13 in figure 5.34, where almost all the measurements are found outside the wide range of synthetic data samples, supporting the assumption of an improper theoretical distribution.

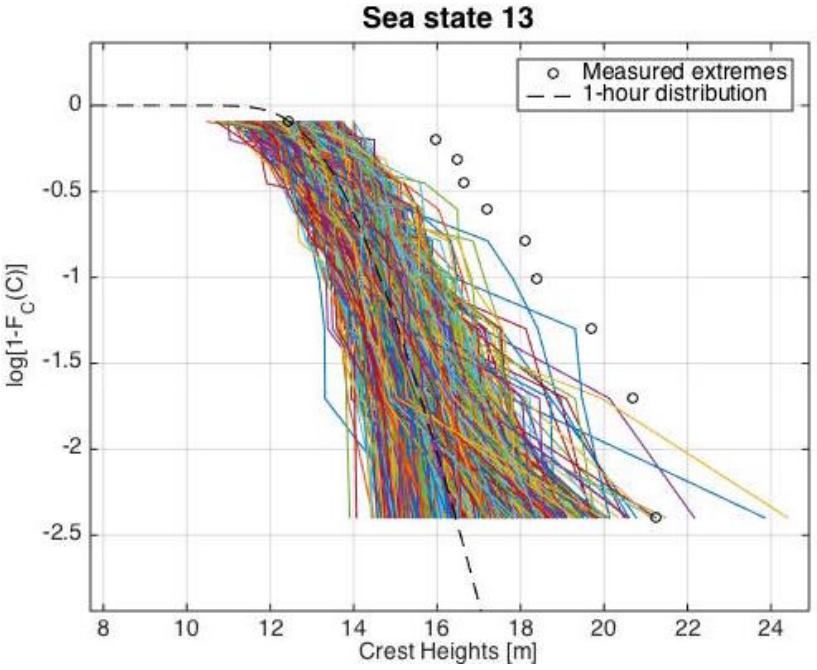

Figure 5.34: Bootstrapping of the 1-hour distribution for sea state 13.

5.5.4 Investigation of sea state 13

The measured $H_{S,out}$ value of sea state 13 is found to be 14.92 [m], which is highly unexpected as it is smaller than the measured value of 14.96 [m] for sea state 12. This tendency is not seen for the $H_{S,pile}$ values, such that there is no reason to believe that the generated time series of sea state 13 consists of generally small waves due to random nature. In order to see if this strange behaviour can be explained by any possible error sources related to the experiment, it would be of interest to perform the model tests of sea state 12 and 13 once more both with and without pile present in the flume. Generation of ten new tests of sea state 13 is also of interest to determine whether this is a repeating trend or not.

The T_P value is 16 [s] for sea state 12 and 16.9 [s] for sea state 13, leading to a larger sea state steepness for sea state 12. As seen in figure 5.35 below, higher wave crests are more probable for sea state 12 than for sea state 13 up to about 16 [m]. Then a sudden drop in the distribution is seen for sea state 12, implying a breaking wave limit. This behaviour is not seen for sea state 13, and breaking does not seem significant for this sea state as the crest heights seem unlimited by external factors. The small number of such high crests introduces large uncertainties in this matter. Still, the extreme values in figure 5.37 also imply the crest heights to grow without any limiting factor and they are much higher than the 1-hour distribution. The extreme wave crests in sea state 12 shown in figure 5.36 are found much closer to the 1-hour distribution, especially for wave crests above 16 [m], where breaking already has been assumed probable.

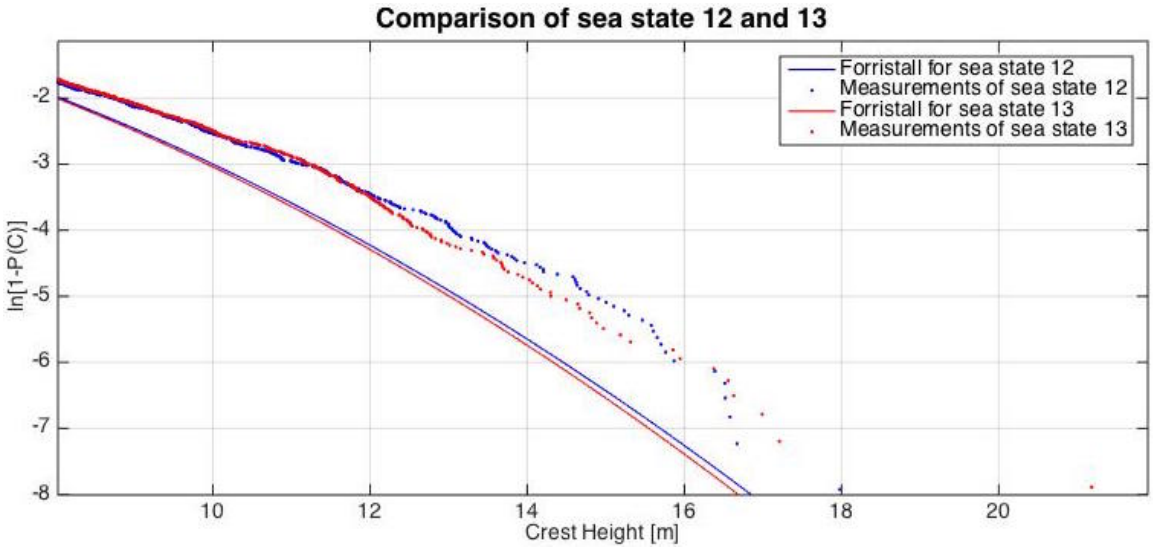

Figure 5.35: Distribution of wave crests for sea state 12 and 13.

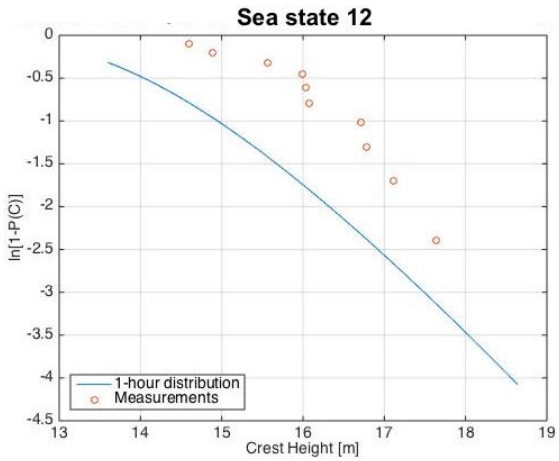

Figure 5.36: Extreme 1-hour distribution of wave crests together with measurements for sea state 12.

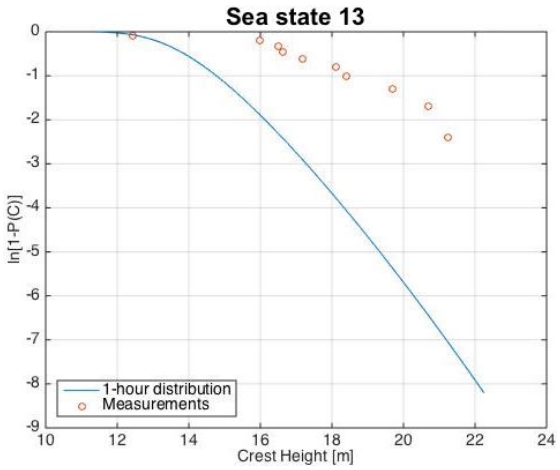

Figure 5.37: Extreme 1-hour distribution of wave crests together with measurements for sea state 13.

It is worth investigating the largest extreme crest heights some more, especially for sea state 13 which has the largest measured crest heights in this experiment. Figure 5.38 and 5.39 show the two largest crest heights in this sea state of 21.25 [m] and 19.70 [m], with corresponding periods of 13.7 [s] and 11.7 [s], respectively. The largest wave has a steepness of 0.1099 [-], whereas the second largest has a steepness of 0.1432 [-] which is above the breaking wave limit and a formation of overturning fluid mass at the crest is seen for this wave. Breaking is now seen to occur for sea state 13, but it is not as probable as for sea state 12. Performing the same investigation of sea state 12, spilling is seen at the largest wave crest. The second largest wave crest in this sea state is unstable as it is way above the breaking limit, and it can be regarded as a pre-breaking wave.

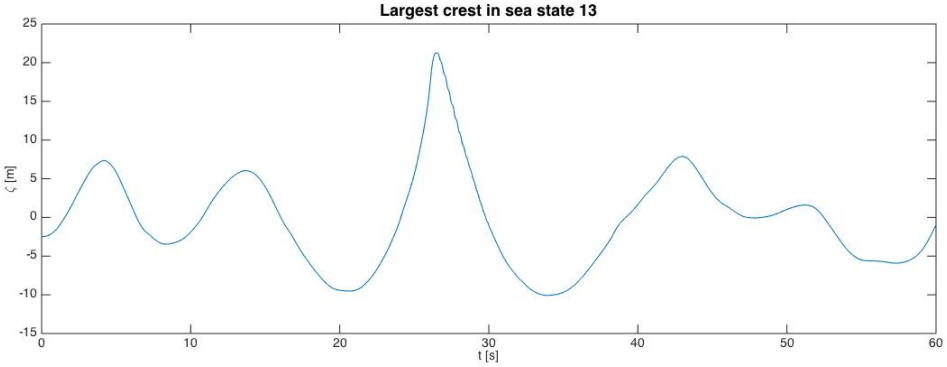

Figure 5.38: The largest crest height measured in sea state 13.

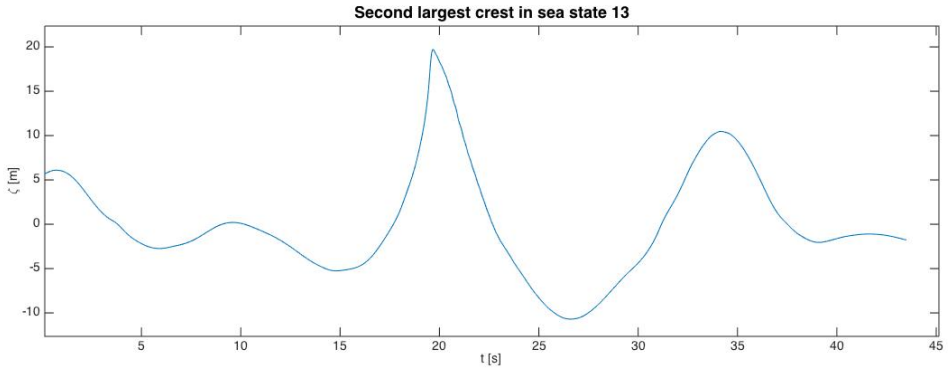

Figure 5.39: The second largest crest height measured in sea state 13.

Now that one of the largest waves in this experiment is seen as a plunging breaker, the forces exerted on the pile by such waves will be investigated further in chapter 6 and 7.

5.5.5 Differences between JONSWAP and Donelan wave spectrums

The theoretical Donelan wave spectrum is seen not to provide satisfactory description of all sea states, as good results are only obtained for sea state steepnesses above 0.0370 [-]. This steepness is found based on a theoretical study of the four tested sea states, but an even more comprehensive investigation should be performed in order to draw a final conclusion.

Deviations between $H_{S,in}$ and $H_{S,out}$ are also seen from the model tests based on the Donelan wave spectrum. For the two sea states on top of the ULS and ALS contour lines, the $H_{S,out}$ value leads to a sea state steepness less than 0.0370 [-], and a theoretical Donelan spectrum can hence not be fitted to the measurements. On the other hand, the two lowest sea states on the ULS and ALS contour lines are well above the validation limit for the theoretical Donelan spectrum. Better accordance between the measured and the theoretical wave spectrum is found using the Donelan spectrum, while some deviations are seen for the high-frequency range when using the JONSWAP spectrum. Figure 5.40 and 5.41 show the measured energy density of sea state 1 based on the JONSWAP and Donelan spectrum, respectively. The two theoretical spectrums are also given in the figures. It is easily seen that the measured wave spectrum deviates much from the JONSWAP spectrum for frequencies around 1 [rad] in figure 5.40, whereas the measured wave spectrum follows the Donelan spectrum better in figure 5.41. This may indicate that the waves with frequencies around the decay of the spectrum is harder to obtain than suggested by the JONSWAP spectrum, such that the Donelan spectrum is a better description.

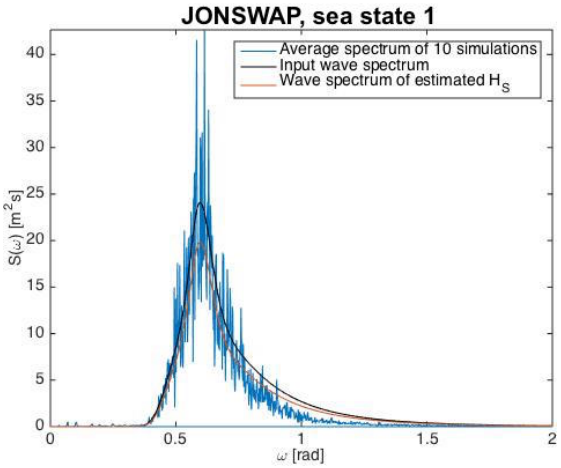

Figure 5.40: Measured wave spectrum for sea state 1 using the JONSWAP spectrum.

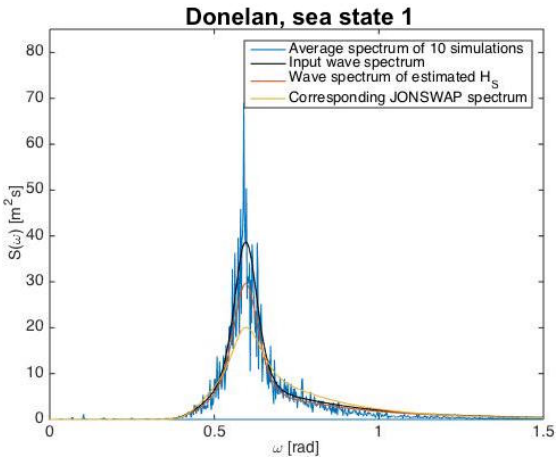

Figure 5.41: Measured wave spectrum for sea state 1 using the Donelan spectrum.

Sea state 1 and 7 are located farthest down on the ULS and ALS contour lines and are among the steepest sea states in the experiment. The differences between the theoretical JONSWAP and Donelan wave spectrums these sea states are based upon are small, where the spectral peak is found approximately equal for both spectrums. The decay is somewhat steeper and the tail is slightly richer for the Donelan spectrum than for the JONSWAP spectrum. This implies that waves of larger frequencies are more probable using the Donelan spectrum, which may lead to lower periods and smaller wave lengths. As the extreme crest heights in sea state 1 and 7 are found to be higher when using the Donelan spectrum than the JONSWAP spectrum, the extreme wave steepnesses within the sea states are expected to be larger for the Donelan spectrum. The extreme crest heights in sea state 1 are seen to stagnate around 11.5 [m], which may be explained by breaking or other non linear limiting effects. This effect is not seen for sea state 7, and the extreme crest heights are much higher than both the 1-hour distribution and the extremes obtained from JONSWAP. Still, it is important to point out that the contrasts between the theoretical spectrums are rather small, such that the differences in wave properties between the two wave spectrums may also be small.

Sea state 6 and 15 are located on top of the ULS and ALS contour lines and are among the least steep sea states in the experiment. The theoretical Donelan spectrum these sea states are based upon are found to have a much smaller peak and a much richer tail for increasing frequencies than the corresponding JONSWAP spectrum. Several waves of frequencies around the spectral peak are hence expected when using the JONSWAP spectrum, and waves of larger frequencies are more probable to occur when using the Donelan spectrum. The waves based on the Donelan spectrum are hence expected to have smaller periods and smaller wave lengths than the waves based upon the JONSWAP spectrum also for these two

sea states. Note that the contrasts between the two theoretical wave spectrums are much larger for these sea states than for sea state 1 and 7, and the wave properties are hence expected to be much more affected by the input wave spectrum. As the extreme wave crests for sea state 6 and 15 tend to be slightly larger when using the JONSWAP spectrum, the extreme crests based on the Donelan spectrum may be affected by a non linear limiting effect.

Chapter 6

Generation of a Plunging Breaker

6.1 Introduction

Breaking is found to be probable in the critical sea states subjected for model testing in chapter 5. The impulsive forces exerted by breaking waves on the pile should hence be examined in order to investigate the different possible wave-induced loads in the most severe sea states. Instead of waiting for breaking to occur at the location of the pile during the sea states, a time series can be generated to ensure breaking at the pile's location. This method of breaking wave generation, called wave focusing, will be the main focus of this chapter and explained in detail. Plunging breakers with crest heights corresponding to the two largest measured crest heights in sea state 13 are attempted in this generation. The results include basic measurements and observations from the model testing which will be used to predict impulsive forces in chapter 7.

6.1.1 Non linear waves

Water waves can be described to first order by linear theory. This is a good approximation for describing the wave profile as long as the wave steepness is low and the shallow water effect approaches zero. The wave steepness ε is given in equation 6.1 in terms of wave height H and wave length λ, and the shallow water criterion is given in equation 6.2 in terms of water depth h and wave length λ. Linear theory leads to vertical symmetry of the wave crests. Additionally, the theory assumes an incompressible, inviscid and irrotational fluid.

$$\varepsilon = \frac{H}{\lambda} \tag{6.1}$$

$$\frac{h}{\lambda} \leqslant \frac{1}{2} \tag{6.2}$$

Higher order effects become important when the wave steepness increases. Stokes perturbation method can be used to describe weakly non linear waves by introducing higher order correction terms to the linear theory. This perturbation is shown in equation 6.3, where ζ_1

is the linear surface elevation, while expressions for the surface elevation terms up to fifth order can be found in appendix F.

$$\zeta = \zeta_1 + \varepsilon\zeta_2 + \varepsilon^2\zeta_3 + ... \tag{6.3}$$

Non linear waves are recognized by sharper and higher wave crests than linear waves, whereas the troughs become flatter. Typical measurements of linear and non linear waves are shown in figure 6.1 and 6.2, where the values of the surface elevations are normalized for comparable reasons. It can be seen that the linear waves are ranging from - 1 to + 1, while the non linear waves are ranging from - 0.6 to 1.

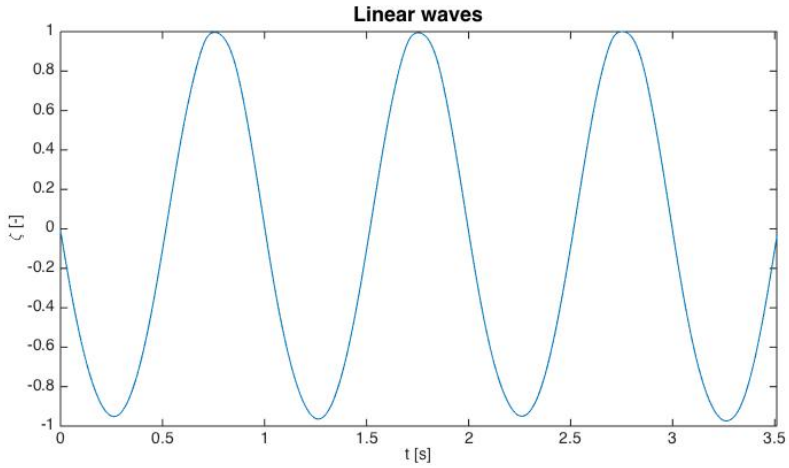

Figure 6.1: Time series for typical linear waves.

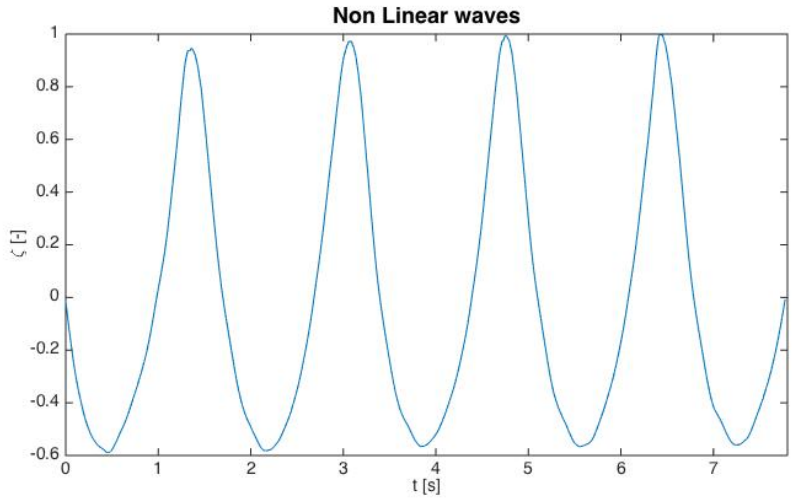

Figure 6.2: Time series for typical non linear waves.

6.1.2 Plunging breakers

Waves of relative steep nature may become unstable and start to break due to their large non linear properties. The breaking criterion given in equation 6.4 shows the steepness at which a wave will start to break [9]. The limiting value for the breaking criterion as the water depth increases is given in equation 6.5.

$$\varepsilon_{cr} = \frac{H}{\lambda} = 0.142 \tanh\left(\frac{2\pi h}{\lambda}\right) \tag{6.4}$$

$$\varepsilon_{cr} = \frac{H}{\lambda} = \frac{1}{7} \tag{6.5}$$

Breaking waves can be classified into four different breaker types: spilling, plunging, collapsing and surging. The plunging breakers will in the following be further investigated due to their severe impact with offshore structures.

Figure 6.3: Sketch of the development of a plunging breaker.

A plunging breaker is characterized by its vertical asymmetry leading to an overturning fluid mass at the wave crest. The formation of a plunging breaker is shown in figure 6.3 where it starts out as a highly non linear wave and then plunges down on the forward face of the wave as a jet. Linear wave theory, and hence also Stokes perturbation method, can therefore only be used to describe an early development of such a wave. As the asymmetry of the wave becomes more significant even more complex descriptions or model testing is necessary. The jet may impact as a tremendous impulse force on the pile, in contrast to forces exerted by continuous wave profiles. Such an impact is illustrated in figure 6.4.

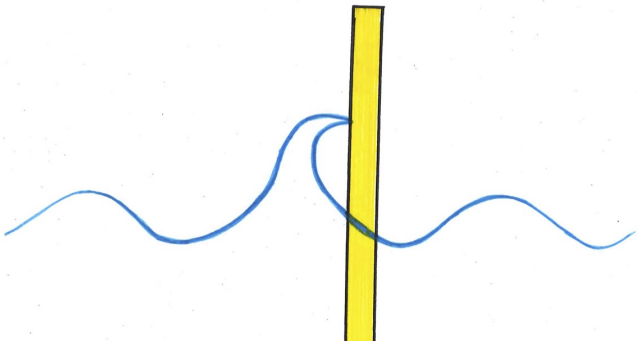

Figure 6.4: Sketch of a plunging breaker hitting a pile.

6.1.3 Impact duration

The impact duration t_1 of the impulsive force from a plunging breaker on a pile with diameter D can be calculated as shown in equation 6.6 when the group velocity is known [9].

$$t_1 = \frac{13D}{64C_g} \tag{6.6}$$

6.1.4 Wave groups

Several waves moving at nearly the same speed such that they keep pace with one another form a wave group. A wave group, or a wave packet, is characterized by lower waves in the front and aft, while the middle waves are generally higher as shown in figure 6.5.

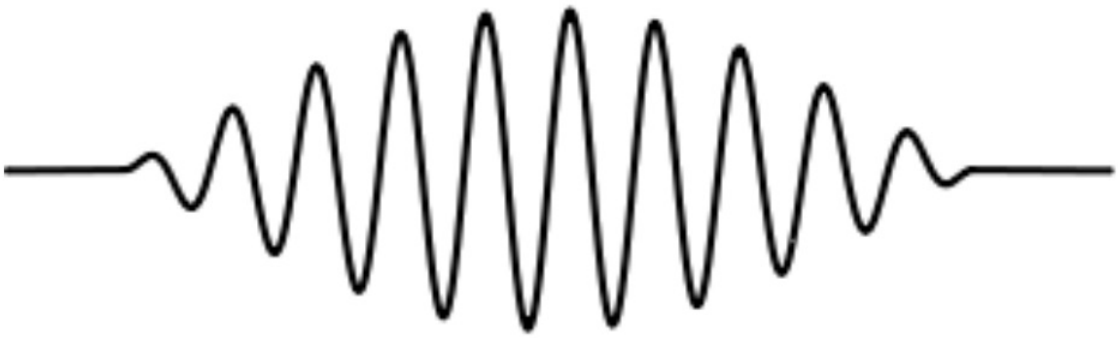

Figure 6.5: Illustration of wave group.

The individual waves enter the wave group in the aft, increasing as they move to the middle, and decreasing again as they reach the front. Then the waves seem to be pulled back and re-enter at the aft of the wave group again. They move with the phase speed C_p shown in equation 6.7.

$$C_p = \frac{\lambda}{T} = \frac{\omega}{k} \tag{6.7}$$

The velocity of the wave group can be described by the energy propagation velocity as shown in equation 6.8 by means of the dispersion relation [54]. It describes the propagation velocity of the front of a harmonically oscillating wavetrain, and can be used to measure the time it takes for a wavetrain to reach a specific location.

$$C_g = \frac{\partial\omega}{\partial k} \tag{6.8}$$

6.2 Wave focusing

Wave focusing can be used to ensure a highly non linear wave at a predefined location. The relation between wave height and wave length given in equation 6.4 determines whether the wave will break or not. The predefined location can be taken as the distance from the wave maker to the pile, and is from now on denoted focus point, x_f. A wavetrain consisting of succeeding waves with decreasing frequency is generated such that several wave components have maximum value simultaneously in space and time. They must hence be in-phase at the focus point.

A wave component i of the wavetrain with angular frequency ω_i uses a certain time to travel the distance x_f. This time is termed focus time and denoted t_{fi}. The next wave component $i+1$ must hence use $t_{fi} - T_i$ [s] to travel the same distance x_f, where T_i is the period of the previous wave. All components in the wavetrain are generated in an equivalent manner, and the method will be explained in detail in the following.

The surface elevation of a single regular wave component i can, according to linear theory, be written as shown in equation 6.9. The wave singlets are defined in time t and space x by the angular wave frequency ω_i with corresponding wave number k_i, as well as the linear wave amplitude ζ_{ai}.

$$\zeta_i(x,t) = \zeta_{ai}\cos(\omega_i t - k_i x - \varphi_i) \tag{6.9}$$

Wave number k_i

The linear dispersion relation is given in equation 6.10. The wave number k_i can be found by iteration using this equation when ω_i is known.

$$\omega_i^2 = k_i g \tanh(k_i h) \tag{6.10}$$

Group velocity C_{gi}

When the dispersion relation is known the group velocity can be calculated according to equation 6.8, such that the expression shown in equation 6.11 is obtained.

$$C_{g0i} = \frac{g\tanh(k_i h) + ghk_i \mathrm{sech}^2(k_i h)}{2\sqrt{gk_i \tanh(k_i h)}} \tag{6.11}$$

As the wave steepness increases, the group velocity may be corrected for second order effects [55]. The group velocity then increases somewhat as shown in equation 6.12.

$$C_{gi} = C_{g0i}\left(1 + \frac{1}{2}(k_i\zeta_{ai})^2\right) \tag{6.12}$$

Focusing time t_{fi}

For one wave singlet the focusing time can be calculated as shown in equation 6.13 when the group velocity is known.

$$t_{fi} = \frac{x_f}{C_{gi}} \tag{6.13}$$

Wave amplitude ζ_{ai}

The wave amplitude for an individual wave component can be determined by a predefined fraction of the critical wave height with respect to breaking [56]. This critical wave height is previously given in equation 6.4. By utilizing $H = 2\zeta_a$ and $\lambda = \frac{2\pi}{k}$ the formula in equation 6.14 is obtained. Here β_b is the predefined fraction of the critical wave height seen as a reduction factor between 0 and 1, and γ_b is introduced as the wave breaking index [57]. This index is found to be 0.833 in shallow water.

$$\zeta_{ai} = \beta_b \frac{0.88}{2k_i} \tanh\left(\frac{\gamma_b h k_i}{0.88}\right) \tag{6.14}$$

Phase shift φ_i

By introducing a phase shift φ_i the wavetrain can easily be controlled such that the surface elevation has a maximum value at the focus point x_f at time t_f. This is done by requiring that the cosine argument of the last wave component is $0 + 2\pi n$ for $n = 0, 1, 2, 3...$ as shown in equation 6.15.

$$\omega_i t_{fi} - k_i x_f - \varphi_i = 0 + 2\pi n \qquad n = 0, 1, 2, 3.... \tag{6.15}$$

It then follows that the phase shift for the last wave singlet must be calculated as shown in equation 6.16 to ensure that all the wave components in the wavetrain coinside and have a maximum value at the focus point x_f.

$$\varphi_i = \omega_i t_{fi} - k_i x_f - 2\pi n \qquad n = 0, 1, 2, 3.... \tag{6.16}$$

Signal sent to wave maker

A plunging breaker is physically generated by sending a signal of the calculated time series to the wave maker. This signal is generated based on equation 6.9 where the x-coordinate is kept fixed. By demanding the origin of the two dimensional function to be at the location of the wave maker, the referance frame shown in figure 6.6 is obtained. The time series for the surface elevation at the location of the wave maker can then be written as shown in equation 6.17, where the x-coordinate is set to zero.

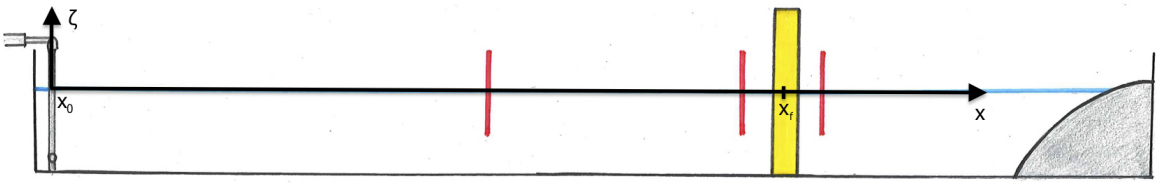

Figure 6.6: Reference frame used in the flume.

$$\zeta_i(t) = \zeta_{ai} \cos(\omega_i t - \varphi_i) \tag{6.17}$$

Waves with large wave lengths travel faster than waves of smaller wave lengths. It then follows that waves with low frequencies travel faster than waves with frequencies of larger magnitude. The ω values of the wavetrain should therefore be defined as a range of linearly decreasing frequencies. Corresponding wave numbers, k, group velocities, C_g, focusing times, t_f, and wave amplitudes ζ_a can be calculated by means of equation 6.10, 6.12, 6.13 and 6.14, respectively. The necessary parameters in the time history in equation 6.17 can then be interpolated for every time instant, such that a plunging breaker occurs at x_f.

The wave length of the breaking wave λ_B can be expressed as shown in equation 6.18, where k_n is the wave number of the last wave in the wavetrain.

$$\lambda_B = \frac{2\pi}{k_n} \tag{6.18}$$

In order to obtain the motion of the flap η_{wm} the time history for the surface elevation in equation 6.17 must be combined with the Biésel transfer function given in equation 4.2 in chapter 4. As the transfer function depends on k it should be combined as shown in equation 6.19 below.

$$\eta_{wm}(t) = \frac{\zeta_{ai} \cos(\omega_i t - \varphi_i)}{\frac{H}{S}(k_i)} \tag{6.19}$$

6.3 Description of the experiment

The distance from the wave maker to the location of the pile in the flume is measured to be 17.69 [m]. It will hence be of interest to carry out most of the calculations regarding wave properties in model scale. Still, the results will be given in full scale for comparable purposes and further use of the measurements in chapter 7. By testing several different frequency intervals, two perfectly focused plunging breakers are chosen for further investigation. These frequency intervals are given in table 6.1 below.

Table 6.1: Frequency intervals giving perfectly focused plunging breakers.

Wavetrain	Model scale ω [rad/s]	Full scale ω [rad/s]
1	3.9 - 5.5	0.39 - 0.55
2	3.9 - 10	0.39 - 0.10

The time history of the surface elevation in model scale at the position of the wave maker for the two wavetrains can be found in picture 6.7 and 6.8.

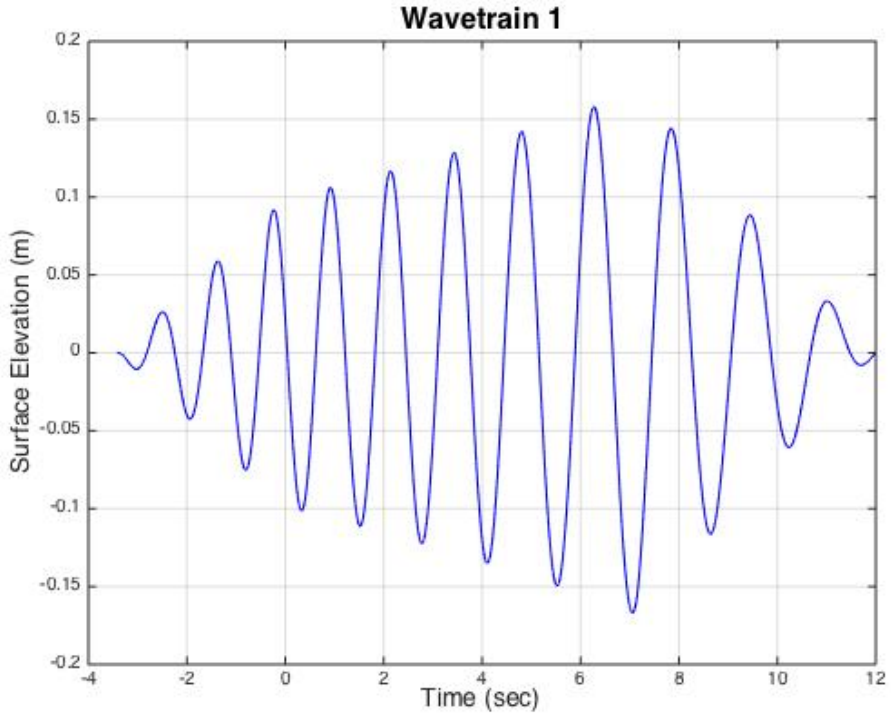

Figure 6.7: Surface elevation in model scale for wavetrain 1 at the position of the wave maker.

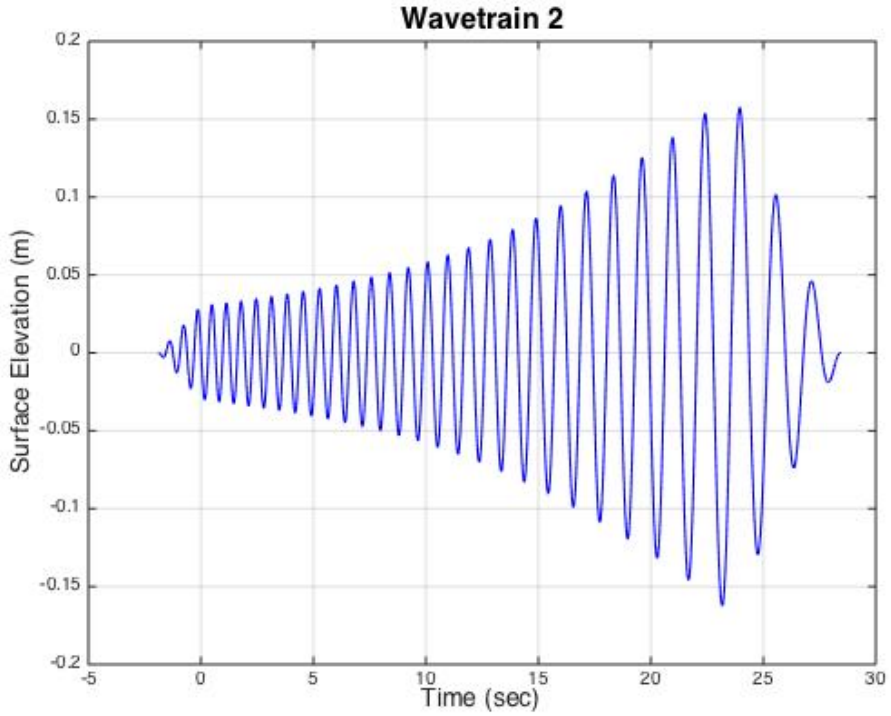

Figure 6.8: Surface elevation in model scale for wavetrain 2 at the position of the wave maker.

The theoretical wave length, λ_B, and focusing time, t_f, of the breaking wave are given for both wavetrains in model scale and full scale in table 6.2, calculated according to equation 6.18 and 6.13. Note that the theoretical wave lengths of the breaking waves are equal for both wavetrains, but that wavetrain 2 uses longer time than wavetrain 1 before breaking occurs. This is because the lower limit of the frequency interval is equal for the two wavetrains, whereas the upper limit is lower for wavetrain 1 than for wavetrain 2. Hence, wavetrain 2 includes waves of higher frequencies than wavetrain 1, which uses longer time to travel the distance x_f.

Table 6.2: Theoretical wave length and focusing time of the plunging breakers.

	Model scale		**Full scale**	
Wavetrain	λ_B [m]	t_f [s]	λ_B [m]	t_f [s]
1	3.75	20.11	375	201.1
2	3.75	37.45	375	374.5

Actual breaking wave heights, crest heights and periods are found by measurements from the waveprobes, and the location of the impact with the pile is estimated from video recordings. The three waveprobes of interest are the ones surrounding the pile, which are waveprobe 2, 3 and 4 as shown in figure 6.9. All tests are conducted both with and without the pile installed in the flume, such that correct recordings of the breaking waves at the location of the pile are obtained. The measured values for the wavetrains are taken as the average value of six tests when the pile is present, whereas only one test is conducted when the pile is absent.

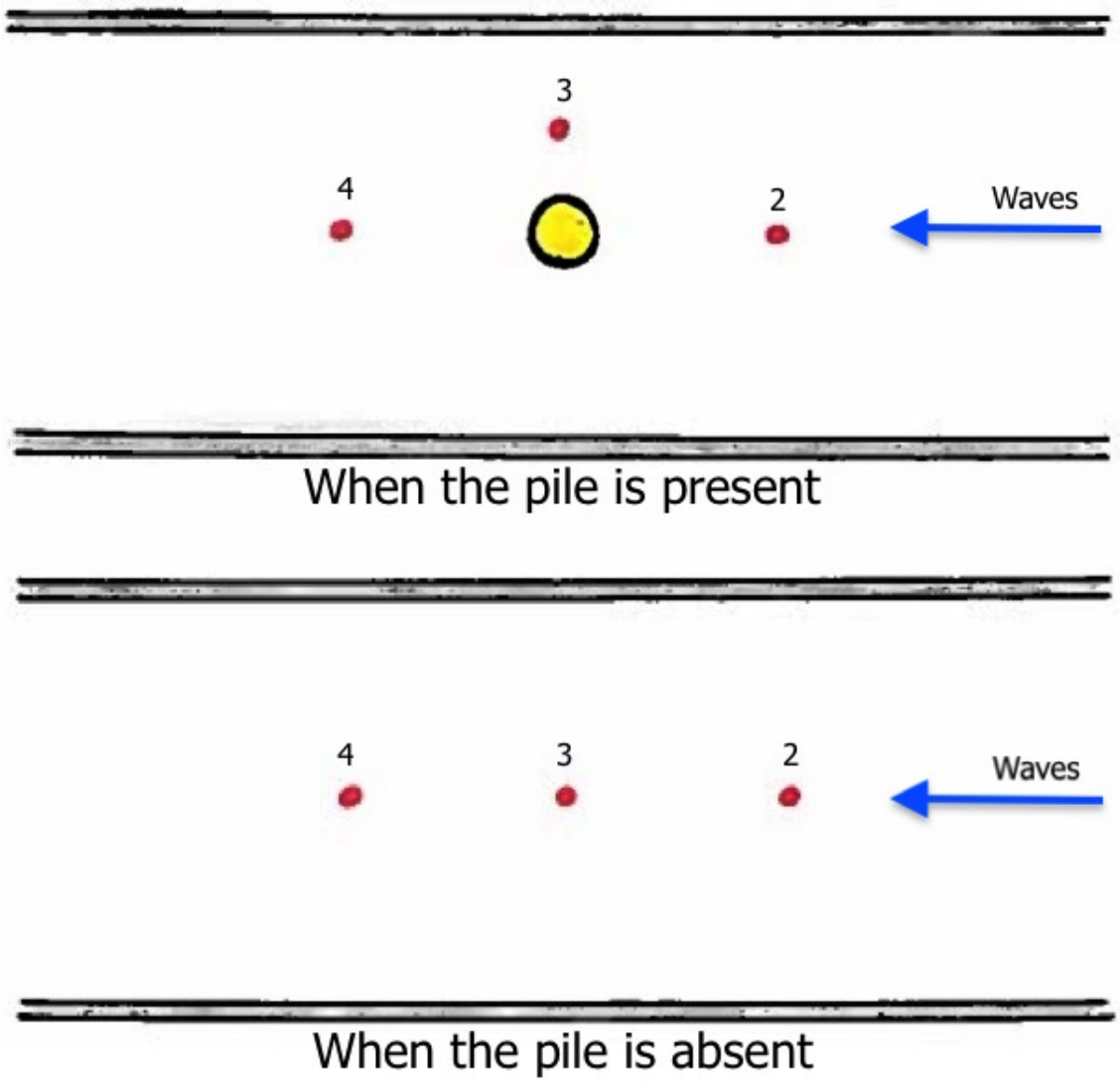

Figure 6.9: Illustration of the flume seen from above both when the pile is present and when it is absent.

6.4 Results and Observations

6.4.1 Measurements from the waveprobes

The measured wave heights, H, crest heights, C, and periods, T, of the breaking waves from the three different waveprobes are given in full scale in table 6.3, 6.4 and 6.5. Detailed measurements can be found in appendix G.

The time histories recorded by waveprobe 2, 3 and 4 when the pile is absent are shown in figure 6.10 and 6.11 for wavetrain 1 and wavetrain 2, respectively.

Table 6.3: Measured values from waveprobe 2.

Wavetrain	Pile	H [m]	C [m]	T [s]
1	No	33.00	20.10	14.4
	Yes	35.11	21.60	14.9
2	No	37.07	22.66	14.2
	Yes	33.68	20.19	14.8

Table 6.4: Measured values from waveprobe 3.

Wavetrain	Pile	H [m]	C [m]	T [s]
1	No	29.09	15.61	14.3
	Yes	35.22	20.87	14.8
2	No	34.99	20.27	13.7
	Yes	34.50	20.61	14.8

Table 6.5: Measured values from waveprobe 4.

Wavetrain	Pile	H [m]	C [m]	T [s]
1	No	28.75	14.06	13.2
	Yes	28.08	14.96	14.1
2	No	29.43	15.15	15.2
	Yes	28.88	15.16	15.1

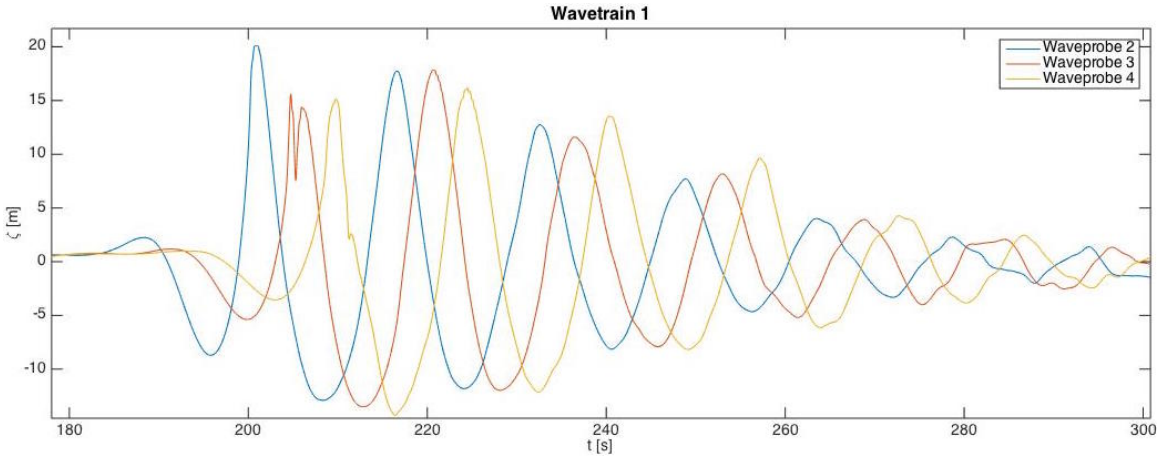

Figure 6.10: The time history for wavetrain 1 recorded by waveprobe 2, 3 and 4.

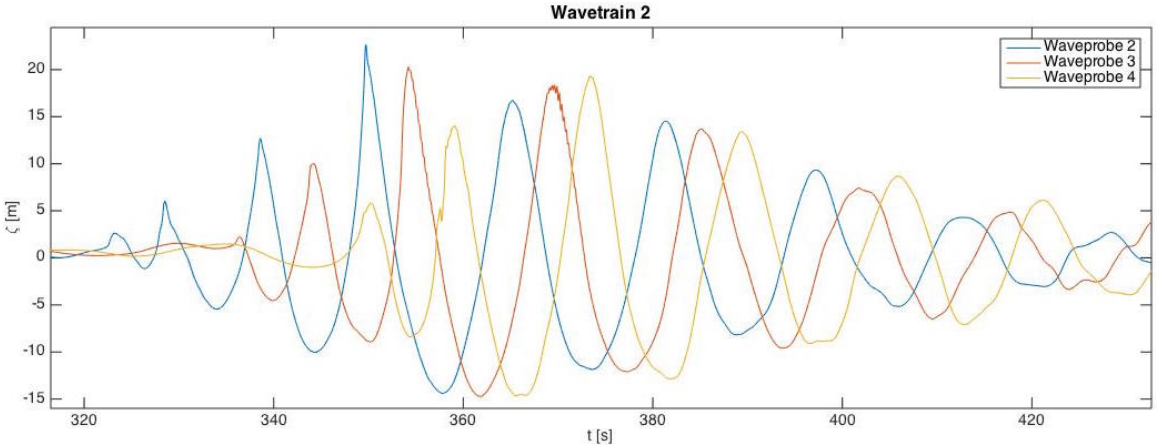

Figure 6.11: The time history for wavetrain 2 recorded by waveprobe 2, 3 and 4.

6.4.2 Measurements from video recordings

The distances from the flume bottom to the location of impact between the breaking waves and the pile, termed z_b, are measured from video recordings and given in table 6.6 below.

Table 6.6: Location of impact between the wave and the pile.

Wavetrain	Model scale z_b [m]	Full scale z_b [m]
1	1.166	116.60
2	1.181	118.10

Figure 6.12 and 6.13 show photos of a plunging breaker hitting the pile. It can be seen from the first photo how the plunge develops as a jet in front of the pile while the second photo shows the impact.

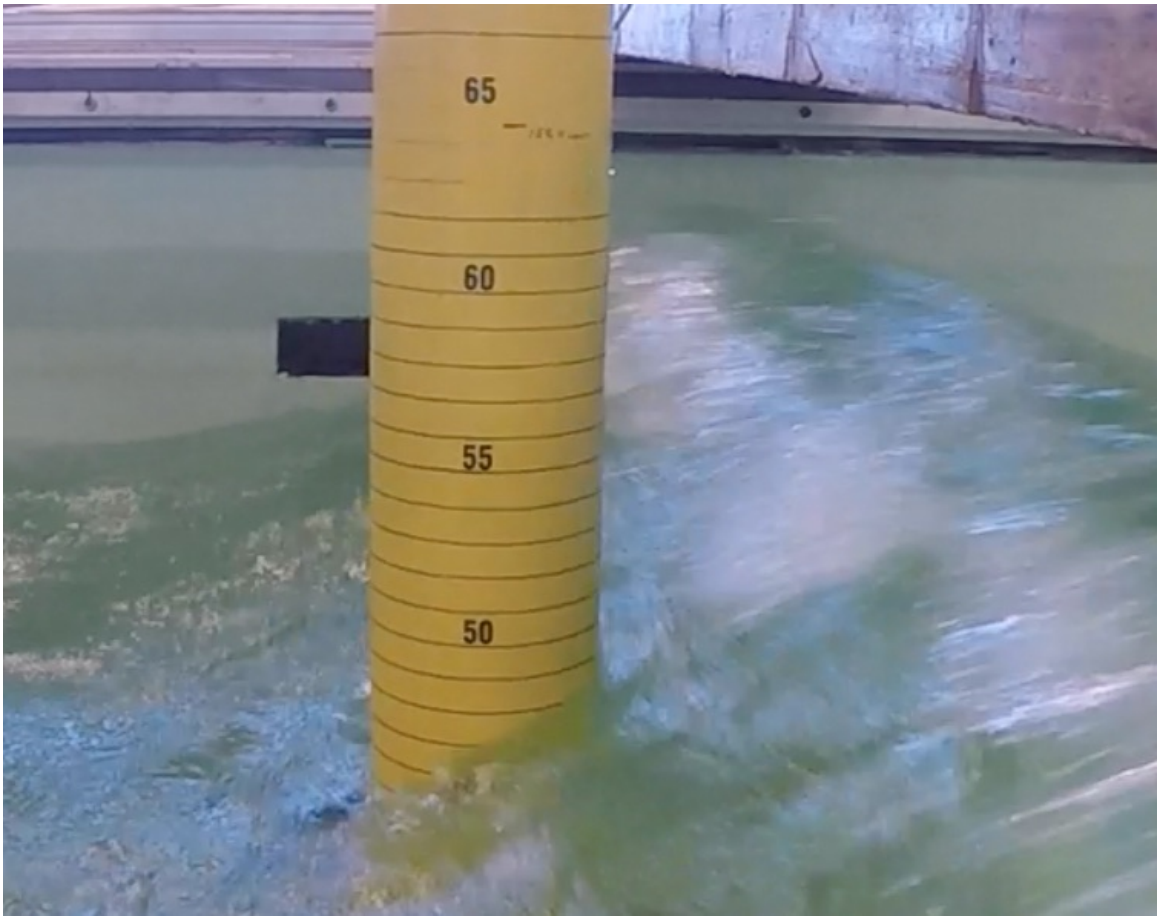

Figure 6.12: Plunging breaker hitting the pile.

Figure 6.13: Plunging breaker hitting the pile.

6.4.3 Calculations

Full scale wave lengths λ and steepnesses ε as well as the breaking wave criterion ε_{cr} according to equation 6.4 are given for the two plunging breakers in table 6.7, 6.8 and 6.9. It is worth noting that the steepnesses of the breaking waves are generally smaller than the breaking wave criterion.

Table 6.7: Calculated values for waveprobe 2.

Wavetrain	Pile	λ [m]	ε [-]	ε_{cr} [-]
1	No	311.13	0.1061	0.1365
	Yes	329.83	0.1064	0.1351
2	No	303.65	0.1221	0.1370
	Yes	326.09	0.1033	0.1354

Table 6.8: Calculated values for waveprobe 3.

Wavetrain	Pile	λ [m]	ε [-]	ε_{cr} [-]
1	No	307.39	0.0947	0.1369
	Yes	326.09	0.1080	0.1354
2	No	285.01	0.1228	0.1381
	Yes	326.09	0.1058	0.1354

Table 6.9: Calculated values for waveprobe 4.

Wavetrain	Pile	λ [m]	ε [-]	ε_{cr} [-]
1	No	266.49	0.1079	0.1391
	Yes	299.92	0.0936	0.1372
2	No	341.05	0.0863	0.1343
	Yes	337.31	0.0856	0.1345

Calculated group velocities, C_g, and impact force durations, t_1, for the two wavetrains are given in full scale in table 6.10. It is seen that wavetrain 2 travels faster than wavetrain 1, which leads to a somewhat shorter impact force duration for the breaking wave in wavetrain 2.

Table 6.10: Calculated group velocity and impact force duration.

Wavetrain	$C_g[\frac{m}{s}]$	t_1 [s]
1	22.2	0.15
2	25.0	0.13

6.5 Discussion and Recommendations

The breaking waves are found in front of the perfectly focused wavetrains at the location of the pile. Figure 6.14 and 6.15 show the first wave of the two wavetrains measured by waveprobe 2, 3 and 4. The first wave of wavetrain 1 is continous at waveprobe 2, whereas a noch is seen at the wave crest for waveprobe 3, which is located at the pile's position. A significant decrease in wave height from waveprobe 2 to waveprobe 3 is also seen. It is likely to believe that the discontinous wave profile represents the formation of a plunging breaker, leading to an overturning fluid mass causing the large decrease in wave height. Regarding wavetrain 2, the first wave is steep with an extremely sharp crest as it reaches waveprobe 2. The crest has decreased in magnitude and is more blunt when it reaches waveprobe 3, which indicates that breaking has occured between these two measurements. The crest height has decreased even more when it comes to the last waveprobe. Another feature worth noting is the serrated wave crest of the following wave in wavetrain 2. This indicates a typical spilling breaker, and is shown in detail in figure 6.16.

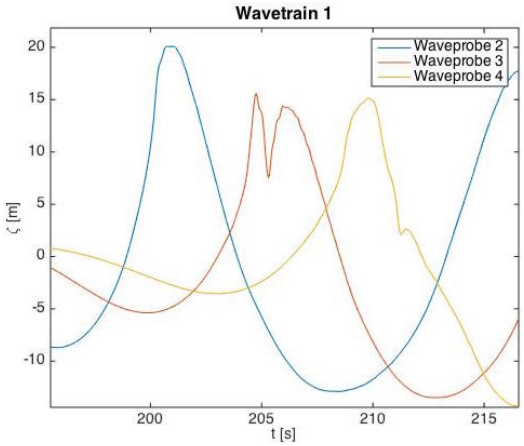

Figure 6.14: Measurements from waveprobe 2, 3 and 4 of the first wave in wavetrain 1.

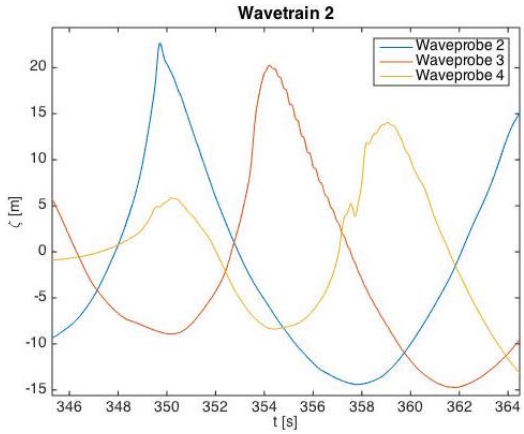

Figure 6.15: Measurements from waveprobe 2, 3 and 4 of the first wave in wavetrain 2.

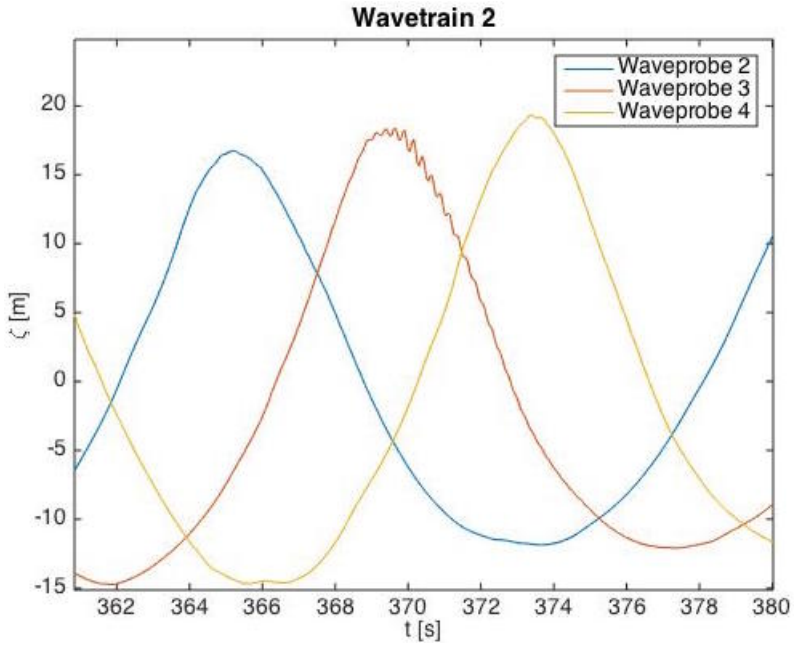

Figure 6.16: Measurements from waveprobe 2, 3 and 4 for the second wave in wavetrain 2.

The steepness of the waves at the location of the waveprobes are generally smaller than the breaking wave criterion. Still, there is no doubt that the waves are breaking. The breaking may occur between the two first waveprobes of interest, such that the wave is growing as it passes the first waveprobe and breaking has already occured when it reaches the second. Some additional waveprobes should therefore have been installed and placed between waveprobe 2 and 3 in order to better control the development of the breaking wave.

The measured wave crests are generally higher for the tests when the pile is present than for the tests when it is absent. It seems like the presence of the pile is disturbing the transient waves somewhat such that they are forced towards a higher crest.

Some differences in the measured wave heights and crest heights from test to test can be found from the tables in appendix G, especially for wavetrain 1. The crest heights in wavetrain 1 are ranging from 19.26 [m] to 22.82 [m] at the location of the pile. A breaking wave is highly unstable, and it can be seen from figure 6.14 that the wave is breaking at the exact location of waveprobe 3. Due to for example different initial flowfields in the flume from test to test, the wave may break just prior to or after this waveprobe, leading to large variations of the measurements. On the other hand, wavetrain 2 seems to be more stable as the measured crest heights range from 19.91 [m] to 21.51 [m]. This wavetrain includes higher frequencies and hence more wave components than wavetrain 1. It can therefore be concluded that a wide frequency interval results in a more stable plunging breaker from test

to test.

As the two largest crest heights in sea state 13 are found to be 21.25 [m] and 19.70 [m] in chapter 5, the two perfectly focused plunging breakers have crest heigths of approximately equal magnitude. Base shear responses, overturning moments and impulsive impact forces exerted by extreme plunging breakers in sea state 13 will hence be investigated in chapter 7.

Chapter 7

Wave-induced loads on the pile

7.1 Introduction

The objective of this chapter is to analyze the measured base shear responses and overturning moments of the pile from the model tests performed in chapter 5 and 6. Predictions of the corresponding wave-induced loads by means of theoretical approaches will be presented in the results.

Loads exerted by the ULS and ALS annual q-probability waves are predicted by Morison's equation, while the impulsive forces exerted by the plunging breakers are predicted by means of a simplified oscillation model of the pile [7]. A probabilistic description of the extreme responses is used to predict the characteristic responses of the most unfavorable ULS and ALS sea states.

The ULS and ALS annual q-probability waves are not subjected for model testing due to a calculation error early in this project. Instead a set of wrongly calculated waves are tested and compared to the theoretical approach in order to verify the predicted q-probability loads. It is also important to bear in mind that the waves within the critical sea states are somewhat lower than expected due to losses related to the model tests. Hence, the measured responses are assumed to underpredict the characteristic responses.

7.1.1 Stokes 5^{th} order theory

A Stokes 5^{th} order wave describes a single wave influenced by fifth order effects. The waves in the Ekofisk area were shown in chapter 5 to be highly non linear and such a description will hence be suitable. A 5^{th} order Stokes wave is described by means of wave height, H, wave length, λ, and mean water depth, h, as shown in figure 7.1 [58].

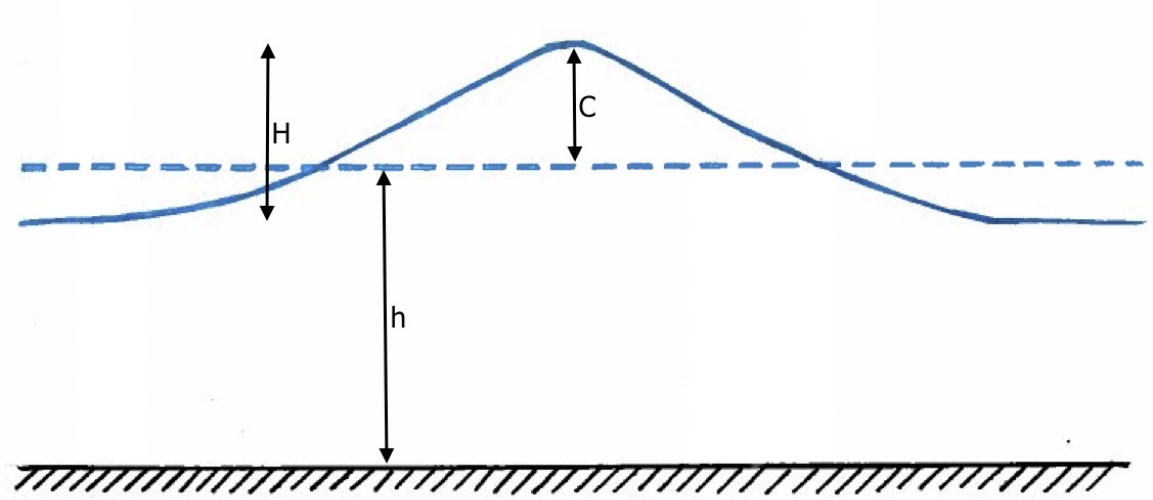

Figure 7.1: Stokes 5^{th} order wave.

Acceptable engineering accuracy of the Stokes 5^{th} order theory is found for $U_r < 40$, where U_r is given in equation 3.19 in chapter 3 [9] [58]. Additionally, it is found to be quite accurate as long as the waves are shorter than ten times the water depth.

The representation of Stokes 5^{th} order waves by means of Fourier series with coefficients written as perturbation expansions of the wave steepness ε are given in appendix F.

7.2 Methodology

7.2.1 Stokes 5^{th} order wave profile in Morison's equation

This section will explain the procedure of predicting the wave-induced loads on the pile by means of a Stokes 5^{th} order wave profile in Morison's equation.

Stokes 5^{th} order program

A freely downloaded computer program developed by John D. Fenton is utilized in order to describe the desired wave profiles of wave height H and period T by use of the Stokes 5^{th} order theory [58] [59]. Horizontal particle velocities u and accelerations $\dot{u}$ are then calculated at a predefined number of integration points both along water depth and wave profile.

It should be noted that all specified data in this program are non dimensional with respect to mean water depth and gravitational acceleration.

Morison's equation

Estimates of the maximum resulting base shear force and overturning moment of the pile along a given wave profile may be determined by Morison's equation. The formula is given in equation 7.1 and describes the wave-induced in-line forces of unit length f on a pile of circular cross section [60]. It consists of one inertia contribution f_M and one drag contribution f_D, where the dimensionless mass coefficient C_M and drag coefficient C_D are used. These coefficients are empirically determined which will be explained later in this section. Morison's equation is found applicable for non-breaking waves with $\lambda > 5D$, which indicates that the incoming waves only get slightly scattered by the obstruction [9]. It does not account for real sea effects like energy spreading and transverse forces.

$$f = f_M + f_D = C_M \rho \frac{\pi D^2}{4} \dot{u} + C_D \frac{1}{2} \rho D u |u| \tag{7.1}$$

The maximum resulting base shear force and overturning moment can now be found by integration along the water depth, as shown in equation 7.2 and 7.3. The integration limit ζ is the wave profile at the position of the pile.

$$F = \int_{-h}^{\zeta} f_M dz + \int_{-h}^{\zeta} f_D dz = F_M + F_D \tag{7.2}$$

$$M = \int_{-h}^{\zeta} (z+h) f_M dz + \int_{-h}^{\zeta} (z+h) f_D dz = M_M + M_D \tag{7.3}$$

Horizontal particle velocities u and accelerations $\dot{u}$ along the water depth are obtained from the Stokes 5^{th} order program. It should be noted that u and $\dot{u}$ are shifted by $\frac{\pi}{2}$ such that

when one of them reaches maximum value the other one will be zero. Morison's equation can therefore be simplified based on whether it is mass or drag dominated as shown in figure 7.2. The drag term dominates when $\frac{D}{H} < 0.1$ and the mass term dominates when $0.5 < \frac{D}{H} < 1.0$. In the interval $0.1 < \frac{D}{H} < 0.5$ none of the forces dominate and the equation can not be simplified [61].

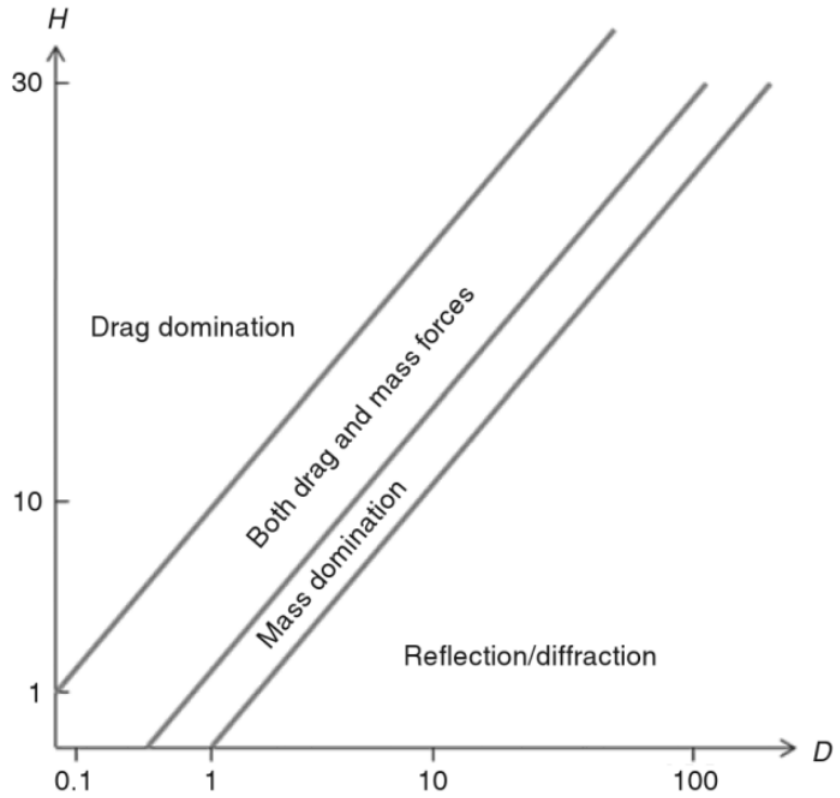

Figure 7.2: Drag and mass domination in terms of wave height H and diameter D [61].

For an mass dominated case the f_D term can be neglected as it is of much smaller magnitude than the f_M term. Assuming u to approach zero the simplified formulas for base shear force and overturning moment shown in equation 7.4 and 7.5 are obtained. The maximum value of $\dot{u}$ is found at the mean water surface level, and integration up to z = 0 is hence convenient.

$$F = \int_{-h}^{0} f_M dz \tag{7.4}$$

$$M = \int_{-h}^{0} (z+h) f_M dz \tag{7.5}$$

For a drag dominated case the f_M term can be neglected such that the simplified formulas for base shear force and overturning moment given in equation 7.6 and 7.7 are obtained. The horizontal particle velocity u reaches its maximum value at the wave crest such that integration up to ζ must be performed.

$$F = \int_{-h}^{\zeta} f_D dz \tag{7.6}$$

$$M = \int_{-h}^{\zeta} (z+h) f_D dz \tag{7.7}$$

Coefficients in Morison's equation

In order to determine proper mass and drag coefficients the Keulegan-Carpenter number K_C must be introduced. It gives the importance of drag forces relative to inertia forces and can be calculated according to equation 7.8, where U_0 is the largest water particle velocity under the wave crest [9].

$$K_C = \frac{TU_0}{D} \tag{7.8}$$

The dimensionless roughness parameter Δ_R relates the surface roughness k_r of the pile to its diameter D as shown in equation 7.9. A structural member is considered smooth if $\Delta_R < 10^{-4}$ and rough if $\Delta_R > 10^{-2}$ [9].

$$\Delta_R = \frac{k_r}{D} \tag{7.9}$$

The drag coefficient C_D can be approximated as shown in equation 7.10 for K_C below 60 [9]. The roughness dependency $C_{DS}(\Delta_R)$ and the wake amplification factor $\Psi(K_C)$ can be calculated according to equation 7.11 and 7.12, where C_π is given in equation 7.13. Note that the equation for $\Psi(K_C)$ only is defined for K_C below 12, while it is obtained from figure 7.3 for K_C up to 60 [9]. For even higher K_C numbers the limiting C_D values in table 7.1 are recommended [9].

$$C_D = C_{DS}(\Delta_R)\Psi(K_C) \tag{7.10}$$

$$C_{DS}(\Delta_R) = \begin{cases} 0.65 & for \quad \Delta_R < 10^{-4} \\ \frac{1}{20}(29 + 4\log(\Delta_R)) & for \quad 10^{-4} < \Delta_R < 10^{-2} \\ 1.05 & for \quad \Delta_R > 10^{-2} \end{cases} \tag{7.11}$$

$$\Psi(K_C) = \begin{cases} C_\pi + 0.10(K_C - 12) & for \quad 2 \leqslant K_C < 12 \\ C_\pi - 1.00 & for \quad 0.75 \leqslant K_C < 2 \\ C_\pi - 1.00 - 2.00(K_C - 0.75) & for \quad K_C < 0.75 \end{cases} \tag{7.12}$$

$$C_\pi = 1.50 - 0.024\left(\frac{12}{C_{DS}} - 10\right) \tag{7.13}$$

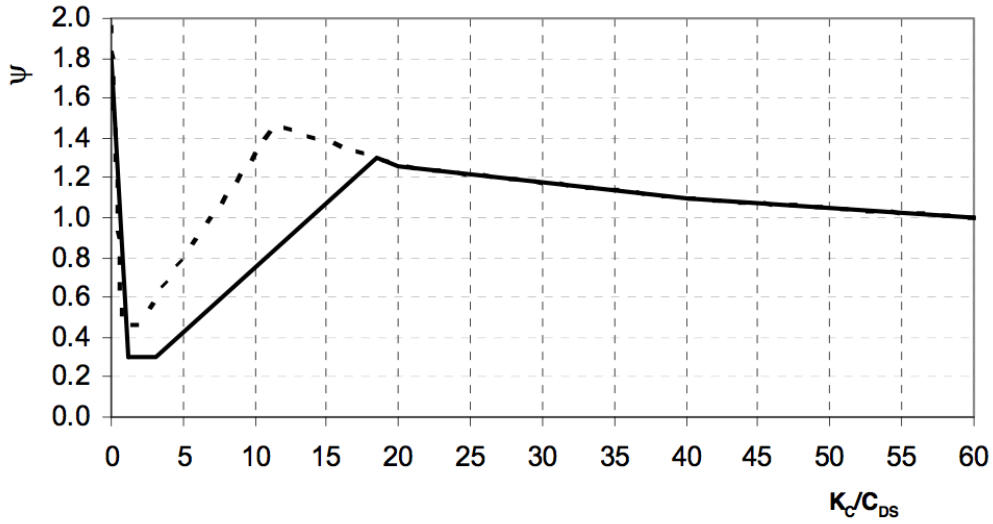

Figure 7.3: Ψ as a function of K_C for smooth and rough cylinders, given by solid and dotted lines, respectively [9].

Table 7.1: Recommended drag coefficients for large K_C numbers [9].

Roughness	C_D
Smooth	0.65
Rough	1.05

The mass coefficient C_M can be calculated by use of equation 7.14, where C_A is the added mass coefficient found from figure 7.4 [9]. For increasing K_C numbers the added mass coefficient stabilizes and the values for C_M become as given in table 7.2.

$$C_M = 1 + C_A \tag{7.14}$$

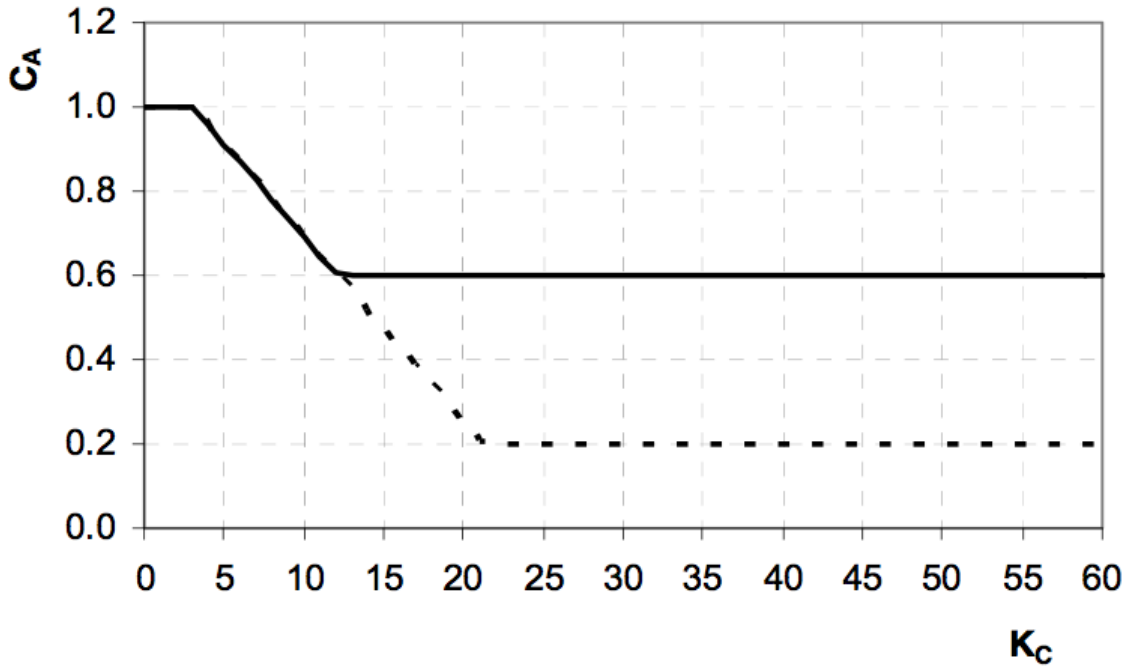

Figure 7.4: C_A as a function of KC for smooth and rough cylinders, given by solid and dotted lines, respectively [9].

Table 7.2: Recommended mass coefficients for large KC numbers [9].

Roughness	C_M
Smooth	1.6
Rough	1.2

Linear interpolation between rough and smooth cylinders are used to find the C_D and C_A values for intermediate roughness. Note that the coefficients are assumed constant, while they in reality may vary.

7.2.2 Method of predicting impulsive forces

This section will present a method for calculating the pile's dynamic response after impact with an impulsive force of magnitude P_0. Recalling from chapter 4 that the pile was assumed infinitely stiff, the simplified oscillation model in figure 7.5 will be used to establish the equation of motion utilizing generalized coordinates.

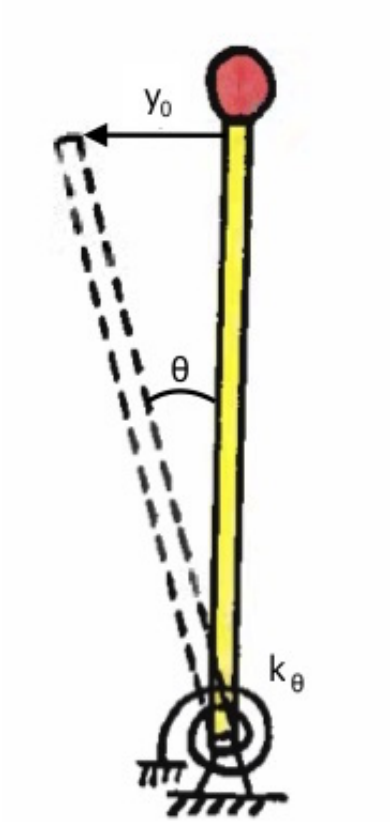

Figure 7.5: Simplified oscillation model.

Equation of motion

The rotational equation of motion for a system with one degree of freedom (DOF) is shown in equation 7.15 in terms of generalized mass, damping, stiffness and external moment.

$$\bar{m}\ddot{\theta} + \bar{c}\dot{\theta} + \bar{k}\theta = \bar{M}(t) \tag{7.15}$$

As the maximum response is expected during the first period of oscillation after an impact, the damping term of the slightly damped system can be neglected [52]. Hence, the equation of motion can be simplified as shown in equation 7.16.

$$\bar{m}\ddot{\theta} + \bar{k}\theta = \bar{M}(t) \tag{7.16}$$

Generalized coordinates

The generalized mass $\bar{m}$ can be calculated from the moment of inertia about the point of rotation. With a mass distribution as shown in figure 7.6 the formula in equation 7.17 is obtained. Note that the second term in the expression for the generalized mass is multiplied by 2 in order to account for added mass.

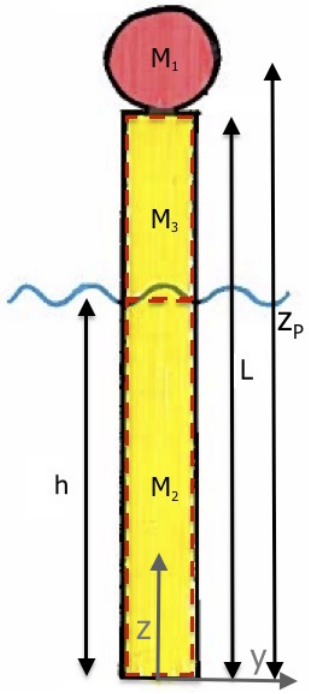

Figure 7.6: Distribution of masses along the pile.

$$\bar{m} = M_1 z_P^2 + 2\int_0^h M_2(z) z^2 dz + \int_h^L M_3(z) z^2 dz \tag{7.17}$$

As the rotational stiffness k_θ is the only stiffness contribution in the system, the generalized stiffness $\bar{k}$ becomes as given in equation 7.18.

$$\bar{k} = k_\theta \tag{7.18}$$

The eigenfrequency and eigenperiod of the pile can now be calculated by means of generalized mass and stiffness as shown in equation 7.19 and 7.20, respectively.

$$\omega_0 = \sqrt{\frac{\bar{k}}{\bar{m}}} \tag{7.19}$$

$$T_0 = \frac{2\pi}{\omega_0} \tag{7.20}$$

The impulsive response for $t \leqslant t_1$

The load impulse I for an impact force of short duration $t_1 < 0.2T_0$ is shown in equation 7.21 [52]. A Dynamic Amplification Factor (DAF) is a dimensionless ratio between dynamic and static response that can be used to describe how the impulsive load history $p(t)$ varies over its short duration t_1. This is shown in equation 7.22 [52]. Figure 7.7 shows different DAFs as a function of duration for four different load forms. The formulas of the four impact load forms are given in table 7.3.

$$I = \int_0^{t_1} p(t)dt \qquad t_1 < 0.2T_0 \tag{7.21}$$

$$DAF = \frac{y_{0,dyn}}{y_{0,stat}} = 2\pi \frac{I}{P_0 T_0} \tag{7.22}$$

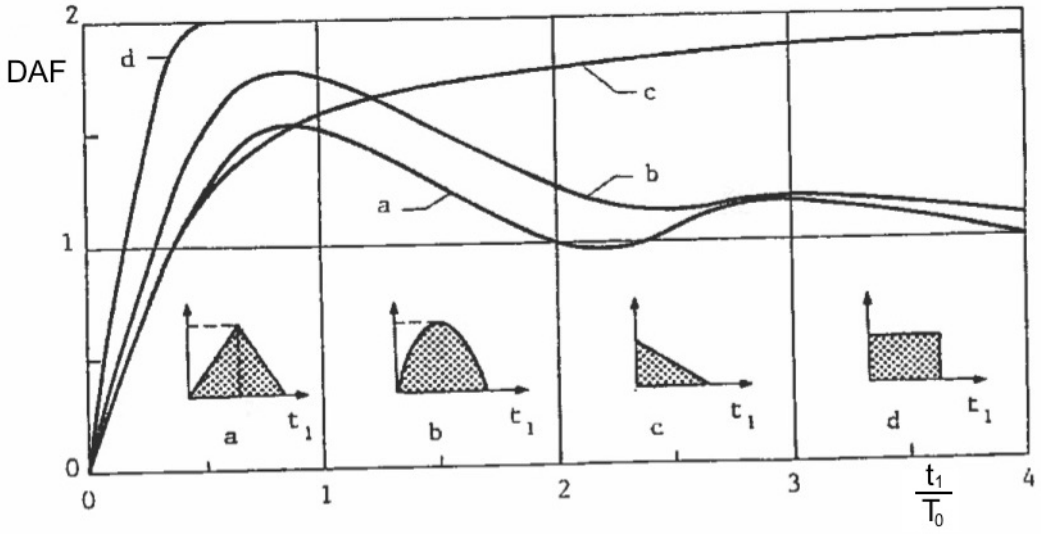

Figure 7.7: DAF as a function of form and duration for four different load impulses [52].

Table 7.3: Formulas for the impact load forms in figure 7.7.

Impact form	$p(t)$	
a	$2P_0\left(\frac{t}{t_1}\right)$	$for \quad 0 \leqslant t \leqslant \frac{t_1}{2}$
	$2P_0\left(1-\frac{t}{t_1}\right)$	$for \quad \frac{t_1}{2} \leqslant t \leqslant t_1$
b	$P_0 \sin(\omega_1 t)$	$for \quad 0 \leqslant t \leqslant t_1$
c	$P_0\left(1-\frac{t}{t_1}\right)$	$for \quad 0 \leqslant t \leqslant t_1$
d	P_0	$for \quad 0 \leqslant t \leqslant t_1$

Generalized moment $\bar{M}$ from a transient impact with the pile at $z = z_b$ is obtained by use of equation 7.23, where $p(t)$ depends on the chosen load form and the shape function $\psi(z)$ depends on the assumed oscillation mode. For the infinitely stiff pile model in figure 7.5 the shape function equals equation 7.24.

$$\bar{M} = \bar{p}(t, z_b)z_b = p(t)\psi(z_b)z_b \tag{7.23}$$

$$\psi(z) = \frac{z}{L} \tag{7.24}$$

The rotational angle θ may now be found by solving equation 7.16. The solution will consist of one homogenous and one particular solution as shown in equation 7.25, where the latter depends on the assumed load form. On the other hand, the homogenous solution will be equal to the expression in equation 7.26 independent of load form. Particular solutions for the three different load forms given as b, c and d in figure 7.7 will be presented in the following. Load form a is excluded as it is considered quite similar to load form b, whereas load form b is assumed to be the most realistic. By assuming the pile to be stationary at the time of impact, the initial conditions $\theta(0) = 0$ and $\dot{\theta}(0) = 0$ are used to obtain the total solutions.

$$\theta(t) = \theta_h(t) + \theta_p(t) \tag{7.25}$$

$$\theta_h(t) = A\sin(\omega_0 t) + B\cos(\omega_0 t) \tag{7.26}$$

Constant load form

Load form d has constant magnitude P_0 throughout the whole impact duration t_1, such that the generalized moment becomes as shown in equation 7.27. The particular solution for this kind of load form is given as a constant C in equation 7.28, which inserted in the equation of motion becomes as shown in equation 7.29. The total solution in equation 7.30 is obtained by using the initial conditions.

$$\bar{M}(z_b, t) = \frac{P_0 z_b^2}{L} \tag{7.27}$$

$$\theta_P(t) = C \tag{7.28}$$

$$C = \frac{P_0 z_b^2}{\bar{k}L} \tag{7.29}$$

$$\theta(t) = \frac{P_0 z_b^2}{L\bar{k}}\left(1 - \cos(\omega_0 t)\right) \qquad t \leqslant t_1 \tag{7.30}$$

Linearly decreasing load form

The linearly decreasing load with initial value P_0 is given as load form c in figure 7.7 and results in the generalized moment given in equation 7.31. For this impulsive load form the particular solution becomes as shown in equation 7.32, which inserted in the equation of motion leads to the the two constants C and D given in equation 7.33 and 7.34, respectively. The total solution obtained by using the intital conditions will in this case be as shown in equation 7.35.

$$\bar{M}(z_b, t) = \frac{P_0 z_b^2}{L}\left(1 - \frac{t}{t_1}\right) \tag{7.31}$$

$$\theta_P(t) = \frac{C}{\bar{k}}t + \frac{D}{\bar{k}} \tag{7.32}$$

$$C = -\frac{P_0 z_b^2}{L t_1} \tag{7.33}$$

$$D = \frac{P_0 z_b^2}{L} \tag{7.34}$$

$$\theta(t) = \frac{P_0 z_b^2}{L\bar{k}}\left(1 - \frac{t}{t_1} + \frac{1}{\omega_0 t_1}\sin(\omega_0 t) - \cos(\omega_0 t)\right) \qquad t \leqslant t_1 \tag{7.35}$$

Sinusoidal load form

The impulsive load form b in figure 7.7 is given as half a sine wave with amplitude P_0 leading to the generalized moment in equation 7.36. In this case the particular solution becomes as shown in equation 7.37, where ω_1 is the frequency of the impulse load calculated according to equation 7.38. By inserting the particular solution in equation 7.16, the constant C is determined to be as shown in equation 7.39 where $\bar{\beta}$ is given in equation 7.40. Using the initial conditions the total expression in equation 7.41 is obtained.

$$\bar{M}(z_b, t) = \frac{P_0 z_b^2}{L}\sin(\omega_1 t) \tag{7.36}$$

$$\theta_p(t) = C\sin(\omega_1 t) \tag{7.37}$$

$$\omega_1 = \frac{\pi}{t_1} \tag{7.38}$$

$$C = \frac{P_0 z_b^2}{L}\frac{1}{\bar{k} - \omega_1^2 \bar{m}} = \frac{P_0 z_b^2}{L\bar{k}}\frac{1}{1 - \bar{\beta}^2} \tag{7.39}$$

$$\bar{\beta} = \frac{\omega_1}{\omega_0} \tag{7.40}$$

$$\theta(t) = \frac{P_0 z_b^2}{\bar{k}L}\frac{1}{1 - \bar{\beta}^2}(\sin(\omega_1 t) - \bar{\beta}\sin(\omega_0 t)) \qquad t \leqslant t_1 \tag{7.41}$$

The response for $t > t_1$

The established impulsive responses are only valid for $t \leqslant t_1$, while for larger t values the pile is assumed to oscillate freely. Hence, the solution $\theta(t)$ for $t > t_1$ only consists of the homogeneous solution given in equation 7.26. In this case the initial conditions become $\theta(t_1) = \theta_0$ and $\dot{\theta}(t_1) = \dot{\theta_0}$. By using these the total expression shown in equation 7.42 is obtained. The corresponding moment response is calculated by equation 7.43.

$$\theta(t) = \frac{\dot{\theta_0}}{\omega_0} \sin(\omega_0 t) + \theta_0 \cos(\omega_0 t) \qquad t > t_1 \tag{7.42}$$

$$M(t) = k_\theta \theta(t) \tag{7.43}$$

7.3 Implementation

7.3.1 Determining pile responses from q-probability waves

Horizontal particle velocities and accelerations for the q-probability waves propagating from north, south, west and total sea established in chapter 3 are found from the Stokes 5^{th} program. Maximum resulting base shear forces and overturning moments of the pile under these wave conditions are further calculated using Morison's equation.

Other waves than the q-probability waves are subjected for model testing due to a calculation error early in this project. The measured pile responses exerted by these are still used in order to validate the method, such that the theoretical predictions regarding the q-probability waves can be assessed.

7.3.2 Determining characteristic pile responses

Extreme pile responses with 90 % bands are determined for all the tested sea states from chapter 5. The characteristic values are found by fitting a Gumbel distribution to a data sample of the maximum response in each of the ten tests as explained in chapter 3.

7.3.3 Determining impact forces from plunging breakers

A known impulse force exerted by the special hammer in figure 4.16 in chapter 4 is used to verify three established dynamic response programs. The impulsive impact forces exerted by the two plunging breakers from chapter 6 are predicted by means of all the three response programs.

7.4 Results and observations

7.4.1 Pile responses exerted by the q-probability waves

Pile responses exerted by the annual q-probability waves determined in chapter 3 will be presented in this section. They are predicted by means of wave kinematics calculated by the Stokes 5^{th} program inserted in Morison's equation.

Verification of the method

Four regular wave trains with theoretical and measured values as given in table 7.4 are tested in the flume. The predicted overturning moments are much smaller than the measured for all four tests, whereas the predicted base shear responses are somewhat larger than the measured. It is therefore likely to believe that forces will be slightly overpredicted and moments clearly underpredicted by use of this method.

Morison's equation is a statical calculation method assuming the pile to be completely rigid. In reality oscillations of the pile will be of significance, which may explain some of the differences. In order to see if the static load predictions can be improved, additional forces and moments due to displacements of the pile will now be included in the theoretical calculations. A detailed description of this improved method is given in appendix H. The improved overturning moments are found to be unchanged, while a small decrease in magnitude is seen for the improved base shear responses.

Table 7.4: Theoretical and measured values from regular wave tests.

	Morison's equation			**Measurements**			**Improved method**	
ID	C [m]	F [MN]	M [GNm]	C [m]	F [MN]	M [GNm]	F [MN]	M [GNm]
1	12.53	44.31	2.65	12.31	39.18	3.69	40.31	2.65
2	14.21	47.74	2.72	14.55	39.98	3.66	43.64	2.72
3	14.63	49.46	2.85	14.54	41.82	3.76	45.16	2.85
4	15.98	51.51	2.88	15.67	48.69	4.77	47.16	2.88

Deviations between theoretical and measured values are calculated by equation 7.44 and given in table 7.5 for both methods. The deviations from the improved method are given by the subscript I, while the deviations using only Morison's equation are given by the subscript M. Deviations between the theoretical and measured crest heights D_C are found to be satisfactory small such that the load differences must be explained by other physical features. As the improved method provides smaller deviations regarding base shear responses, this method will be used in further calculations of the annual q-probability values. The deviations are still large when it comes to overturning moments predicted by this method

and the static calculations should hence be carefully used.

$$D_X = \frac{X_{theoretical} - X_{measured}}{X_{theoretical}} \tag{7.44}$$

Table 7.5: Deviations using Morison's equation and the improved method.

	Deviations				
ID	D_C [%]	$D_{F,M}$ [%]	$D_{F,I}$ [%]	$D_{M,M}$ [%]	$D_{M,I}$ [%]
1	1.76	11.58	2.80	-39.25	-39.25
2	-2.39	16.26	8.39	-34.56	-34.56
3	0.62	15.44	7.40	-31.93	-31.93
4	1.94	5.47	-3.24	-65.63	-65.63

Wave kinematics from the Stokes 5^{th} program

The annual q-probability crest heights C_q from chapter 3 are given in table 7.6, together with necessary wave heights H and periods T for correct wave descriptions by the Stokes 5^{th} program.

Table 7.6: Annual q-probability crest heights and corresponding input values to the Stokes 5^{th} program.

	ULS			**ALS**		
Direction	C_q [m]	H [m]	T [s]	C_q [m]	H [m]	T [s]
North	16.25	27.88	16.85	22.85	36.97	19.51
South	12.61	22.03	13.33	16.66	28.41	15.12
West	14.95	25.83	14.92	19.83	33.03	17.17
Total	15.69	27.02	16.15	20.79	34.29	18.37

Figure 7.8 shows the wave profiles of the ULS and ALS q-probability waves for total sea obtained from the Stokes 5^{th} program. Highly non linear waves are indicated as the wave crests have much larger magnitudes than the troughs, and a theoretical description up to 5^{th} order is hence necessary for these waves.

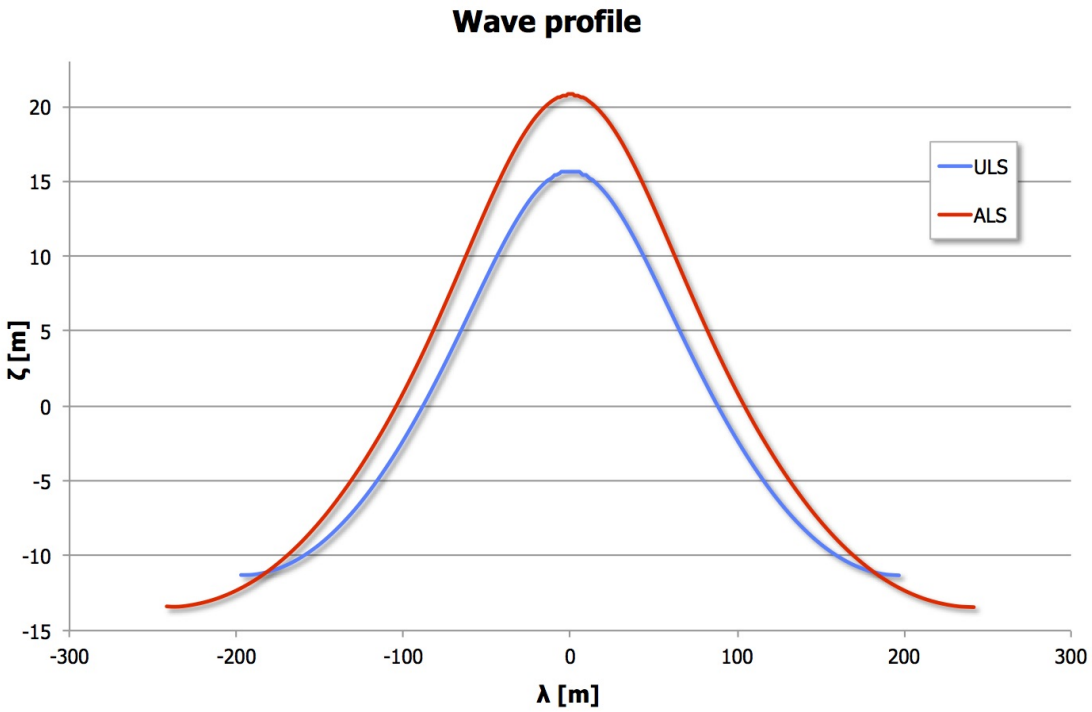

Figure 7.8: Wave profiles of the q-probability waves for total sea.

The Stokes 5^{th} program is used to obtain wave kinematics of the ULS and ALS q-probability waves that can be utilized to find the maximum value of Morison's equation. Figure 7.9 shows the horizontal particle velocities u in which the drag contribution is maximum, whereas figure 7.10 shows the horizontal particle accelerations $\dot{u}$ for maximum mass contribution. Recall from section 7.2.1 that the maximum value of the drag contribution in Morison's equation occurs when the wave crest strikes the pile. Hence, u is plotted up to the C_q values. On the other hand, $\dot{u}$ is plotted up to the mean water surface level, where the maximum value of the mass contribution occurs. If both contributions are significant the maximum of the total expression is of interest. Hence, other calculated values of u and $\dot{u}$ are used. Note that u is non-zero at the sea bottom, implying that shallow water effects are of significance.

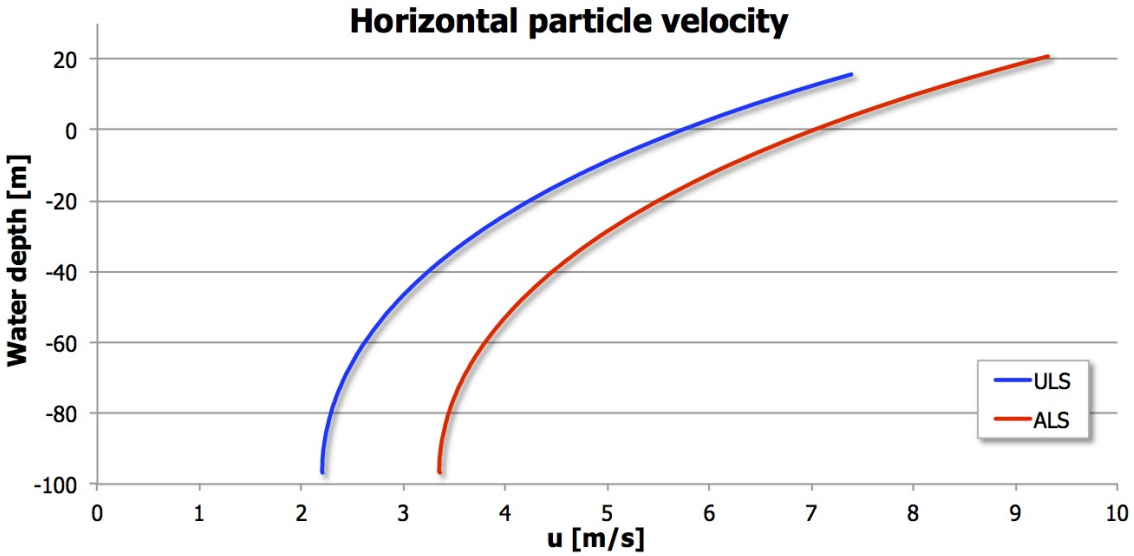

Figure 7.9: Horizontal particle velocity for the q-probability waves up to the wave crest.

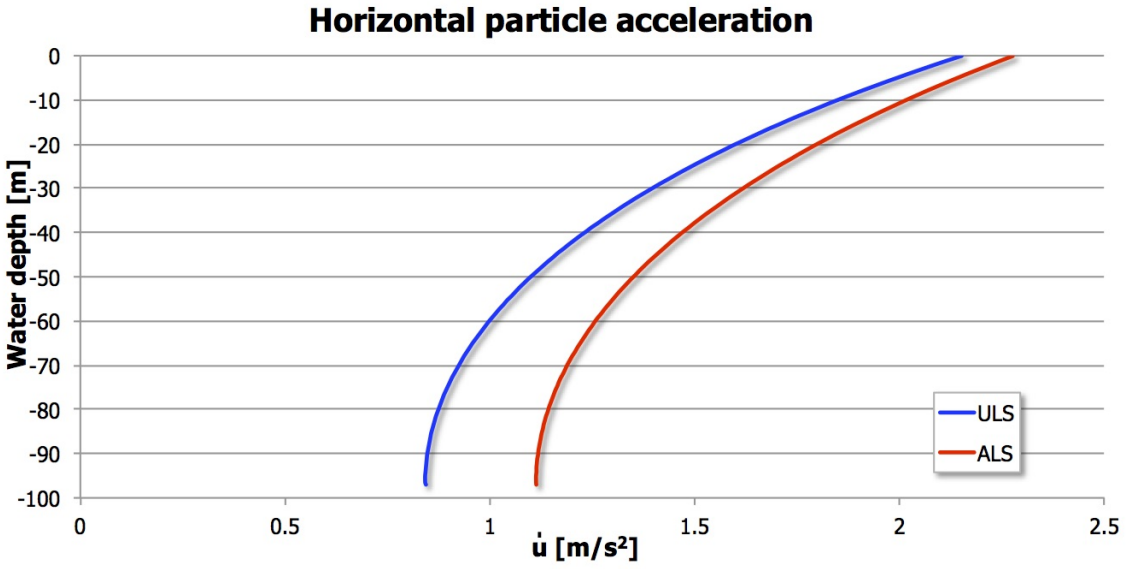

Figure 7.10: Horizontal particle acceleration for the q-probability waves up to the mean surface level.

Load predictions by means of Morison's equation

Morison's equation is used to predict the base shear responses and overturning moments that can be expected from the ULS and ALS q-probability waves. Due to the large diameter of the pile this will be a mass dominated system for all the ULS waves, whereas some of the wave heights from the ALS q-probability waves are so large that both drag and mass contributions must be included.

The maximum predicted base shear forces F_q and overturning moments M_q with corresponding hydrodynamic mass and drag coefficients for the ULS and ALS q-probability waves are given in table 7.7. The forces are assumed to be somewhat overpredicted and the moments are assumed to be excessively underpredicted based on the results in table 7.4.

Table 7.7: Maximum predicted annual q-probability loads.

	ULS				**ALS**			
Direction	C_M [-]	C_D [-]	F_q [MN]	M_q [GNm]	C_M [-]	C_D [-]	F_q [MN]	M_q [GNm]
North	2	-	48.12	2.95	1.91	0.38	57.75	3.94
South	2	-	40.61	2.75	2.00	-	50.67	3.23
West	2	-	46.43	2.98	1.94	0.35	52.51	3.68
Total	2	-	47.37	2.94	1.92	0.36	53.52	3.69

7.4.2 Pile responses exerted by the waves in the critical sea states

The largest measured responses during the critical sea states selected in chapter 3 and subjected for model testing in chapter 5 will be investigated by means of probabilistic approaches in this section.

Measurements

The largest measured base shear responses F_{max} and overturning moments M_{max} during each sea state are given in table 7.8. Sea state 3 is shown to have the largest ULS responses, whereas sea state 13 has the largest ALS responses. The H_S and T_P values for these two sea states are rendered in table 7.9. The base shear responses are ranging between 59.18 [MN] and 83.03 [MN], with corresponding overturning moments ranging between 5.77 [GNm] and 8.95 [GNm].

Table 7.8: Largest measured base shear responses and overturning moments from the critical sea states.

ULS			**ALS**		
ID	$F_{max}[MN]$	$M_{max}[GNm]$	ID	$F_{max}[MN]$	$M_{max}[GNm]$
1	64.49	7.24	7	59.18	5.77
2	62.62	6.90	8	60.44	6.56
3	71.86	7.82	9	63.62	7.21
4	65.73	7.16	10	72.01	7.74
5	63.76	6.95	11	73.24	7.91
6	66.83	7.08	12	81.66	8.91
			13	83.03	8.95
			14	68.53	7.34
			15	72.07	7.28

Table 7.9: Repeated sea state parameters for sea state 3 and 13.

ID	H_S [m]	T_P [s]
3	10.97	11.3
13	14.92	16.9

Relation between crest heights and loads

A considerable surface elevation is expected when large base shear forces and overturning moments occur. It is therefore of interest to verify the measured responses by comparing their time series to the time series of the surface elevation at the pile's location. Such a comparison will be presented in the following for sea state 3 and 13.

Normalized time series regarding the largest measured responses in sea state 3 are shown in figure 7.11. The surface elevation occuring at the same time as F_{max} and M_{max} is found to be unexpectedly low. One can then assume that another wave property than a large crest height has caused these loads. Still, this is the only unexpected relation between measured responses and corresponding crest heights for this sea state as shown in figure 7.11.

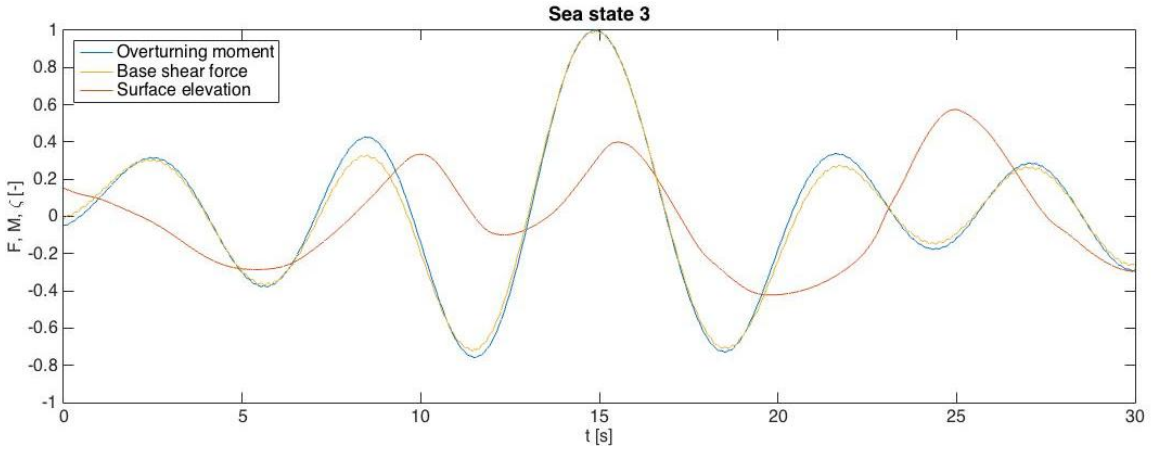

Figure 7.11: Largest overturning moment and base shear response with corresponding surface elevation for sea state 3.

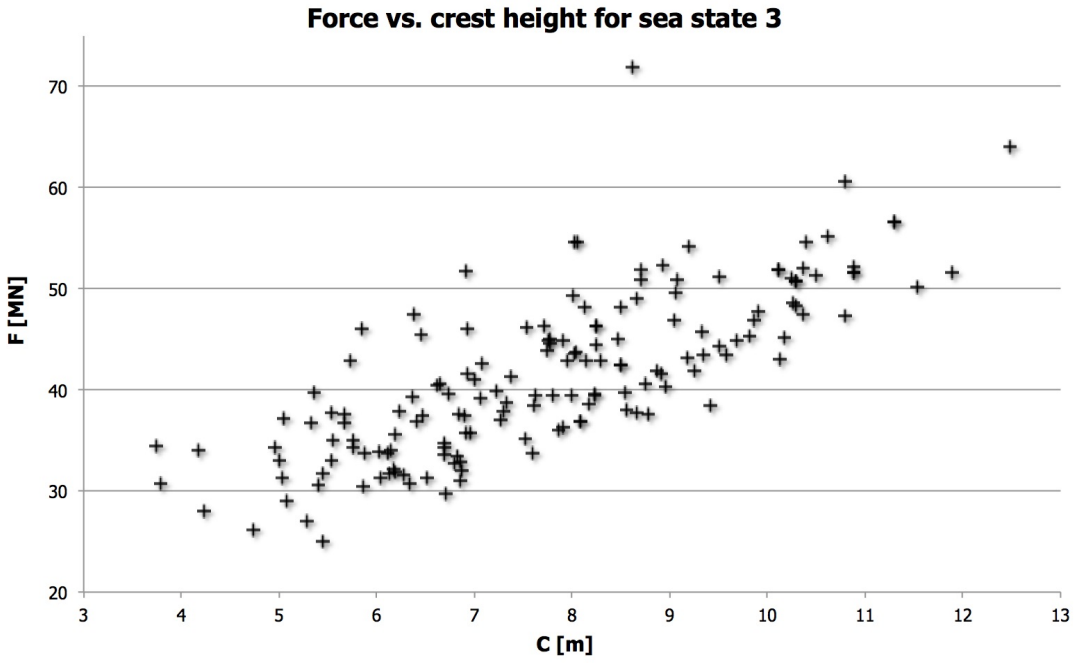

Figure 7.12: Relation between base shear response and crest height for sea state 3.

Good accordance between measured responses and surface elevation for sea state 13 is shown in figure 7.13. It can hence be concluded that F_{max} and M_{max} are induced by one of the largest crest heights measured in this sea state. The relation between a selection

of significant base shear responses and corresponding crest heights is shown in figure 7.13 without any clear outliers. Still, considerable scatter are seen in the figure.

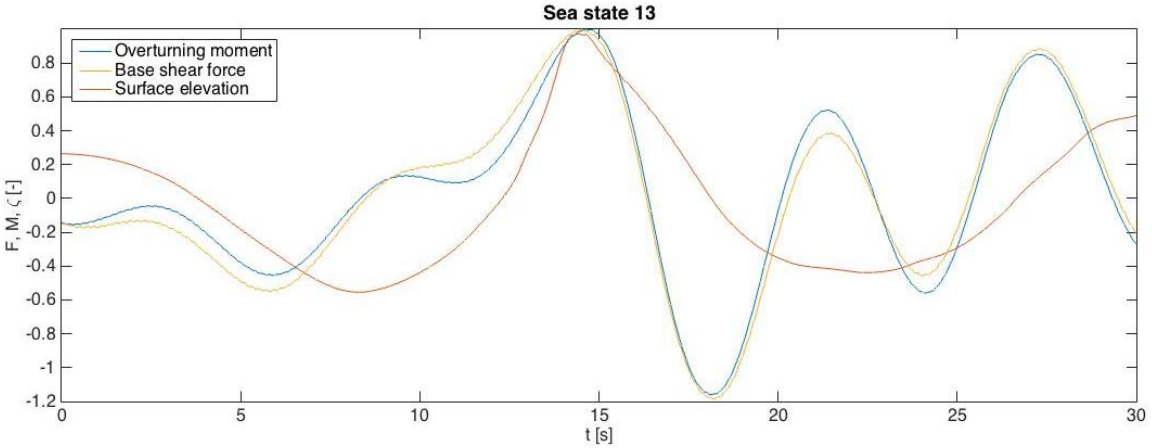

Figure 7.13: Largest overturning moment and base shear response with corresponding surface elevation for sea state 13.

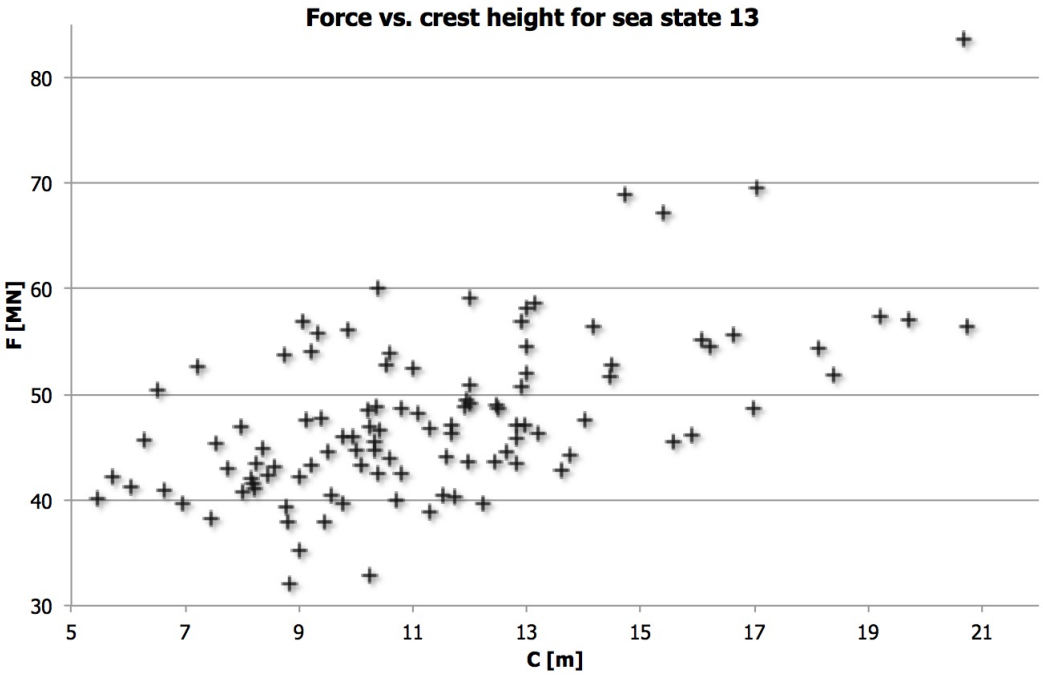

Figure 7.14: Relation between base shear response and crest height for sea state 13.

Extreme value distributions

Gumbel distributions are fitted to samples of 1-hour response maximum in order to estimate the characteristic largest ULS and ALS overturning moment and base shear responses. The samples of response maximum for each sea state with corresponding Gumbel distributions can be found in appendix D. These distributions are exemplified for the base shear responses and overturning moments of sea state 3 and 13 in figure 7.15, 7.16, 7.17 and 7.18. The characteristic largest values are expected to be found within the recommended fractile intervals from table 3.1 in chapter 3, shown as yellow lines in the figures. The largest extremes seem to deviate somewhat from the established distributions, whereas the lowest extremes tend to follow the distributions in a satisfactory manner for both sea states.

Intervals of characteristic pile responses corresponding to the respective limit states annual for the tested sea states are given in table 7.10 as F_α and M_α. Generally, the measured F_{max} and M_{max} values in table 7.8 are found to be larger than the estimated F_α and M_α intervals. It is also worth noting that sea state 3 and 13 are the ULS and ALS sea states of largest F_{max} and M_{max} values, as well as largest F_α and M_α intervals.

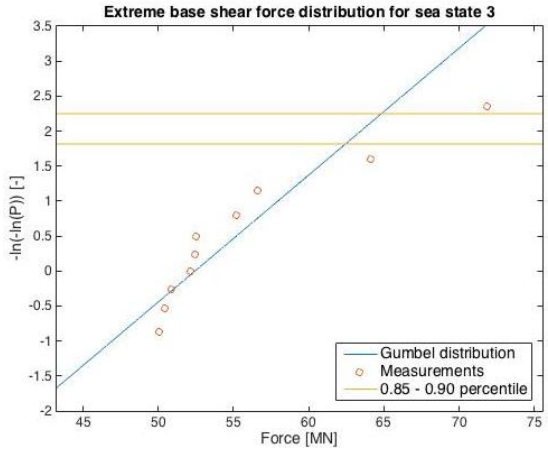

Figure 7.15: Fitted gumbel distribution for extreme base shear responses of sea state 3 with measurements.

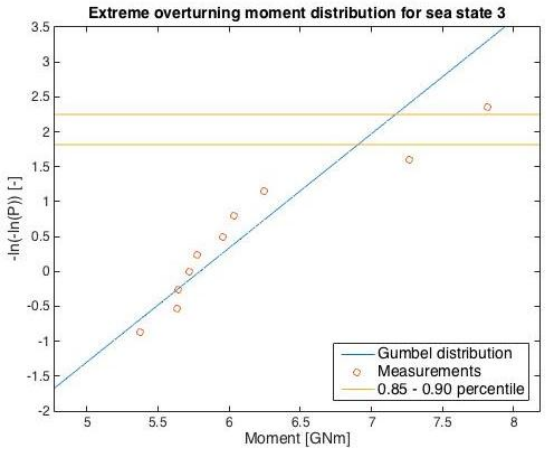

Figure 7.16: Fitted gumbel distribution for extreme overturning moments of sea state 3 with measurements.

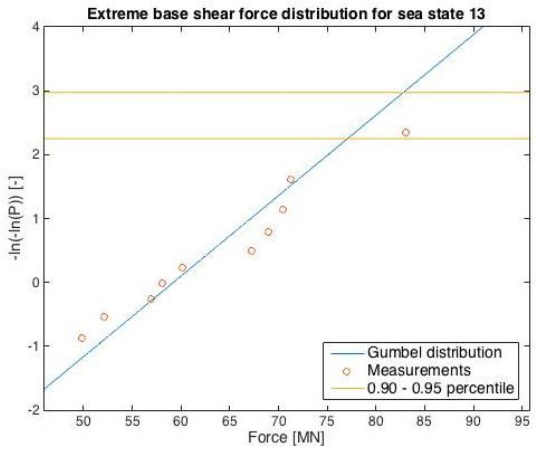

Figure 7.17: Fitted gumbel distribution for extreme base shear responses of sea state 13 with measurements.

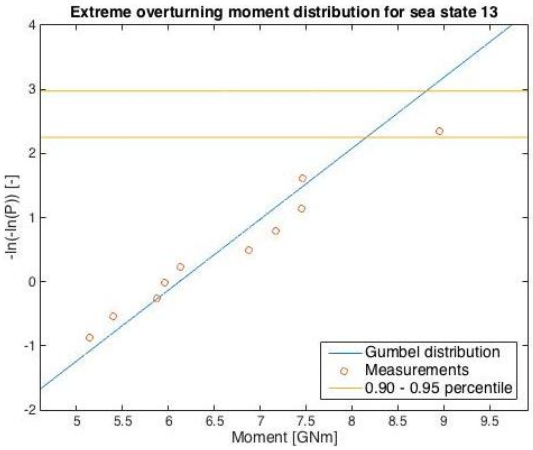

Figure 7.18: Fitted gumbel distribution for extreme overturning moments of sea state 13 with measurements.

Table 7.10: Intervals of characteristic pile responses from the fitted Gumbel distributions.

ULS			**ALS**		
ID	F_α [MN]	M_α [GNm]	ID	F_α [MN]	M_α [GNm]
1	59.11 - 60.64	6.64 - 6.81	7	59.16 - 61.15	6.58 - 6.82
2	58.58 - 59.98	6.42 - 6.59	8	58.41 - 61.16	6.49 - 6.76
3	62.44 - 64.83	6.91 - 7.17	9	60.96 - 63.71	6.90 - 7.23
4	58.94 - 60.66	6.38 - 6.57	10	65.93 - 70.22	7.08 - 7.48
5	58.75 - 60.67	6.34 - 6.55	11	69.64 - 74.21	7.45 - 7.94
6	60.77 - 63.09	6.46 - 6.75	12	73.85 - 79.05	7.86 - 8.43
			13	77.07 - 82.79	8.16 - 8.81
			14	66.80 - 69.76	7.06 - 7.42
			15	70.39 - 74.51	7.28 - 7.70

Uncertainties related to the estimated Gumbel distributions are investigated as they are fitted to samples of limited size. The samples should be representative for the physical problems, which may not be the case for such small samples of size ten. It is therefore recommended to perform bootstrapping in order to obtain 90 % bands for F_α and M_α [62]. This will be exemplified in the following for the characteristic responses of the upper ULS and ALS fractile using sea state 3 and 13.

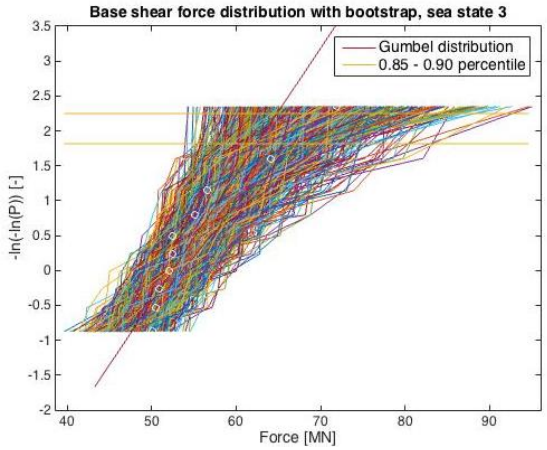

Figure 7.19: Fitted gumbel distribution for extreme base shear responses in sea state 3 with measurements.

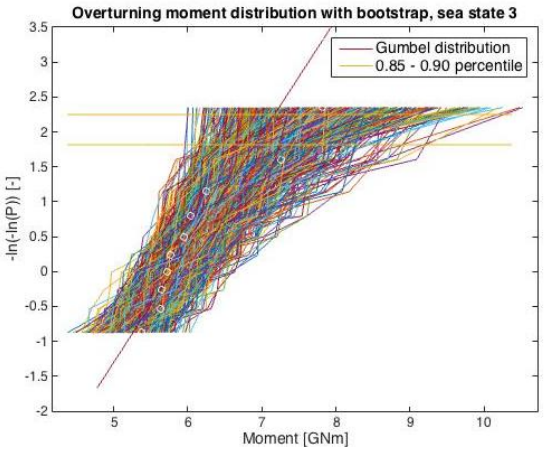

Figure 7.20: Fitted gumbel distribution for extreme overturning moments in sea state 3 with measurements.

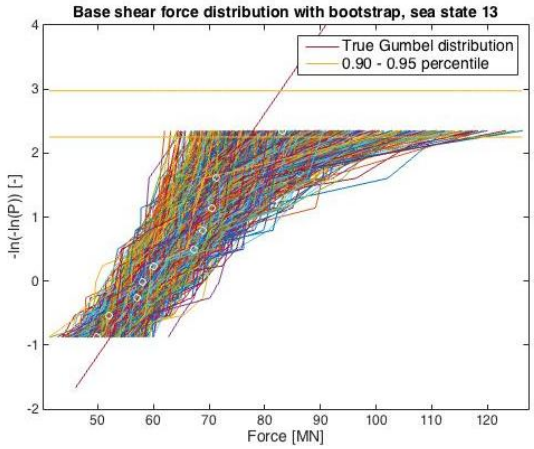

Figure 7.21: Fitted gumbel distribution for extreme base shear response in sea state 13 with measurements.

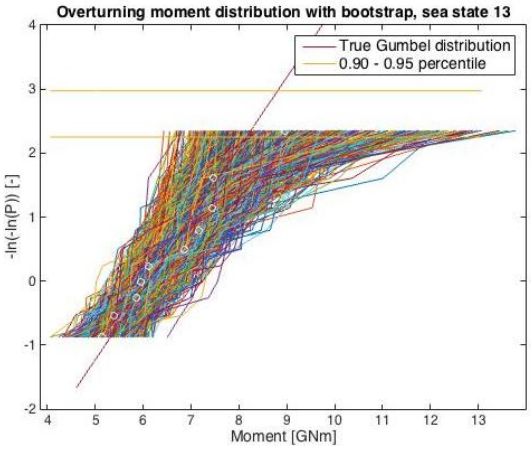

Figure 7.22: Fitted gumbel distribution for extreme overturning moments in sea state 13 with measurements.

Monte Carlo simulated synthetic data samples of size 10 are plotted together with the estimated Gumbel distributions for sea state 3 and 13 in figure 7.19, 7.20, 7.21 and 7.22. Large uncertainties are observed as there are large scatter in the simulated data samples. By performing even more tests for each sea state, more reliable Gumbel distributions will be obtained. As the upper fractile values of the F_α and M_α intervals are most severe, the uncertainties related to these are presented by 90 % bands in table 7.11. These bands are based on 1000 simulated samples as it is recommended to simulate 1000 - 2000 samples for prediction of 90 % bands [62] [63]. Note that the largest uncertainty bands for ULS and ALS are found for sea state 3 and 13, respectively.

Table 7.11: 90 % bands for the largest characteristic ULS and ALS pile responses.

Base shear force					
	ULS			**ALS**	
ID	$F_{\alpha,0.90}$ [MN]	90% band [MN]	ID	$F_{\alpha,0.95}$ [MN]	90% band [MN]
1	60.64	56.40 - 64.41	7	61.15	56.85 - 65.68
2	59.98	56.11 - 64.47	8	61.16	55.66 - 67.10
3	64.83	58.12 - 72.90	9	63.71	57.73 - 70.34
4	60.66	55.82 - 65.77	10	70.22	60.67 - 79.79
5	60.67	55.22 - 66.75	11	74.21	64.36 - 85.60
6	63.09	56.28 - 70.28	12	79.05	68.12 - 90.72
			13	82.79	69.62 - 94.55
			14	69.76	63.44 - 76.81
			15	74.51	65.86 - 83.89
Overturning moment					
	ULS			**ALS**	
ID	$M_{\alpha,0.90}$ [GNm]	90% band [GNm]	ID	$M_{\alpha,0.95}$ [GNm]	90% band [GNm]
1	6.81	6.33 - 7.34	7	6.82	6.30 - 7.36
2	6.59	6.14 - 7.11	8	6.76	6.21 - 7.36
3	7.17	6.43 - 8.07	9	7.23	6.53 - 8.00
4	6.57	6.05 - 7.12	10	7.48	6.58 - 8.39
5	6.55	5.96 - 7.21	11	7.94	6.89 - 9.15
6	6.75	5.90 - 7.46	12	8.43	7.22 - 9.83
			13	8.81	7.31 - 10.15
			14	7.42	6.65 - 8.29
			15	7.70	6.82 - 8.66

Comparison of extreme loads using JONSWAP and Donelan wave spectrum

The largest measured base shear responses F_{max} and overturning moments M_{max} for sea state 1, 6, 7 and 15 using both the JONSWAP and the Donelan wave spectrum are given in table 7.12. Recall that sea state 1 and 7 are among the steepest in the experiment, while sea state 6 and 15 are among the least steep sea states. Larger maximum responses are measured when using the JONSWAP spectrum for sea state 6 and 15. Maximum responses of approximately equal magnitude are seen for sea state 1, whereas larger responses are measured using the Donelan spectrum for sea state 7.

Table 7.12: Largest measured pile responses using JONSWAP and Donelan wave spectrum.

	JONSWAP		**Donelan**	
ID	F_{max} [MN]	M_{max} [GNm]	F_{max} [MN]	M_{max} [GNm]
1	64.49	7.24	64.17	7.15
6	66.83	7.08	60.39	6.74
7	59.18	5.77	64.67	6.99
15	72.07	7.28	66.79	6.81

Gumbel distributions are fitted to the largest measured responses of all the ten tests in the four sea states using both JONSWAP and Donelan wave spectrum. These distributions are shown in figure 7.23 - 7.30. As can be seen the measured extremes using both wave spectrums are quite similar, except for sea state 7 where an obvious distinction is found. Still, clear differences are observed between the fitted Gumbel distributions using the two wave spectrums.

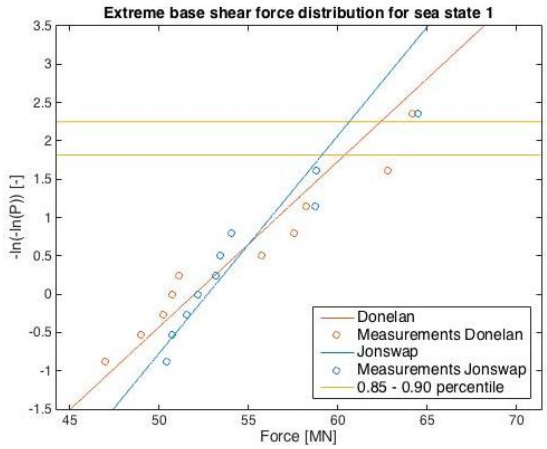

Figure 7.23: Extreme base shear response distributions of sea state 1 for Donelan and JONSWAP with measurements.

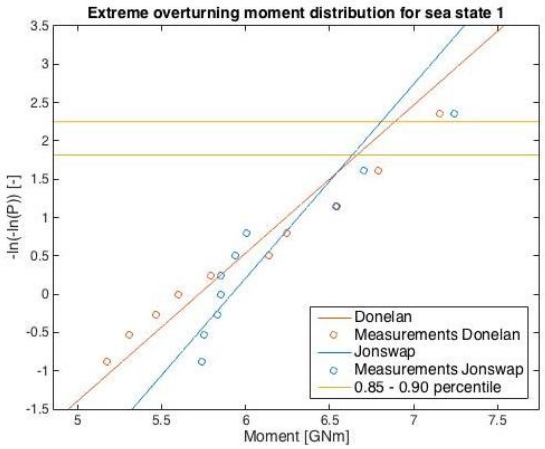

Figure 7.24: Extreme overturning moment distributions of sea state 1 for Donelan and JONSWAP with measurements.

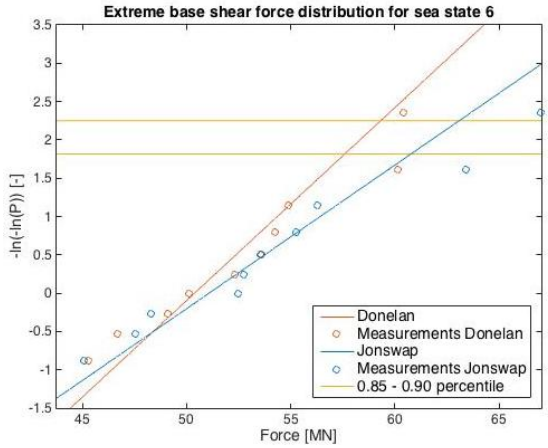

Figure 7.25: Extreme base shear response distributions of sea state 6 for Donelan and JONSWAP with measurements.

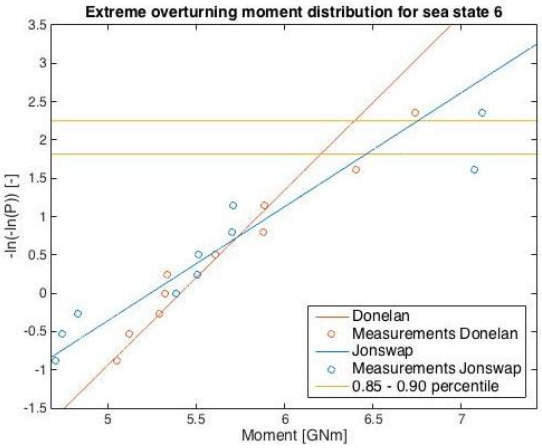

Figure 7.26: Extreme overturning moment distributions of sea state 6 for Donelan and JONSWAP with measurements.

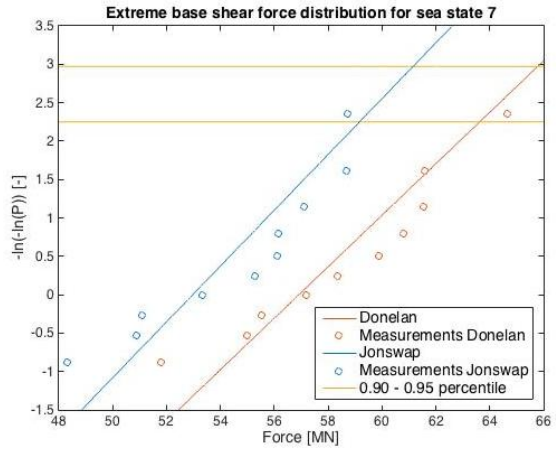

Figure 7.27: Extreme base shear response distributions of sea state 7 for Donelan and JONSWAP with measurements.

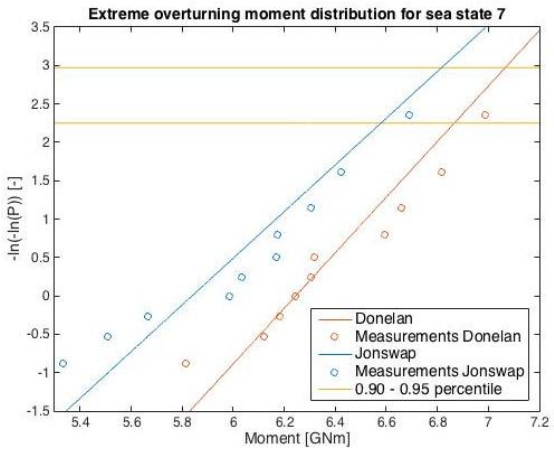

Figure 7.28: Extreme overturning moment distributions of sea state 7 for Donelan and JONSWAP with measurements.

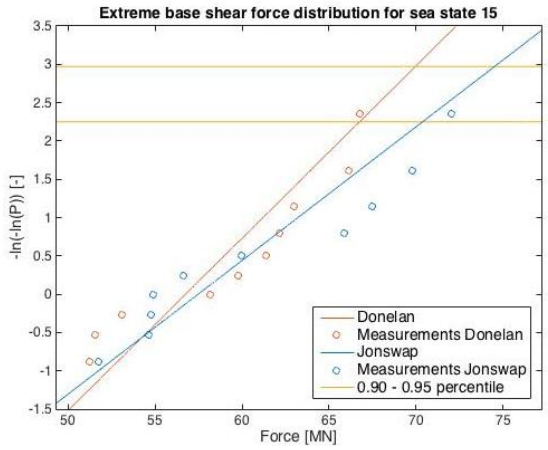

Figure 7.29: Extreme base shear response distributions of sea state 15 for Donelan and JONSWAP with measurements.

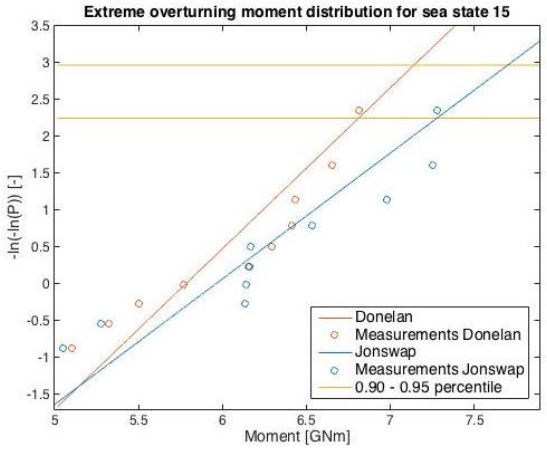

Figure 7.30: Extreme overturning moment distributions of sea state 15 for Donelan and JONSWAP with measurements.

The intervals where the two distributions for base shear response and overturning moment cross the percentile levels are given as F_α and M_α in table 7.13. Higher values are found for sea state 6 and 15 when using the JONSWAP spectrum than the Donelan spectrum, whereas the opposite is seen for sea state 1 and 7. Even though F_{max} and M_{max} are quite similar using both wave spectrums for sea state 1, the extreme distributions still indicate that Donelan provides larger characteristic responses.

Table 7.13: Predicted characteristic responses using JONSWAP and Donelan wave spectrum.

	JONSWAP		**Donelan**	
ID	F_α [MN]	M_α [GNm]	F_α [MN]	M_α [GNm]
1	59.11 - 60.64	6.64 - 6.81	60.39 - 62.40	6.66 - 6.88
6	60.77 - 63.09	6.46 - 6.75	57.60 - 59.32	6.21 - 6.40
7	59.16 - 61.15	6.58 - 6.82	63.63 - 65.78	6.87 - 7.07
15	70.39 - 74.51	7.28 - 7.70	66.76 - 69.96	6.81 - 7.14

7.4.3 Local impact forces and global responses from plunging breakers

Estimates of the impact force magnitudes P_0 from the two perfectly focused plunging breakers will be presented in this section, as well as a verification of the dynamic response programs that are utilized to determine such estimates. The overturning moments predicted by the different response programs by inserting P_0 are termed:

- M_C Moment predicted by assuming constant impulse load form.
- M_L Moment predicted by assuming linearly decreasing impulse load form.
- M_S Moment predicted by assuming sinusoidal impulse load form.

Verification of the method

Four known impulse forces P_0 from impacts between hammer and pile are given in table 7.14, together with corresponding durations t_1 and measured overturning moments M_H. Since both the impact forces and the dynamic responses are known for these tests, they can be used to verify the goodness of the three established dynamic response programs. Such a verification is carried out by inserting P_0 in the programs and comparing measured and calculated moments $M(t)$ for the first oscillation period. Predicted values of M_C, M_L and M_S are also given in table 7.14. The predicted M_S values are closest to the measured M_H values for all four tests, such that the most suitable impact load form in this case seem to be the sinusoidal. As expected, M_L is found to be half the value of M_C, indicating that

the linearly decreasing load form provides a moment of half the magnitude provided by the constant load form for the same P_0 values.

Table 7.14: Impact force magnitude and duration with resulting measured and estimated overturning moment assuming constant, linearly decreasing and sinusoidal impact load form.

Test	P_0 [MN]	t_1 [s]	M_H [GNm]	M_C [GNm]	M_L [GNm]	M_S [GNm]
1	64.07	0.28	1.70	2.68	1.34	1.71
2	58.74	0.28	1.53	2.46	1.23	1.57
3	58.27	0.28	1.51	2.44	1.22	1.55
4	46.59	0.30	1.29	2.04	1.02	1.30

A comparison of measured and calculated dynamic responses for hammer test 1 is shown in figure 7.31. This figure verifies that there is good accordance between measured and calculated response during the first oscillation assuming sinusoidal impact load form. Assuming constant impact load form the responses are overpredicted, whereas an underprediction is provided by the linearly decreasing impact load form.

After the first oscillation the measured response in figure 7.31 is seen to be slightly damped, which is not accounted for in any of the response programs. Still, it is the first period of oscillation that is of interest.

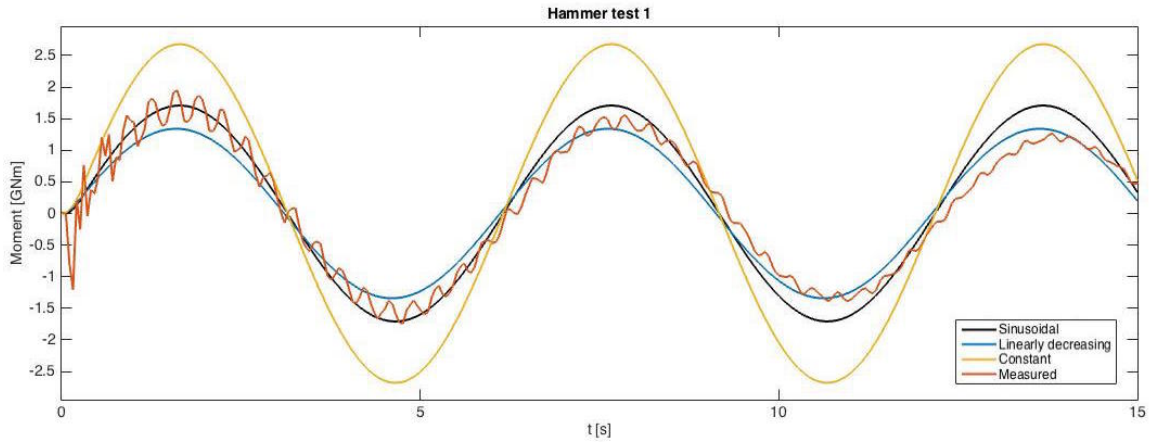

Figure 7.31: Comparison of measured and predicted responses for hammer test 1.

By inserting P_0 for test 1 in the different response programs the impact load forms with magnitude P_0 in figure 7.32 are obtained. The impulses I are given as the area under the load forms and will therefore be different for the various response programs. The largest impulse is provided by the constant load form, while the linearly decreasing provides the smallest.

An impulse in between is found for the sinusoidal load form, which is shown to coincide best with the impulse of the hammer stroke. The response program for the sinusoidal load form is hence shown to provide satisfactory predictions of the dynamic response for hammer test 1.

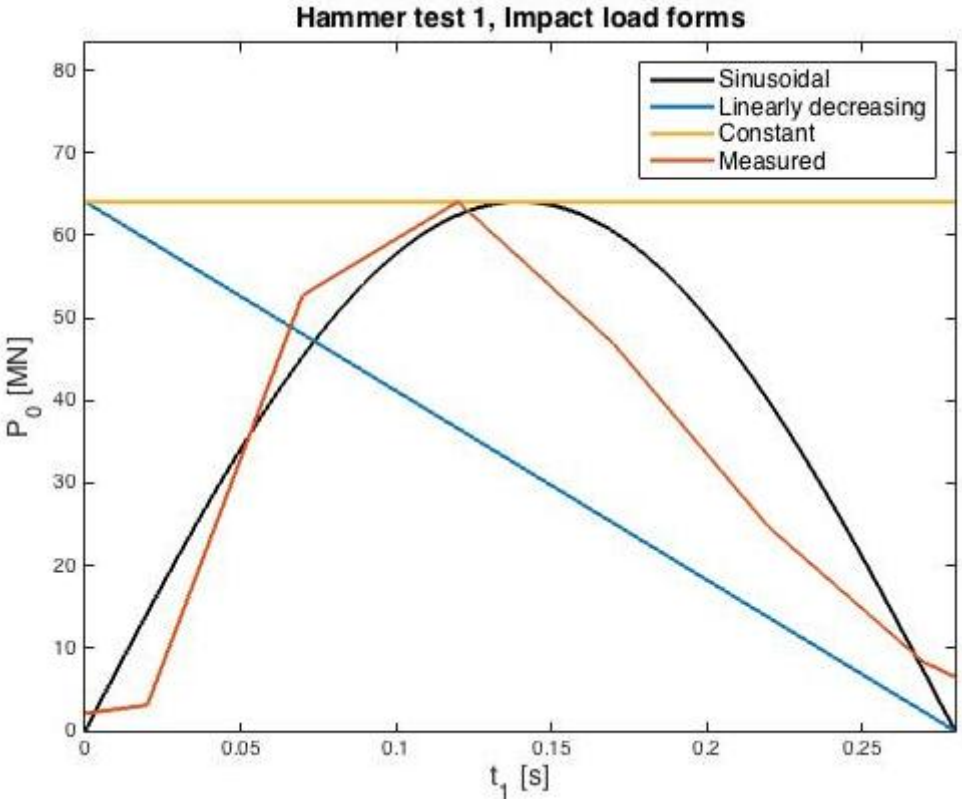

Figure 7.32: Impact load forms for hammer test 1.

The dynamic rotations θ_{dyn} obtained by the three different response programs are given in table 7.15 for all the four tests. Corresponding static rotations θ_{stat} for the same P_0 values are calculated in order to find the DAF provided by the different response programs, termed DAF_{prog}. By comparing these to the real DAFs calculated by means of equation 7.22, only small deviations between 0.01 - 0.02 are seen for all the tests. The established response programs can hence be assumed to provide responses satisfactory close to the theoretical for the first period of oscillation.

Table 7.15: DAFs for the four different tests assuming constant, linearly decreasing and sinusoidal impact load form.

Test	Load form	θ_{stat} [rad]	θ_{dyn} [rad]	DAF_{prog} [-]	DAF_{real} [-]
1	Constant	0.0244	0.0069	0.28	0.29
	Linear	0.0244	0.0035	0.14	0.15
	Sinusoidal	0.0244	0.0044	0.18	0.19
2	Constant	0.0224	0.0063	0.28	0.29
	Linear	0.0224	0.0032	0.14	0.15
	Sinusoidal	0.0224	0.0040	0.18	0.19
3	Constant	0.0224	0.0063	0.28	0.29
	Linear	0.0224	0.0031	0.14	0.15
	Sinusoidal	0.0224	0.0040	0.18	0.19
4	Constant	0.0174	0.0053	0.28	0.30
	Linear	0.0174	0.0026	0.14	0.15
	Sinusoidal	0.0174	0.0034	0.18	0.19

Plots of the four applied impulsive loads exerted by the hammer are shown in figure 7.33, indicating a sinusoidal impact load form for the hammer tests. Exact representations of the load forms are hard to determine as the resolution of the plots is somewhat coarse due to the short impact duration combined with the sampling frequency of the measured forces.

The impulse load plotted together with the corresponding measured base shear response for test 1 is shown in figure 7.34. A harmonic response of much lower magnitude than P_0 is seen after the impulse load, i.e. for $t > t_1$. The large vibrations that occur after the impulse load may be due to a higher order mode with eigenperiod equal to the duration of the impulse load. It should be mentioned that the area under the impulse graph corresponds to the area under the first oscillation of the response, which means that the impulse is transfered to oscillations of the pile.

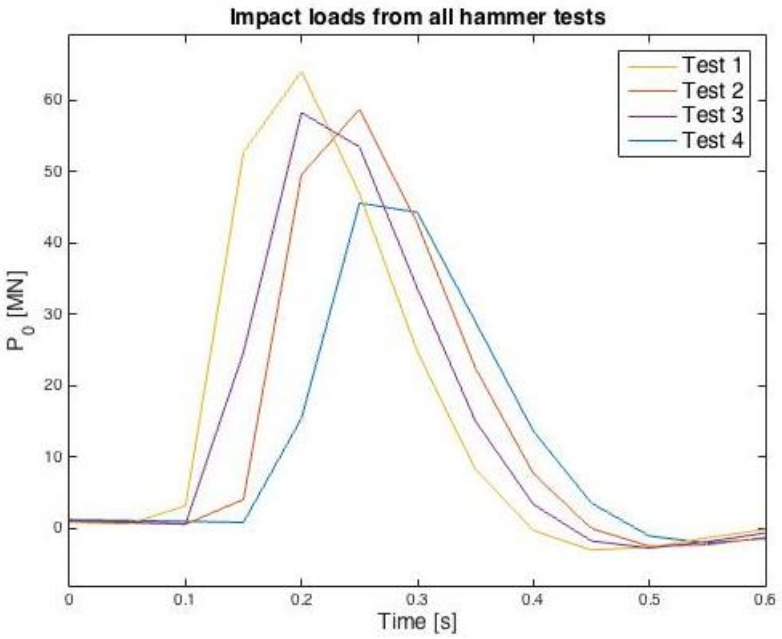

Figure 7.33: Impulse forces from all the four hammer tests.

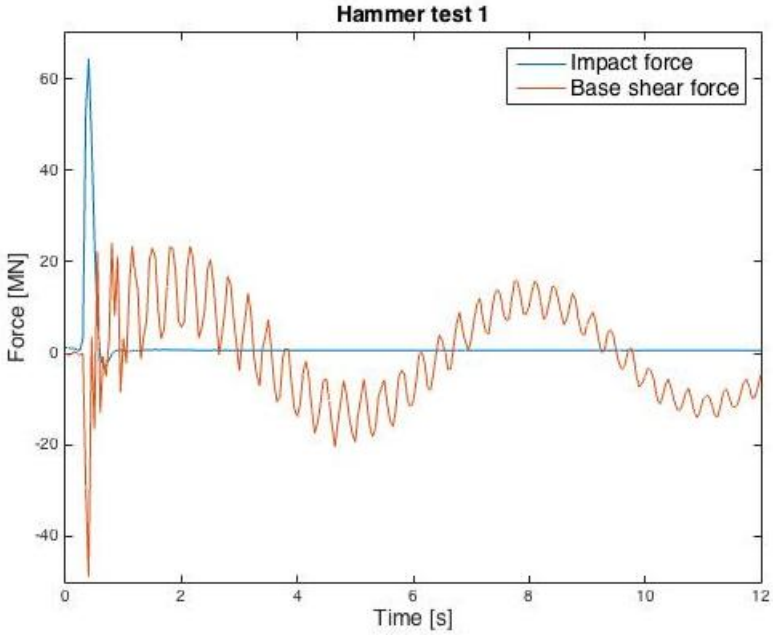

Figure 7.34: Plot of impulse load and corresponding base shear response for hammer test 1.

Measurements

Measured base shear responses F_P and overturning moments M_P of the pile exerted by the two plunging breakers from chapter 6 are given in table 7.16 for six different tests with crest heights C_P. The measured responses are found to be larger for wavetrain 2 than for wavetrain 1. Hence, larger responses are seen for the wavetrain with largest frequency range and thereby also the highest frequencies. Low variations between the six tests are seen for both wavetrains.

Table 7.16: Measured responses from the plunging breakers in wavetrain 1 and 2.

	Wavetrain 1			**Wavetrain 2**		
Test	C_P [m]	F_P [MN]	M_P [GNm]	C_P [m]	F_P [MN]	M_P [GNm]
1	19.58	60.90	7.31	21.51	77.13	9.23
2	19.26	60.07	7.18	20.68	71.54	8.71
3	19.41	60.06	7.21	20.31	75.14	9.25
4	22.45	60.30	7.30	20.16	72.17	8.85
5	22.82	56.63	6.91	19.91	70.91	8.72
6	21.67	57.84	7.08	21.11	72.31	8.67

Test 1 for wavetrain 1 has a crest height closest to the second largest crest height in sea state 13 of 19.7 [m] and M_P equal to 7.31 [GNm]. Test 6 for wavetrain 2 is closest to the largest measured crest height in sea state 13 of 21.25 [m] and has M_P equal to 8.67 [GNm]. These two tests will hence be used for impulsive load prediction of the two plunging breakers in the following, and their corresponding M_P values are attempted in the response programs.

Impulsive load prediction

The impulsive P_0 forces required for the three different response programs to obtain M_C, M_L and M_S values equal to the two measured M_P values are given in table 7.17. Figure 7.35 and 7.36 show the three different impact load forms using the impact durations t_1 from chapter 6 and the predicted P_0 values. It is seen that the impulse loads of wavetrain 2 have larger magnitudes and shorter durations than those in wavetrain 1.

Table 7.17: Predicted P_0 values by the three response programs for the two plunging breakers.

	Calculated P_0 [MN]	
Impact load form	Wavetrain 1	Wavetrain 2
Constant	538.66	703.61
Linear	1077.00	1406.90
Sinusoidal	845.76	1104.90

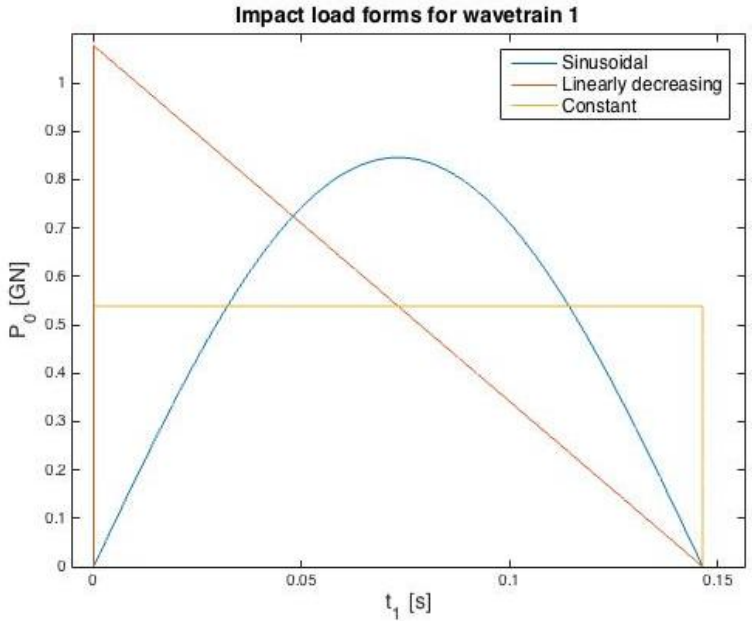

Figure 7.35: Plot of the assumed impulsive load forms using the predicted P_0 values for wavetrain 1.

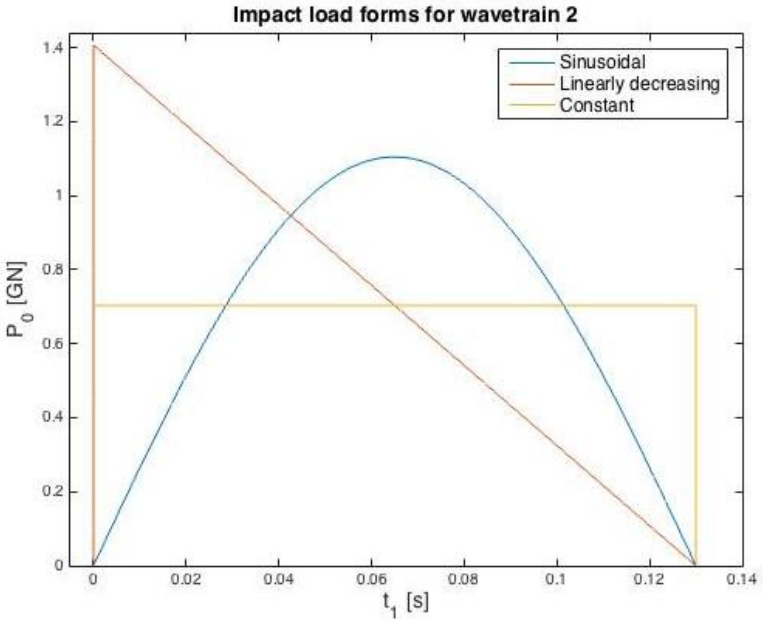

Figure 7.36: Plot of the assumed impulsive load forms using the predicted P_0 values for wavetrain 2.

The time histories of the impulsive forces and the moment response plotted together for wavetrain 1 and 2 are shown in figure 7.37 and 7.38, respectively. For comparable reasons the impulse forces are divided by a factor of 10. The time course of the dynamic response from a transient load impulse is assumed be composed of two parts, one with forced oscillations due to the impact force and a following with free oscillations. As can be seen the maximum response takes place around 1.7 [s] for both wavetrains, which is approximately the sum of t_1 and a quarter of the eigenperiod of the pile T_0. This late response maximum occurs during the free oscillations due to the large inertia effects related to the motion of the pile.

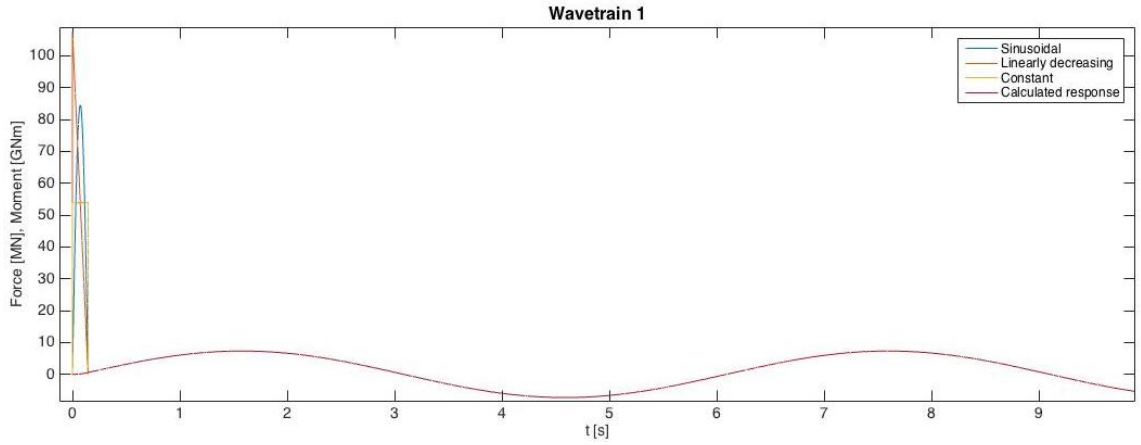

Figure 7.37: Impact forces and dynamic moment response for wavetrain 1 plotted together.

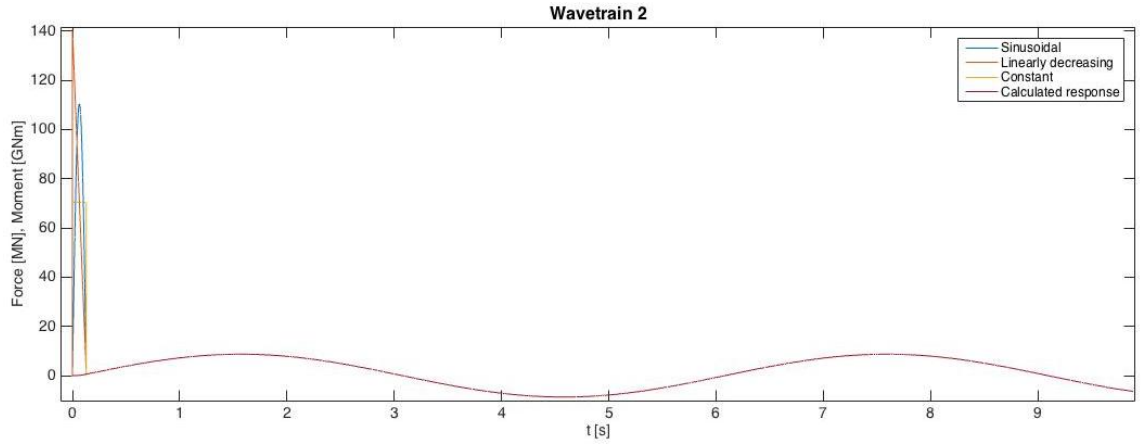

Figure 7.38: Impact forces and dynamic moment response for wavetrain 2 plotted together.

Comparison of measured and predicted response

The time histories of the measured and predicted dynamic responses by means of the three response programs are compared for wavetrain 1 and 2 in figure 7.39 and 7.40, respectively. The graphs are found to follow each other closely around the first maximum value, whereas larger differences are seen before and after this time interval. It should be noted that the measured response magnitudes are much larger than the predicted for the first maximum negative moment. This is when the motion of the pile is oppositely directed relative to the consecutive incoming waves, such that the pile experiences larger resistance during this period. These incoming waves can also explain that the first measured response period is 0.6 [s] larger than the eigenperiod used in the predicted responses. As the wavetrain passes, this effect vanishes such that the measured response periods equal the eigenperiod. The difference between the measured and predicted response at the second positive maximum moment occurs as expected because the damping term is neglected.

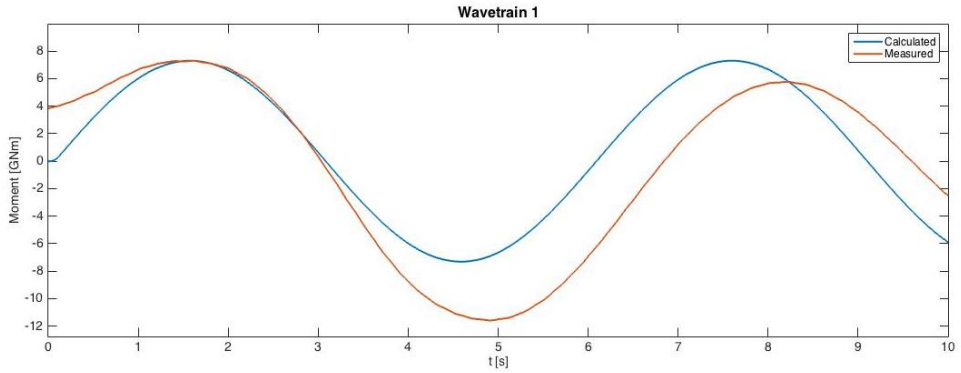

Figure 7.39: Comparison of measured and calculated dynamic moment response for wavetrain 1.

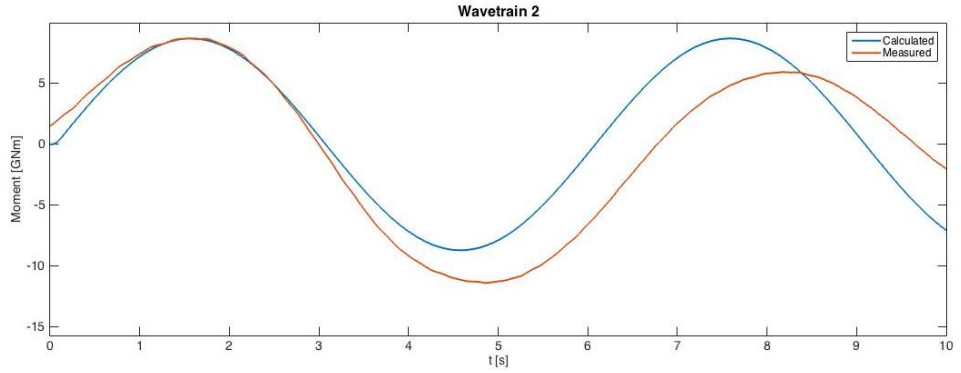

Figure 7.40: Comparison of measured and calculated dynamic moment response for wavetrain 2.

7.5 Discussion and recommendations

7.5.1 Goodness of using Stokes 5^{th} order wave in Morison's equation

Morison's equation assumes a fixed pile such that no energy from the incoming waves is carried out as motions. All the wave-induced loads are then assumed transferred to base shear forces and overturning moments. In reality the pile will oscillate when facing the incoming waves such that the concentrated mass on top of the pile and the mass of the pile itself may influence the responses. This behaviour was tried accounted for statically in an improved calculation method, leading to a small reduction in base shear forces and no change in overturning moments. A statical approach is therefore concluded to give poor results for this pile system, as the dynamics seem to be of significance. Due to this discovery it will be of interest to predict the loads by means of the equation of motion in a future study. In order to verify the method of using Stokes 5^{th} order waves in Morison's equation model tests should also be performed with a restrained pile.

Another feature not taken into account in the theoretical prediction methods is the effect of limited flume length. As the Stokes 5^{th} program assumes potential theory, the theoretical elliptical motion paths for u and $\dot{u}$ may be disturbed by the unrealistic backflow in the flume. The calculated values of u and $\dot{u}$ may therefore not be applicable for describing the conditions in the flume, such that poor load predictions are obtained by using these values in Morison's equation.

7.5.2 Predicted pile responses from the q-probability waves

Large differences are seen between measured and predicted responses by use of Stokes 5^{th} order waves in Morison's equation. The suggested improved statical method provides base shear forces close to the measured and unchanged underpredicted overturning moments. Hence, the overturning moments calculated for the annual q-probability waves are expected to be excessively underpredicted while the base shear responses can be assumed more realistic.

The waves of correct annual q-probability crest heights have not been subjected for model testing due to a calculation error in an early phase of this project. It will therefore be of interest to test these waves in a future extension.

7.5.3 Accuracy of the extreme response distributions

All the measured extreme base shear responses and overturning moments are found to lie within the range of thousand synthetic data samples, generated from the estimated Gumbel distributions. These distributions are hence found to describe the ten extremes during the critical sea states in a satisfactory manner. Large uncertainties related to the small data samples of size ten are still seen as the synthetic data samples have a wide range. More

reliable Gumbel distributions with narrower uncertainty bands can be obtained by performing even more tests of each sea state in a future experiment, such that the size of the data samples increases.

The characteristic largest base shear responses and overturning moments based on combining the estimated Gumbel distributions with the ULS and ALS fractiles are found for sea state 3 and 13, respectively. All the measured responses of significance in these two sea states are found to occur due to considerable crest heights, except for the largest extreme in sea state 3. It is then likely to believe that this extreme pile response occurs due to another wave property than a large crest height, for example breaking. Figure D.27 in appendix D indicates that breaking is probable for this sea state when the pile is present, whereas minor breaking is indicated for sea state 13 in figure D.127.

7.5.4 Differences between JONSWAP and Donelan wave spectrum

Sea state 1, 6, 7 and 15 are tested using both the JONSWAP and the Donelan wave spectrum. Recall that sea state 6 and 15 are located on top of the ULS and ALS contour lines and are among the least steep sea states in this experiment. Generally higher waves and larger extreme crest heights were found for these sea states when using the JONSWAP spectrum in chapter 5. The largest base shear responses and overturning moments determined by the ULS and ALS percentiles are also found using the JONSWAP spectrum for sea state 6 and 15.

On the other hand, sea state 1 and 7 are located farthest down on the contour lines and are among the steepest sea states in this experiment. For these steep sea states generally higher waves and larger extreme crest heights were found using the Donelan wave spectrum. The same tendency regarding extreme responses is found for sea state 7, as the measurements using the Donelan wave spectrum provides the largest values. Small differences between the responses by using the two spectrums are seen for sea state 1. Since the extreme crest heights in sea state 1 are found to be affected by a limiting factor, the extreme responses using both JONSWAP and Donelan spectrum may be caused by breaking waves. This limiting factor is not seen for sea state 7 such that the extreme responses are assumed to be caused by the large extreme crest heights.

Still, the small number of compared sea states make it hard to draw any clear conclusions and even more sea states should be tested in a further experiment.

7.5.5 Plunging breakers

The known impulsive forces of sinusoidal load form applied by the hammer verifies the sinusoidal response program, as the predicted overturning moments equal the corresponding measured time series. The real DAFs for each load form are approximately equal to the DAFs calculated by means of the three response programs. As all the three programs are

established by the same method, they are assumed to provide satisfactory descriptions of the response in calm water.

The predicted impulsive forces depend on the choice of load form such that large variations are seen between the different P_0 values. It may be difficult to select the right P_0-prediction as it is hard to decide upon the most suitable load form of the impact from a plunging breaker. A tiny water jet hits the pile at the very beginning of t_1 inducing a small load compared to the following P_0 caused by the overturning fluid mass, which has passed at the very end of t_1. Hence, a sinusoidal load form may be assumed most suitable for the impact during t_1. This assumed load form resembles the triangular load form termed a in figure 7.7 and a prediction of the responses caused by this load form will be of future interest.

The predicted response follows the measured closely at the first positive maximum, whereas for the first negative maximum the predicted response has smaller magnitude than the measured. As the pile motion is oppositely directed relative to the consecutive waves after the plunging breaker, the pile experiences larger resistance than it would in calm water. Hence, a larger moment response is measured when the pile moves countercurrent than when it moves cocurrent. This pile motion is illustrated in figure 7.41. Due to this matter the first oscillation period is somewhat larger than the eigenperiod of the pile. This effect will vanish when the consecutive waves have passed, and the pile will then oscillate with the eigenperiod.

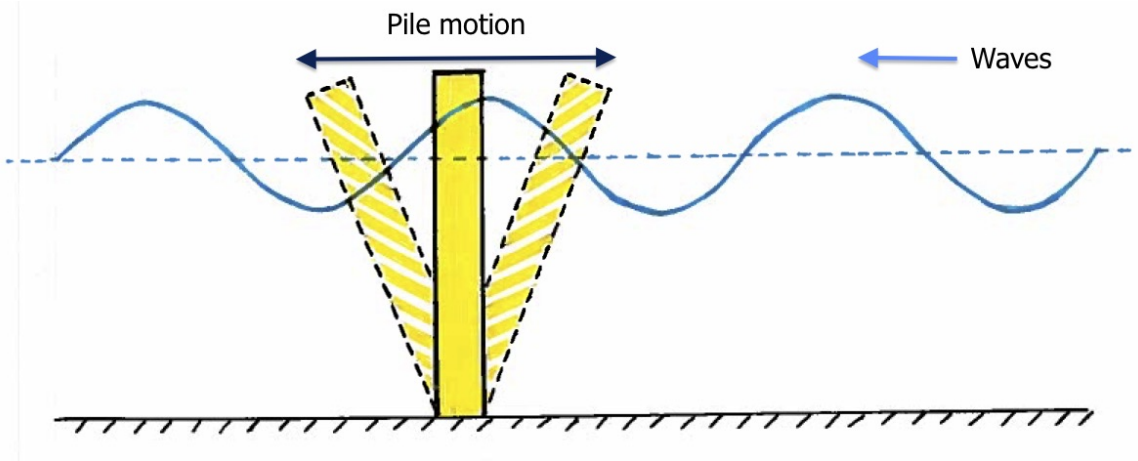

Figure 7.41: Cocurrent and countercurrent pile motion in waves.

In the future, the effect of larger overturning moments when the pile moves countercurrent may be accounted for by including Morison's equation in the response programs. Morison's equation assumes a fixed pile in incoming waves, while the response programs assume an oscillating pile in calm water. The response predictions in calm water by the three programs

have already been verified by the hammer tests, whereas an underprediction of moment responses is seen when using Morison's equation for the oscillating pile. Hence, a more reliable description of the responses from incoming waves may be obtained by improving the programs. Another improvement for obtaining more reliable results can be to include the damping term, which has been established in chapter 4.

A concentrated impulsive force is assumed in this experiment. In reality a plunging breaker will impact a limited area of the pile. The load distribution along the impact area of the pile should hence be included in a future extension of the response programs in order to obtain more reliable P_0 predictions. A sinusoidal load distribution which is assumed the most correct distribution of the impulse force from a plunging breaker is shown in figure 7.42.

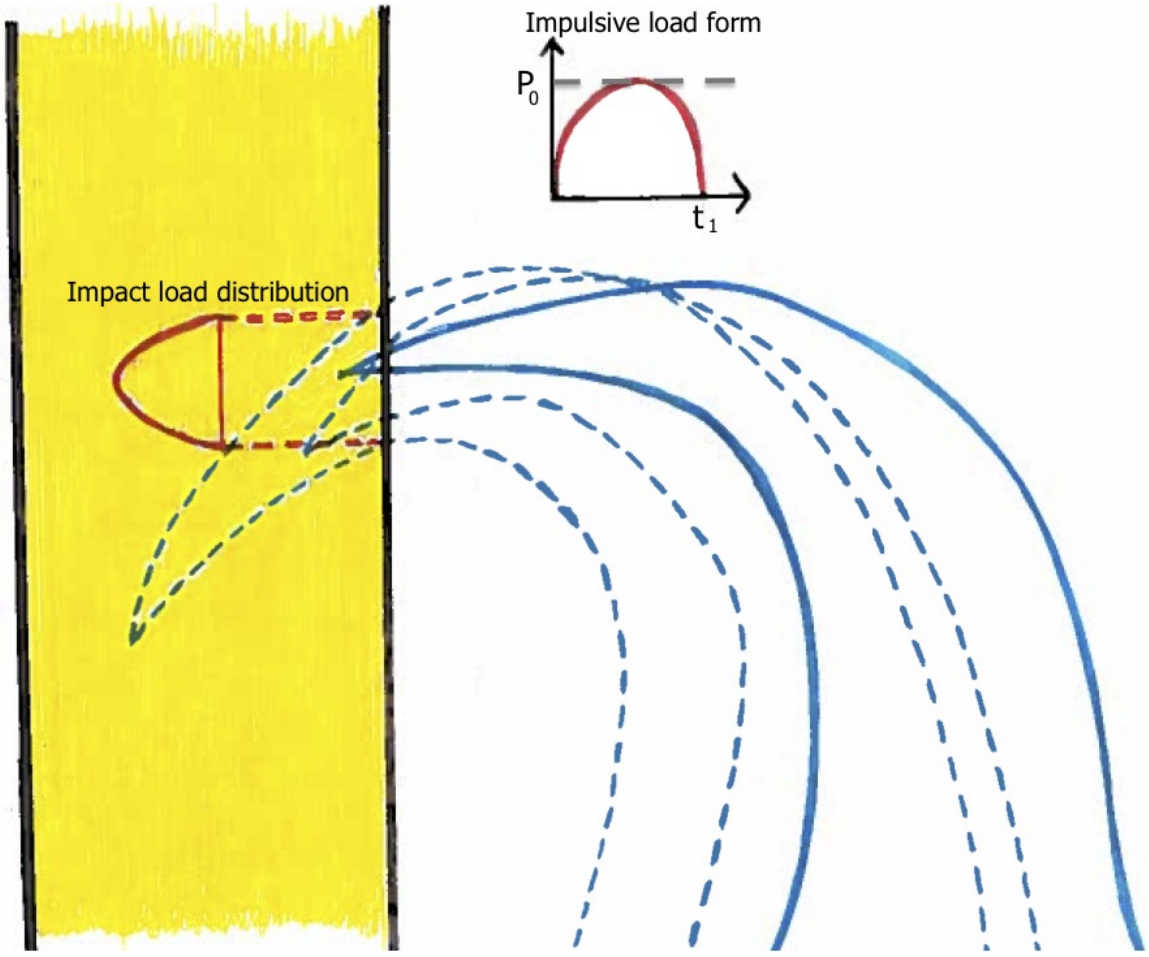

Figure 7.42: An illustration of the assumed impulsive load form and impact load distribution from a plunging breaker.

7.5.6 Importance of breaking waves

The two wavetrains subjected for investigation result in plunging breakers of approximately equal crest height. The average crest heights and pile responses from the six tests of each wavetrain are given in table 7.18 as $\bar{C}_P$, $\bar{F}_P$ and $\bar{M}_P$. Even though the crest heights are quite similar, the pile responses induced by wavetrain 2 are considerably larger. In order to investigate this observation further, wave properties of test 1 for wavetrain 1 and test 6 for wavetrain 2 are rendered in table 7.19. Note that these two tests are the ones presented in the results of this chapter.

Table 7.18: Average values from six tests of wavetrain 1 and 2.

Wavetrain	$\bar{C}_P$ [m]	$\bar{F}_P$ [MN]	$\bar{M}_P$ [GNm]
1	20.87	59.30	7.17
2	20.61	73.20	8.91

From table 7.19 the crest height for the plunging breaker in wavetrain 1 is found to be 7 % smaller than the crest height in wavetrain 2, whereas the measured pile responses are 16 % smaller. The main difference in wave properties between these two plunging breakers are seen for the C_g values. These values are measured at the position of the pile, where the jet caused by the overturning fluid mass at the wave crest influences the measurements. The jet at the crest of the plunging breaker in wavetrain 2 is then assumed to impact with a larger velocity than for wavetrain 1. Hence, larger responses of the pile are found for this perfectly focused wavetrain. The location of impact z_b is also seen to be different for the two plunging breakers, which may also explain some of the differences in response magnitudes [20] [28].

Table 7.19: Wave properties of plunging breakers in wavetrain 1 and 2.

		Wavetrain 1	**Wavetrain 2**
C	[m]	19.58	21.11
H	[m]	33.96	34.79
T	[s]	14.90	14.90
λ	[m]	329.83	329.83
t_1	[s]	0.15	0.13
C_g	[m/s]	22.20	25.00
z_b	[m]	116.60	118.10
F	[MN]	60.90	72.31
M	[GNm]	7.31	8.67
P_0	[MN]	845.76	1104.90

In order to determine whether breaking waves must be taken into account when predicting

extreme responses of the pile, they are compared to the characteristic extremes in the most unfavorable ALS sea state, i.e. sea state 13. These values are given in table 7.20. The measured overturning moment exerted by the plunging breaker in wavetrain 2 as given in table 7.19 is found within the characteristic values of this sea state. Recall the large uncertainties related to the established Gumbel distributions due to limited sample size which introduce an even wider range of possible characteristic values as shown in table 7.20. All the measured pile responses from the two plunging breakers, except the base shear response of wavetrain 1, are now found within the uncertainty bands related to the characteristic ALS values.

Table 7.20: Characteristic pile responses for sea state 13 with corresponding 90 % bands.

	Characteristic values	**90 % uncertainty bands**		
Response	0.9 - 0.95 percentile	0.9 percentile	0.95 percentile	Total
Base shear [MN]	77.07 - 82.79	66.78 - 88.89	69.62 - 94.55	66.78 - 94.55
Moment [GNm]	8.16 - 8.81	6.98 - 9.51	7.31 - 10.15	6.98 - 10.15

It is now shown that breaking waves may be of importance in the prediction of extreme ALS responses of the pile. For the plunging breakers to be of importance, breaking at the exact location of the pile with a sufficiently large crest height is required. The velocity of the water jet from the overturning fluid mass is also assumed crucial for the magnitude of the pile responses in this matter.

In addition, the tremendous impulsive impact forces P_0 are assumed to exert extensive local loads on the pile. This may cause local damage or in worst case threaten the stability of the pile in whole [64].

Chapter 8

Conclusion

Possible error sources related to the model tests

Possible error sources in conjunction with the experimental setup in the flume may be wave reflections, the pile's interaction with the waves, losses in connection with the wave maker or inaccurate measurements.

The beach design used in this experiment was shown to provide rather small wave reflections, while larger reflections were indicated when the pile is present in the flume. This may be explained by wave diffractions from the cylinder wall for small waves, while for larger waves the pile will fluctuate with, and amplify, the incident waves. Additionally, the pile's presence in the flume combined with the limited flume width may force the waves to higher amplitudes.

Internal flow in the flume due to limited flume length may also affect the incident waves in a way not present in the full scale problem. The duration of each test was therefore limited in order to ensure that both reflections and unrealistic flows did not grow extensively large. If succeeding tests had been performed without sufficient waiting time in between, this might have affected the tests.

The relation between wave heights in the flume and corresponding real motion of the wave maker was shown to coincide good with the Biésel transfer function for almost all periods. Some small deviations were seen for periods below 0.6 [s], which are out of the applied range for this experiment. It can hence be concluded that the Biésel transfer function is a good description of the generated waves in the flume. Still, the real motion of the wave maker was shown to be somewhat smaller than desired, such that lower waves may be obtained due to mechanical losses in the flap.

Not perfectly calibrated waveprobes may lead to imprecise wave measurements. Worn strain gauges may additionally lead to uncertainties related to the measured base shear

responses and overturning moments of the pile.

Choosing a proper scaling ratio based on the water depth in the flume is important to ensure representative and useful results for the location of interest. The scaling ratio was kept constant throughout the whole experiment, while the water depth was found to vary somewhat as water slowly seeps out of the flume. These differences were attempted considered in the wave generation, such that the input files are generated and tested for the respective water depths. Sloppiness in the wave generation or reading of the different water depths may lead to improper representation of the real problem. If such an error has occurred, the effect is only assumed to result in $\pm$ 1 [m] of the full scale water depth, and can be assumed to represent irregularities along the real seabed.

Critical sea states from contour lines

The sea states subjected for model testing were selected from a set of wrongly established contour lines due to a calculation error early in this project. The wrongly selected sea states are described by somewhat higher H_S values than the sea states selected from the correct contour lines. Still, the sea states obtained from the model tests have much lower H_S values than both the wrongly and correctly selected sea states. They are in addition closer to the correctly selected sea states than the wrongly selected sea states subjected for model testing, as rendered in figure 8.1 and 8.2 for ULS and ALS, respectively. It is worth noting that the differences seem to increase for increasing H_S values. The obtained $H_{S,out}$ values were found to be 82 % - 92 % of the $H_{S,in}$ value, whereas they are 86 % - 98 % of the H_S values for the correct sea states. The effect of wrongly selected sea states is hence assumed to be of minor significance relative to the losses related to the experiment.

The measured H_S values from the obtained sea states in the model tests were also seen to be higher when the pile was present in the flume. These H_S values were measured to be 89 % - 99 % of the correct H_S values. This means that the pile responses are measured under wave conditions pretty close to the correct sea states, dispite the wrongly selected sea states and losses related to the model tests.

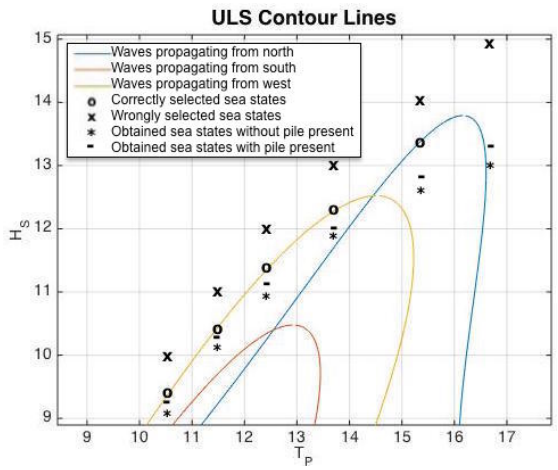

Figure 8.1: Wrongly and correctly selected ULS sea states and actual ULS sea states from model testing.

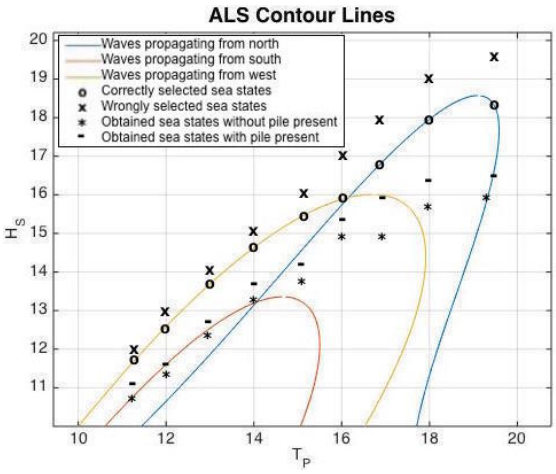

Figure 8.2: Wrongly and correctly selected ALS sea states and actual ALS sea states from model testing.

The losses in relation to the model tests may be explained by the discovered mechanical losses in the flap or by the unphysical backflows in the flume. For optimal model tests this error should have been accounted for by introducing an amplification of the wavemaker signal or by testing sea states of larger H_S values than necessary in order to iterate until the correct sea state was obtained.

Design sea states

The most unfavorable sea states along the ULS and ALS contour lines are found to be sea state 3 and 13, respectively. These design sea states are chosen as they provide the largest extreme responses that most probably will occur only once every 100 years for ULS and every 10 000 years for ALS. Sea state 3 is one of the intermediate steep sea states in this experiment and located at the ULS contour line for waves propagating from west, whereas sea state 13 is among the least steep sea states and located at the ALS contour line for waves propagating from north. Sea state parameters and extreme responses for sea state 3 and 13 are rendered in table 8.1. Recalling that an underprediction is assumed due to losses related to the model testing, the characteristic responses corresponding to the upper fractile levels are presented.

Table 8.1: Sea state parameters and characteristic responses for the ULS and ALS design sea state.

	Sea state parameters			**Characteristic responses**	
Limit state	$H_{S,out}$ [m]	$H_{S,pile}$ [m]	T_P [s]	F [MN]	M [GNm]
ULS	10.97	11.09	12.38	64.83	7.17
ALS	14.92	15.97	16.90	82.79	8.81

The fitted Gumbel distributions that were used to determine the characteristic responses are found to describe the ten extremes for each sea state in a satisfactory manner. At the same time bootstrapping revealed that there are wide uncertainty bands related to the distributions of both sea states due to the limited sample size. A proper choice of design sea states is still assumed as the highest upper uncertainty bounds for ULS and ALS are found for these.

Even though sea state 3 was not the ULS sea state with the largest measured crest heights in this experiment, it was found to provide the largest extreme base shear responses and overturning moments. As the largest measured extreme responses in this sea state occured without a significant surface elevation, another wave property was assumed to induce these responses. A limiting factor was seen for crest heights above 13 [m] with the pile present in the flume, indicating that breaking is probable for this sea state. The presence of the pile is hence assumed to evoke crest heights above a breaking wave limit. Extreme base shear responses and overturning moments may therefore be induced by both steep extreme waves and breaking waves in this sea state.

Sea state 13 had the largest measured crest heights in this experiment. All the extreme crest heights were found to lie far above the suggested second order 1-hour distribution and implied growth without any limiting factor. This observation indicated that breaking will be of minor significance in this sea state and that large responses could be expected due to the large crest heights, which was supported by the good accordance between response and surface elevation. A more detailed investigation of the largest crests in sea state 13 still revealed that breaking may occur in this sea state as the second largest crest was above the breaking wave limit. The extreme base shear responses and overturning moments may therefore be induced by both extreme continous wave profiles and breaking waves.

Donelan vs. JONSWAP wave spectrum

Sea state 1, 6, 7 and 15 were tested using both the JONSWAP wave spectrum and the Donelan wave spectrum. Sea state 1 and 7 are located farthest down on the ULS and ALS contour lines and are hence among the steepest sea states in this experiment. On the other hand, sea state 6 and 15 are among the least steep sea states and located on top of the two

contour lines.

The Donelan wave spectrum is a corrected version of the JONSWAP spectrum with a higher order decay and a somewhat richer tail. It then follows that the peak of the Donelan wave spectrum may fall below the JONSWAP peak. The wave energy within a sea state based on the JONSWAP spectrum is expected to be concentrated around the peak period, whereas the wave energy when it is based on the Donelan spectrum is more spread such that waves of higher frequencies are more probable. Higher frequencies lead to smaller periods and hence shorter wave lengths. Steeper waves are therefore expected when using the Donelan wave spectrum.

Small differences between the two wave spectrums were seen for the two steepest sea states, exemplified by sea state 1 in figure 8.3 below. On the other hand, significant differences were seen between the two spectrums for the sea states on top of the contour lines, as shown in figure 8.4 for sea state 15. The effect of different input wave spectrums is hence assumed to be most important regarding sea state 6 and 15, while it is assumed to be small for sea state 1 and 7.

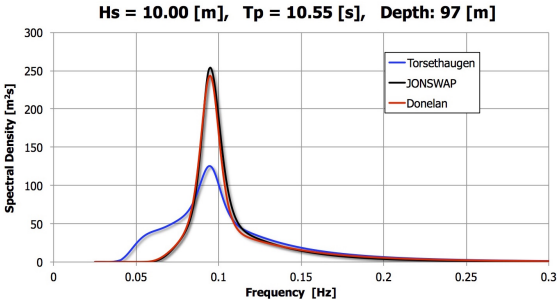

Figure 8.3: Wave spectrums for sea state 1.

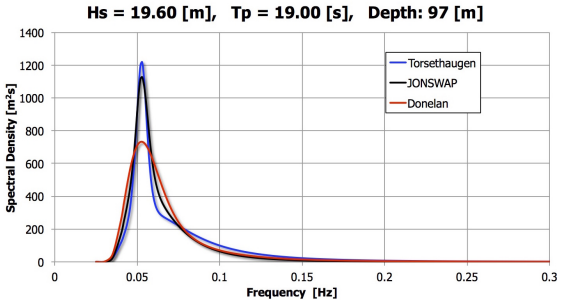

Figure 8.4: Wave spectrums for sea state 15.

Somewhat larger $H_{S,out}$ values were found from the measurements based on the Donelan spectrum compared to the JONSWAP spectrum for sea state 1 and 7. In addition, the extreme crest heights were significantly higher from the Donelan-based model tests, especially for sea state 7. No limiting factor seemed to affect the crest heights in this sea state when using the Donelan spectrum, such that they grew considerably large. It then follows an even larger difference between the extreme pile responses by use of the two wave spectrums for this sea state. The extreme pile responses in sea state 1 were harder to distinguish from each other. In this sea state a limiting factor seemed to affect the growth of crest heights above 10 [m] and 11 [m] using the JONSWAP and Donelan wave spectrum, respectively. If the extreme pile responses are caused by waves limited by for example breaking, they may be very equal even though the crest heights are generally larger when the Donelan wave spectrum is used.

The measured $H_{S,out}$ values were found to be smaller when the Donelan spectrum was used in the model tests of sea state 6 and 15. Extreme crest heights for sea state 6 based on the JONSWAP spectrum were larger than when using the Donelan spectrum, whereas the difference between the two wave spectrums was rather small regarding sea state 15. No limiting factor affecting the crest heights was insinuated for sea state 15. In sea state 6 the crest heights above 13 [m] and 14 [m] seemed affected by a limiting factor when using the Donelan and JONSWAP wave spectrum, respectively. The extreme pile responses were smaller when using the Donelan spectrum for these sea states, especially for sea state 15.

It is then likely to believe that the waves within the two steepest sea states based on the Donelan spectrum induce somewhat larger pile responses as they are slightly steeper than the waves based on the JONSWAP spectrum. On the other hand, the wave-induced pile responses for the two sea states on top of the contour lines are assumed smaller when using the Donelan spectrum as a greater part of the wave energy is found for shorter wave periods. The assumed smaller wave lengths using the Donelan spectrum for sea state 6 and 15 may induce steeper waves restricting the wave heights to grow extensively high.

The Donelan wave spectrum may be a better choice for the steep sea states as it provides the largest extreme crest heights and pile responses. In addition, the measured averaged wave spectrums are shown to fit the theoretical wave spectrum in a better way using the Donelan spectrum for these sea states. The most unfavorable ULS sea state is intermediate steep, and a model test based on the Donelan spectrum could hence provide larger extreme pile responses. The largest extreme pile responses are expected to be found by using the JONSWAP spectrum for less steep sea states, and is therefore assumed a better choice for the most unfavorable ALS sea state.

Are breaking waves important?

Breaking waves were seen to occur in both the steep and the less steep critical sea states. In addition, the presence of the pile led to somewhat larger wave heights which increased the amount of breaking waves. Two perfectly focused wavetrains generated to break at the exact location of the pile were subjected for model testing in order to determine the importance of breaking waves regarding global design. For comparable reasons plunging breakers with crest heights corresponding to the largest measured crest heights in the ALS design sea state were attempted.

Even though wave breaking is not considered very important regarding global design of slender structures, the comparison of characteristic responses in the ALS design sea state and measured responses from the two plunging breakers implied otherwise. Breaking waves can therefore be assumed important relative to other extreme waves with regard to global response of the slender pile structure in this experiment. It should be pointed out that the response magnitudes from the plunging breakers seem strongly influenced by the wave

breaking point, the crest height and the velocity of the overturning water jet. In reality the probability of such a crucial plunging breaker to occur at the exact location of the pile is extremely low.

Impact force magnitudes corresponding to the two plunging breakers were estimated based on the measured responses. As these magnitudes were found to be considerably large, local damage of the pile where the water jet hits may be expected. The total capacity of the pile may then be reduced or in worst case it may loose the overall structural strength.

All in all breaking waves are considered important as they induce large global and local loads on the pile.

Chapter 9

Further Work

In a future model test experiment it will be of interest to include a correction term for the wave heights in the wave maker signal. It may then be possible to obtain the desired wave heights in the flume, or at least reduce the losses in the wave maker motion considerably. More reliable results with regard to crest heights and loads corresponding to the most unfavourable ULS and ALS sea state can then be obtained. The measured crest heights, base shear responses and overturning moments are then expected to correspond well with the actual sea states, unlike the somewhat underpredicted values obtained in this project.

It will also be of interest to extend the number of tests conducted for each of these sea states in order to obtain data samples of increased size. Such an increase in sample size will lead to less uncertainty considering the extreme responses, resulting in even greater reliability.

Model testing of the correct annual q-probability waves from all directions of propagation will also be of future interest. A comparison of responses from these waves, characteristic responses from the design sea states and measured responses from the plunging breakers would then be possible. A further improved prediciton method for the loads exerted by the regular q-probability waves would also be an advantageous improvement in the future. This can be done by including dynamics through the equation of motion.

If the model testing had spanned over a longer period of time it would have been rewarding to try a different scaling ratio. The importance of breaking waves relative to other extreme waves on a more or less slender structure can then be investigated. This would further open for the opportunity to model test annual q-probability waves corresponding to both ULS and ALS, as the maximum allowable motion of the flap may limit the possible wave heights.

It will also be beneficial to perform a more comprehensive study of the Donelan wave spectrum in a future experiment, as the limited amount of tested sea states made it hard to draw any clear conclusions. Model testing of an extended number of sea states, includ-

ing both the steepest, the least steep and some intermediate steep sea states is therefore recommended as a continuation of this project. In order to get reliable results with regard to crest heights and responses, each sea state should be conducted numerous times.

Another favorable expansion in a future model test experiment will be to perform tests while keeping the pile restrained. It is then possible to determine the importance of wave diffractions relative to the oscillatory behaviour of the pile. Model tests with a restrained pile will also be advantageous in order to verify the goodness of the statical method based on using Stokes 5^{th} order wave profiles in Morison's equation.

An improvement of the response programs will also be valuable in an extension of this project. Firstly it will be of interest to take into account the effect of consecutive waves after the plunging breaker by including for example Morison's equation. Secondly the damping term can be included such that the predicted response follows the measured response after the first period of oscillation as well. An establishment of a response program for the triangular load form excluded in this thesis will for comparable reasons also be preferable in the future.

By installing even more waveprobes prior to the focus point of the plunging breakers, it would be easier to measure exact properties and wave development. The breaking waves could then be studied in more detail with regard to important factors like breaking point and water jet velocity. In addition, measuring devices at the impact area of the pile would make it easier to predict the extent of local damage one can expect. The latter could also indicate which vertical load distribution that would be preferable to investigate in an extended study. An expanded experimental setup including more measuring devices is therefore of future interest.

Chapter 10

Bibliography

[1] DNV. Design of Offshore Steel Structures, General (LRFD method), April 2011. Offshore Standard DNV-OS-C101.

[2] NORSOK. Integrity of offshore structures, Edition 7, June 2010. NORSOK standard, N-001.

[3] International Organisation for Standardisation. ISO 19901-1: Petroleum and natural gas industries – Specific requirements for offshore structures – Part 1: Metocean design and operating considerations, 2005.

[4] S. Winterstein, T.C. Ude, C.A. Cornell, P. Bjerager, S. Haver, editor. *"Environemntal Parameters for Extreme Response: Inverse FORM with omission Sensitivity"*, Innsbruck, 1993. Proc. ICOSSAR-93.

[5] S. Haver, G. Sagli, T.M. Gran, editor. *"Long term response analysis of fixed and floating structures"*. Proc., Wave'98, Ocean Wave Kinematics, Dynamics and Loads on Structures, International OTRC Symposium, April 1998.

[6] S. Winterstein, K. Engebretsen, editor. *"Reliability-Based Prediction of Design Loads and Responses for Floating Ocean Structures"*, Lisbon, Portugal, 1998. OMAE-1998.

[7] NORSOK. Actions and action effects, Edition 2, September 2007. NORSOK standard, N-003.

[8] S.K. Haver, K.A. Nyhus, editor. *"Environmental Contour Lines for Design Purposes – Why and When?"*, Vancouver, June 2004. OMAE 2004.

[9] DNV. Environmental Conditions and Environmental Loads, April 2014. DNV-RP-C205.

[10] International Association of Oil and Gas Producers. Health, Safety and Environmental guidelines for metocean and Arctic surveys, 2011. Report No. 477.

[11] S.K. Haver, K.A. Nyhus, editor. *"A wave climate description for long term response calculations"*, volume 4, Tokyo, April 1986. Proceedings of the Fifth International Offshore Mechanics and Arctic Engineering Symposium.

[12] S.K. Haver, K.A. Nyhus, editor. *"Met-Ocean Contour Lines for Design; Correction for Omitted Variability in the Response Process"*, Toulon, France, May 2004. Proceedings of 14th International Offshore and Polar Engineering Conference.

[13] S.K. Haver, S.R. Winterstein. "Environmental Contour Lines: A Method for Estimating Long Term Extremes by a Short Term Analysis". Technical report, Transactions, Society of Naval Architects and Marine Engineers, 2008.

[14] G. Baarholm, S.K. Haver, O.D. Økland. "A method to predict long-term distributions of waves and wave-induced motions and loads on ships and other floating structures". Technical report, Marine Structures, 23, 2010.

[15] J.R. Morison, J.W. Johnson, M.P. O'brien, editor. *"Experimental Studies of Forces on Piles"*, volume 4, Chicago, 1953. Proceedings 4th Conference on Coastal Engineering.

[16] D. D. Gaillard. *Wave Action in Relation to Engineering Structures.* The Engineer School, Washington, 1904. U.S. Army Corps of Engineers.

[17] J. Larras. "Recherches experimentales sur le deferlement des lames". Technical report, Annales Fonts et chausse'es, October 1952.

[18] A.de Rouville, P. Besson und P. Petry. "Etat actual des e'tudes internati onal es sur les efforts dus aux lames" (Development of International Studies on Wave Force). Technical Report 7, Annales des Ponts et Chaussee's, July 1938. Translated by U.S. Army Engineer Waterways Experiment Station Research Center, Vicksburg, Miss., Tr. No. 40-13, May 1940.

[19] R. A. Bagnold. "Interim Report on Wave Pressure Research". Journal, Institution of Civil Engineering, London, June 1938-1939.

[20] M. A. Hall. "Laboratory Study of Breaking Wave Forces on Piles". Technical Memorandum 106, Beach Erosion Board, August 1958.

[21] C.W. Ross. "Laboratory study of shock pressures of breaking waves", 1955. TM 59.

[22] C.W. Ross. "Large-scale tests of wave forces on piling", 1959. TM 111.

[23] Y. Goda, S. Haranaka, M. Kitahata. "Study of Impulsive- Breaking Wave Forces on Piles". Report 6, Port and Harbor Research Institute, Ministry of Transport, Japan, 1966.

[24] T. Sawaragi, M. Nochino, editor. *"Impact forces of nearly breaking waves on a vertical circular cylinder"*, volume 27, Japan, 1984. Coastal Engineering.

[25] H. Wagner. "Uber stoss-und gleitvorgange an der oberflache von flussigkeiten", 1932.

[26] Th. Von Karman. "The impact on sea plane float during landing", 1929.

[27] K. Tanimoto, S. Takahashi, T. Kaneko, K. Shiota, editor. *"Impulsive breaking wave forces on an inclined pile exerted by random waves"*. Proc. 20th Intern. Conf. on Coastal Eng, 1986.

[28] J. Wienke, H. Oumeraci, editor. *"Breaking wave impact force on vertical and inclined slender pile- theoretical and large-scale model investigations"*. Coastal Engineering 52, 2005.

[29] X. Ros. "Impact forces from plunging breaking waves on a vertical pile", Master thesis, technical. Technical report, University of Catalonia, Barcelona, Spain, 2011. Carried out at the Department of Civil and Transport Engineering, NTNU, Trondheim, Norway, under the Erasmus Socrates student exchange program.

[30] Ø. Arntsen, X. Ros, A. Tørum, editor. *"Impact forces on vertical pile from plunging breaking waves"*, Japan, 2011. Proc. International Conference on Coastal Structures.

[31] Y. Goda, S. Haranaka, M. Kitahata. "Study of impulsive breaking wave forces on piles". Technical Report 6, Rept. of Port and Harbour Res. Inst., 1966. in Japanese.

[32] N. C. Ushanth. "Wave slamming forces on truss structures for wind turbines". Technical report, Norwegian University of Science and Technology, Trondheim, 2013. Erasmus Mundus M.Sc. program, Coastal and Marine Engineering and Management.

[33] E. P. D Mansard, E.R. Funke, editor. *"A new approach to transient wave generation"*. Coastal Engineering, 1982.

[34] E.R. Funke, E. P. D Mansard. "On the Synthesis of realistic sea states in a laboratory flume". Technical report, Report LTR-HY-66, National Research Council, Canada, 1979.

[35] E.R. Funke, E. P. D Mansard. "SPLSH A Program for the Synthesis of Episodic Waves". Technical report, Hydraulics Laboratory Technical Report LTR-HY-65, National Research Council, Ottawa, Canada, 1979.

[36] W.J. Pierson, L. Moskowitz, editor. *"A Proposed Spectral Form for Fully Developed Wind Seas Based on Similarity The- ory of S.A. Kitaigorodskii"*. Journal of Geophysical Research, 1964.

[37] K. Hasselmann et al. "Measurements of Wind-Wave Growth and Swell Decay during The Joint North Sea Wave Project (JONSWAP)". Technical Report 12, Deutschen Hydro-graphischen Institut, Hamburg, Germany, 1973.

[38] M. Donelan, J. Hamilton, W. H. Hui, editor. *"Directional spectra of wind generated waves"*, London, A 315, 1985. Philosophical Transactions of Royal Society.

[39] Y. Toba, editor. *"Local balance in the air-sea boundary processes, III. On the spectrum of wind waves"*, volume 29, Japan, 1973. J. Oceanogr. Soc.

[40] K. Torsethaugen. "Model for Double Peaked Wave Spectrum". Rep. no. stf22 a96204, SINTEF Civil and Envir. Engineering, Trondheim, Norway, 1996.

[41] K. Torsethaugen, S.K. Haver, editor. *"Simplified Double Peak Spectral Model for Ocean Waves"*, Toulon, France, May 2004. Proceedings of the Fourteenth International Offshore and Polar Engineering Conference.

[42] N. Nordenstrøm. "Combining contours of significant wave height and peak period with platform response distributions for predicting design response". Technical report 81, Det Norske Veritas, Oslo, 1973.

[43] Karl Pearson. Contributions to the mathematical theory of evolution, 1894.

[44] Karl V. Bury. *Statistical models in applied science*. Wiley, London, 1975.

[45] E. M. Bitner-Gregersen. "Joint Long Term Distribution of Hs, Tp", Appendix. Report 87-31, Det Norske Veritas, Høvik, 1988. Probabilistic Calculation of Design Criteria for Ultimate Tether Capacity of Snorre TLP" by Madsen, H. O., Rooney, P., and Bitner-Gregersen, E. M.

[46] G.Z. Forristall. "Wave Crest Distributions: Observations and Second-Order Theory". Technical Report 8, Journal of Physical Oceanography, 2000.

[47] E. J. Gumbel. "Statistical Theory of Extreme Values and Some Practical Applications: Applied Mathematics Series". *National Bureau of Standards*, 1954.

[48] E. J. Gumbel. *Statistics of extremes*. Columbia University Press, New York, 1958.

[49] Sverre Haver. Oral communication, January 2016.

[50] Sverre Steen. *Lecture notes TMR7 Experimental Methods in Marine Hydrodynamics*. Faculty of Engineering Science and Technology – NTNU Norwegian University of Science and Technology, Trondheim, August 2014.

[51] F. Biésel et F. Suquet. Les appareils generateurs de houle en laboratoire. *La Houille Blanche*, 6(2):147–165, 1951.

[52] Carl M. Larsen. *Kompendium TMR4182 Marin Dynamikk*. NTNU trykk, Kompendieforlaget, NTNU, Trondheim, Januar 2014.

[53] I.R. Young, editor. *"The determination of spectral parameters from significant wave height and peak period"*, volume 19. Ocean Engineering, 1992.

[54] John N. Newman. *Marine Hydrodynamics*. MIT Press, Cambridge, 1977.

[55] Trygve Kristiansen. Oral communication, January 2016.

[56] R. Miche, editor. *"Le pouvoir reflechissant des ouvrages maritime exposes a l'action de la houle"*. Annales Punts et Chaussees 121, 1951.

[57] J.A. Battjes, J.P.F.M. Janssen, editor. *"Energy loss and set-up due to breaking of random waves"*, Hamburg, Germany, 1978. Proceedings of 16th Conference on Coastal Engineering.

[58] J.D. Fenton, editor. *"A fifth-order Stokes theory for steady waves"*, Toulon, France, 1985. J. Waterway Port Coastal and Ocean Engineering 111.

[59] John D. Fenton. Coastal and Ocean Engineering - Steady water waves Use of the programs FOURIER, CNOIDAL and STOKES for steady waves, 2015.

[60] J.R. Morison, M.P. O'brien, J.W. Johnson, S.A. Schaaf, editor. *"The force exerted by surface waves on piles"*, volume 189. Petroleum Trans., 1950.

[61] O.T. Gudmestad. *Marine Technology and Operations Theory and Practice*. WIT Press, 2015.

[62] T. J. DiCiccio, Bradley Efron, editor. *"Bootstrap confidence intervals"*, volume 11. Statistical Science, 1996.

[63] A. C. Davison, D. V. Hinkley. *Bootstrap Methods and their Application*. Cambridge Series in Statistical and Probabilistic Mathematics, Cambridge University Press, October 1997.

[64] S.A. Azarmsa, T. Yasuda, H. Mutsuda, editor. *"Cause and Characteristics of Impact Pressure exerted by Spilling and Plunging Breakers on a Vertical Wall"*. Coastal Engineering, 1996.

Appendix A

Assignment description

It is generally expected that wave breaking is not very important regarding global design of slender structures, e.g. jackets and jack-ups where member diameters in the breaking zone could be 2-3m or less. In this master thesis one shall investigate if breaking waves are of more importance for a pile structure with a diameter the order of 6-8m. The global response, bases shear and overturning moment, shall be investigated by planning a proper model test in "Lilletanken". One shall use an existing pile model. Thus the model scale is given by requiring that the full scale diameter of the pile is within 6-8m. The full scale water depth will then be given by the water depth in Lilletanken. The purpose of this thesis is to investigate breaking wave impacts may influence the global responses of the structure, i.e. proper estimates for the quasi-static characteristic base shear and over turning moment shall be estimated by neglecting breaking waves and by properly accounting for breaking waves.

The necessary weather information will be given by the Norwegian hindcast data base, NORA10, giving weather characteristics every 3 hours from 1957 – 2014. Below a possible division into sub-tasks is given.

1. Establish metocean conditions for the site – either by reassessing the conditions established in the project work or prepare from a NORA10 location with a depth close the selected full scale depth.

2. Assuming that the pile structure behaves essentially quasi-statically, one can use the design wave method to get a first idea of the base shear and overturning moment. Use a Stokes 5th profile determined such that the crest height of the Stokes 5th wave height agrees with the q-probability crest height. Do the calculations in model scale and determine proper hydrodynamic coefficients to be used in model scale.

3. Plan the model test to be performed in Lilletanken. It is important that we know the wave conditions the pile is facing. Thus the first phase of the model test is to run the wave conditions which will be used for assessing pile loading prior to installing.

- Assess the reflection coefficients for the tank layout for a range of heights and periods.
- One should prepare regular wave conditions.
- One shall prepare irregular sea conditions corresponding both to 10- 2 and 10– 4 annual exceedance probability.
- During this first phase one shall also prepare some wave groups that are designed such that they will break more or less violently at the position of the pile.

4. Install the pile in the basin. An investigate the properties of the pile structure. Prepare a simple model for estimating the local loads from the breaking waves. (We are not measuring the impact load, we are measuring the response to an impact load.) Prepare a simple structural model where you can estimate how the impact load must look like in order to obtain a measured base shear and overturning moment. (This can of course be done after the model test is completed.)

5. Perform the model test with both regular waves and irregular waves. The test must be done such that we have a sufficient number of repeats to estimate q-probability loads using the metocean contour method.

   - Do tests with regular Stokes waves for both ULS and ALS.
   - Do irregular sea tests utilizing environmental contour method both for ULS and ALS sea states.
   - Do a special tests of breaking waves using the wave groups prepared during the calibration phase.

6. Post processing of model tests results.

   - How important is breaking waves? For global loads and local impact loads?

The candidates may of course select another scheme as the preferred approach for solving the requested problem. They may also involve other subjects than those mentioned above if found to be important for answering the overall question: Is breaking wave impacts important regarding the design of the pile structure.

Supervisor: Sverre Haver, NTNU.

Appendix B

Metocean

B.1 Scatter diagram

B.1.1 Waves from North

Hs \ Tp		0	1	2	3	4	5	6	7	8	9	10	11	12	13	14	15	16	17	18	19	sum
		1	2	3	4	5	6	7	8	9	10	11	12	13	14	15	16	17	18	19	20	
0.0	0.5	0	1	18	109	16	38	48	28	25	30	13	4	2	3	5	0	0	0	0	0	340
0.5	1.0	0	6	76	764	1520	1534	1111	819	577	348	214	110	67	28	17	11	4	0	3	0	7209
1.0	1.5	0	0	13	353	1343	2426	2833	2356	1849	1140	553	274	114	50	37	13	6	2	1	0	13363
1.5	2.0	0	0	0	6	398	1710	2169	2260	1877	1754	1062	514	195	77	39	8	4	0	0	0	12073
2.0	2.5	0	0	0	0	22	505	1691	1742	1376	1101	1039	610	295	103	37	11	7	0	0	0	8539
2.5	3.0	0	0	0	0	0	45	695	1389	1087	675	539	513	276	126	49	9	6	1	0	0	5410
3.0	3.5	0	0	0	0	0	6	155	708	937	623	359	284	192	107	44	18	7	2	1	0	3443
3.5	4.0	0	0	0	0	0	1	14	246	697	612	269	171	131	73	29	14	7	3	0	0	2267
4.0	4.5	0	0	0	0	0	0	1	58	347	522	315	148	75	32	42	10	6	1	0	0	1557
4.5	5.0	0	0	0	0	0	0	0	9	106	381	301	121	43	24	25	6	2	0	0	0	1018
5.0	5.5	0	0	0	0	0	0	0	1	22	228	298	130	36	15	13	6	3	0	0	0	752
5.5	6.0	0	0	0	0	0	0	0	0	7	99	234	123	56	10	7	0	1	0	0	0	537
6.0	6.5	0	0	0	0	0	0	0	0	1	9	110	121	62	9	5	6	2	0	0	0	325
6.5	7.0	0	0	0	0	0	0	0	0	1	3	49	107	77	17	3	0	0	0	0	0	257
7.0	7.5	0	0	0	0	0	0	0	0	0	1	11	51	45	16	3	1	0	0	0	0	128
7.5	8.0	0	0	0	0	0	0	0	0	0	0	4	32	25	15	3	0	0	0	0	0	79
8.0	8.5	0	0	0	0	0	0	0	0	0	0	0	13	13	15	8	1	1	0	0	0	51
8.5	9.0	0	0	0	0	0	0	0	0	0	0	0	3	11	14	4	1	0	0	0	0	33
9.0	9.5	0	0	0	0	0	0	0	0	0	0	0	1	3	6	7	5	0	0	0	0	22
9.5	10.0	0	0	0	0	0	0	0	0	0	0	0	0	8	6	4	0	0	0	0	0	18
10.0	10.5	0	0	0	0	0	0	0	0	0	0	0	0	2	6	5	1	0	0	0	0	14
10.5	11.0	0	0	0	0	0	0	0	0	0	0	0	0	0	0	2	0	0	0	0	0	2
11.0	11.5	0	0	0	0	0	0	0	0	0	0	0	0	0	0	5	1	0	0	0	0	6
11.5	12.0	0	0	0	0	0	0	0	0	0	0	0	0	0	0	2	0	0	0	0	0	2
	sum	0	7	107	1232	3299	6265	8717	9616	8909	7526	5370	3330	1728	752	395	122	56	9	5	0	57445

Figure B.1: Scatter diagram for waves propagating from north.

B.1.2 Waves from South

Hs	Tp	0 1	1 2	2 3	3 4	4 5	5 6	6 7	7 8	8 9	9 10	10 11	11 12	12 13	13 14	14 15	15 16	16 17	17 18	sum
0.0	0.5	0	2	18	65	3	0	1	3	2	2	0	0	0	0	0	0	0	0	96
0.5	1.0	0	5	114	1167	1176	278	53	29	19	7	9	7	6	2	1	2	0	0	2875
1.0	1.5	0	0	18	793	2970	2273	562	89	52	41	21	4	6	4	3	1	1	0	6838
1.5	2.0	0	0	0	40	1289	2905	1550	349	46	29	20	14	14	5	2	3	0	0	6266
2.0	2.5	0	0	0	0	100	1551	2098	777	128	27	11	9	2	1	2	0	1	0	4707
2.5	3.0	0	0	0	0	6	331	1543	1120	288	29	9	5	3	1	0	0	0	0	3335
3.0	3.5	0	0	0	0	1	17	613	1174	486	54	4	2	1	0	0	1	0	0	2353
3.5	4.0	0	0	0	0	0	1	143	817	629	111	5	0	1	0	1	1	0	0	1709
4.0	4.5	0	0	0	0	0	0	18	351	627	167	14	0	0	0	0	0	0	0	1177
4.5	5.0	0	0	0	0	0	0	1	93	491	204	18	0	0	0	1	0	0	0	808
5.0	5.5	0	0	0	0	0	0	0	12	244	231	36	3	0	0	0	0	0	0	526
5.5	6.0	0	0	0	0	0	0	0	4	66	236	54	1	0	0	0	0	0	0	361
6.0	6.5	0	0	0	0	0	0	0	0	8	107	46	5	0	0	0	0	0	0	166
6.5	7.0	0	0	0	0	0	0	0	0	0	35	35	6	0	0	0	0	0	0	76
7.0	7.5	0	0	0	0	0	0	0	0	0	5	28	2	0	0	0	0	0	0	35
7.5	8.0	0	0	0	0	0	0	0	0	0	3	11	5	0	0	0	0	0	0	19
8.0	8.5	0	0	0	0	0	0	0	0	0	0	3	6	0	0	0	0	0	0	9
8.5	9.0	0	0	0	0	0	0	0	0	0	0	1	2	0	0	0	0	0	0	3
	sum	0	7	150	2065	5545	7356	6582	4818	3086	1288	325	71	33	13	10	8	2	0	31359

Figure B.2: Scatter diagram for waves propagating from south.

B.1.3 Waves from West

Hs	Tp	0 1	1 2	2 3	3 4	4 5	5 6	6 7	7 8	8 9	9 10	10 11	11 12	12 13	13 14	14 15	15 16	16 17	17 18	18 19	19 20	20 21	sum
0.0	0.5	0	2	30	84	11	8	11	11	10	17	4	2	3	5	0	1	1	0	0	0	0	200
0.5	1.0	0	3	160	1275	1256	275	144	129	123	135	90	63	38	31	20	23	14	6	1	1	1	3788
1.0	1.5	0	0	25	668	2393	2540	781	348	295	225	148	99	68	39	26	24	17	10	2	2	0	7710
1.5	2.0	0	0	0	43	890	3192	2167	554	271	220	169	108	75	47	33	19	12	4	1	0	0	7805
2.0	2.5	0	0	0	0	126	1403	2837	1317	330	206	165	95	51	41	15	11	10	3	4	0	0	6614
2.5	3.0	0	0	0	0	1	265	1888	1997	524	151	79	63	52	13	7	4	1	0	0	0	0	5045
3.0	3.5	0	0	0	0	0	29	763	2050	887	170	61	39	34	22	5	3	1	0	0	0	0	4064
3.5	4.0	0	0	0	0	0	4	157	1284	1114	255	47	29	13	10	7	1	1	0	1	0	0	2923
4.0	4.5	0	0	0	0	0	0	25	495	1165	374	61	15	4	6	4	1	1	1	1	0	0	2153
4.5	5.0	0	0	0	0	0	0	2	111	809	479	80	12	5	1	3	0	1	0	0	0	0	1503
5.0	5.5	0	0	0	0	0	0	0	13	328	452	132	16	2	1	2	1	0	0	0	0	0	947
5.5	6.0	0	0	0	0	0	0	0	1	62	399	148	24	2	1	0	0	0	0	0	0	0	637
6.0	6.5	0	0	0	0	0	0	0	0	7	200	145	40	1	1	0	0	0	0	0	0	0	394
6.5	7.0	0	0	0	0	0	0	0	0	1	48	133	41	5	0	1	0	0	0	0	0	0	229
7.0	7.5	0	0	0	0	0	0	0	0	0	11	88	27	8	1	2	0	0	0	0	0	0	137
7.5	8.0	0	0	0	0	0	0	0	0	0	3	29	25	10	1	0	0	0	0	0	0	0	68
8.0	8.5	0	0	0	0	0	0	0	0	0	0	23	23	15	2	0	0	0	0	0	0	0	63
8.5	9.0	0	0	0	0	0	0	0	0	0	0	3	16	10	3	0	0	0	0	0	0	0	32
9.0	9.5	0	0	0	0	0	0	0	0	0	0	0	13	5	3	0	0	0	0	0	0	0	21
9.5	10.0	0	0	0	0	0	0	0	0	0	0	2	8	3	2	1	0	0	0	0	0	0	16
10.0	10.5	0	0	0	0	0	0	0	0	0	0	0	3	8	3	0	0	0	0	0	0	0	14
10.5	11.0	0	0	0	0	0	0	0	0	0	0	0	1	4	2	0	0	0	0	0	0	0	7
11.0	11.5	0	0	0	0	0	0	0	0	0	0	0	0	3	2	4	0	0	0	0	0	0	9
11.5	12.0	0	0	0	0	0	0	0	0	0	0	0	0	0	3	0	0	0	0	0	0	0	3
	sum	0	5	215	2070	4677	7716	8775	8310	5926	3345	1607	762	419	240	130	88	59	24	10	3	1	44382

Figure B.3: Scatter diagram for waves propagating from west.

B.2 Marginal Distribution of H_S

B.2.1 Waves from North

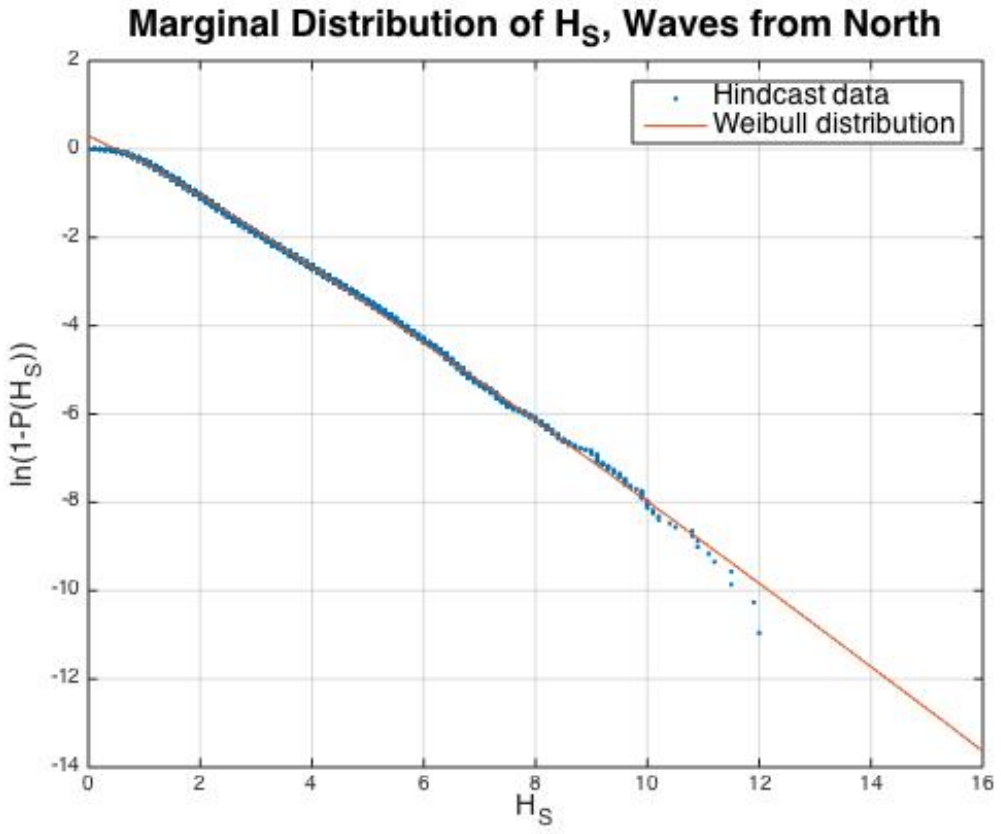

Figure B.4: Marginal distribution of H_S for waves propagating from north.

Table B.1: Estimated parameters for the three parameter Weibull distribution for waves propagating from north.

Parameter	Estimated value
α	1.4240
β	1.0944
λ	0.5020

B.2.2 Waves from South

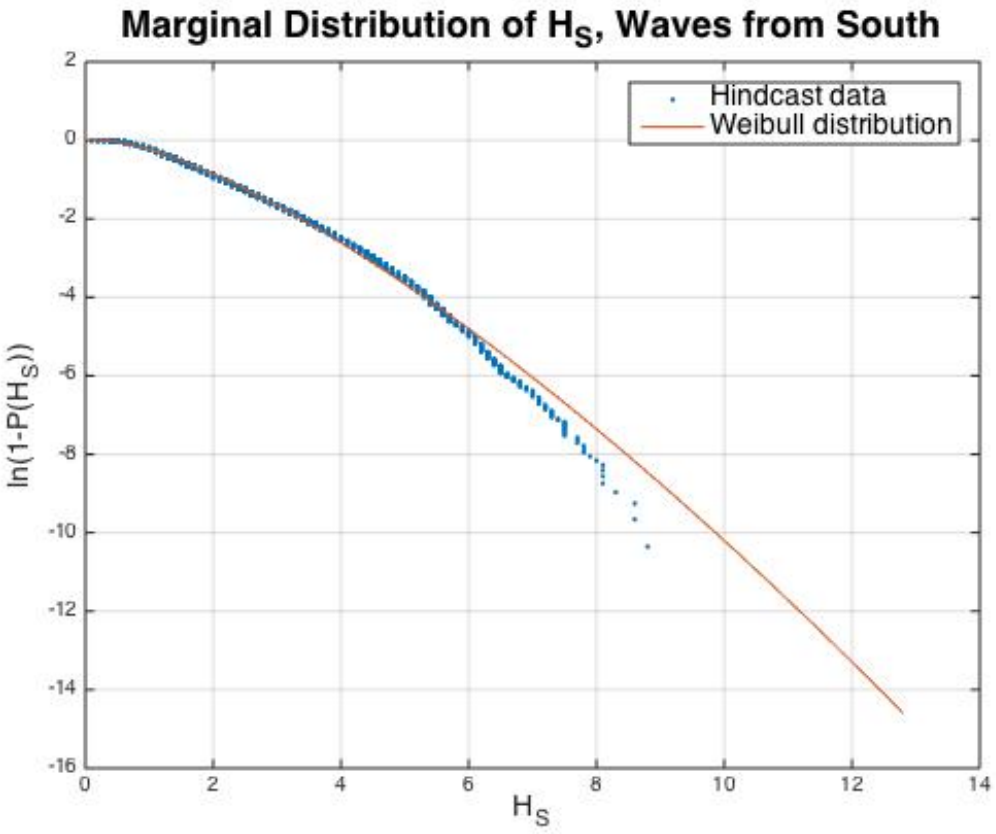

Figure B.5: Marginal distribution of H_S for waves propagating from south.

Table B.2: Estimated parameters for the three parameter Weibull distribution for waves propagating from south.

Parameter	Estimated value
α	1.8595
β	1.4086
λ	0.3287

B.2.3 Waves from West

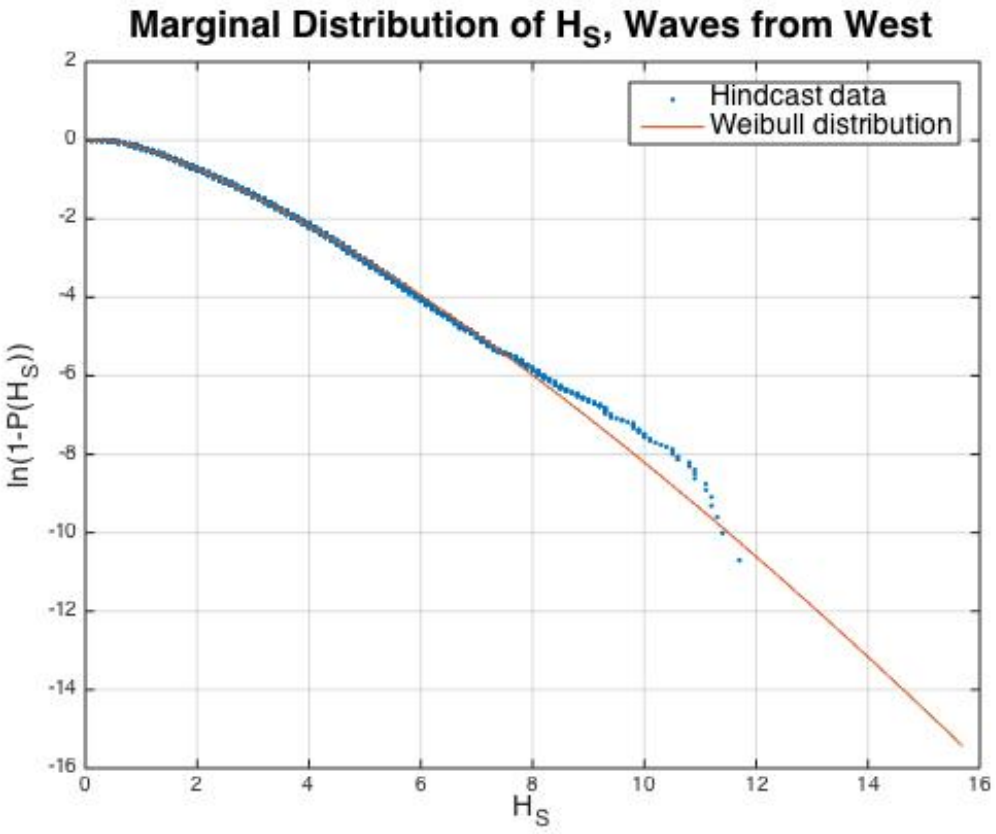

Figure B.6: Marginal distribution of H_S for waves propagating from west.

Table B.3: Estimated parameters for the three parameter Weibull distribution for waves propagating from west.

Parameter	Estimated value
α	2.0375
β	1.3571
λ	0.3869

B.3 Conditional distribution of T_P given H_S

B.3.1 Waves from North

Table B.4: Estimated coefficients for the expected value of $\ln(T_P)$ given H_S for waves propagating from north.

Coefficient	Estimated value
a_0	1.0410
a_1	0.8739
a_2	0.2647

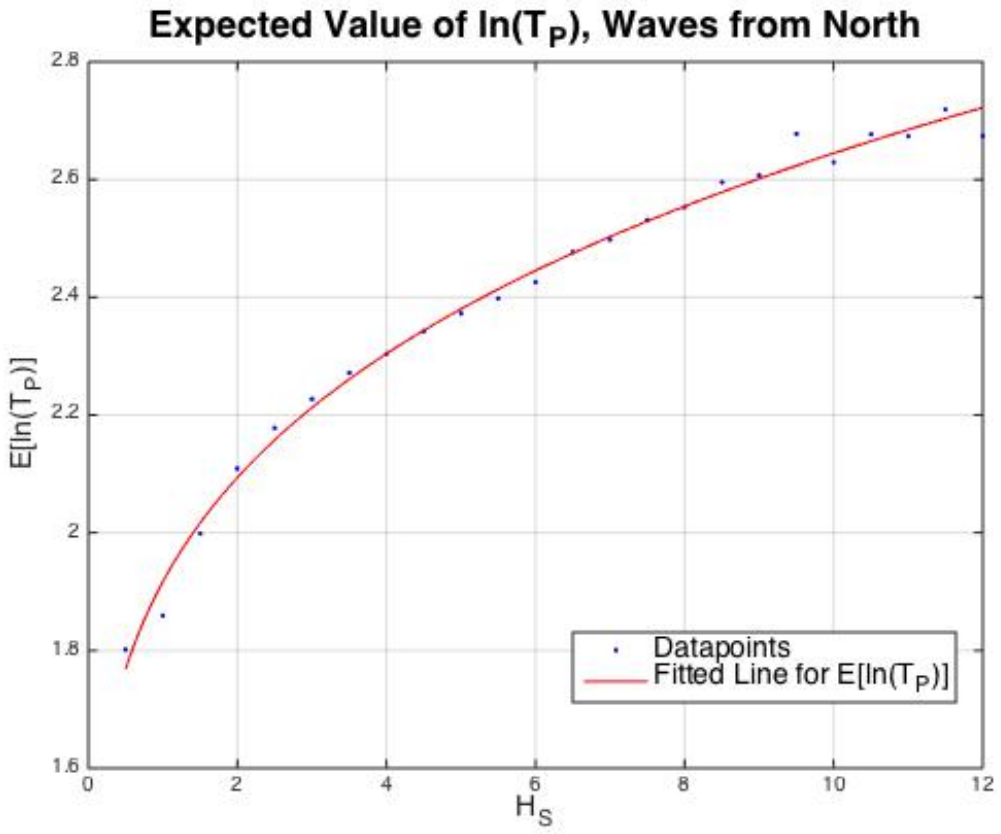

Figure B.7: Curvefitting for the expected value for T_P given H_S for waves propagating from north.

Table B.5: Estimated coefficients for the standard deviation of $\ln(T_P)$ given H_S for waves propagating from north.

Coefficient	Estimated value
b_0	0.0381
b_1	0.3922
b_2	0.3061

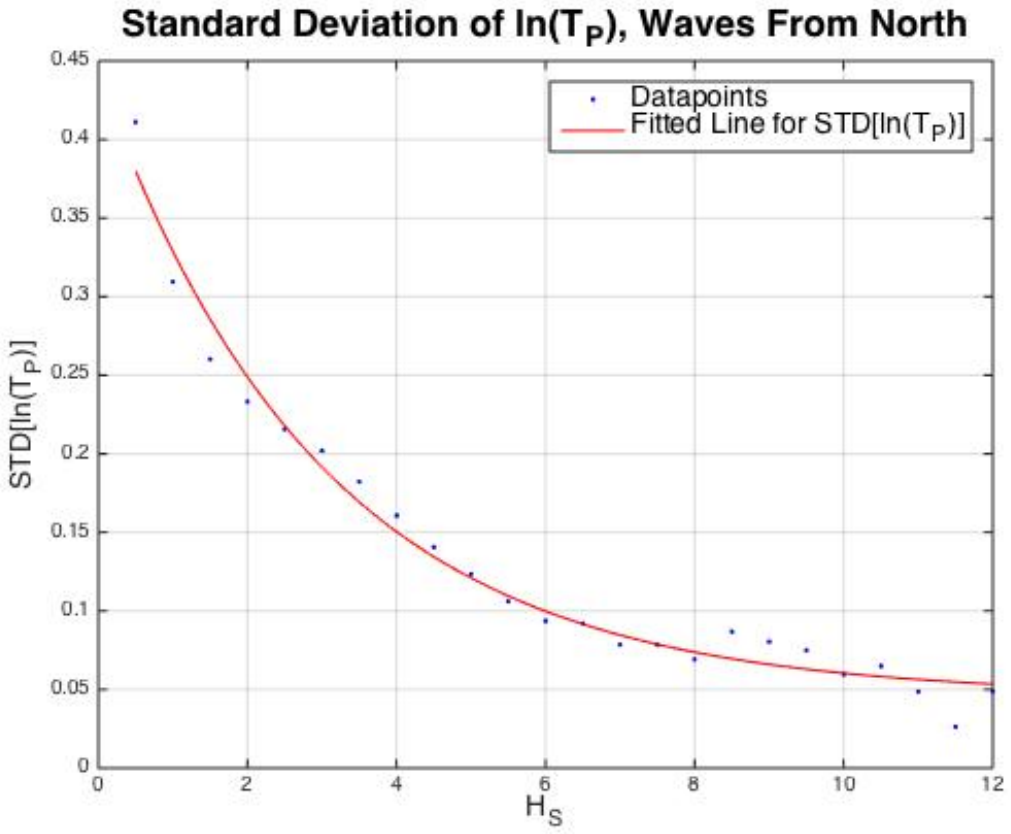

Figure B.8: Curvefitting for the standard deviation for T_P given H_S for waves propagating from north.

B.3.2 Waves from Soth

Table B.6: Estimated coefficients for the expected value of $\ln(T_P)$ given H_S for waves propagating from south.

Coefficient	Estimated value
a_0	-0.1879
a_1	1.7690
a_2	0.1888

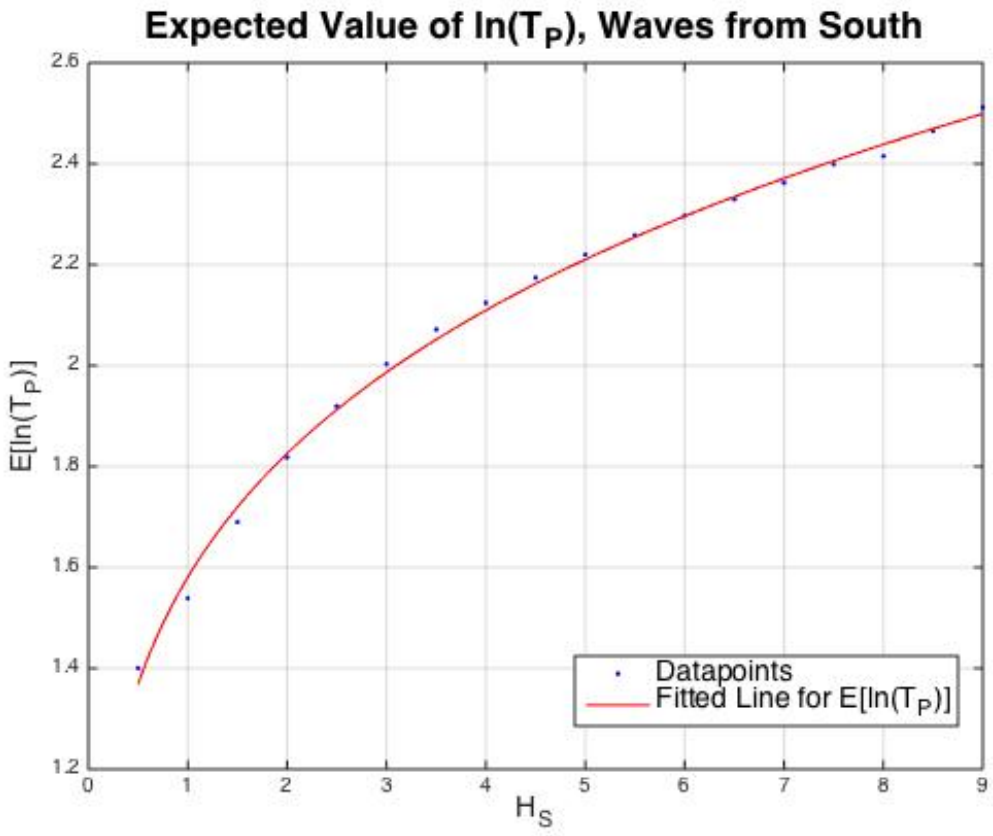

Figure B.9: Curvefitting for the expected value for T_P given H_S for waves propagating from south.

Table B.7: Estimated coefficients for the standard deviation of $\ln(T_P)$ given H_S for waves propagating from south.

Coefficient	Estimated value
b_0	0.0585
b_1	0.2758
b_2	0.5458

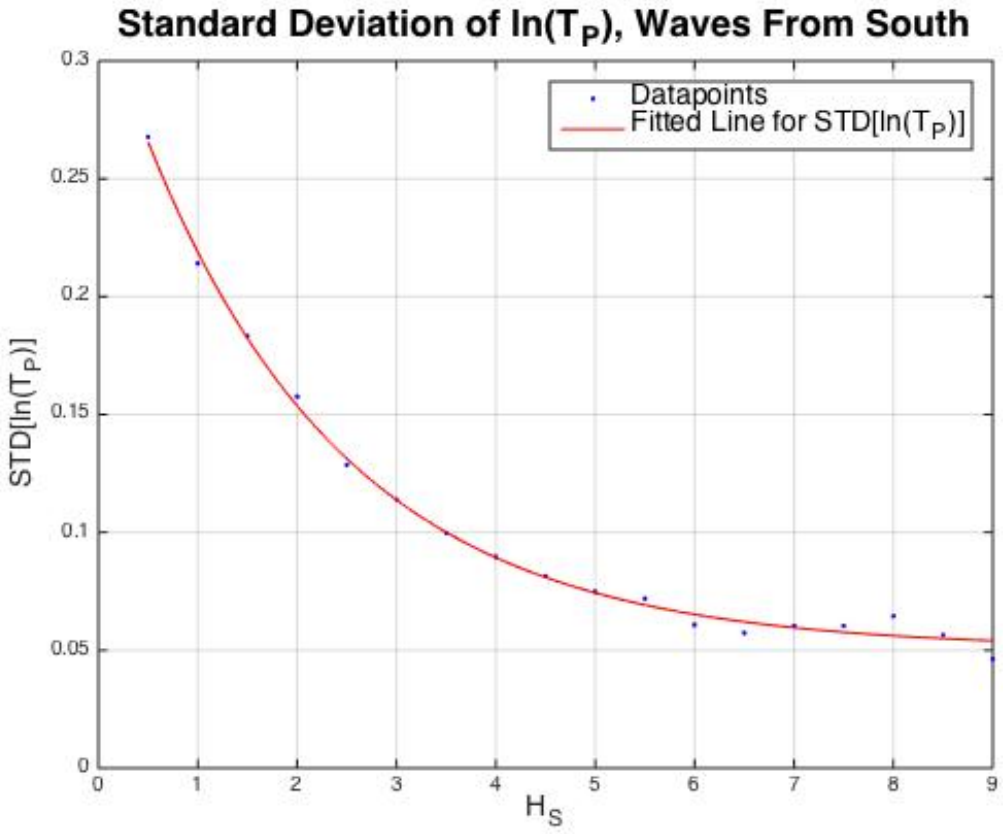

Figure B.10: Curvefitting for the standard deviation for T_P given H_S for waves propagating from soth.

B.3.3 Waves from West

Table B.8: Estimated coefficients for the expected value of $\ln(T_P)$ given H_S for waves propagating from west.

Coefficient	Estimated value
a_0	0.9815
a_1	0.7504
a_2	0.3193

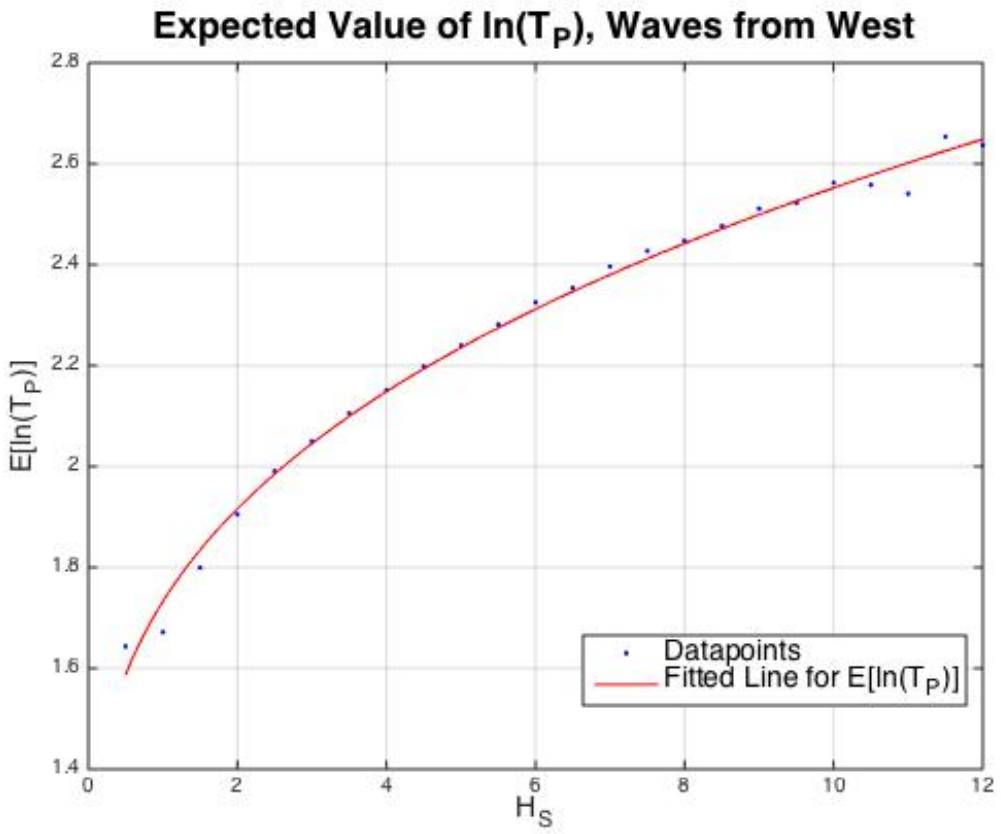

Figure B.11: Curvefitting for the expected value for T_P given H_S for waves propagating from west.

Table B.9: Estimated coefficients for the standard deviation of $\ln(T_P)$ given H_S for waves propagating from west.

Coefficient	Estimated value
b_0	0.0668
b_1	0.5658
b_2	0.6429

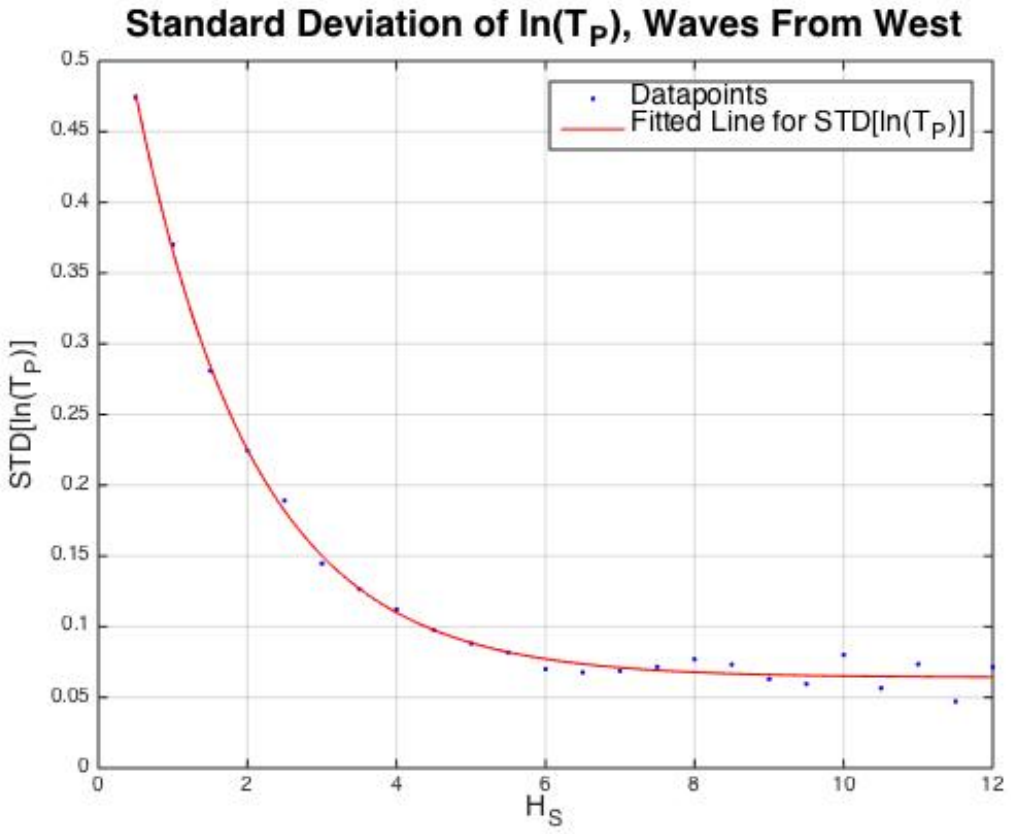

Figure B.12: Curvefitting for the standard deviation for T_P given H_S for waves propagating from west.

B.4 Contour Lines

B.4.1 Waves from North

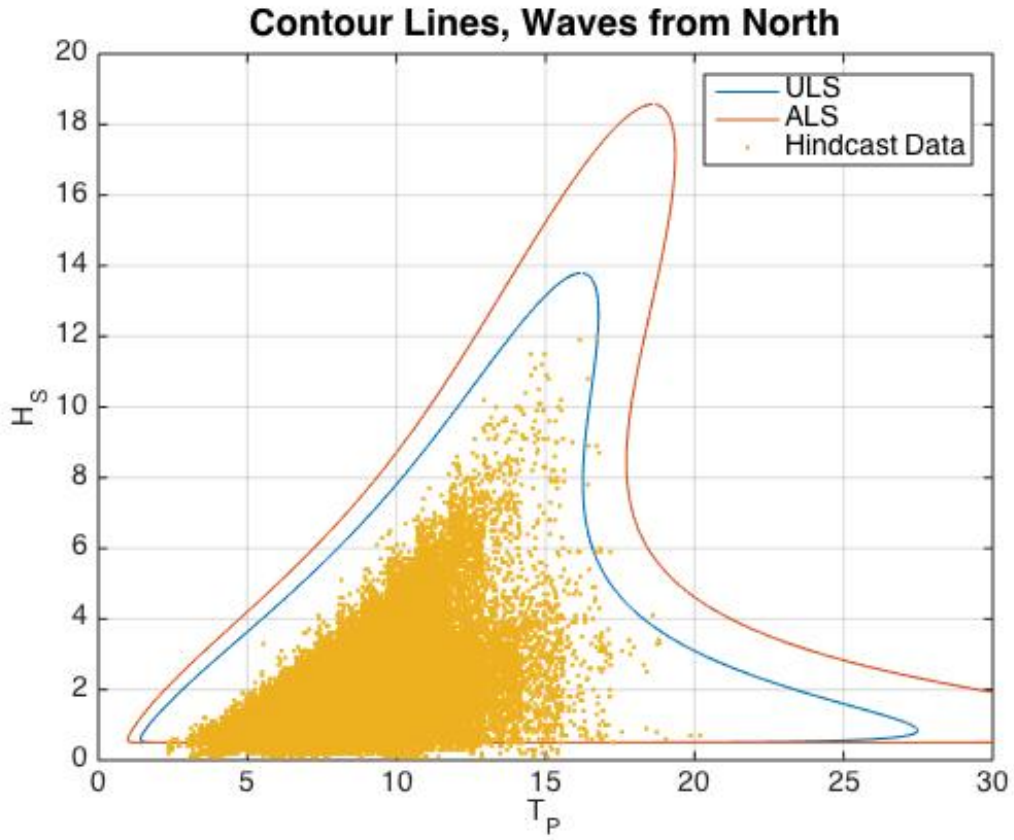

Figure B.13: ULS and ALS contour line for the waves propagating from North.

B.4.2 Waves from South

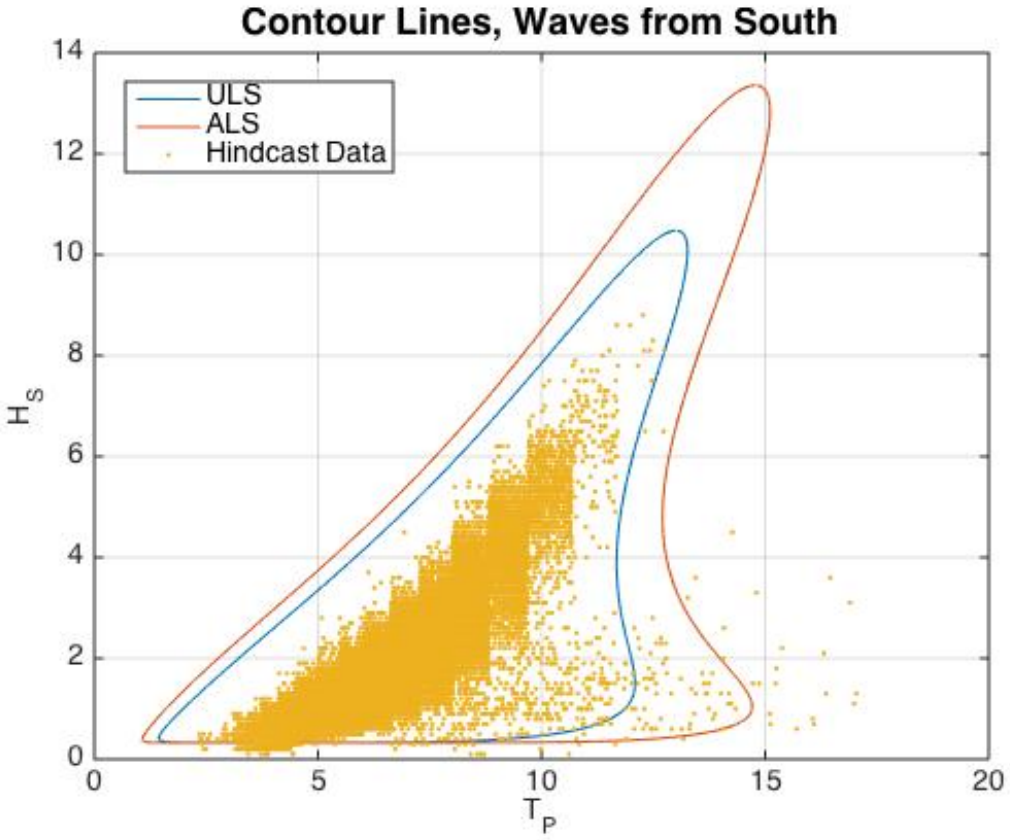

Figure B.14: ULS and ALS contour line for the waves propagating from south.

B.4.3 Waves from West

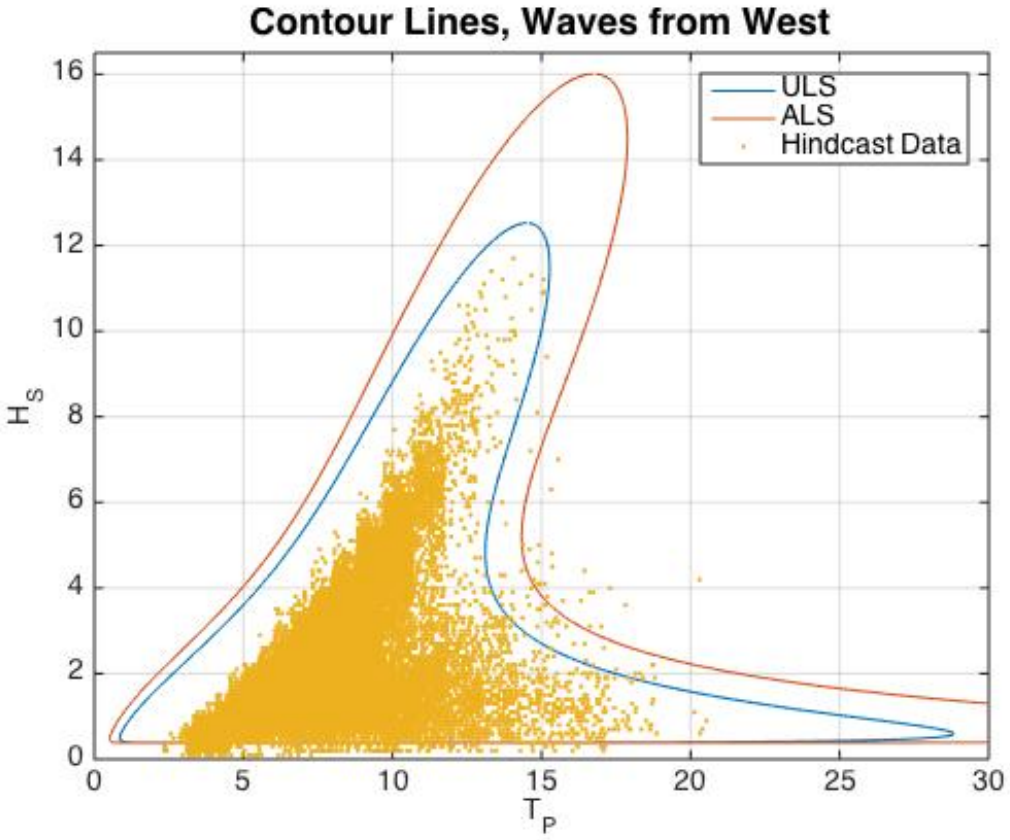

Figure B.15: ULS and ALS contour line for the waves propagating from west.

B.5 Bootstrapping

B.5.1 Waves propagating from North

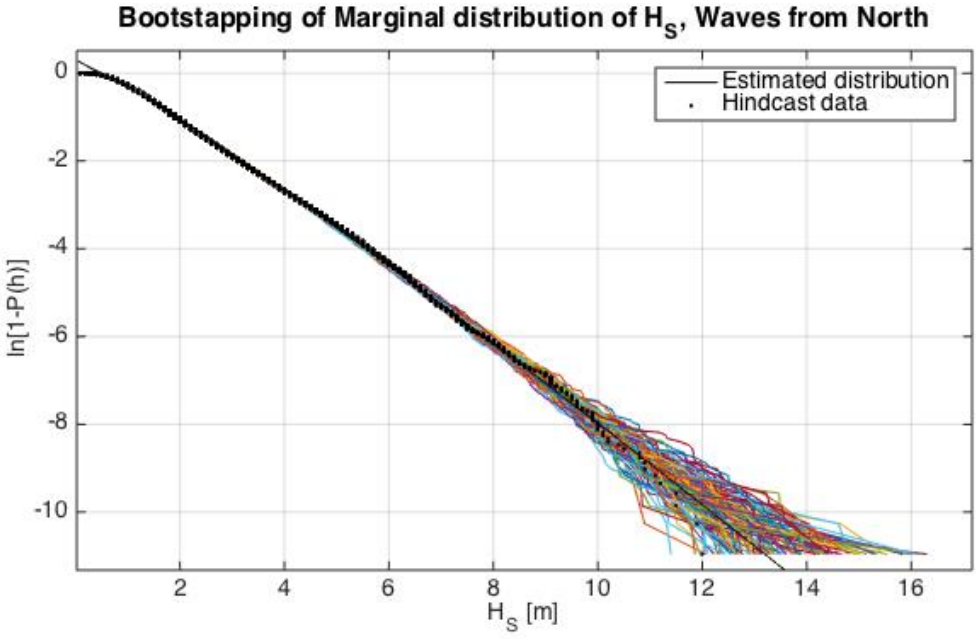

Figure B.16: Bootstrapping by means of Monte Carlo simulation for the marginal distribution of H_S for waves propagating from north.

B.5.2 Waves propagating from South

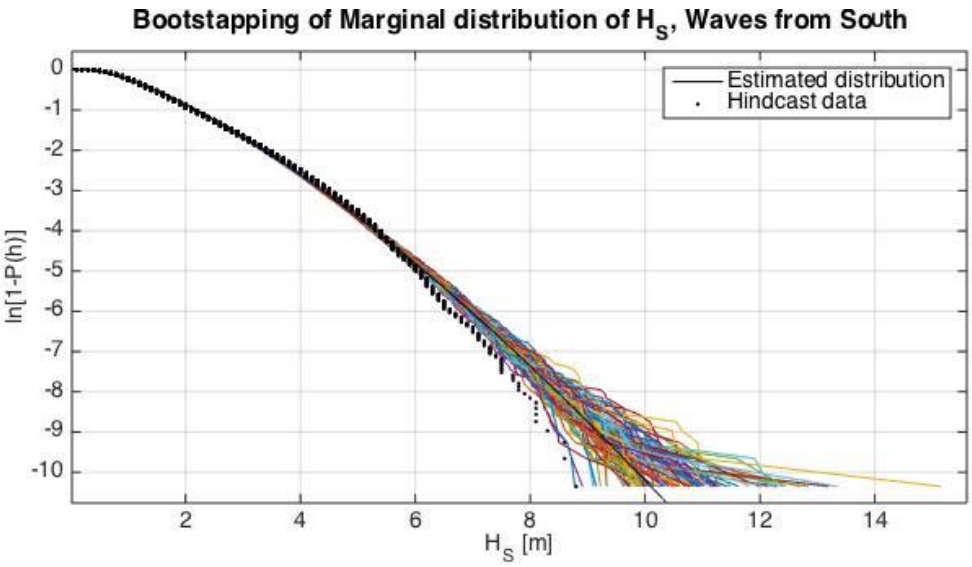

Figure B.17: Bootstrapping by means of Monte Carlo simulation for the marginal distribution of H_S for waves propagating from south.

B.5.3 Waves propagating from West

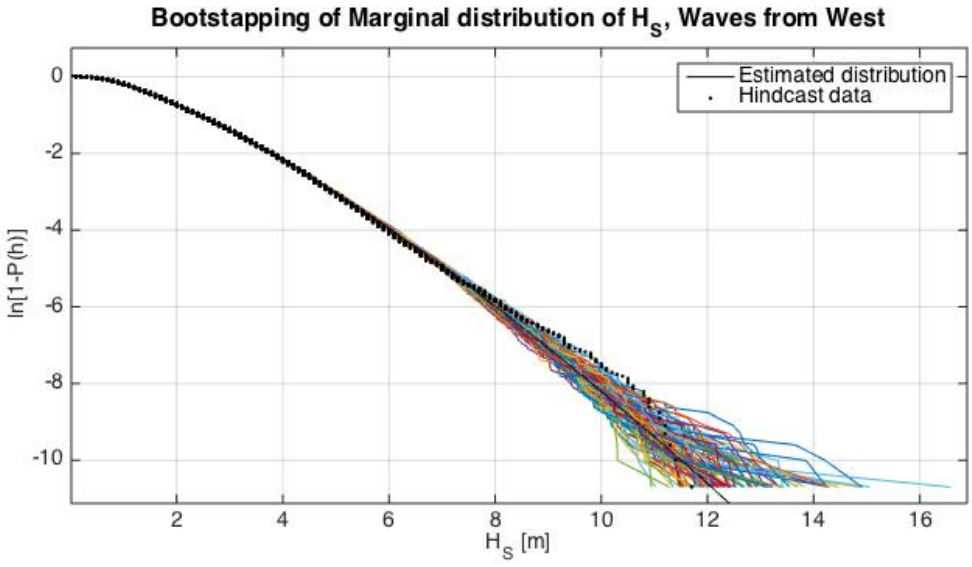

Figure B.18: Bootstrapping by means of Monte Carlo simulation for the marginal distribution of H_S for waves propagating from west.

Appendix C

q-probability waves

C.1 ULS

Table C.1: ULS h_{sq} values with 90 percent bands for t_{pq} and the corresponding largest C_q for waves propagating from north, south, west and total sea.

Direction	h_{sq} [m]	t_{pq} [s]	C_q [m]
North	13.79	16.52 - 17.17	16.25
South	10.48	13.00 - 13.65	12.61
West	12.52	14.48 - 15.35	14.95
ULS	13.26	15.57 - 16.77	15.69

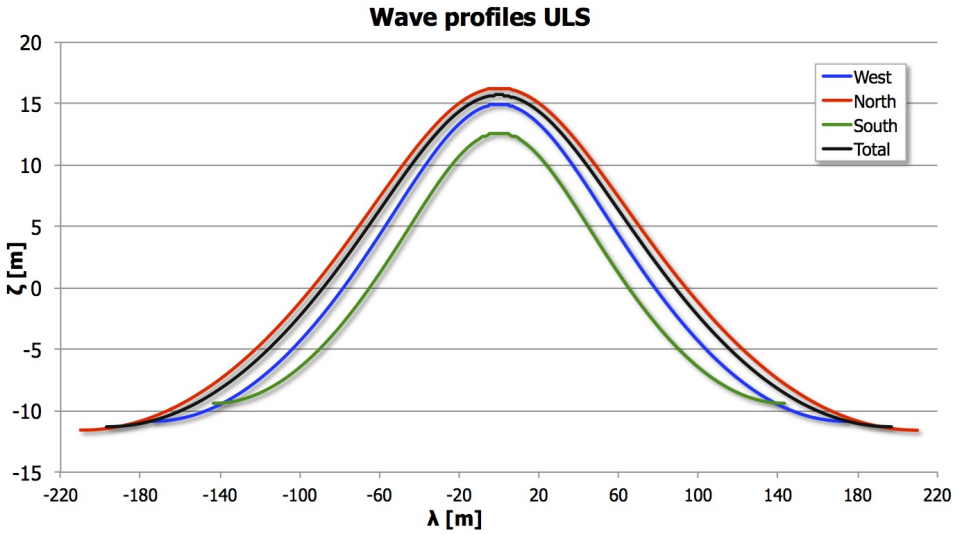

Figure C.1: Wave profile for the ULS q-probability waves.

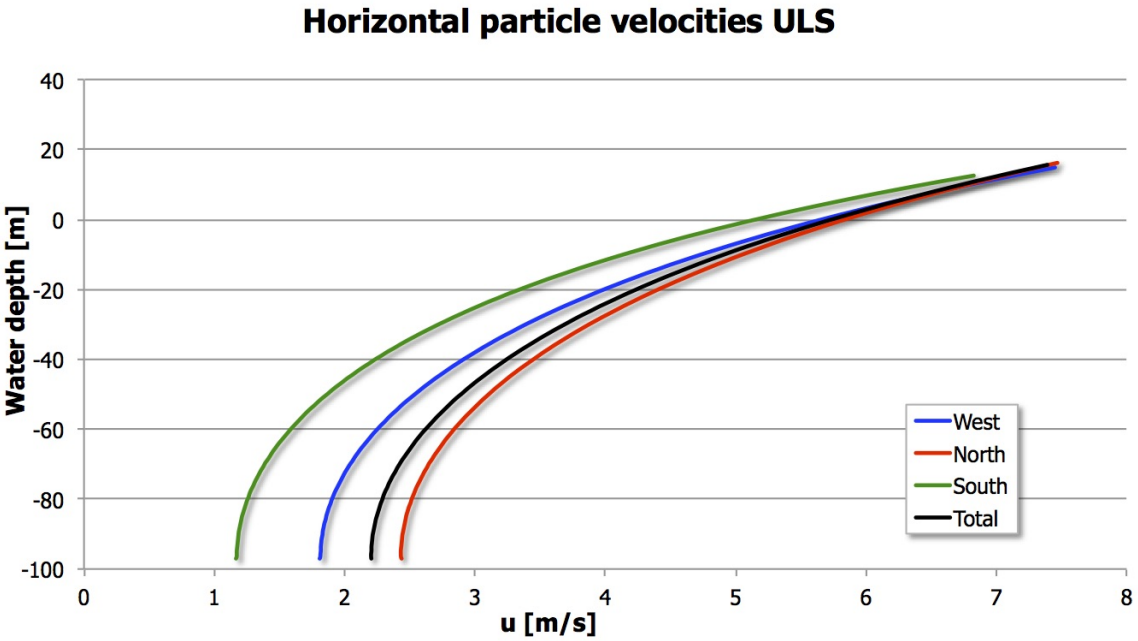

Figure C.2: Horizontal particle velocities for the ULS q-probability waves.

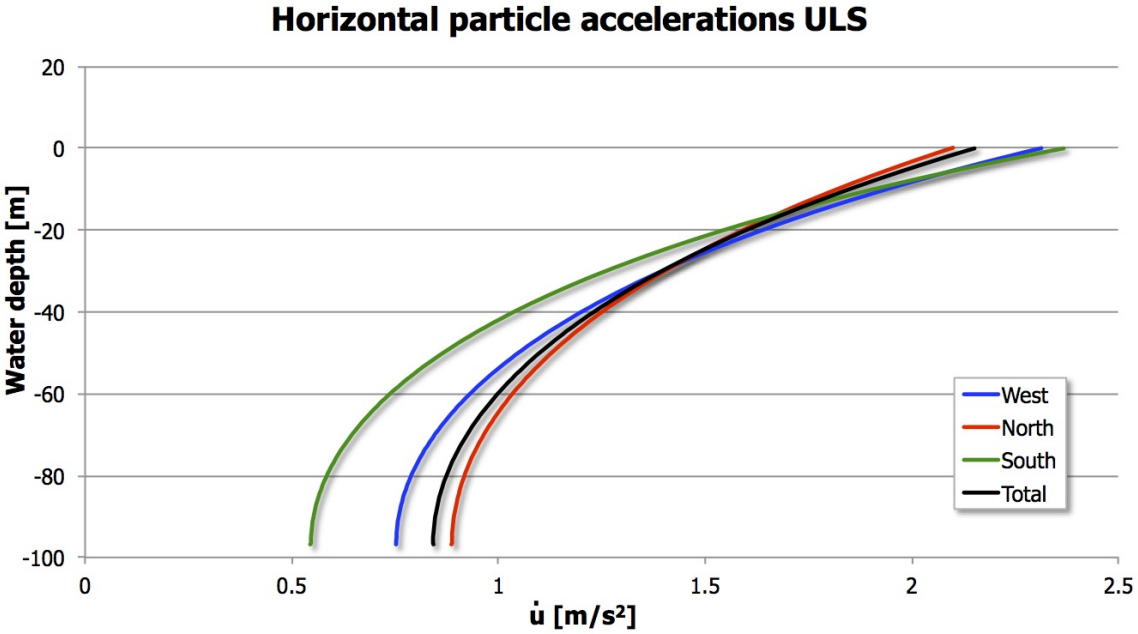

Figure C.3: Horizontal particle accelerations for the ULS q-probability waves.

C.2 ALS

Table C.2: ALS h_{sq} values with 90 percent bands for t_{pq} and the corresponding largest C_q for waves propagating from north, south, west and total sea.

Direction	h_{sq} [m]	t_{pq} [s]	C_q [m]
North	18.57	19.17 - 19.84	22.85
South	13.36	14.75 - 15.48	16.66
West	16.01	16.66 - 17.67	19.85
ALS	16.89	17.88 - 19.25	20.79

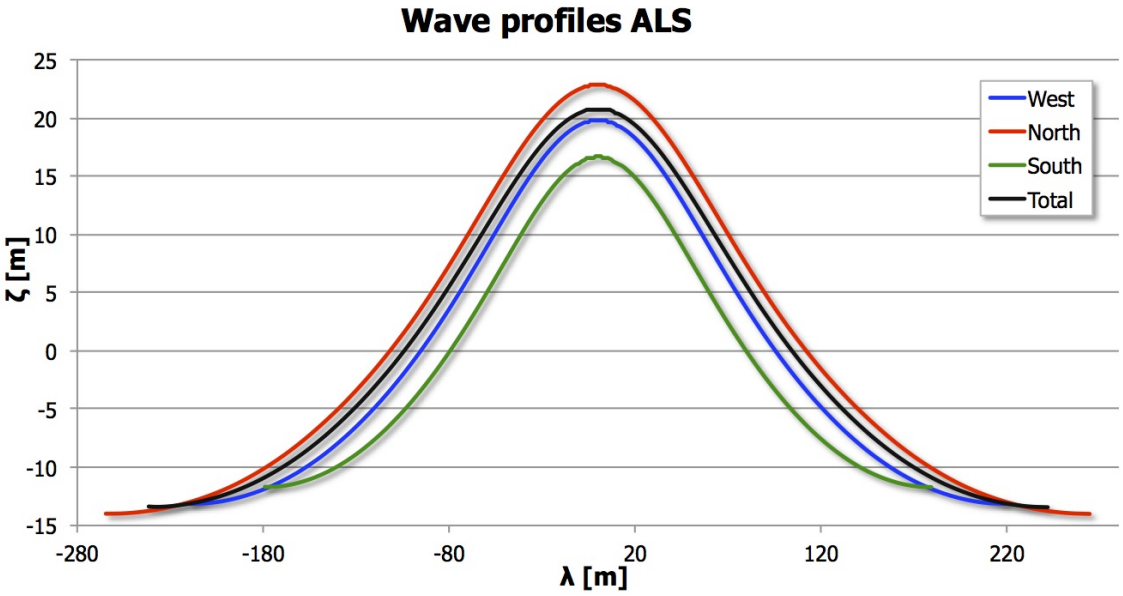

Figure C.4: Wave profile for the ALS q-probability waves.

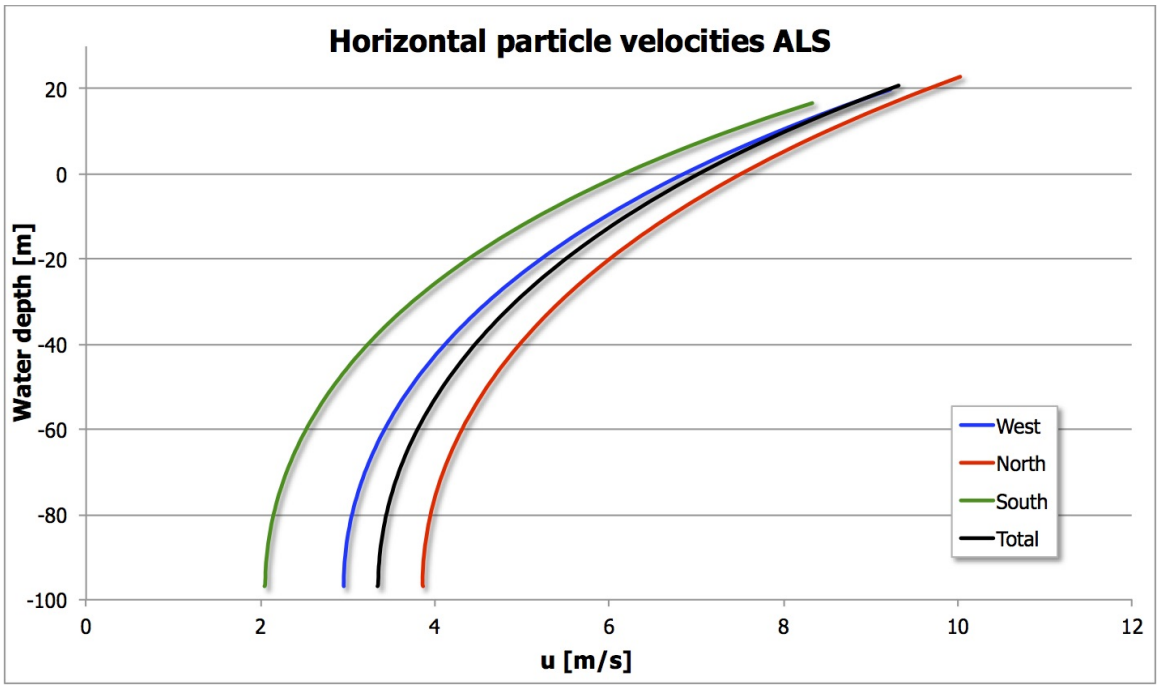

Figure C.5: Horizontal particle velocities for the ALS q-probability waves.

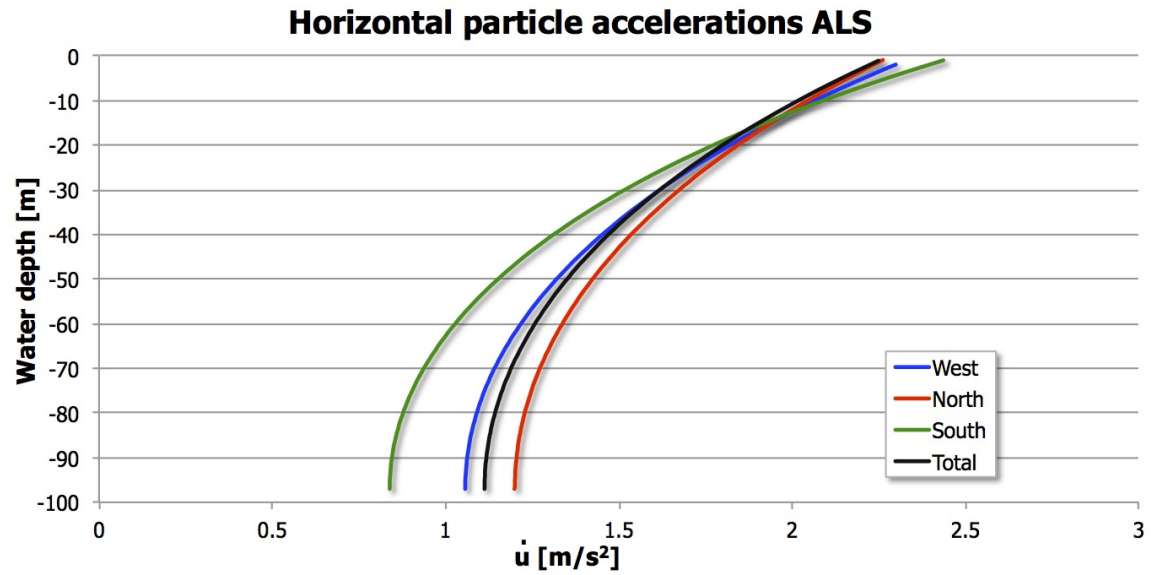

Figure C.6: Horizontal particle accelerations for the ALS q-probability waves.

Appendix D

Critical sea states

D.1 Sea state 1

Table D.1: Input information of sea state 1.

Significant wave height	H_S	10.00	[m]
Spectral peak period	T_P	10.55	[s]
Water depth	h	96.1	[m]
Number of tests	#	10	[-]
Duration of each test	d	1	[h]

Table D.2: Variances and significant waveheights for all 10 tests of sea state 1.

	Without pile		With pile	
Test	σ^2 [m^2]	H_S [m]	σ^2 [m^2]	H_S [m]
1	5.38	9.28	5.65	9.51
2	5.35	9.25	5.52	9.40
3	5.15	9.07	5.68	9.53
4	4.68	8.66	5.14	9.07
5	5.12	9.05	5.25	9.16
6	5.23	9.15	5.44	9.33
7	4.76	8.73	4.99	8.94
8	5.17	9.09	5.43	9.32
9	5.21	9.13	5.40	9.29
10	5.47	9.35	5.67	9.52
avg	5.15	9.08	5.42	9.31

Table D.3: Largest measured crest heights, overturning moment and base shear force for all 10 tests of sea state 1.

Test	C_{max} [m]	$C_{max,pile}$ [m]	F_{max} [MN]	M_{max} [GNm]
1	10.11	11.11	58.71	6.71
2	10.12	11.79	50.76	5.83
3	10.25	9.55	58.78	6.54
4	10.00	10.81	51.56	5.74
5	10.62	10.31	52.14	5.94
6	11.56	10.01	53.17	5.86
7	9.47	11.48	54.06	6.01
8	10.64	9.97	50.41	5.75
9	10.10	8.92	53.39	5.85
10	9.90	10.01	64.49	7.24

Table D.4: Output information of sea state 1.

Variance	σ^2_{out}	5.15	[m^2]	σ^2_{pile}	5.42	[m^2]
Standard deviation	σ_{out}	2.27	[m]	σ_{pile}	2.33	[m]
Significant wave height	$H_{S,out}$	9.08	[m]	$H_{S,pile}$	9.31	[m]
Sea state steepness	ε_{out}	0.0523	[-]	ε_{pile}	0.0537	[-]
Range $\frac{H_{S,min}-H_{S,max}}{H_{S,mean}} \cdot 100$	$\Delta H_{S,out}$	7.60	[%]	$\Delta H_{S,pile}$	6.34	[%]
Deviation from $H_{S,in}$	$\frac{H_{S,out}}{H_{S,in}}$	0.9080	[-]	$\frac{H_{S,pile}}{H_{S,in}}$	0.9310	[-]

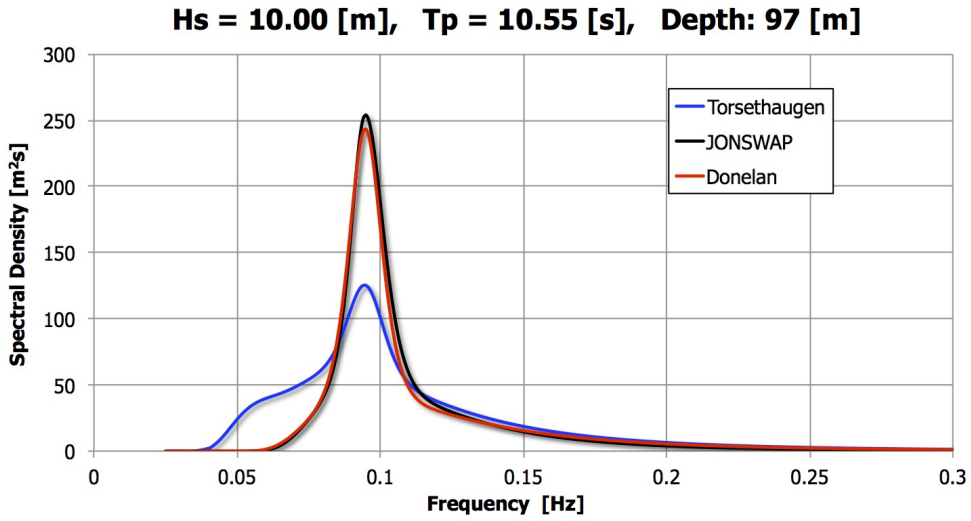

Figure D.1: Comparison of the JONSWAP, Torsethaugen and Donelan spectrum for sea state 1.

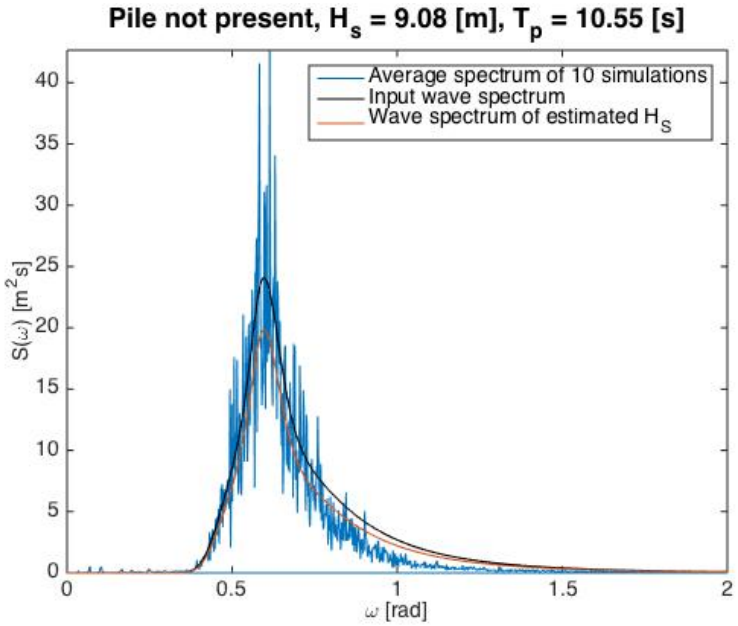

Figure D.2: Averaged estimated wave spectrum for all ten tests of sea state 1 without the pile present.

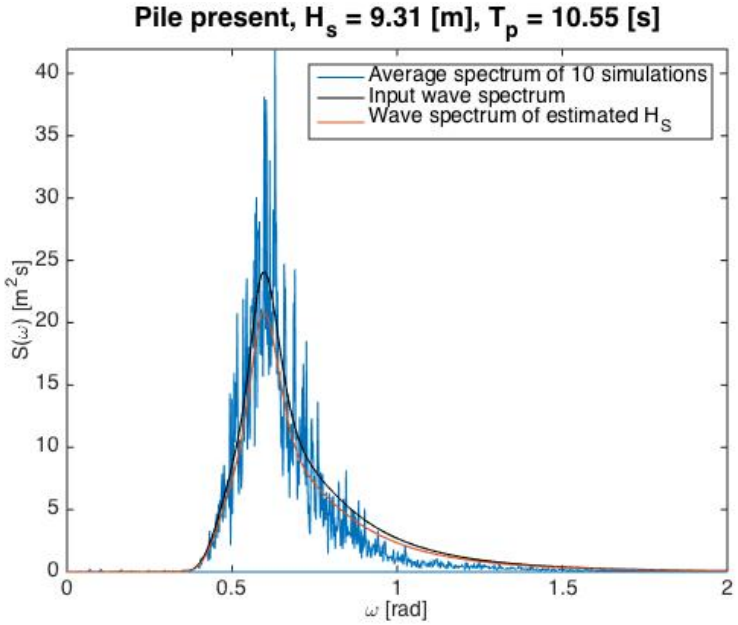

Figure D.3: Averaged estimated wave spectrum for all ten tests of sea state 1 with the pile present.

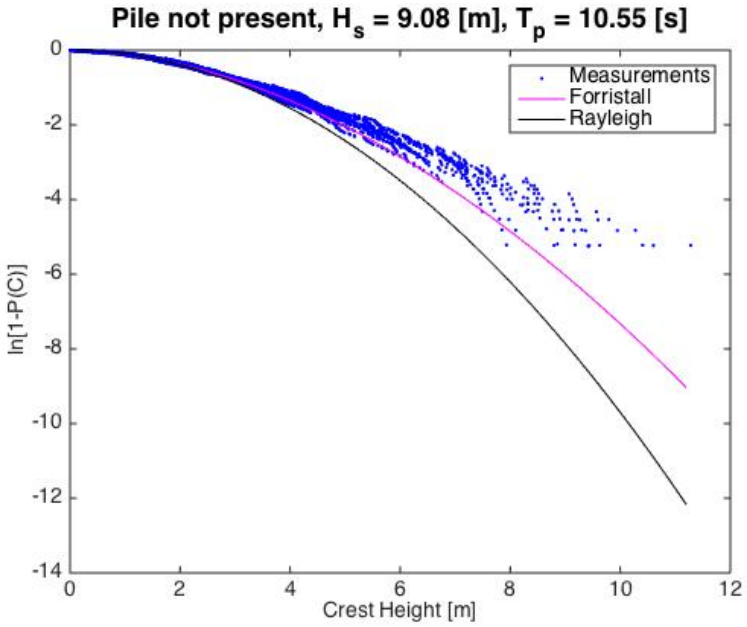

Figure D.4: Distribution of wave crests for all the ten tests of sea state 1 without the pile present.

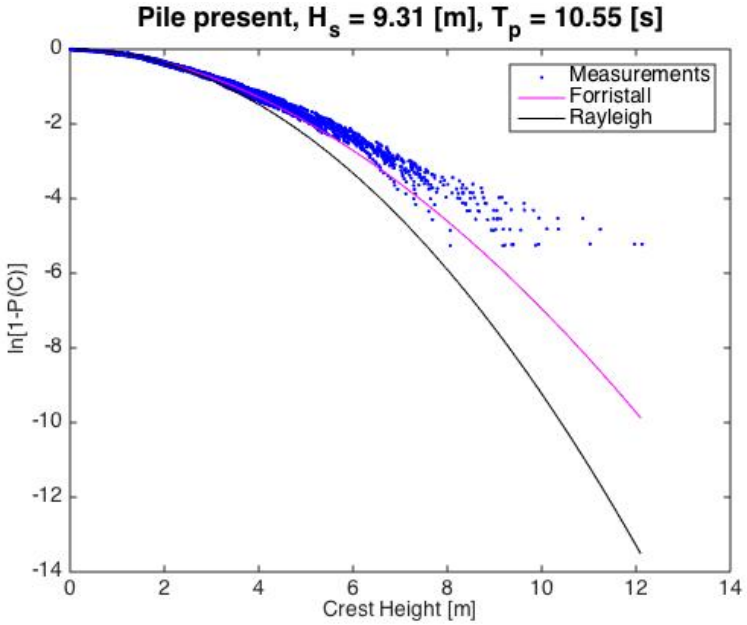

Figure D.5: Distribution of wave crests for all the ten tests of sea state 1 with the pile present.

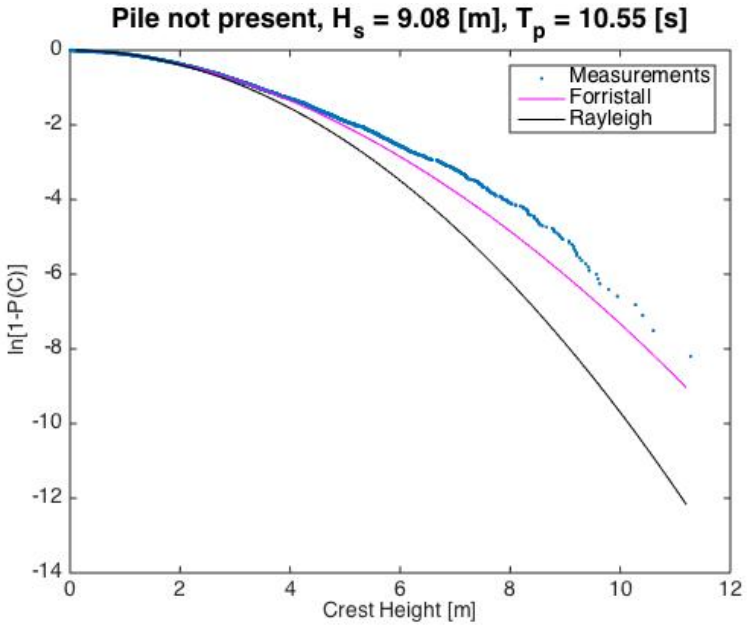

Figure D.6: Distribution of wave crests for all tests smeared together of sea state 1 without the pile present.

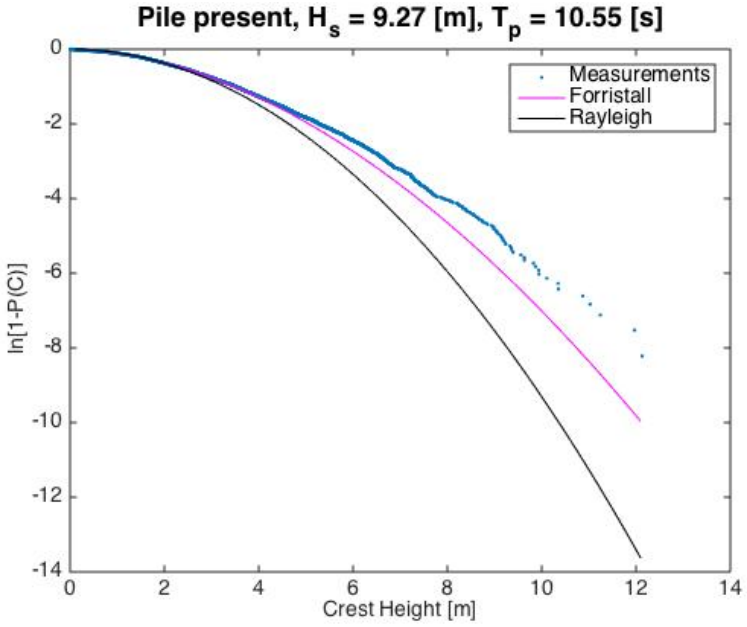

Figure D.7: Distribution of wave crests for all tests smeared together of sea state 1 with the pile present.

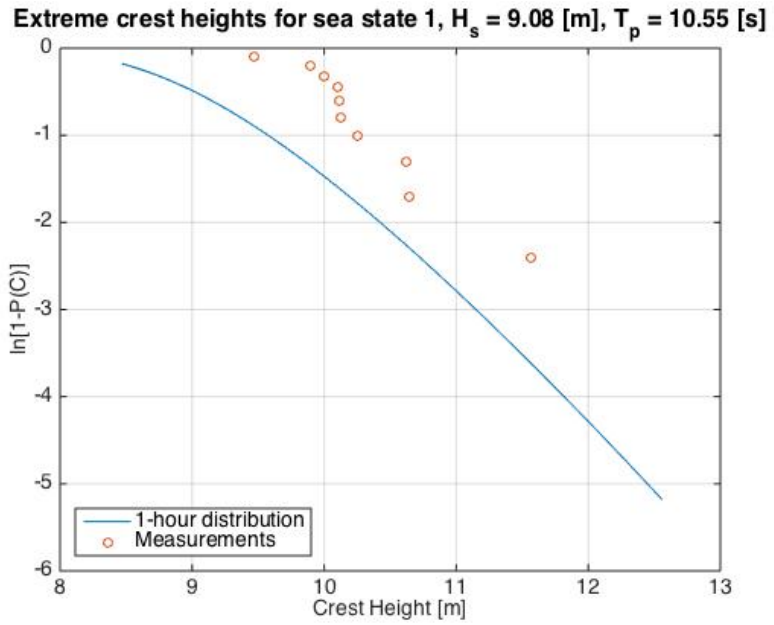

Figure D.8: Distribution of extreme wave crests in sea state 1.

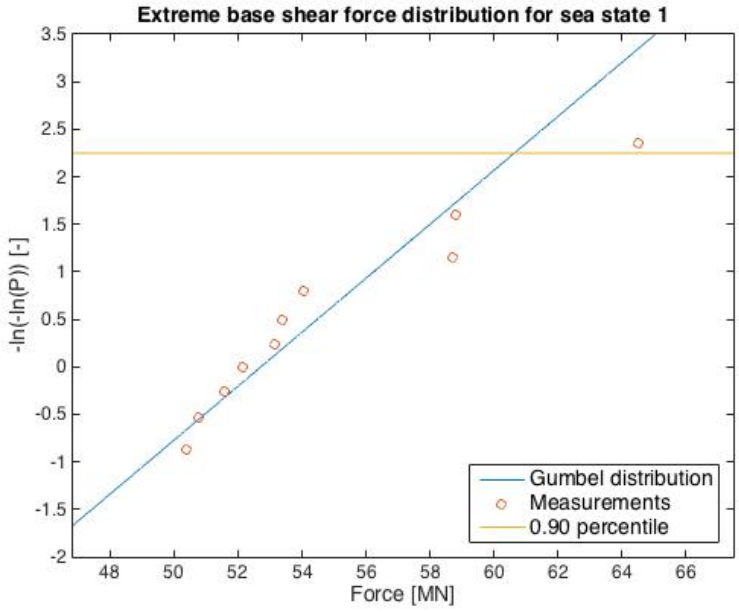

Figure D.9: Distribution of extreme base shear forces in sea state 1.

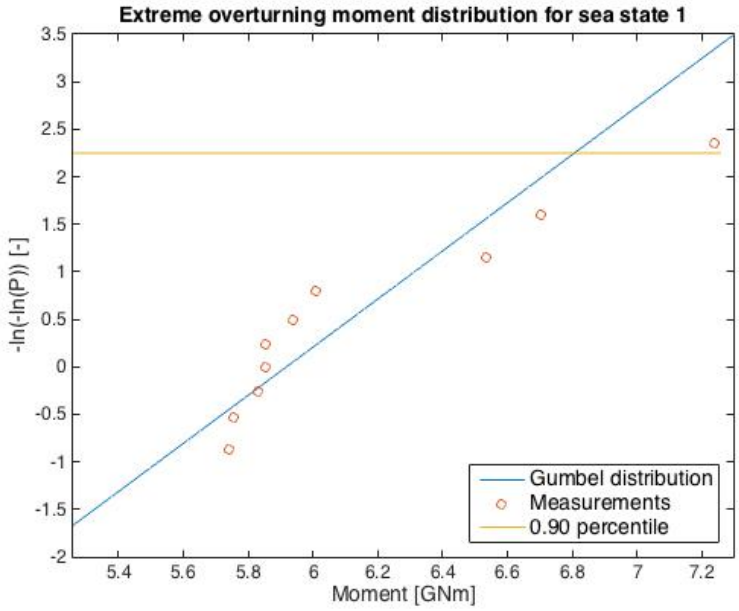

Figure D.10: Distribution of extreme overturning moments in sea state 1.

D.2 Sea state 2

Table D.5: Input information of sea state 2.

Significant wave height	H_S	11.00	[m]
Spectral peak period	T_P	11.48	[s]
Water depth	h	96.0	[m]
Number of tests	#	10	[-]
Duration of each test	d	1	[h]

Table D.6: Variances and significant wave heights for all 10 tests of sea state 2.

	Without pile		With pile	
Test	σ^2 [m^2]	H_S [m]	σ^2 [m^2]	H_S [m]
1	6.19	9.95	6.34	10.07
2	6.46	10.15	6.56	10.25
3	7.26	10.78	7.40	10.88
4	6.70	10.36	7.06	10.63
5	5.85	9.67	6.11	9.88
6	6.26	10.01	6.48	10.18
7	6.23	9.99	6.49	10.19
8	5.92	9.74	6.09	9.87
9	6.60	10.27	7.04	10.62
10	5.97	9.77	6.17	9.94
avg	6.35	10.07	6.57	10.25

Table D.7: Largest measured crest heights, overturning moment and base shear force for all 10 tests of sea state 2.

Test	C_{max} [m]	$C_{max,pile}$ [m]	F_{max} [MN]	M_{max} [GNm]
1	9.56	10.46	47.81	5.22
2	13.53	11.69	51.04	5.59
3	13.27	14.79	58.50	6.55
4	10.90	12.63	55.62	6.05
5	9.73	9.74	62.62	6.90
6	10.62	11.10	52.24	5.66
7	10.90	11.77	51.68	5.65
8	10.39	10.55	55.84	6.06
9	10.24	11.00	55.45	5.92
10	10.46	11.04	54.76	5.92

Table D.8: Output information of sea state 2.

Variance	σ^2_{out}	6.35	[m^2]	σ^2_{pile}	6.57	[m^2]
Standard deviation	σ_{out}	2.52	[m]	σ_{pile}	2.56	[m]
Significant wave height	$H_{S,out}$	10.07	[m]	$H_{S,pile}$	10.25	[m]
Sea state steepness	ε_{out}	0.0492	[-]	ε_{pile}	0.0501	[-]
Range $\frac{H_{S,min}-H_{S,max}}{H_{S,mean}} \cdot 100$	$\Delta H_{S,out}$	11.02	[%]	$\Delta H_{S,pile}$	9.85	[%]
Deviation from $H_{S,in}$	$\frac{H_{S,out}}{H_{S,in}}$	0.9155	[-]	$\frac{H_{S,pile}}{H_{S,in}}$	0.9318	[-]

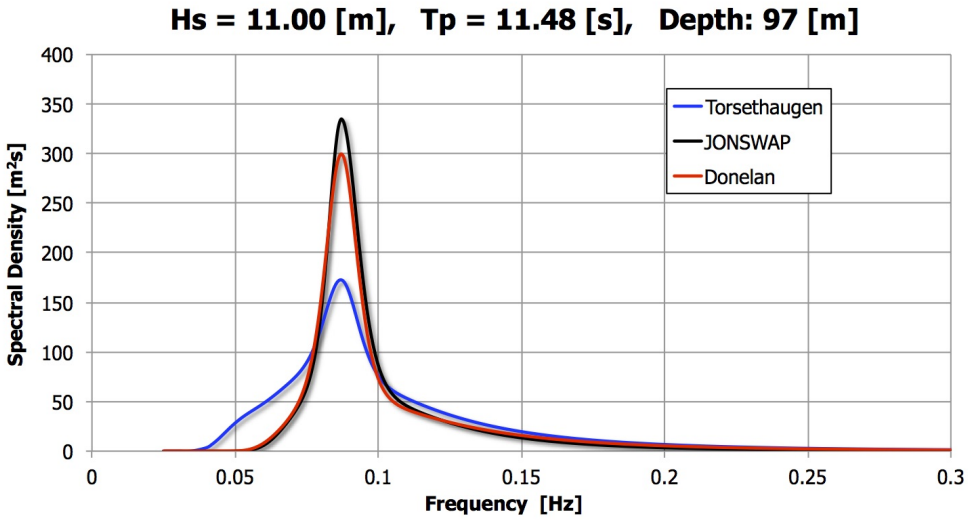

Figure D.11: Comparison of the JONSWAP, Torsethaugen and Donelan spectrum for sea state 2.

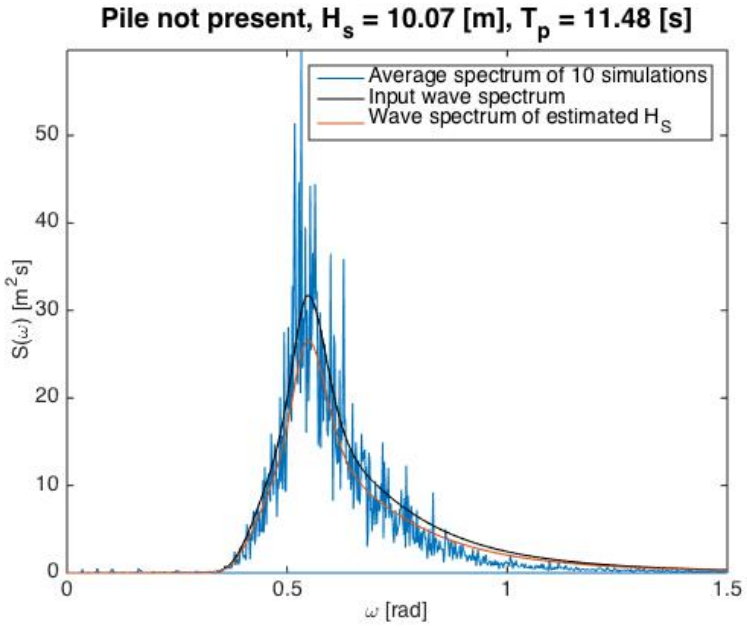

Figure D.12: Averaged estimated wave spectrum for all ten tests of sea state 2 without the pile present.

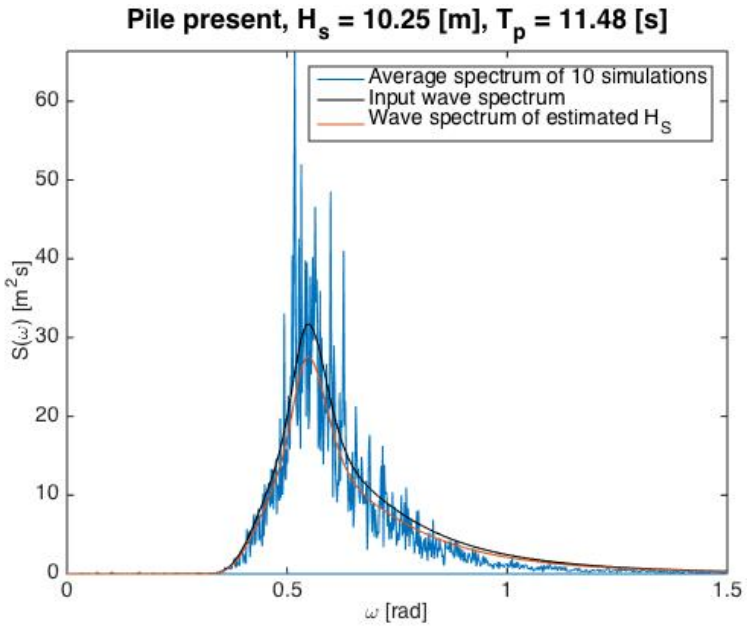

Figure D.13: Averaged estimated wave spectrum for all ten tests of sea state 2 with the pile present.

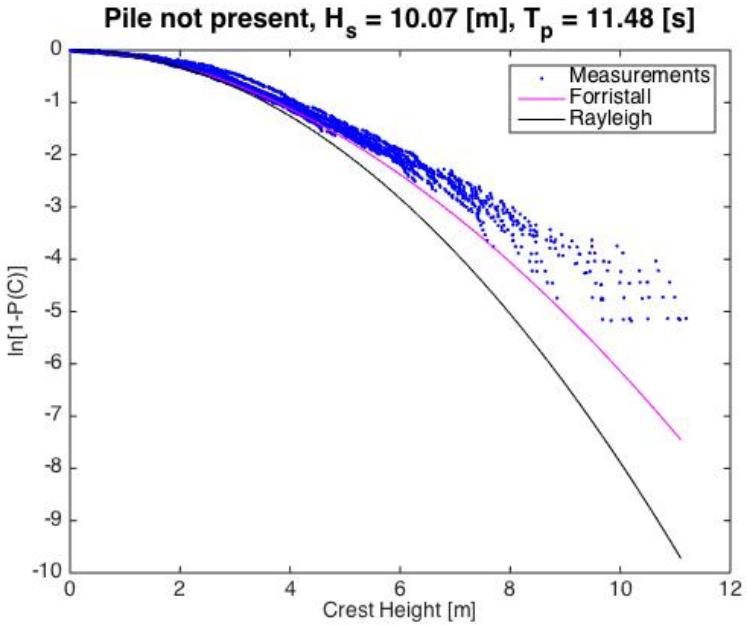

Figure D.14: Distribution of wave crests for all the ten tests of sea state 2 without the pile present.

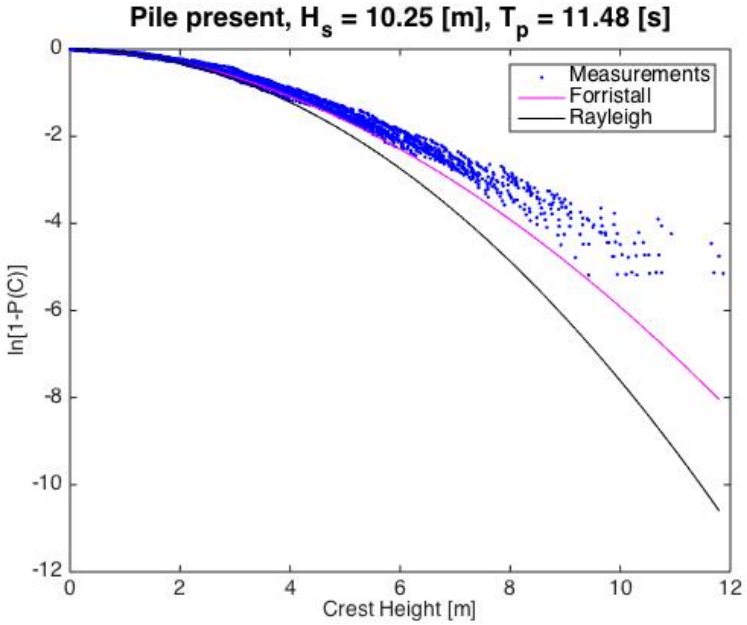

Figure D.15: Distribution of wave crests for all the ten tests of sea state 2 with the pile present.

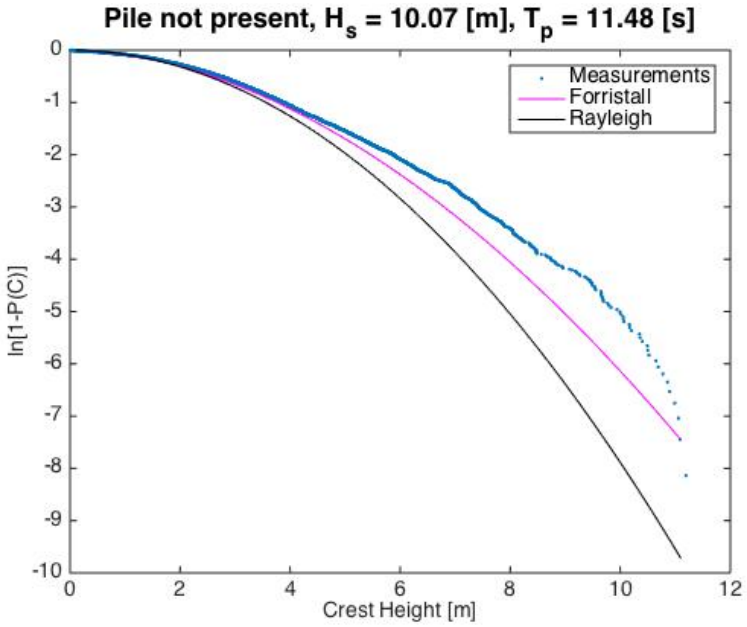

Figure D.16: Distribution of wave crests for all tests smeared together of sea state 2 without the pile present.

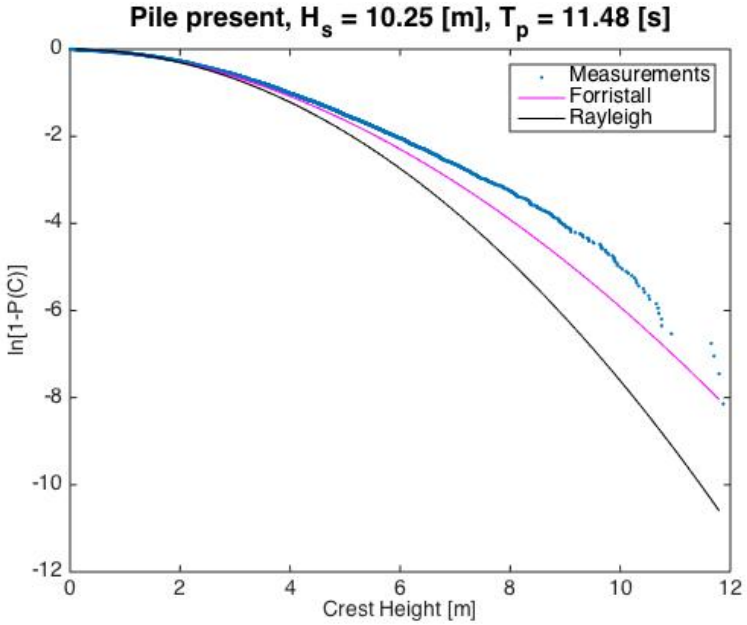

Figure D.17: Distribution of wave crests for all tests smeared together of sea state 2 with the pile present.

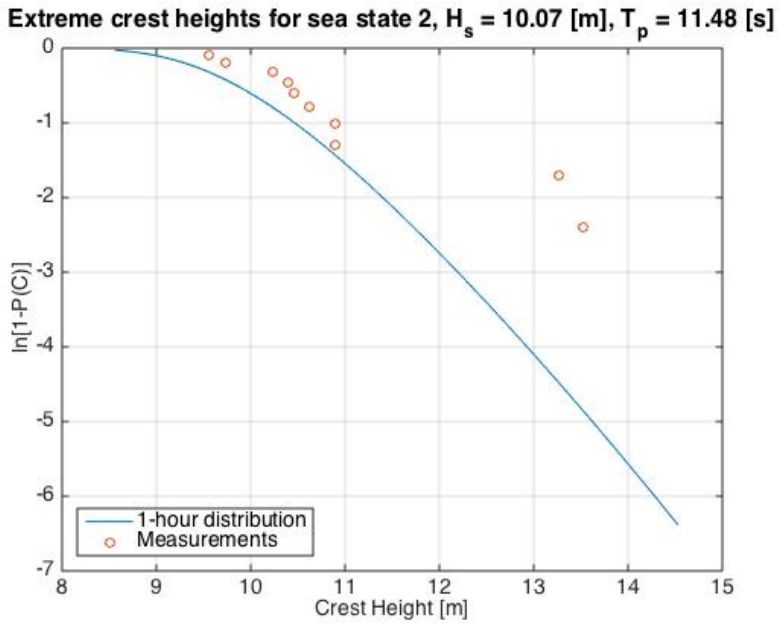

Figure D.18: Distribution of extreme wave crests in sea state 2.

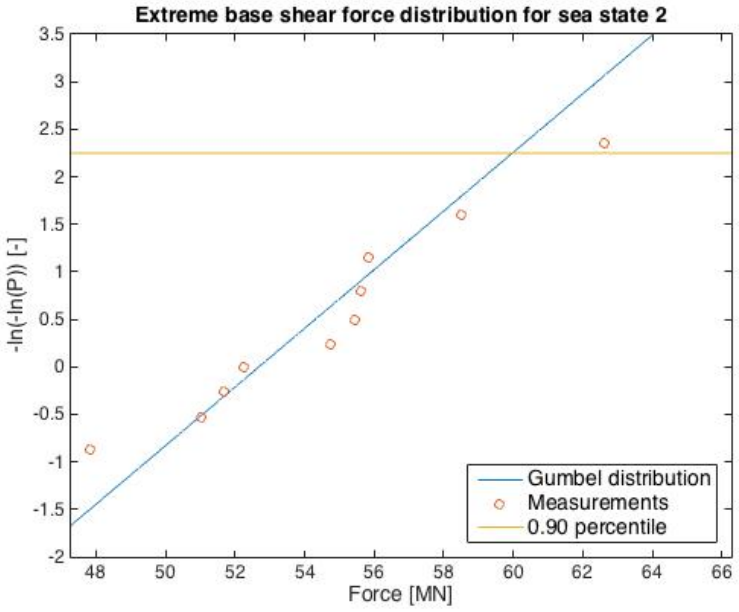

Figure D.19: Distribution of extreme base shear forces in sea state 2.

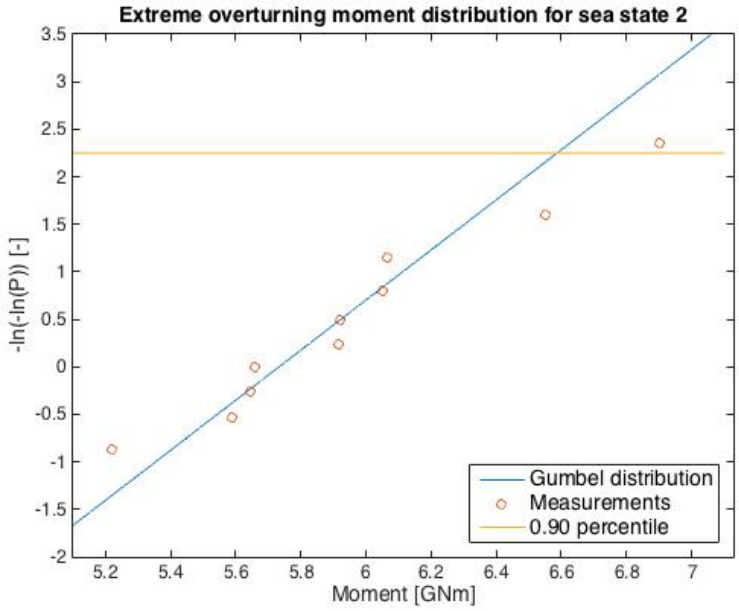

Figure D.20: Distribution of extreme overturning moments in sea state 2.

D.3 Sea state 3

Table D.9: Input information of sea state 3.

Significant wave height	H_S	12.00	[m]
Spectral peak period	T_P	12.38	[s]
Water depth	h	96.1	[m]
Number of tests	#	10	[-]
Duration of each test	d	1	[h]

Table D.10: Variances and significant wave heights for all 10 tests of sea state 3.

	Without pile		With pile	
Test	σ^2 [m^2]	H_S [m]	σ^2 [m^2]	H_S [m]
1	7.60	11.03	7.80	11.17
2	7.46	10.92	7.43	10.90
3	7.39	10.87	7.65	11.07
4	7.55	10.99	7.96	11.28
5	7.19	10.73	7.46	10.92
6	8.06	11.36	8.14	11.41
7	7.31	10.82	7.39	10.88
8	6.92	10.52	7.10	10.66
9	7.93	11.26	7.93	11.27
10	7.87	11.22	8.06	11.35
avg	7.53	10.97	7.69	11.09

Table D.11: Largest measured crest heights, overturning moment and base shear force for all 10 tests of sea state 3.

Test	C_{max} [m]	$C_{max,pile}$ [m]	F_{max} [MN]	M_{max} [GNm]
1	12.79	12.32	50.91	5.64
2	11.03	12.29	52.48	5.77
3	10.80	13.25	55.15	6.25
4	11.21	12.08	50.42	5.72
5	15.00	14.34	52.13	6.03
6	11.79	12.90	52.41	5.64
7	11.54	12.83	71.86	7.82
8	11.30	11.32	56.59	5.95
9	13.11	12.29	64.11	7.27
10	12.58	12.60	50.09	5.38

Table D.12: Output information of sea state 3.

Variance	σ^2_{out}	7.53	[m^2]	σ^2_{pile}	7.69	[m^2]
Standard deviation	σ_{out}	2.74	[m]	σ_{pile}	2.77	[m]
Significant wave height	$H_{S,out}$	10.97	[m]	$H_{S,pile}$	11.09	[m]
Sea state steepness	ε_{out}	0.0464	[-]	ε_{pile}	0.0469	[-]
Range $\frac{H_{S,min}-H_{S,max}}{H_{S,mean}} \cdot 100$	$\Delta H_{S,out}$	7.66	[%]	$\Delta H_{S,pile}$	6.76	[%]
Deviation from $H_{S,in}$	$\frac{H_{S,out}}{H_{S,in}}$	0.9142	[-]	$\frac{H_{S,pile}}{H_{S,in}}$	0.9242	[-]

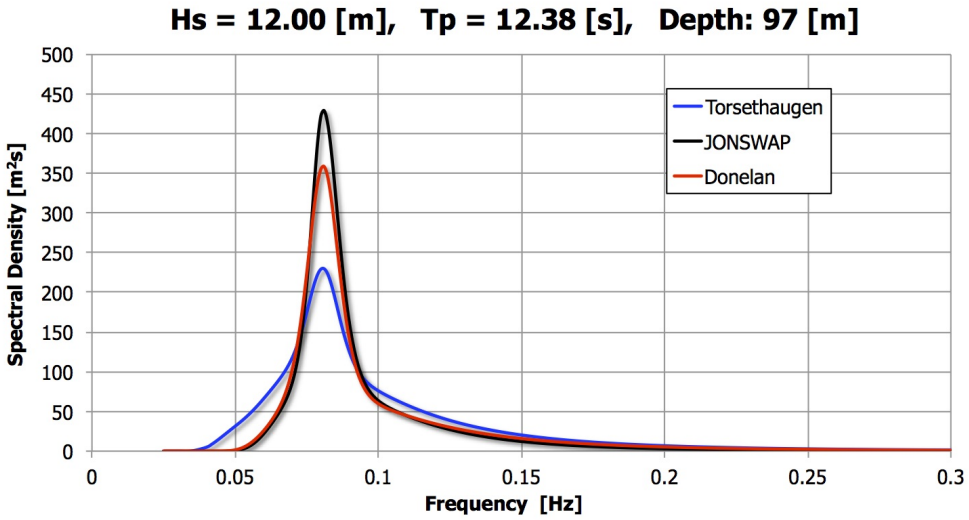

Figure D.21: Comparison of the JONSWAP, Torsethaugen and Donelan spectrum for sea state 3.

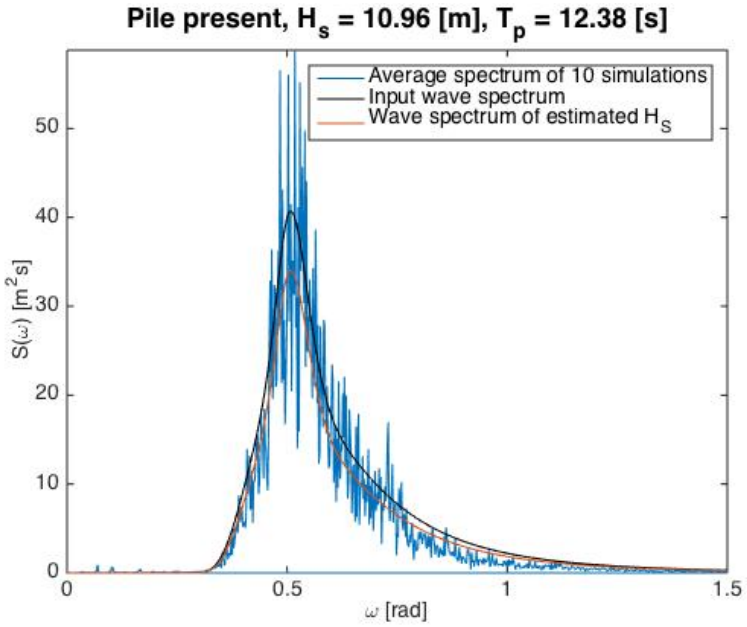

Figure D.22: Averaged estimated wave spectrum for all ten tests of sea state 3 without the pile present.

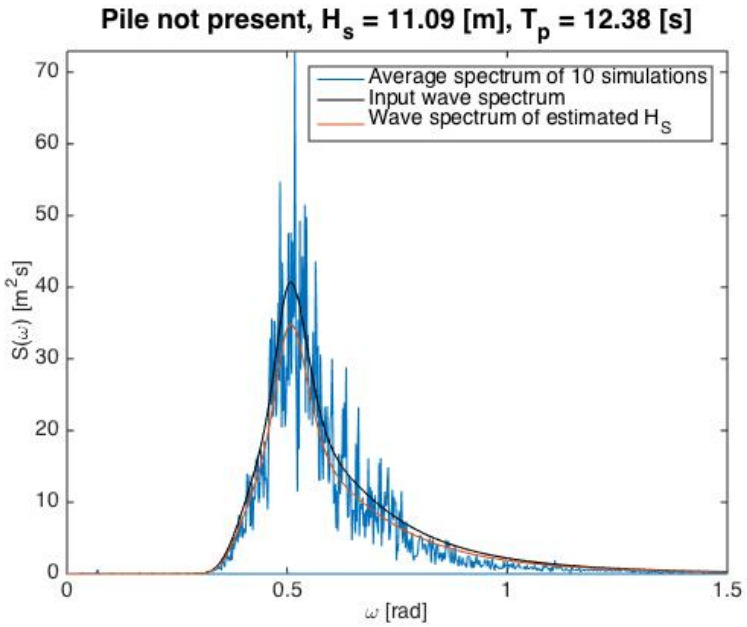

Figure D.23: Averaged estimated wave spectrum for all ten tests of sea state 3 with the pile present.

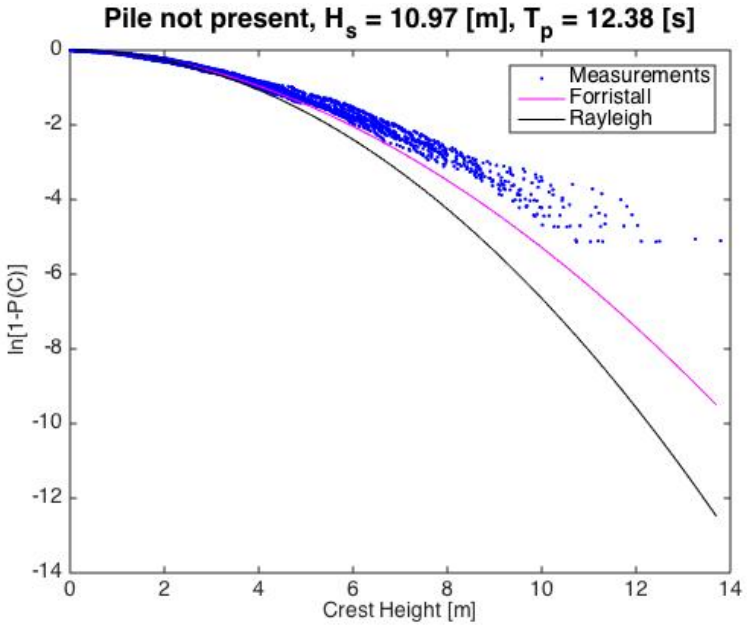

Figure D.24: Distribution of wave crests for all the ten tests of sea state 3 without the pile present.

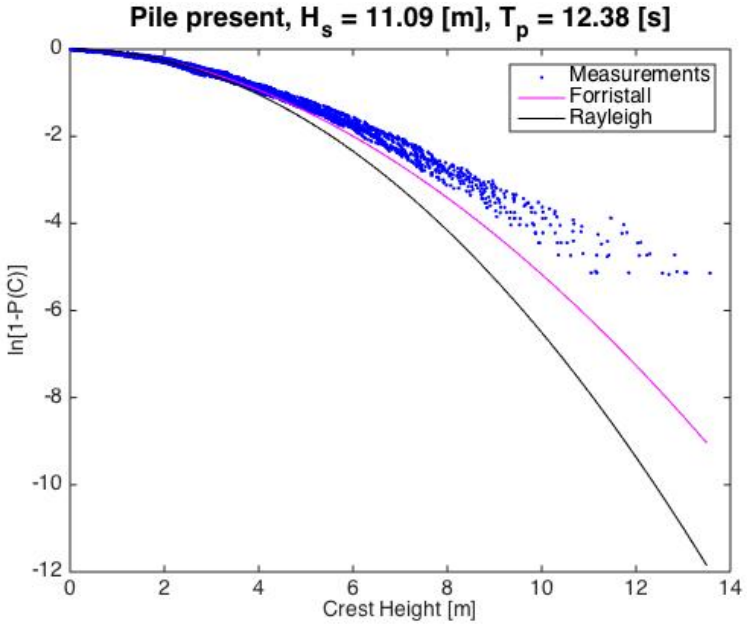

Figure D.25: Distribution of wave crests for all the ten tests of sea state 3 with the pile present.

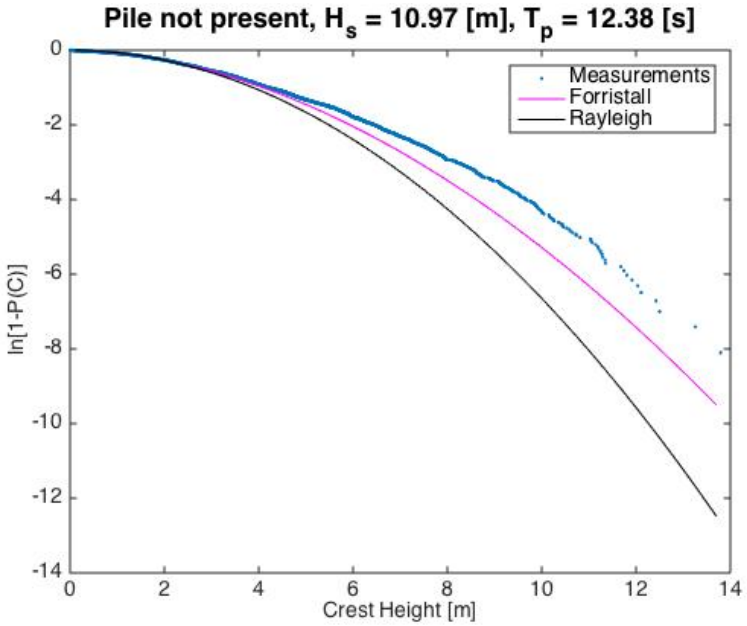

Figure D.26: Distribution of wave crests for all tests smeared together of sea state 3 without the pile present.

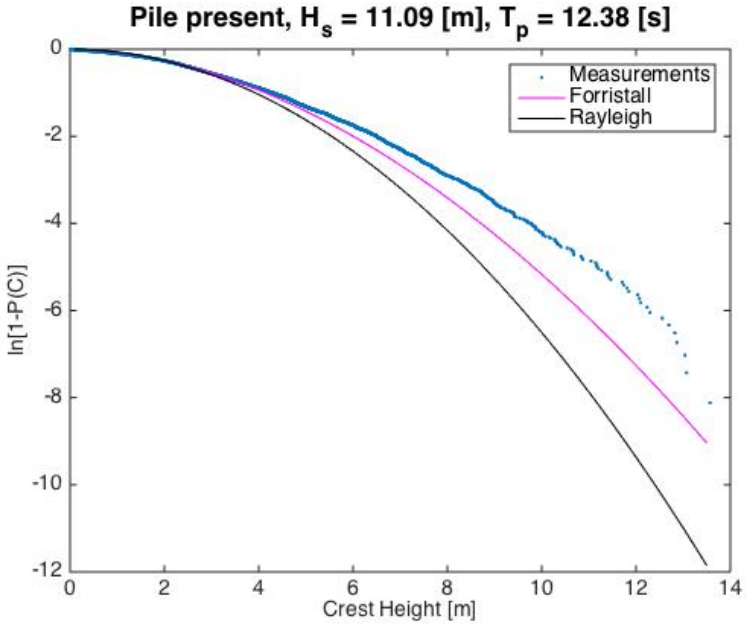

Figure D.27: Distribution of wave crests for all tests smeared together of sea state 3 with the pile present.

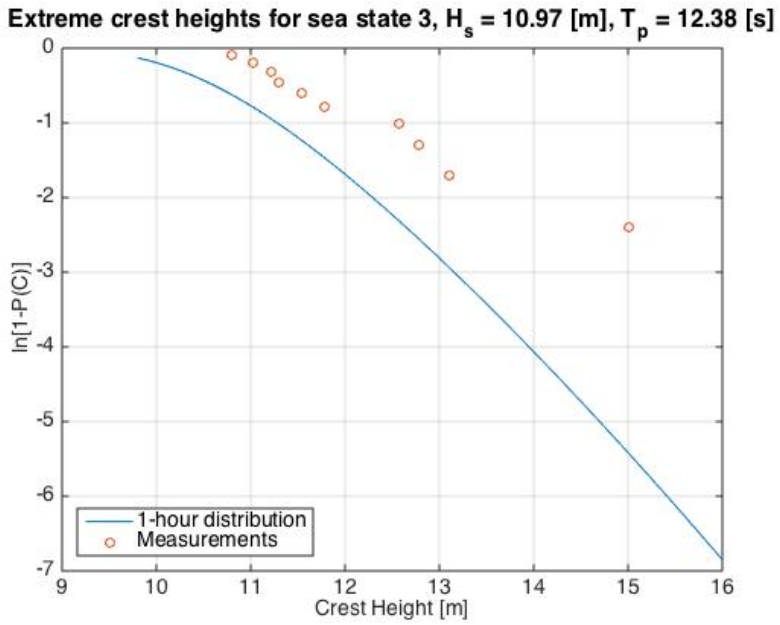

Figure D.28: Distribution of extreme wave crests in sea state 3.

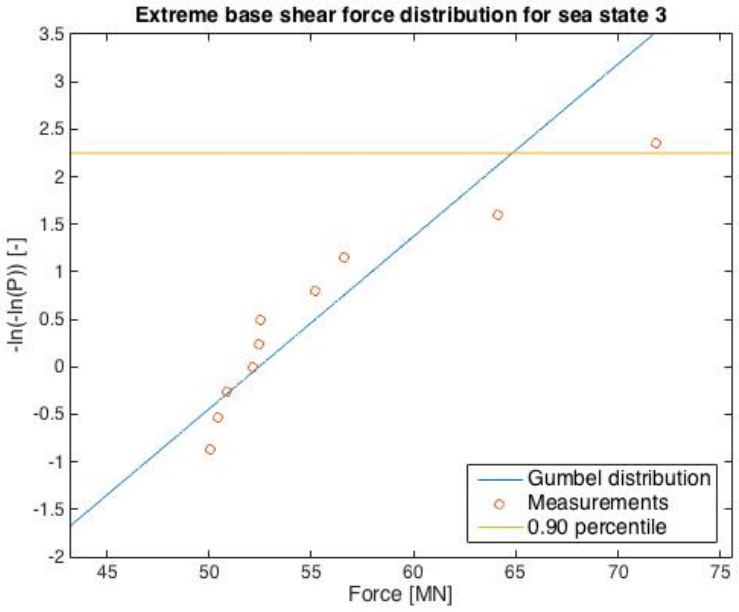

Figure D.29: Distribution of extreme base shear forces in sea state 3.

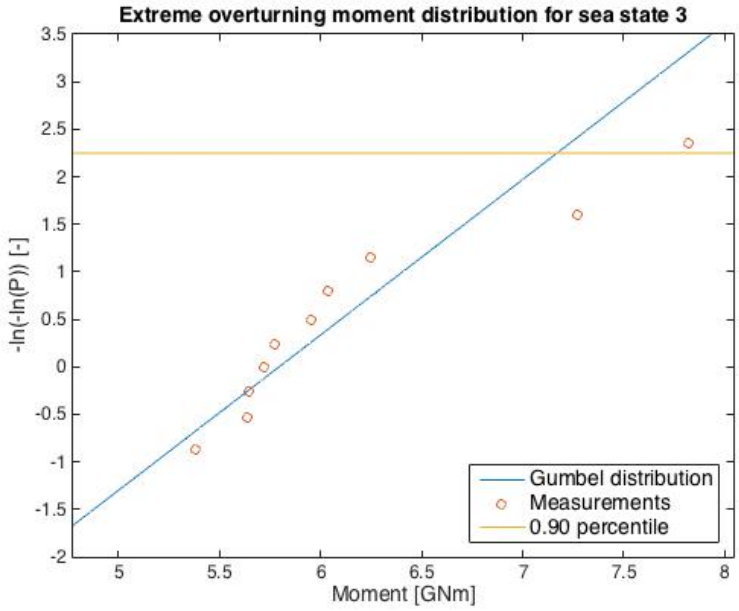

Figure D.30: Distribution of extreme overturning moments in sea state 3.

D.4 Sea state 4

Table D.13: Input information of sea state 4.

Significant wave height	H_S	13.00	[m]
Spectral peak period	T_P	13.71	[s]
Water depth	h	96.1	[m]
Number of tests	#	10	[-]
Duration of each test	d	1	[h]

Table D.14: Variances and significant wave heights for all 10 tests of sea state 4.

	Without pile		With pile	
Test	σ^2 [m^2]	H_S [m]	σ^2 [m^2]	H_S [m]
1	8.06	11.36	8.21	11.46
2	8.54	11.69	8.66	11.77
3	9.19	12.13	9.62	12.41
4	7.82	11.19	8.00	11.31
5	8.99	11.99	9.15	12.10
6	8.56	11.70	8.60	11.73
7	8.42	11.61	8.25	11.49
8	10.15	12.74	10.14	12.73
9	9.99	12.65	10.19	12.77
10	9.27	12.18	9.49	12.32
avg	8.90	11.92	9.03	12.01

Table D.15: Largest measured crest heights, overturning moment and base shear force for all 10 tests of sea state 4.

Test	C_{max} [m]	$C_{max,pile}$ [m]	F_{max} [MN]	M_{max} [GNm]
1	11.04	10.67	53.55	5.90
2	12.87	11.94	51.07	5.60
3	14.65	17.35	57.07	6.23
4	11.49	11.90	49.18	5.30
5	15.15	13.77	65.92	7.16
6	13.01	11.59	53.87	5.89
7	13.05	13.25	57.42	5.94
8	16.24	14.87	49.00	5.25
9	13.35	12.07	52.26	5.60
10	15.74	15.18	50.90	5.71

Table D.16: Output information of sea state 4.

Variance	σ^2_{out}	8.90	[m^2]	σ^2_{pile}	9.03	[m^2]
Standard deviation	σ_{out}	2.98	[m]	σ_{pile}	3.00	[m]
Significant wave height	$H_{S,out}$	11.92	[m]	$H_{S,pile}$	12.01	[m]
Sea state steepness	ε_{out}	0.0418	[-]	ε_{pile}	0.0421	[-]
Range $\frac{H_{S,min}-H_{S,max}}{H_{S,mean}} \cdot 100$	$\Delta H_{S,out}$	13.00	[%]	$\Delta H_{S,pile}$	12.16	[%]
Deviation from $H_{S,in}$	$\frac{H_{S,out}}{H_{S,in}}$	0.9169	[-]	$\frac{H_{S,pile}}{H_{S,in}}$	0.9238	[-]

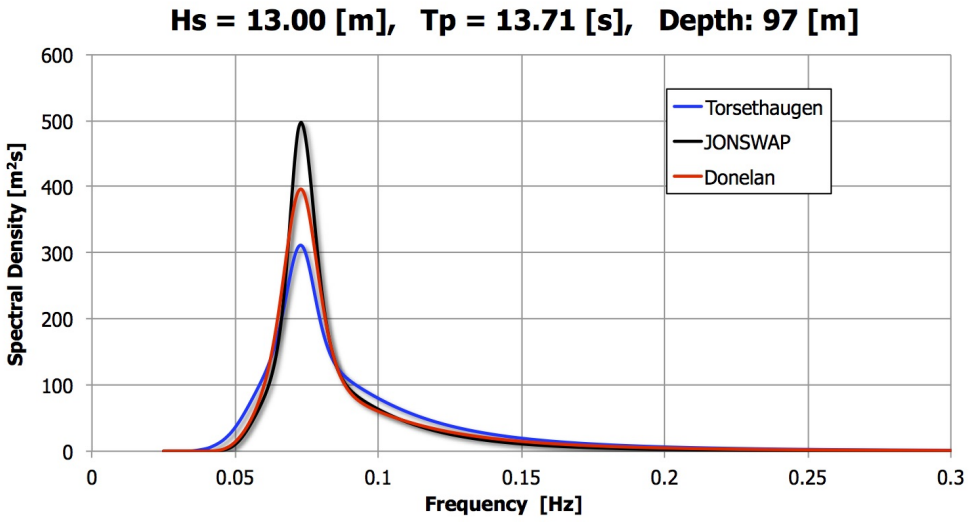

Figure D.31: Comparison of the JONSWAP, Torsethaugen and Donelan spectrum for sea state 4.

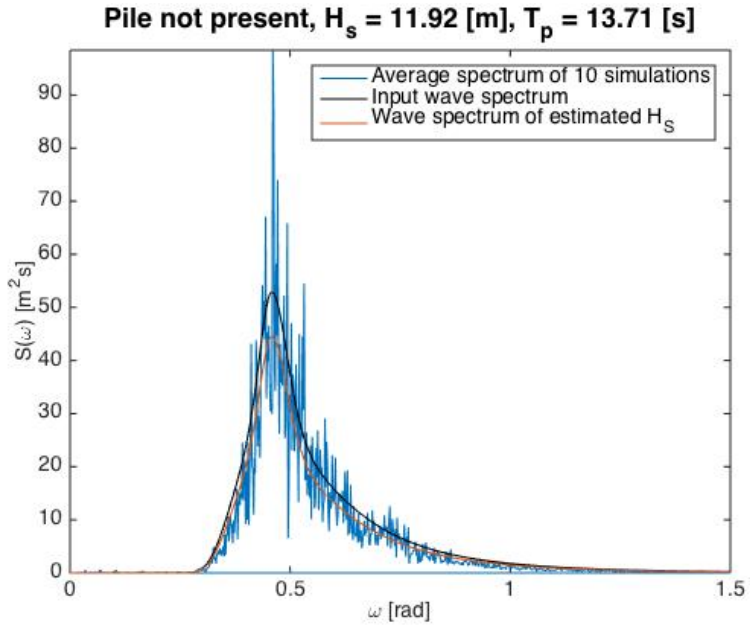

Figure D.32: Averaged estimated wave spectrum for all ten tests of sea state 4 without the pile present.

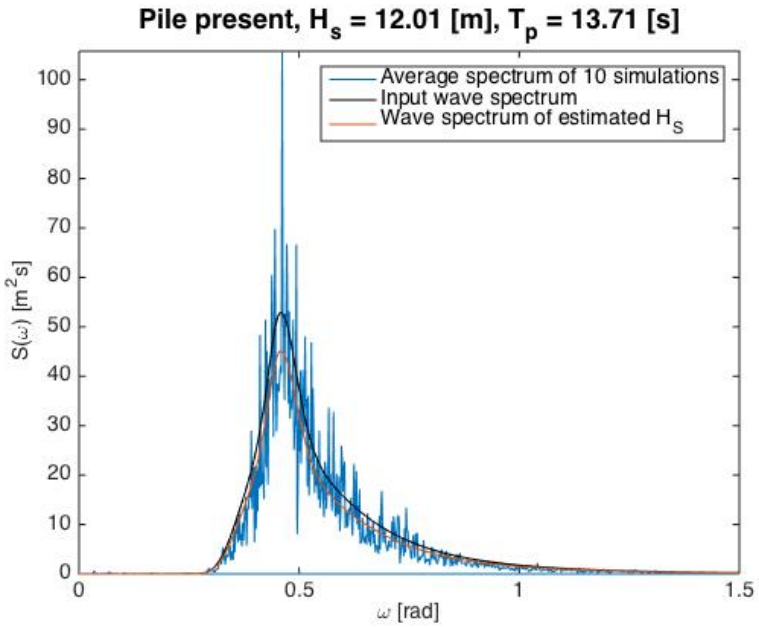

Figure D.33: Averaged estimated wave spectrum for all ten tests of sea state 4 with the pile present.

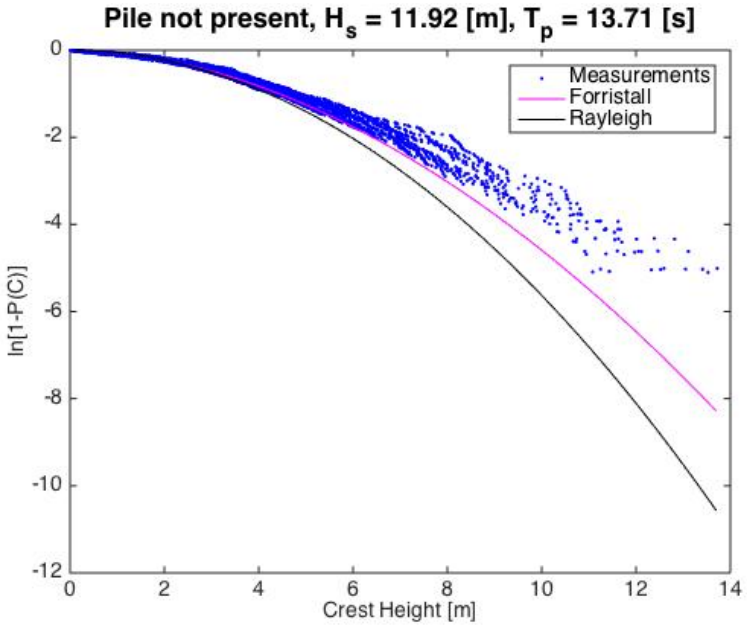

Figure D.34: Distribution of wave crests for all the ten tests of sea state 4 without the pile present.

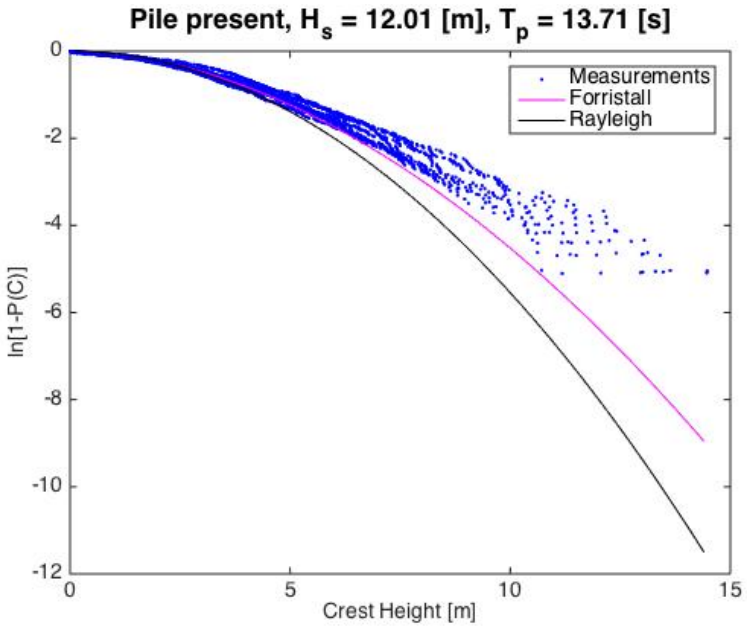

Figure D.35: Distribution of wave crests for all the ten tests of sea state 4 with the pile present.

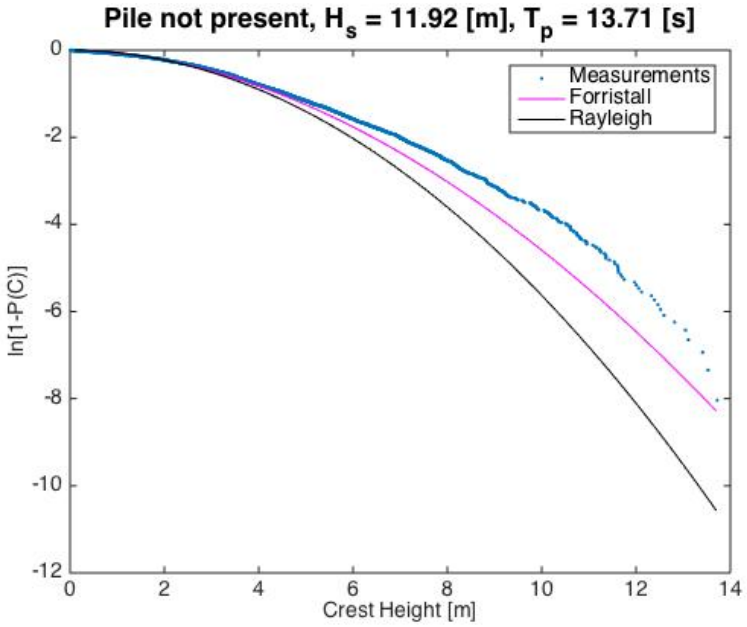

Figure D.36: Distribution of wave crests for all tests smeared together of sea state 4 without the pile present.

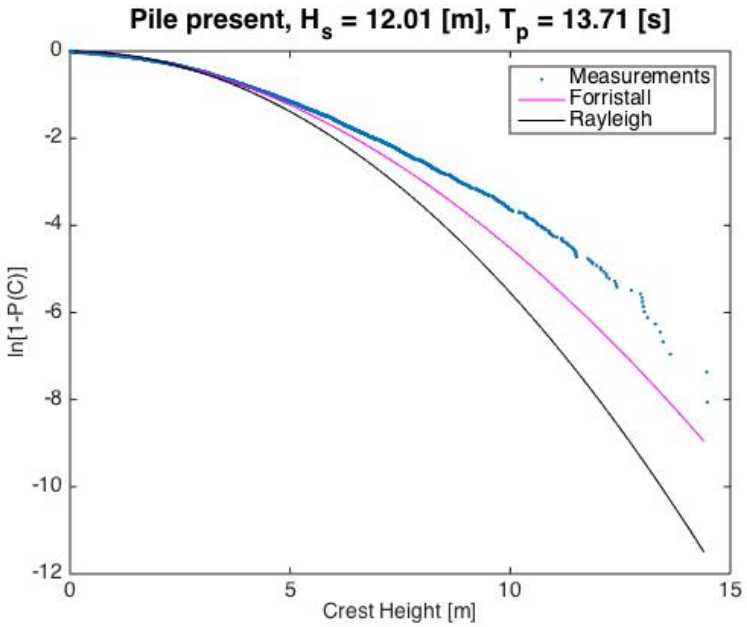

Figure D.37: Distribution of wave crests for all tests smeared together of sea state 4 with the pile present.

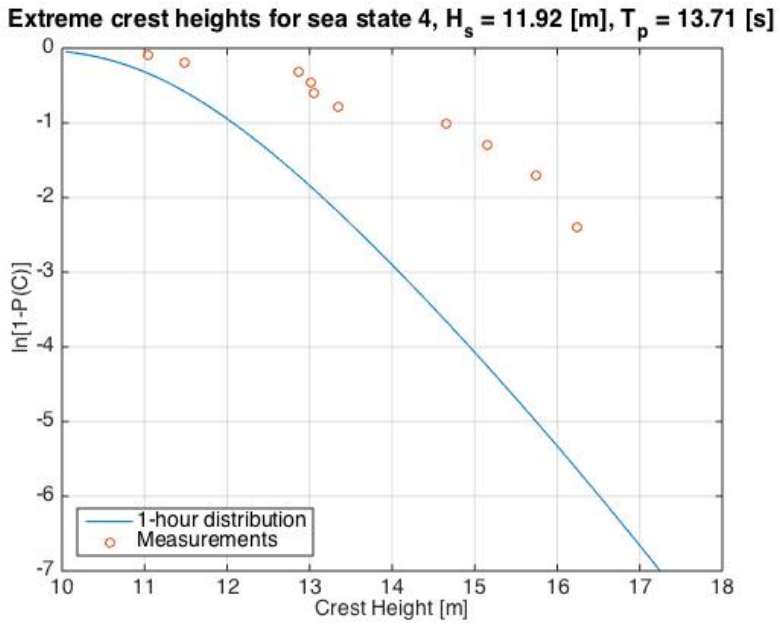

Figure D.38: Distribution of extreme wave crests in sea state 4.

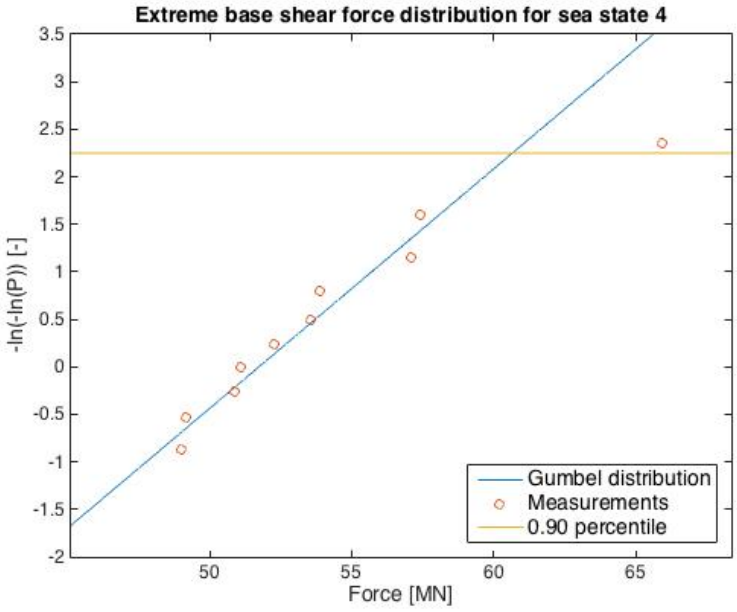

Figure D.39: Distribution of extreme base shear forces in sea state 4.

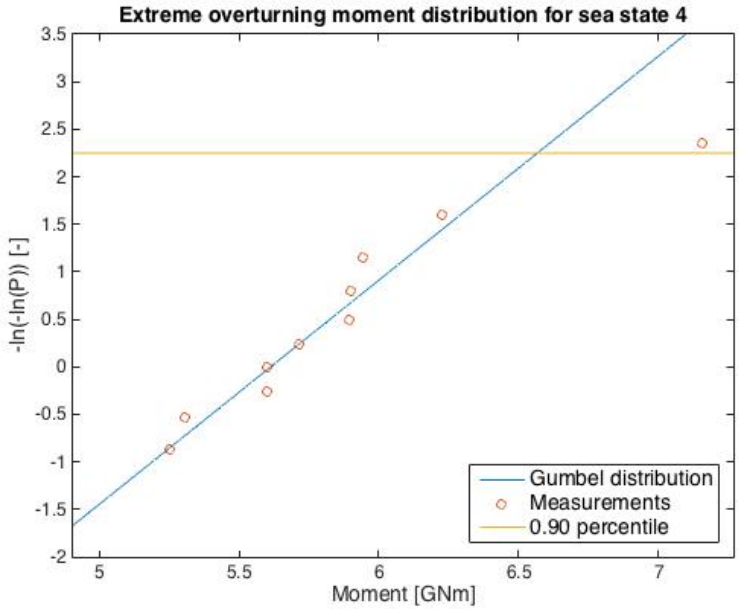

Figure D.40: Distribution of extreme overturning moments in sea state 4.

D.5 Sea state 5

Table D.17: Input information of sea state 5.

Significant wave height	H_S	14.00	[m]
Spectral peak period	T_P	15.40	[s]
Water depth	h	96.5	[m]
Number of tests	#	10	[-]
Duration of each test	d	1	[h]

Table D.18: Variances and significant wave heights for all 10 tests of sea state 5.

	Without pile		With pile	
Test	σ^2 [m^2]	H_S [m]	σ^2 [m^2]	H_S [m]
1	9.85	12.56	10.22	12.79
2	9.64	12.42	9.95	12.62
3	9.75	12.49	10.12	12.72
4	10.91	13.21	11.32	13.46
5	9.05	12.03	9.46	12.30
6	10.10	12.71	10.50	12.96
7	10.03	12.67	10.38	12.89
8	9.70	12.46	10.19	12.77
9	9.94	12.61	10.62	13.03
10	9.46	12.30	9.91	12.59
avg	9.84	12.55	10.27	12.81

Table D.19: Largest measured crest heights, overturning moment and base shear force for all 10 tests of sea state 5.

Test	C_{max} [m]	$C_{max,pile}$ [m]	F_{max} [MN]	M_{max} [GNm]
1	13.11	15.42	47.29	5.41
2	15.93	17.34	52.01	5.75
3	13.19	13.21	63.81	6.95
4	12.65	12.21	44.88	4.87
5	13.59	14.66	53.13	5.91
6	13.14	15.96	50.99	5.28
7	13.54	15.13	60.79	6.52
8	15.43	16.01	55.44	5.93
9	11.92	13.14	51.61	5.46
10	16.24	15.85	52.88	5.45

Table D.20: Output information of sea state 5.

Variance	σ^2_{out}	9.84	[m^2]	σ^2_{pile}	10.27	[m^2]
Standard deviation	σ_{out}	3.14	[m]	σ_{pile}	3.20	[m]
Significant wave height	$H_{S,out}$	12.55	[m]	$H_{S,pile}$	12.81	[m]
Sea state steepness	ε_{out}	0.0360	[-]	ε_{pile}	0.0368	[-]
Range $\frac{H_{S,min}-H_{S,max}}{H_{S,mean}} \cdot 100$	$\Delta H_{S,out}$	9.40	[%]	$\Delta H_{S,pile}$	9.06	[%]
Deviation from $H_{S,in}$	$\frac{H_{S,out}}{H_{S,in}}$	0.8964	[-]	$\frac{H_{S,pile}}{H_{S,in}}$	0.9150	[-]

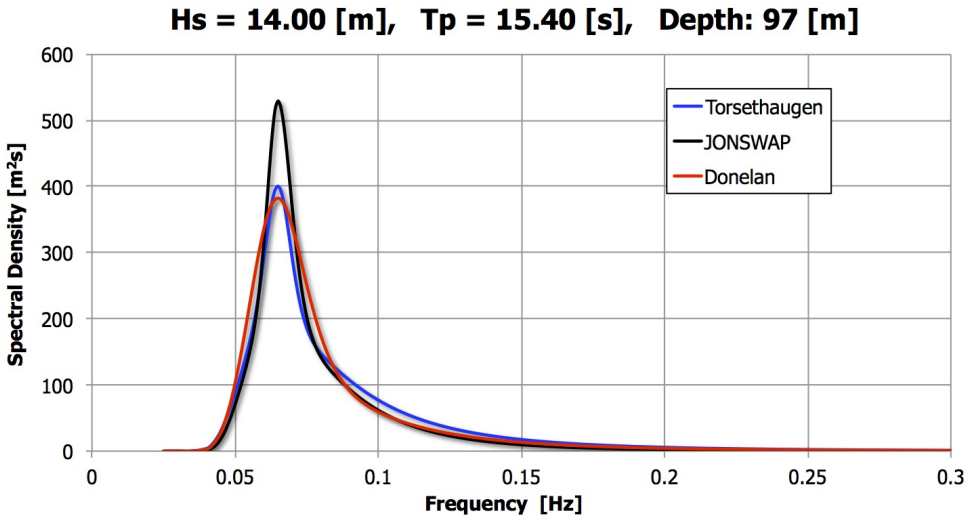

Figure D.41: Comparison of the JONSWAP, Torsethaugen and Donelan spectrum for sea state 5.

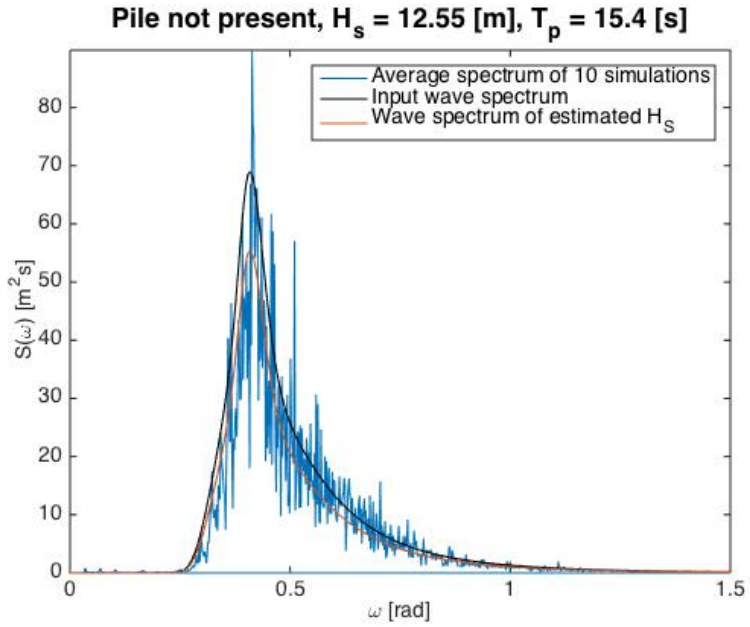

Figure D.42: Averaged estimated wave spectrum for all ten tests of sea state 5 without the pile present.

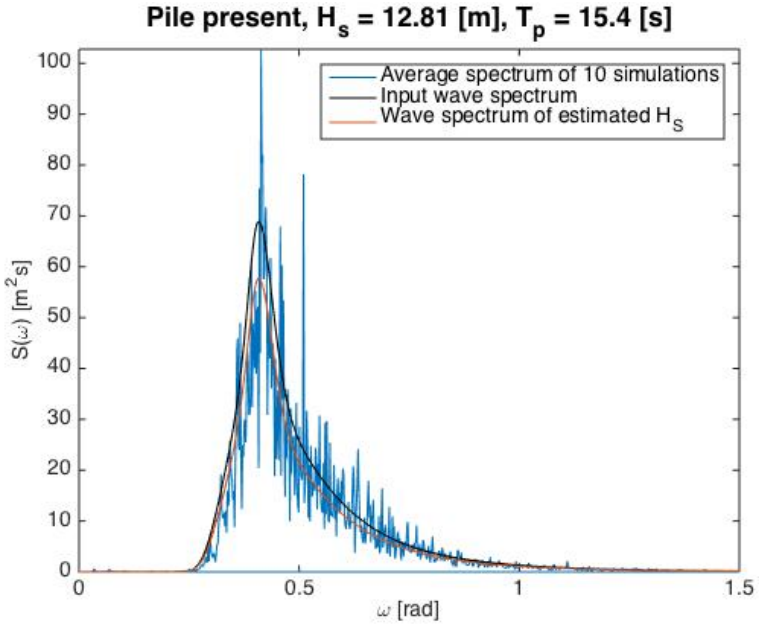

Figure D.43: Averaged estimated wave spectrum for all ten tests of sea state 5 with the pile present.

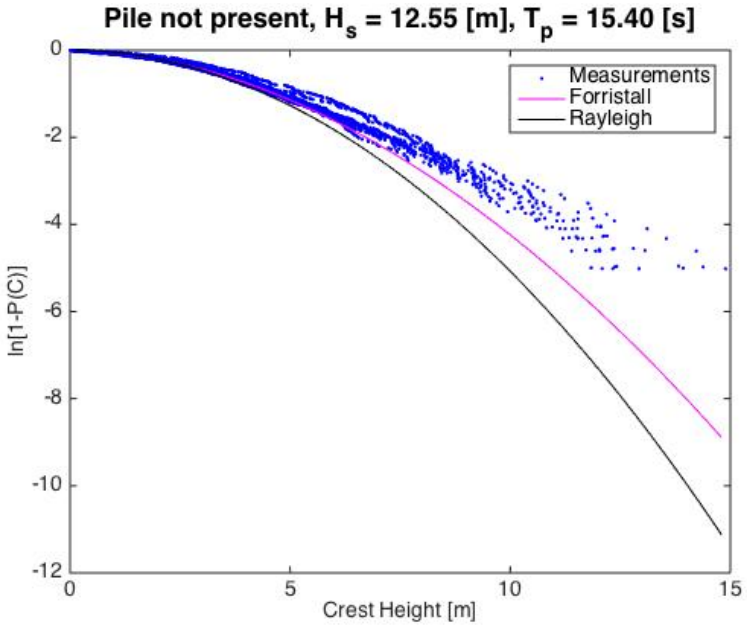

Figure D.44: Distribution of wave crests for all the ten tests of sea state 5 without the pile present.

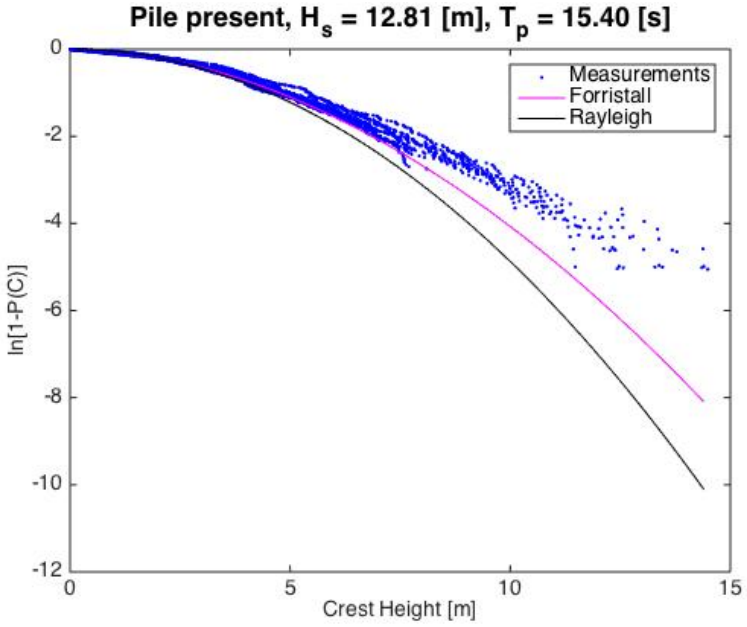

Figure D.45: Distribution of wave crests for all the ten tests of sea state 5 with the pile present.

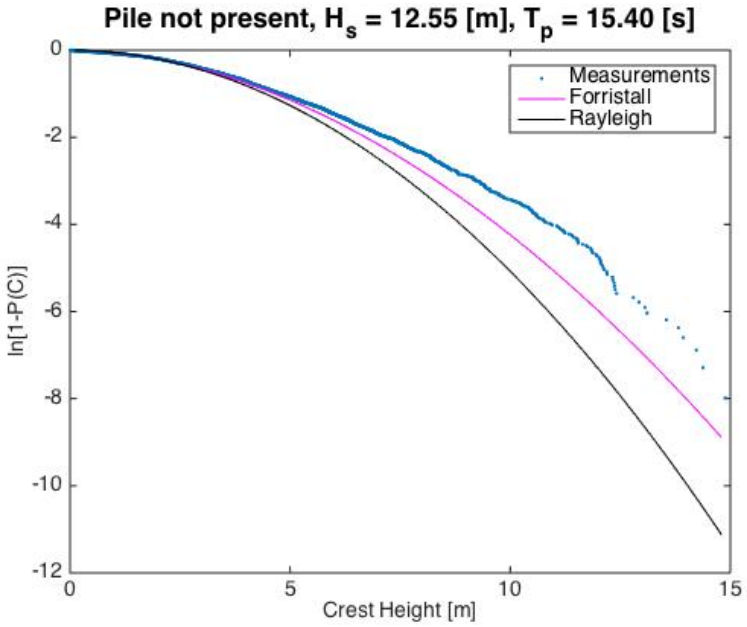

Figure D.46: Distribution of wave crests for all tests smeared together of sea state 5 without the pile present.

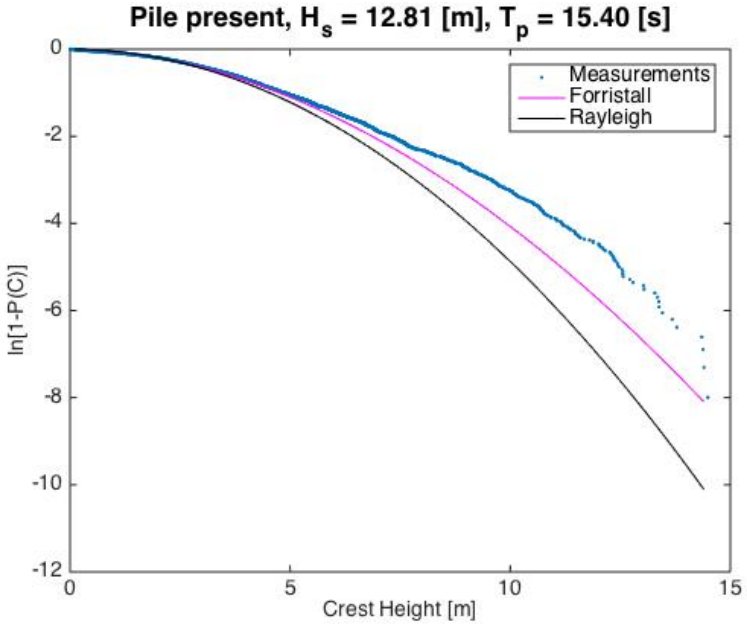

Figure D.47: Distribution of wave crests for all tests smeared together of sea state 5 with the pile present.

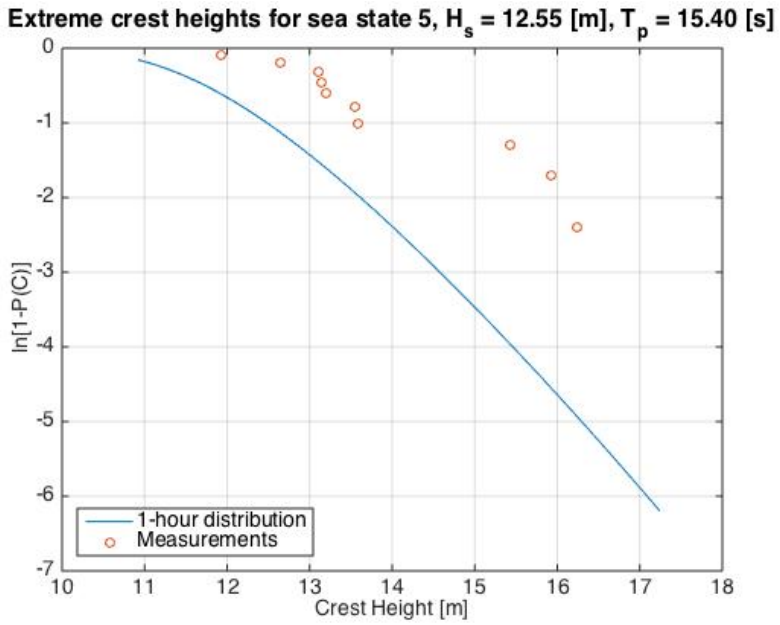

Figure D.48: Distribution of extreme wave crests in sea state 5.

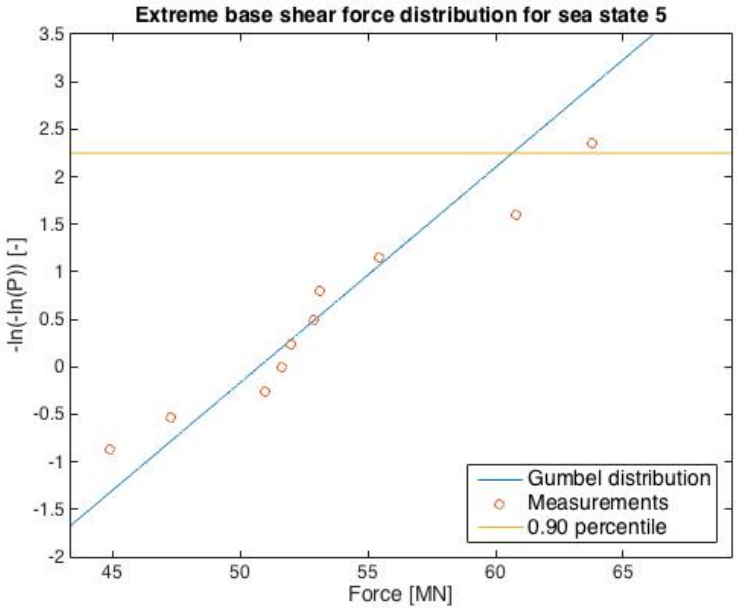

Figure D.49: Distribution of extreme base shear forces in sea state 5.

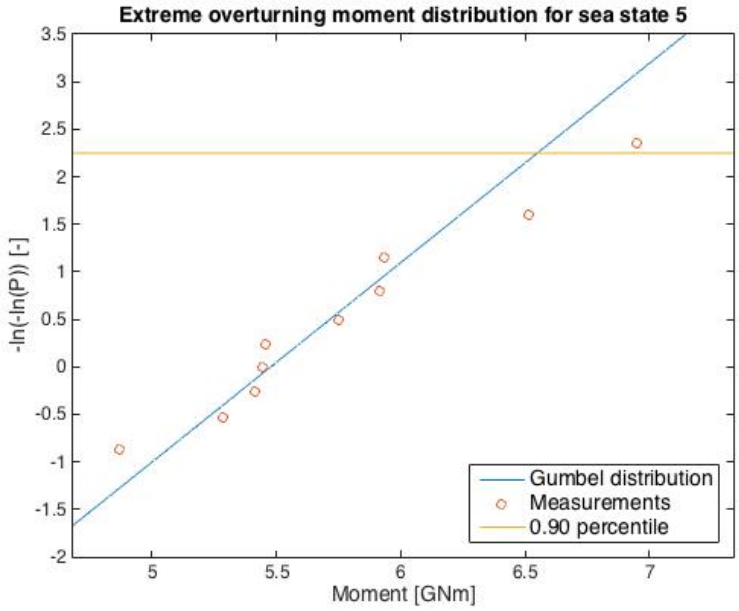

Figure D.50: Distribution of extreme overturning moments in sea state 5.

D.6 Sea state 6

Table D.21: Input information of sea state 6.

Significant wave height	H_S	14.91	[m]
Spectral peak period	T_P	16.76	[s]
Water depth	h	96.6	[m]
Number of tests	#	10	[-]
Duration of each test	d	1	[h]

Table D.22: Variances and significant wave heights for all 10 tests of sea state 6.

	Without pile		With pile	
Test	σ^2 [m^2]	H_S [m]	σ^2 [m^2]	H_S [m]
1	10.65	13.05	10.89	13.20
2	11.58	13.61	12.41	14.09
3	10.79	13.14	10.99	13.26
4	10.29	12.83	10.64	13.05
5	10.14	12.73	10.47	12.94
6	10.57	13.01	10.92	13.22
7	10.03	12.67	10.36	12.88
8	11.39	13.50	11.80	13.74
9	9.52	12.34	10.02	12.66
10	10.67	13.07	11.20	13.39
avg	10.56	12.99	10.97	13.24

Table D.23: Largest measured crest heights, overturning moment and base shear force for all 10 tests of sea state 6.

Test	C_{max} [m]	$C_{max,pile}$ [m]	F_{max} [MN]	M_{max} [GNm]
1	15.09	19.85	52.74	5.71
2	13.43	13.72	48.27	4.71
3	11.99	13.85	47.54	4.83
4	12.30	11.13	53.55	5.51
5	14.68	14.20	63.39	7.12
6	12.52	13.07	45.10	4.74
7	14.45	16.03	56.26	5.51
8	14.37	14.53	55.27	5.39
9	12.23	14.25	52.48	5.70
10	13.21	15.45	67.00	7.08

Table D.24: Output information of sea state 6.

Variance	σ^2_{out}	10.56	[m^2]	σ^2_{pile}	10.97	[m^2]
Standard deviation	σ_{out}	3.25	[m]	σ_{pile}	3.31	[m]
Significant wave height	$H_{S,out}$	12.99	[m]	$H_{S,pile}$	13.24	[m]
Sea state steepness	ε_{out}	0.0326	[-]	ε_{pile}	0.0332	[-]
Range $\frac{H_{S,min}-H_{S,max}}{H_{S,mean}} \cdot 100$	$\Delta H_{S,out}$	9.76	[%]	$\Delta H_{S,pile}$	10.80	[%]
Deviation from $H_{S,in}$	$\frac{H_{S,out}}{H_{S,in}}$	0.8712	[-]	$\frac{H_{S,pile}}{H_{S,in}}$	0.8880	[-]

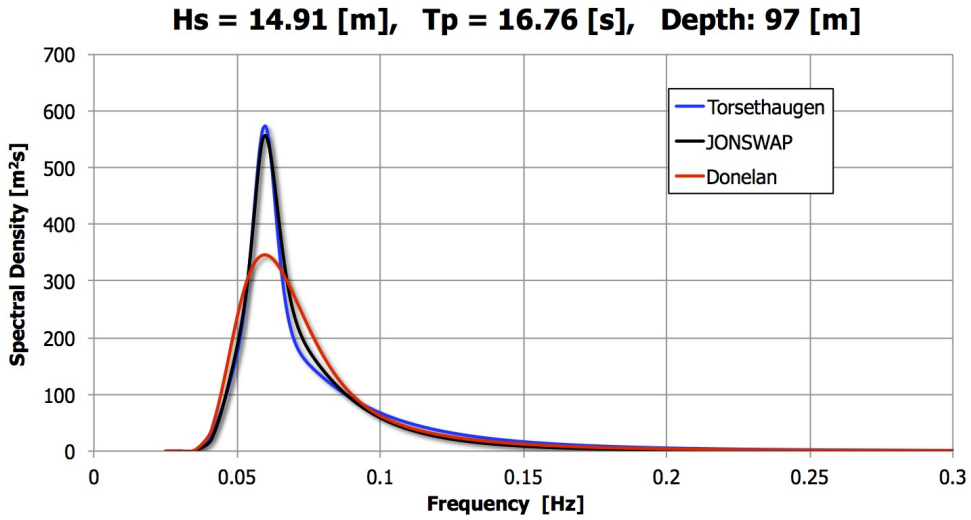

Figure D.51: Comparison of the JONSWAP, Torsethaugen and Donelan spectrum for sea state 6.

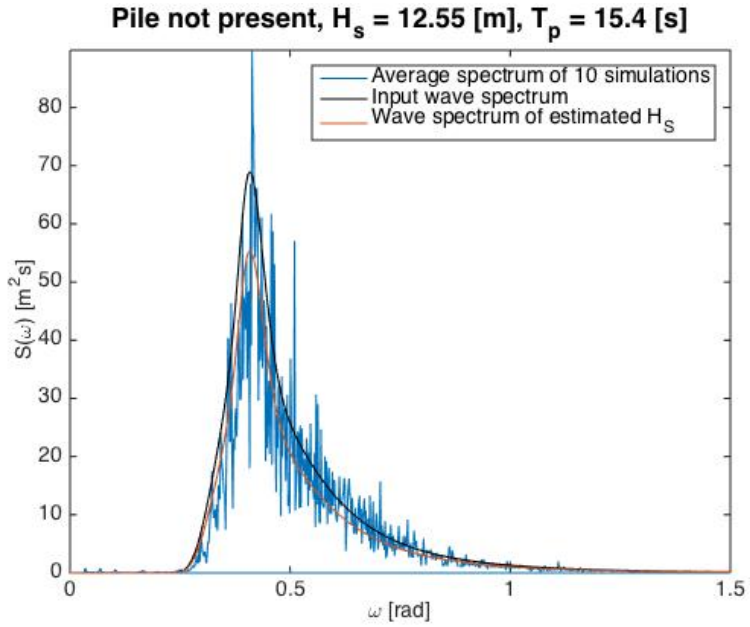

Figure D.52: Averaged estimated wave spectrum for all ten tests of sea state 6 without the pile present.

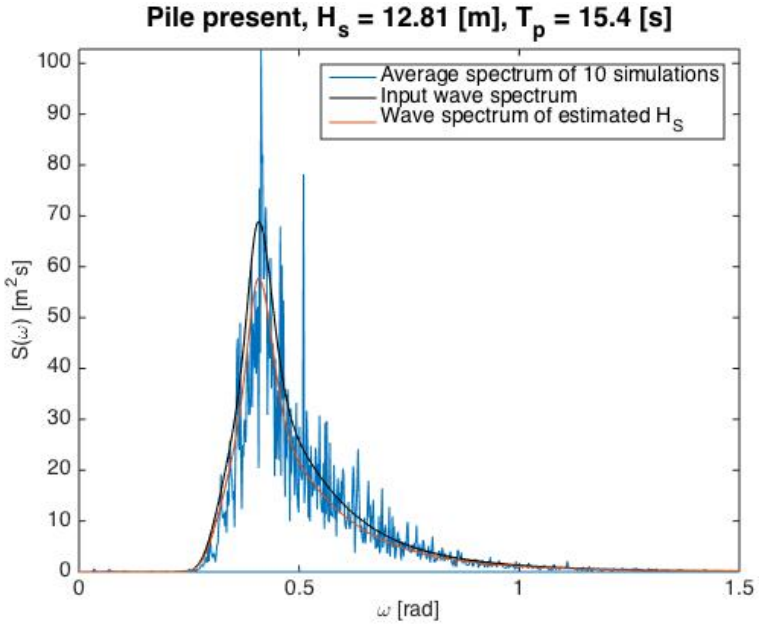

Figure D.53: Averaged estimated wave spectrum for all ten tests of sea state 6 with the pile present.

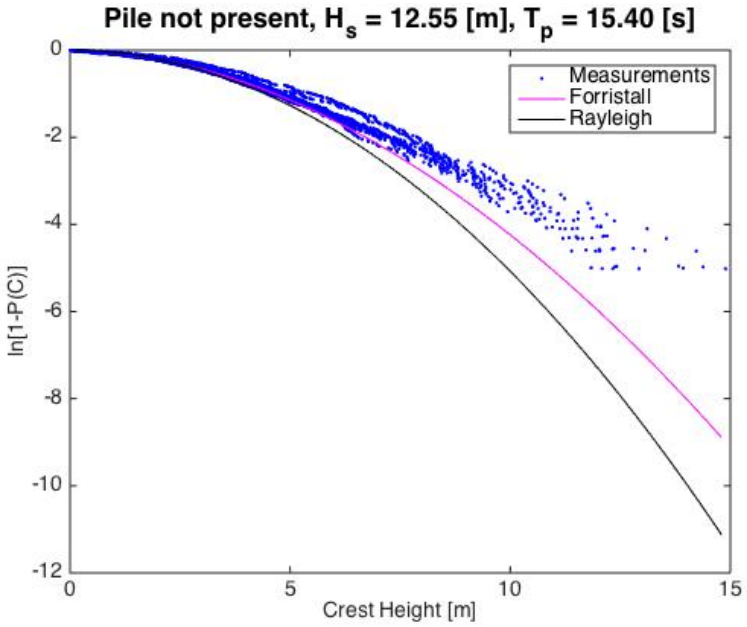

Figure D.54: Distribution of wave crests for all the ten tests of sea state 6 without the pile present.

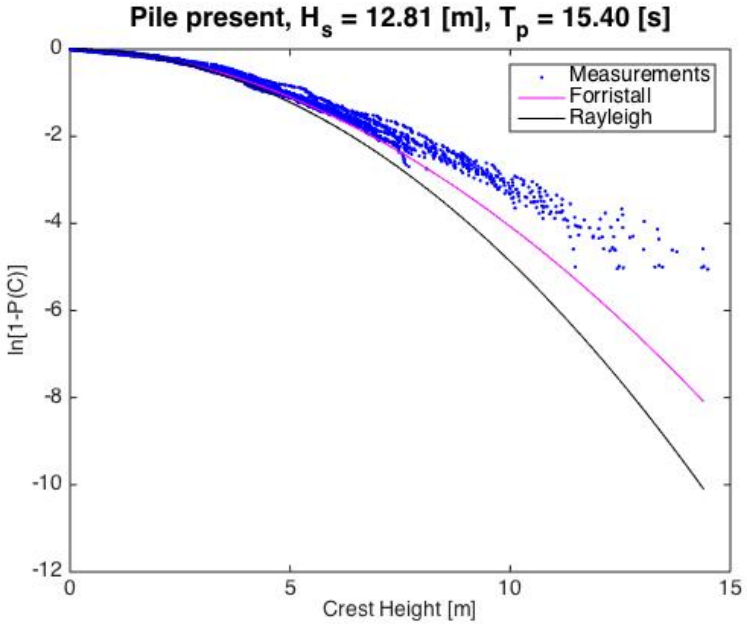

Figure D.55: Distribution of wave crests for all the ten tests of sea state 6 with the pile present.

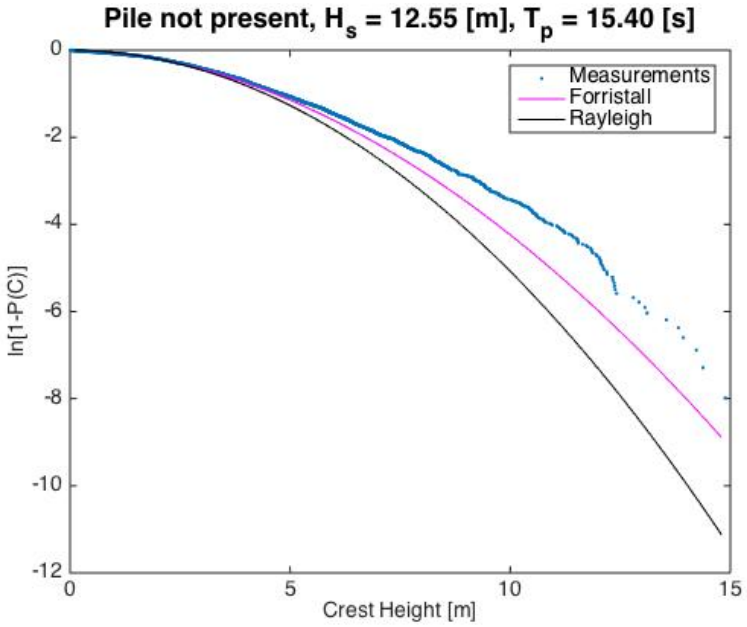

Figure D.56: Distribution of wave crests for all tests smeared together of sea state 6 without the pile present.

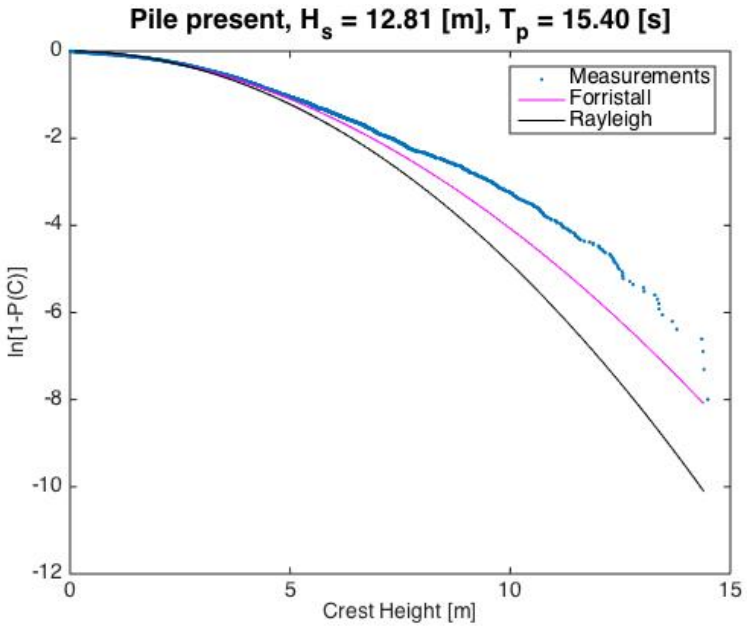

Figure D.57: Distribution of wave crests for all tests smeared together of sea state 6 with the pile present.

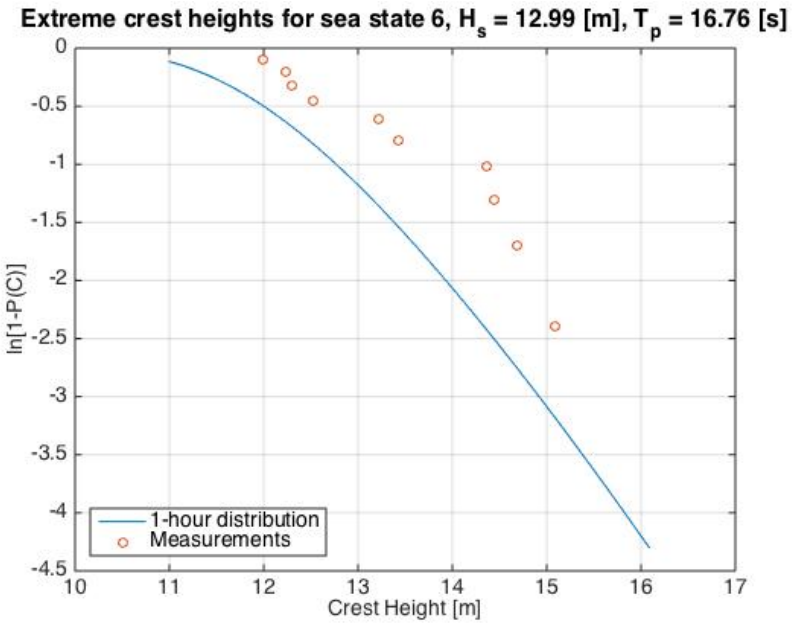

Figure D.58: Distribution of extreme wave crests in sea state 6.

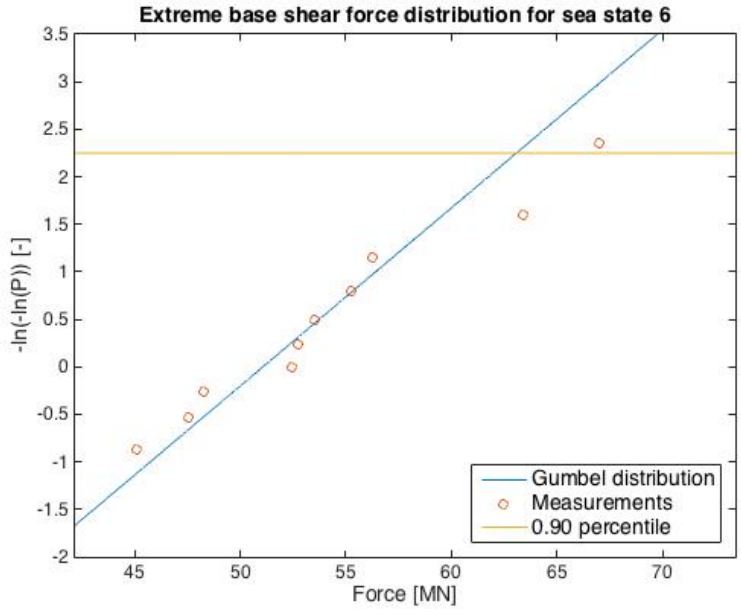

Figure D.59: Distribution of extreme base shear forces in sea state 6.

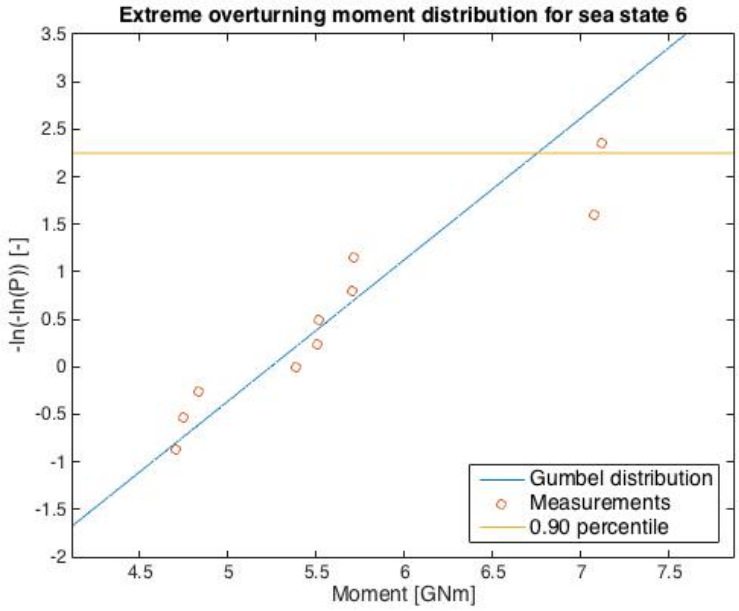

Figure D.60: Distribution of extreme overturning moments in sea state 6.

D.7 Sea state 7

Table D.25: Input information of sea state 7.

Significant wave height	H_S	12.00	[m]
Spectral peak period	T_P	11.30	[s]
Water depth	h	97.0	[m]
Number of tests	#	10	[-]
Duration of each test	d	1	[h]

Table D.26: Variances and significant wave heights for all 10 tests of sea state 7.

	Without pile		With pile	
Test	σ^2 [m^2]	H_S [m]	σ^2 [m^2]	H_S [m]
1	7.35	10.84	7.74	11.13
2	7.51	10.96	7.95	11.26
3	7.79	11.16	8.18	11.44
4	6.91	10.52	7.25	10.77
5	7.51	10.96	7.84	11.20
6	7.16	10.71	7.39	10.87
7	6.95	10.54	7.29	10.80
8	7.04	10.61	7.53	10.97
9	6.96	10.55	7.30	10.81
10	6.69	10.34	7.34	10.84
avg	7.19	10.72	7.58	11.01

Table D.27: Largest measured crest heights, overturning moment and base shear force for all 10 tests of sea state 7.

Test	C_{max} [m]	$C_{max,pile}$ [m]	F_{max} [MN]	M_{max} [GNm]
1	12.78	12.30	50.89	5.67
2	11.50	11.06	57.10	6.03
3	11.49	12.78	53.31	5.99
4	11.58	13.12	58.71	6.69
5	12.29	13.70	56.17	6.31
6	13.37	12.46	58.67	6.42
7	12.55	10.86	55.28	6.17
8	10.59	10.46	56.09	6.17
9	11.90	10.92	51.08	5.51
10	11.11	10.79	48.32	5.33

Table D.28: Output information of sea state 7.

Variance	σ^2_{out}	7.19	[m^2]	σ^2_{pile}	7.58	[m^2]
Standard deviation	σ_{out}	2.68	[m]	σ_{pile}	2.75	[m]
Significant wave height	$H_{S,out}$	10.72	[m]	$H_{S,pile}$	11.01	[m]
Sea state steepness	ε_{out}	0.0540	[-]	ε_{pile}	0.0555	[-]
Range $\frac{H_{S,min}-H_{S,max}}{H_{S,mean}} \cdot 100$	$\Delta H_{S,out}$	7.65	[%]	$\Delta H_{S,pile}$	6.09	[%]
Deviation from $H_{S,in}$	$\frac{H_{S,out}}{H_{S,in}}$	0.8933	[-]	$\frac{H_{S,pile}}{H_{S,in}}$	0.9175	[-]

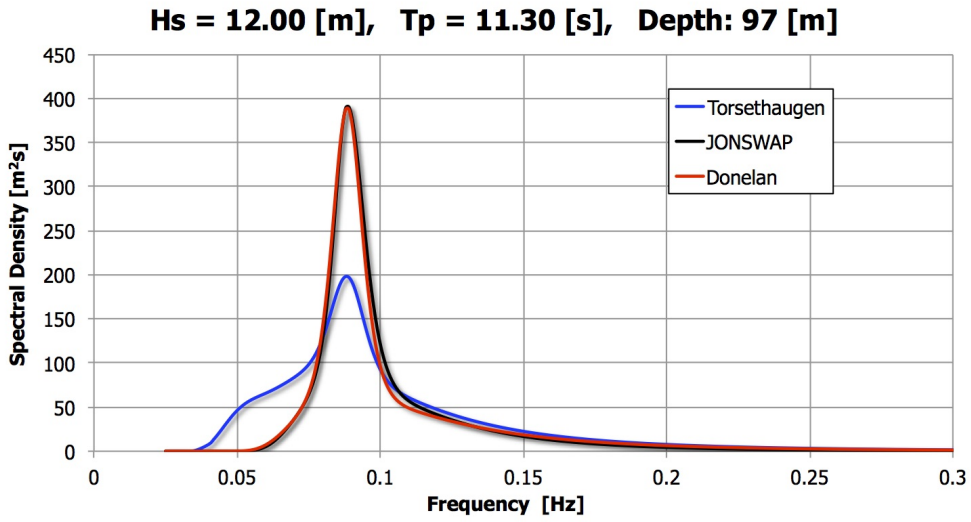

Figure D.61: Comparison of the JONSWAP, Torsethaugen and Donelan spectrum for sea state 7.

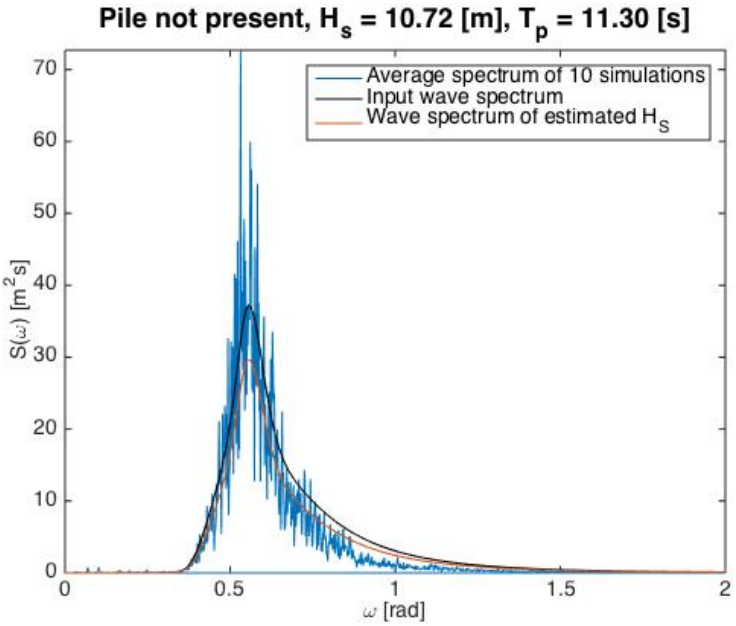

Figure D.62: Averaged estimated wave spectrum for all ten tests of sea state 7 without the pile present.

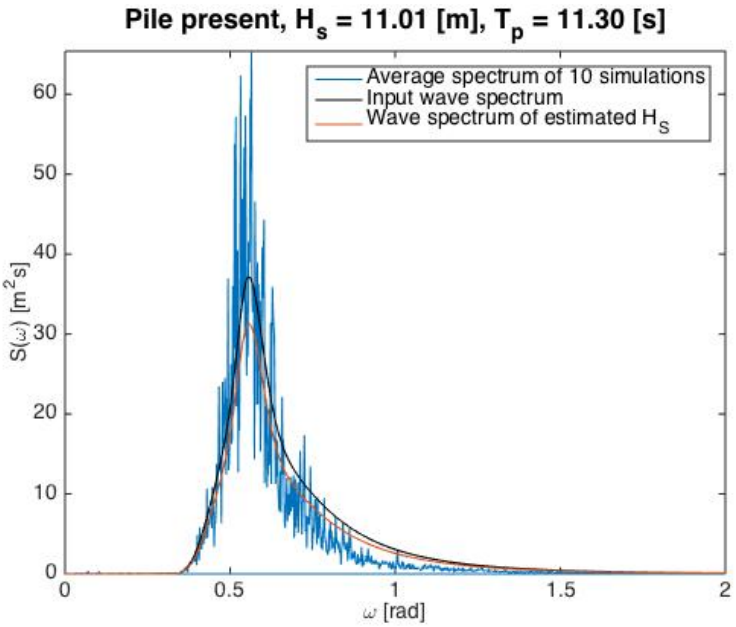

Figure D.63: Averaged estimated wave spectrum for all ten tests of sea state 7 with the pile present.

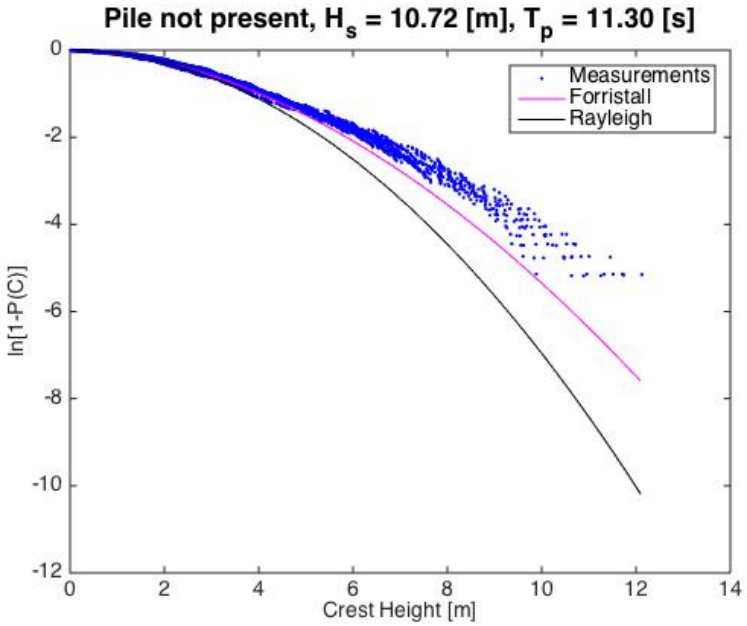

Figure D.64: Distribution of wave crests for all the ten tests of sea state 7 without the pile present.

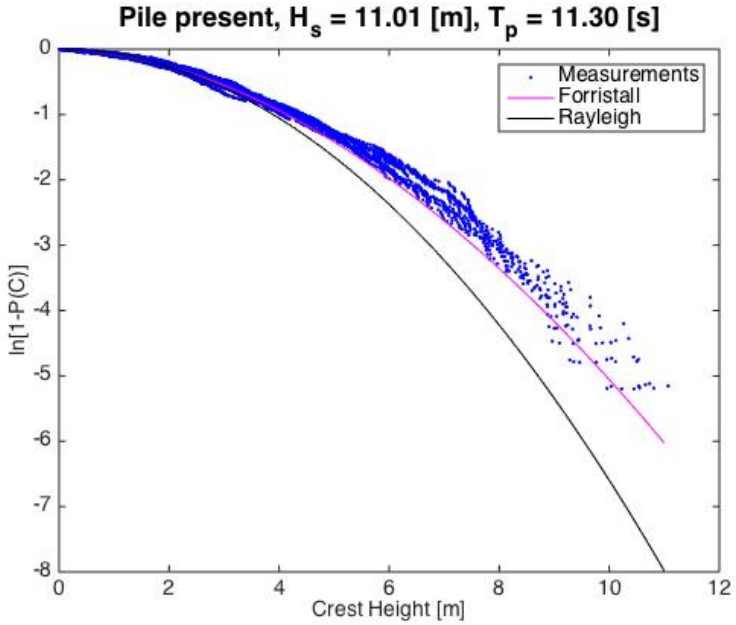

Figure D.65: Distribution of wave crests for all the ten tests of sea state 7 with the pile present.

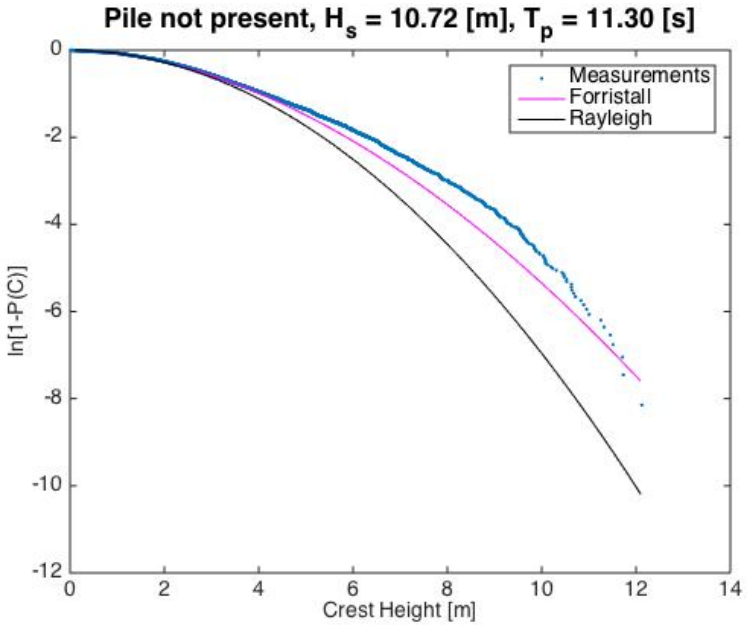

Figure D.66: Distribution of wave crests for all tests smeared together of sea state 7 without the pile present.

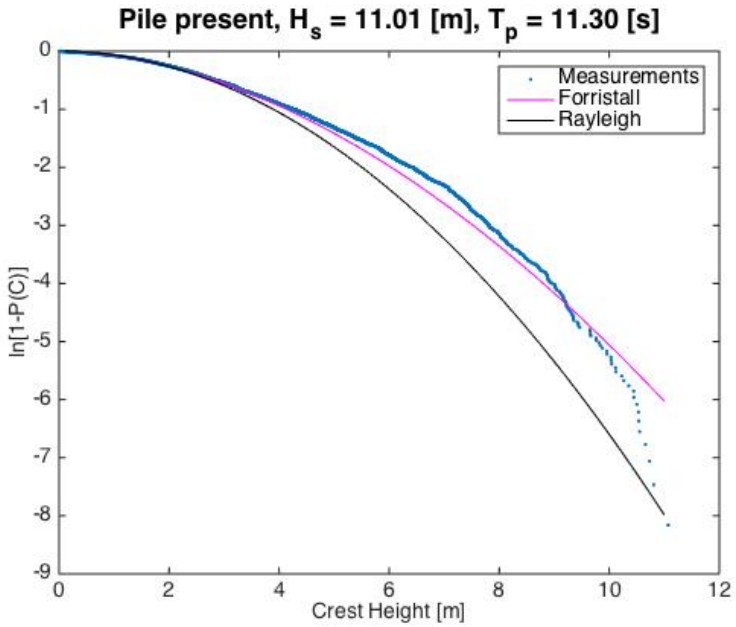

Figure D.67: Distribution of wave crests for all tests smeared together of sea state 7 with the pile present.

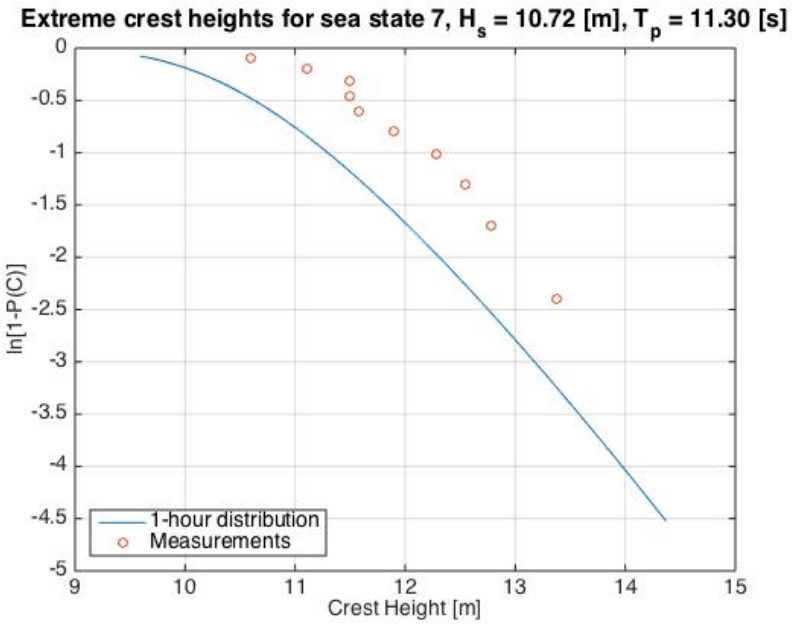

Figure D.68: Distribution of extreme wave crests in sea state 7.

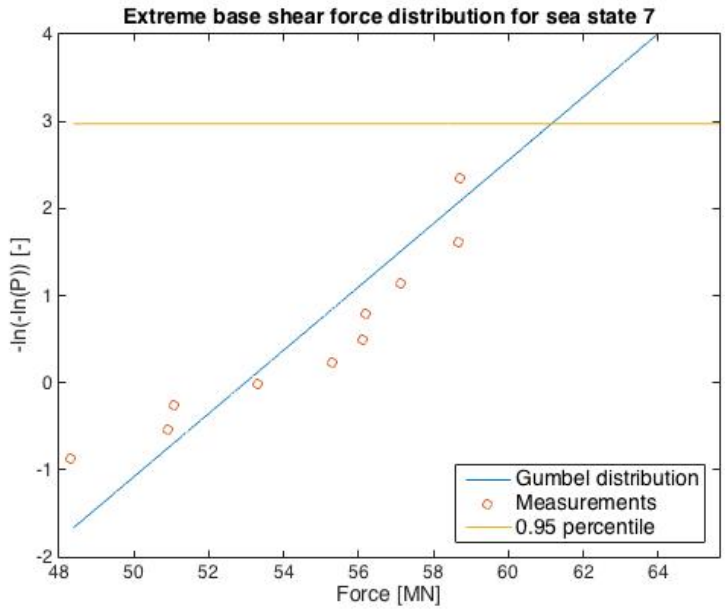

Figure D.69: Distribution of extreme base shear forces in sea state 7.

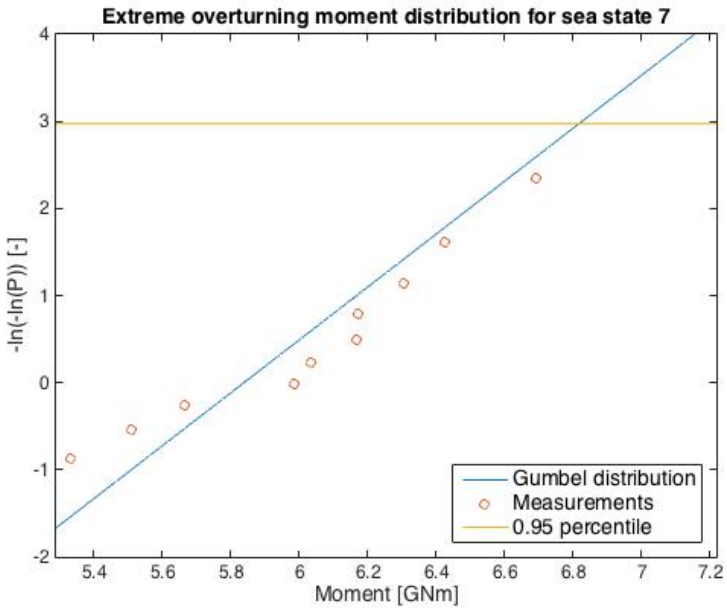

Figure D.70: Distribution of extreme overturning moments in sea state 7.

D.8 Sea state 8

Table D.29: Input information of sea state 8.

Significant wave height	H_S	13.00	[m]
Spectral peak period	T_P	12.00	[s]
Water depth	h	95.5	[m]
Number of tests	#	10	[-]
Duration of each test	d	1	[h]

Table D.30: Variances and significant wave heights for all 10 tests of sea state 8.

	Without pile		With pile	
Test	σ^2 [m^2]	H_S [m]	σ^2 [m^2]	H_S [m]
1	8.17	11.43	8.68	11.79
2	7.65	11.06	7.81	11.18
3	7.28	10.79	7.56	11.00
4	7.91	11.25	8.22	11.47
5	8.08	11.37	8.56	11.70
6	7.41	10.89	7.55	10.99
7	8.25	11.49	8.67	11.78
8	8.29	11.51	8.67	11.78
9	8.02	11.33	8.18	11.44
10	8.69	11.79	9.15	12.10
avg	7.97	11.29	8.31	11.52

Table D.31: Largest measured crest heights, overturning moment and base shear force for all 10 tests of sea state 8.

Test	C_{max} [m]	$C_{max,pile}$ [m]	F_{max} [MN]	M_{max} [GNm]
1	11.02	12.36	47.73	5.41
2	14.81	12.34	57.82	6.69
3	13.26	13.04	45.46	5.34
4	12.04	10.14	48.63	5.40
5	12.05	12.75	49.45	5.49
6	13.22	13.03	50.02	5.67
7	12.03	12.63	50.26	5.77
8	13.45	13.85	56.33	6.06
9	14.28	13.06	54.26	6.12
10	15.00	14.63	60.44	6.56

Table D.32: Output information of sea state 8.

Variance	σ^2_{out}	7.97	[m^2]	σ^2_{pile}	8.31	[m^2]
Standard deviation	σ_{out}	2.82	[m]	σ_{pile}	2.88	[m]
Significant wave height	$H_{S,out}$	11.29	[m]	$H_{S,pile}$	11.52	[m]
Sea state steepness	ε_{out}	0.0506	[-]	ε_{pile}	0.0517	[-]
Range $\frac{H_{S,min}-H_{S,max}}{H_{S,mean}} \cdot 100$	$\Delta H_{S,out}$	8.86	[%]	$\Delta H_{S,pile}$	9.64	[%]
Deviation from $H_{S,in}$	$\frac{H_{S,out}}{H_{S,in}}$	0.8685	[-]	$\frac{H_{S,pile}}{H_{S,in}}$	0.8862	[-]

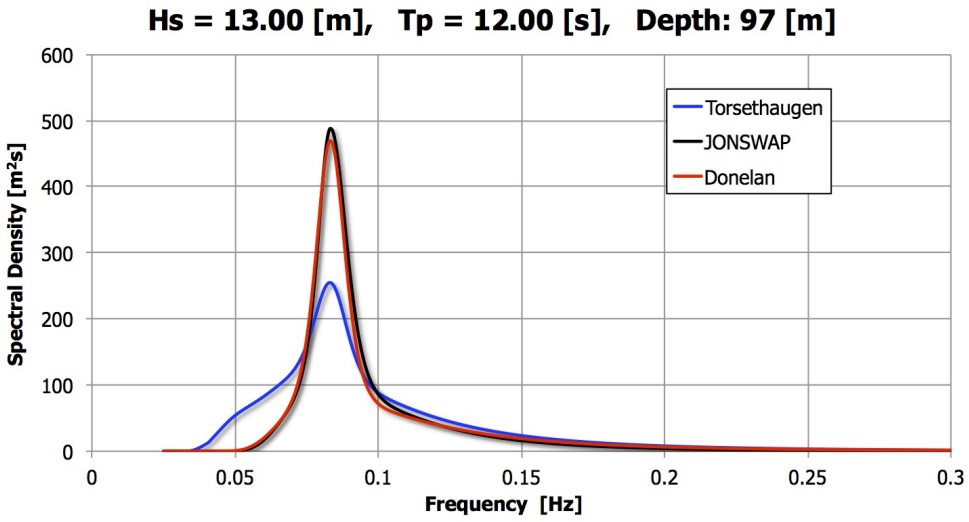

Figure D.71: Comparison of the JONSWAP, Torsethaugen and Donelan spectrum for sea state 8.

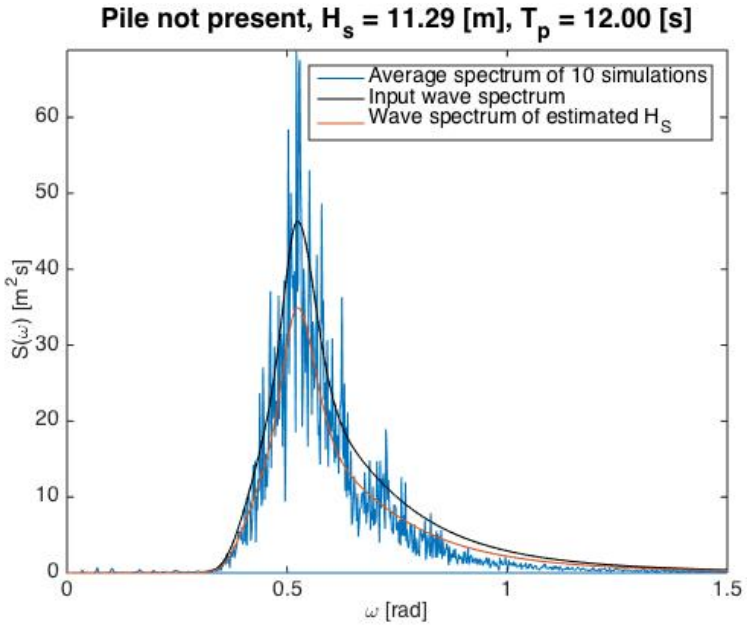

Figure D.72: Averaged estimated wave spectrum for all ten tests of sea state 8 without the pile present.

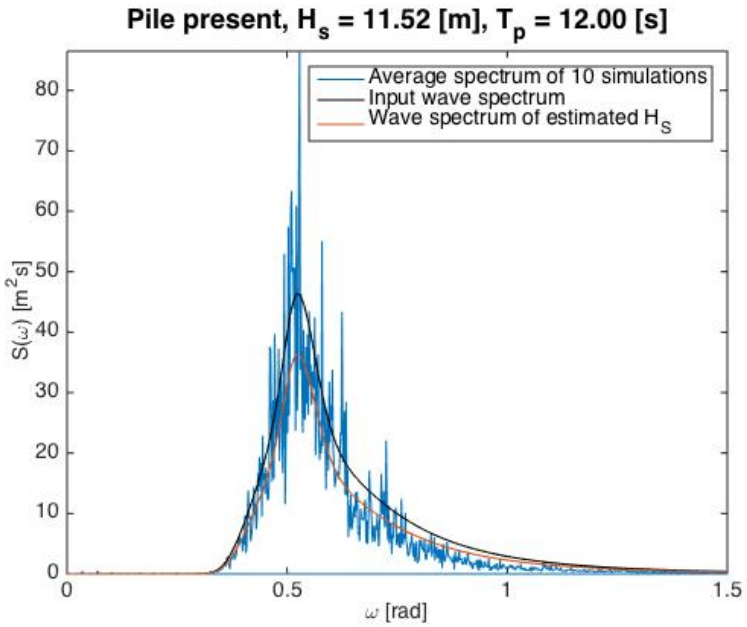

Figure D.73: Averaged estimated wave spectrum for all ten tests of sea state 8 with the pile present.

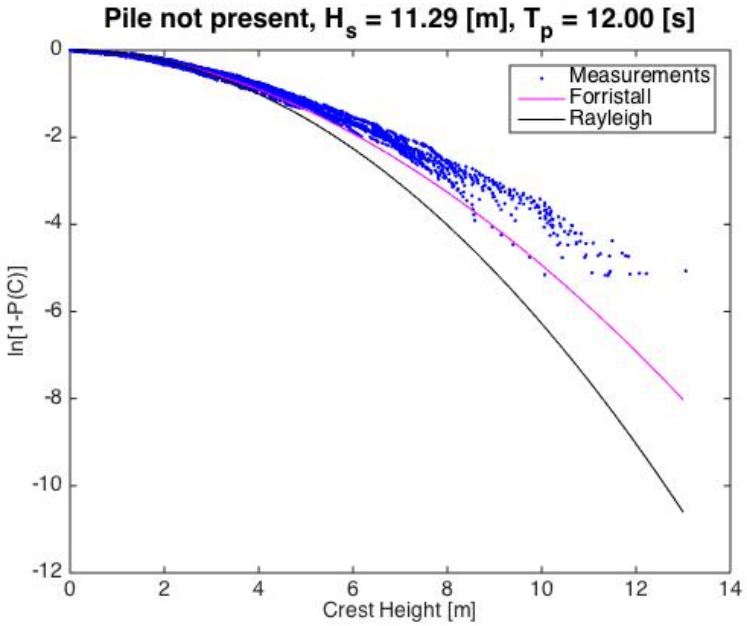

Figure D.74: Distribution of wave crests for all the ten tests of sea state 8 without the pile present.

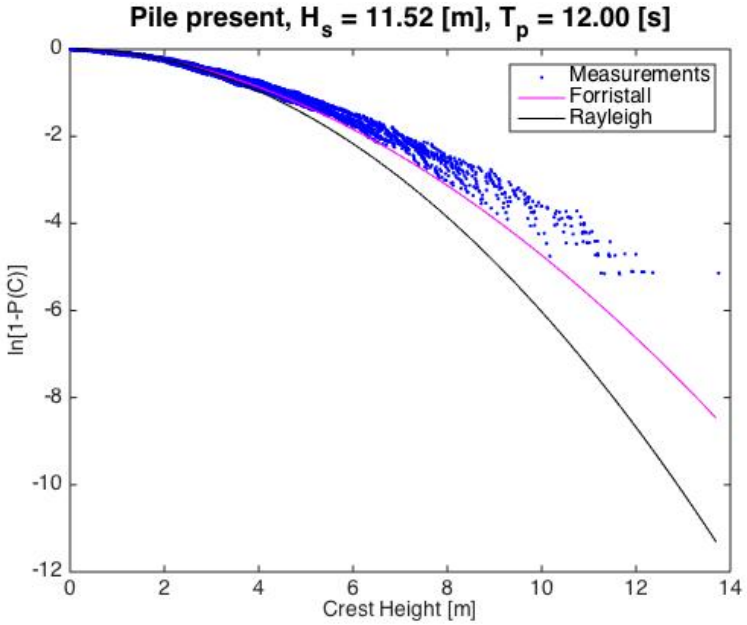

Figure D.75: Distribution of wave crests for all the ten tests of sea state 8 with the pile present.

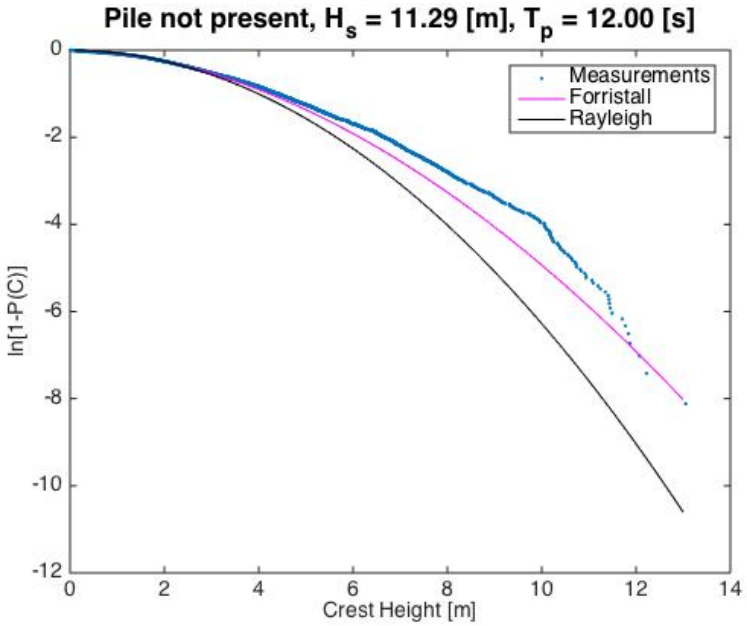

Figure D.76: Distribution of wave crests for all tests smeared together of sea state 8 without the pile present.

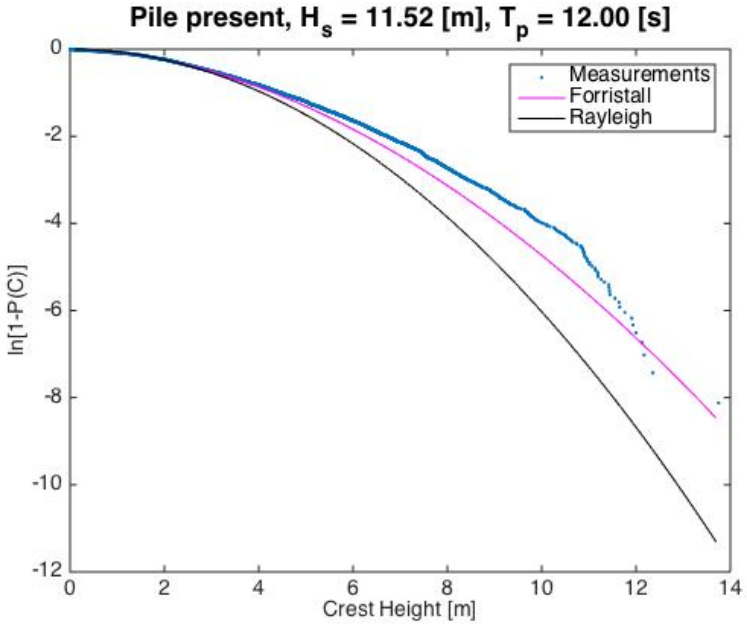

Figure D.77: Distribution of wave crests for all tests smeared together of sea state 8 with the pile present.

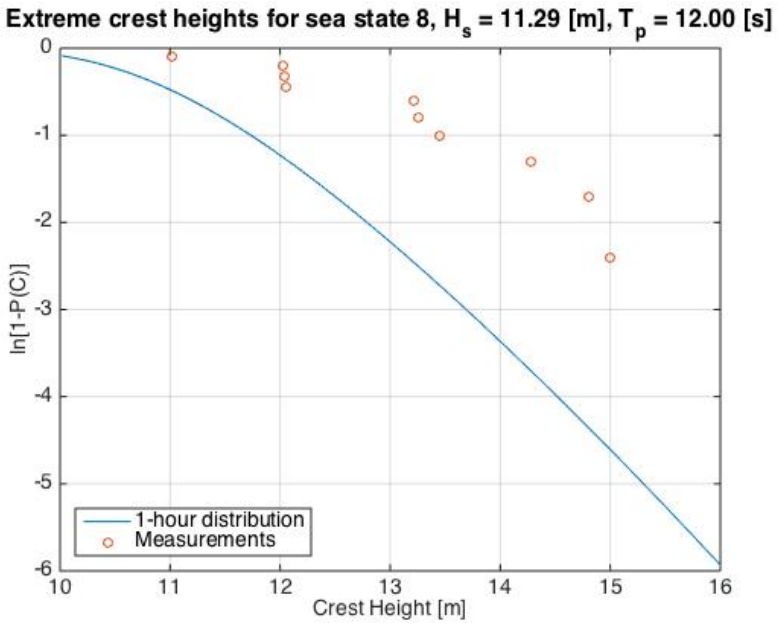

Figure D.78: Distribution of extreme wave crests in sea state 8.

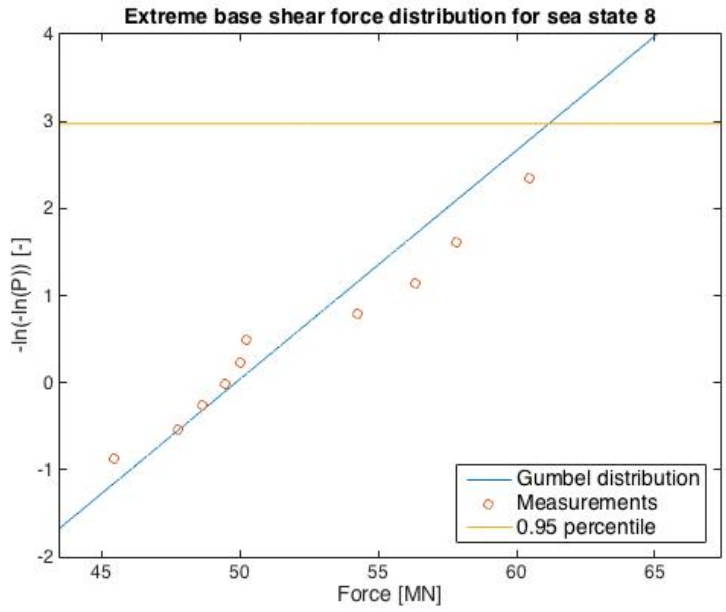

Figure D.79: Distribution of extreme base shear forces in sea state 8.

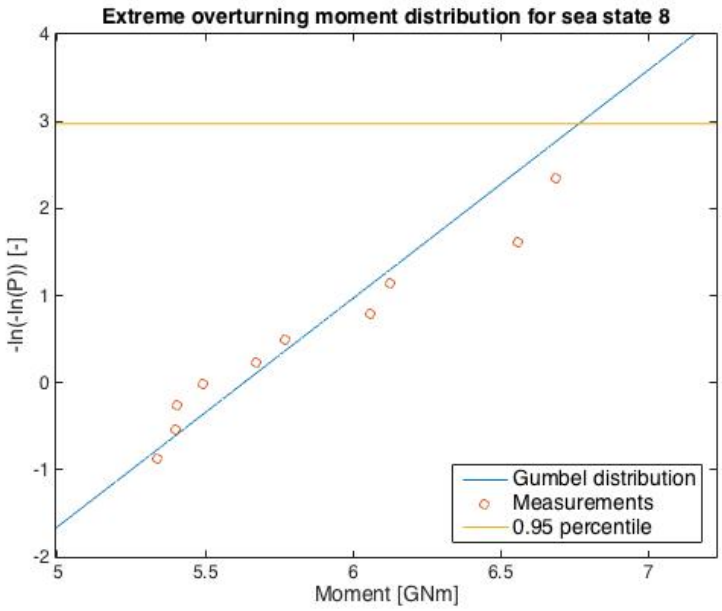

Figure D.80: Distribution of extreme overturning moments in sea state 8.

D.9 Sea state 9

Table D.33: Input information of sea state 9.

Significant wave height	H_S	14.00	[m]
Spectral peak period	T_P	13.00	[s]
Water depth	h	97	[m]
Number of tests	#	10	[-]
Duration of each test	d	1	[h]

Table D.34: Variances and significant wave heights for all 10 tests of sea state 9.

	Without pile		With pile	
Test	σ^2 [m^2]	H_S [m]	σ^2 [m^2]	H_S [m]
1	9.11	12.07	9.61	12.40
2	9.93	12.60	10.34	12.87
3	9.53	12.35	9.96	12.62
4	9.99	12.65	10.44	12.92
5	9.82	12.54	10.39	12.90
6	10.15	12.74	11.04	13.29
7	8.79	11.86	9.10	12.07
8	8.54	11.69	8.86	11.91
9	10.01	12.65	10.67	13.07
10	10.23	12.79	10.93	13.22
avg	9.61	12.39	10.13	12.73

Table D.35: Largest measured crest heights, overturning moment and base shear force for all 10 tests of sea state 9.

Test	C_{max} [m]	$C_{max,pile}$ [m]	F_{max} [MN]	M_{max} [GNm]
1	15.02	15.16	54.26	6.20
2	16.75	17.00	54.78	6.05
3	15.63	18.56	48.48	5.55
4	14.92	18.04	63.62	7.21
5	13.36	15.68	54.66	6.05
6	14.17	13.84	50.94	5.82
7	12.78	12.80	49.04	5.36
8	12.41	13.17	52.53	6.11
9	14.63	14.25	61.49	6.99
10	15.53	16.14	55.79	6.24

Table D.36: Output information of sea state 9.

Variance	σ^2_{out}	9.61	[m^2]	σ^2_{pile}	10.13	[m^2]
Standard deviation	σ_{out}	3.10	[m]	σ_{pile}	3.18	[m]
Significant wave height	$H_{S,out}$	12.39	[m]	$H_{S,pile}$	12.73	[m]
Sea state steepness	ε_{out}	0.0478	[-]	ε_{pile}	0.0491	[-]
Range $\frac{H_{S,min}-H_{S,max}}{H_{S,mean}} \cdot 100$	$\Delta H_{S,out}$	8.88	[%]	$\Delta H_{S,pile}$	10.84	[%]
Deviation from $H_{S,in}$	$\frac{H_{S,out}}{H_{S,in}}$	0.8850	[-]	$\frac{H_{S,pile}}{H_{S,in}}$	0.9093	[-]

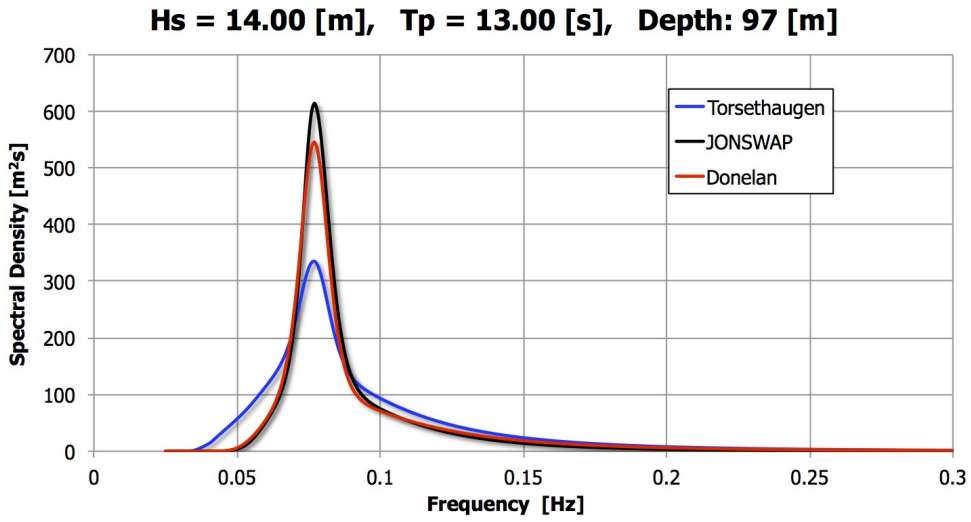

Figure D.81: Comparison of the JONSWAP, Torsethaugen and Donelan spectrum for sea state 9.

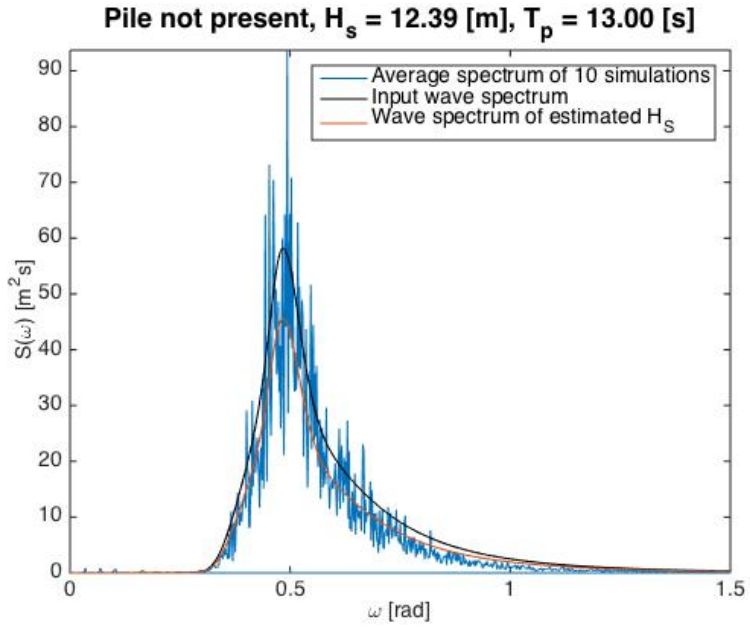

Figure D.82: Averaged estimated wave spectrum for all ten tests of sea state 9 without the pile present.

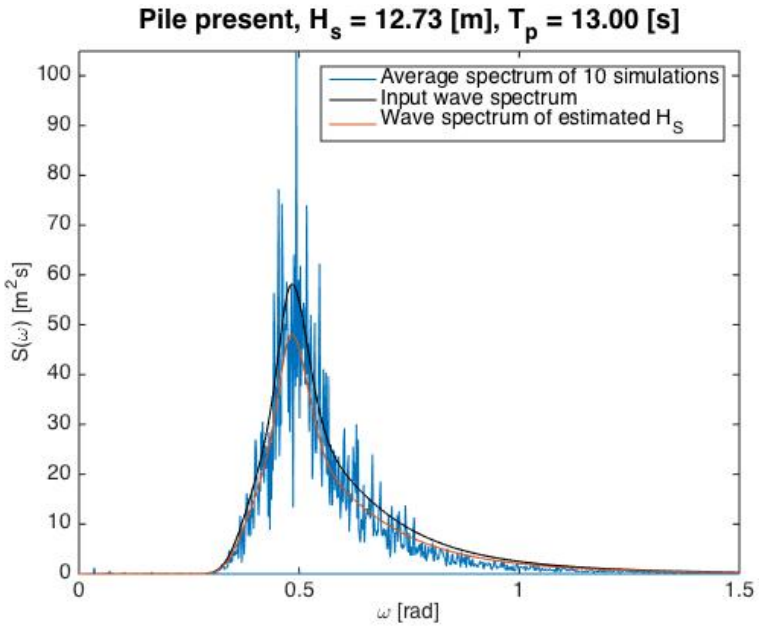

Figure D.83: Averaged estimated wave spectrum for all ten tests of sea state 9 with the pile present.

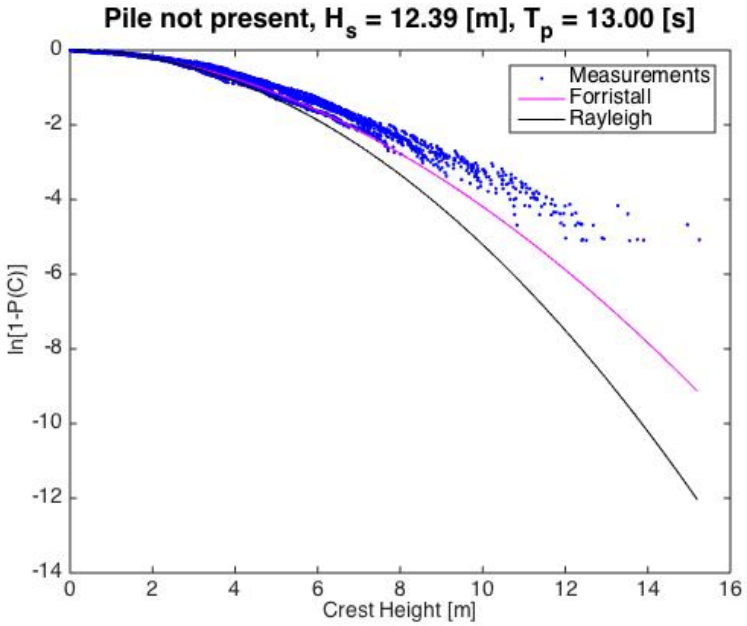

Figure D.84: Distribution of wave crests for all the ten tests of sea state 9 without the pile present.

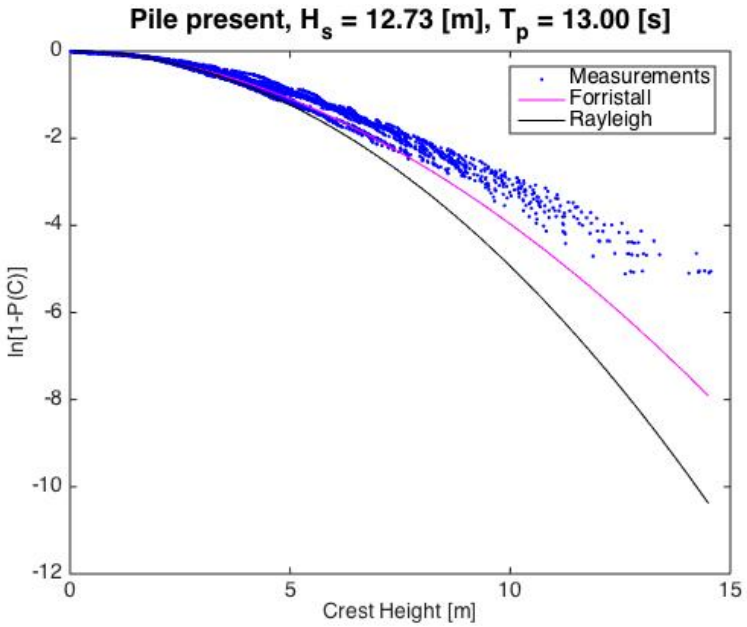

Figure D.85: Distribution of wave crests for all the ten tests of sea state 9 with the pile present.

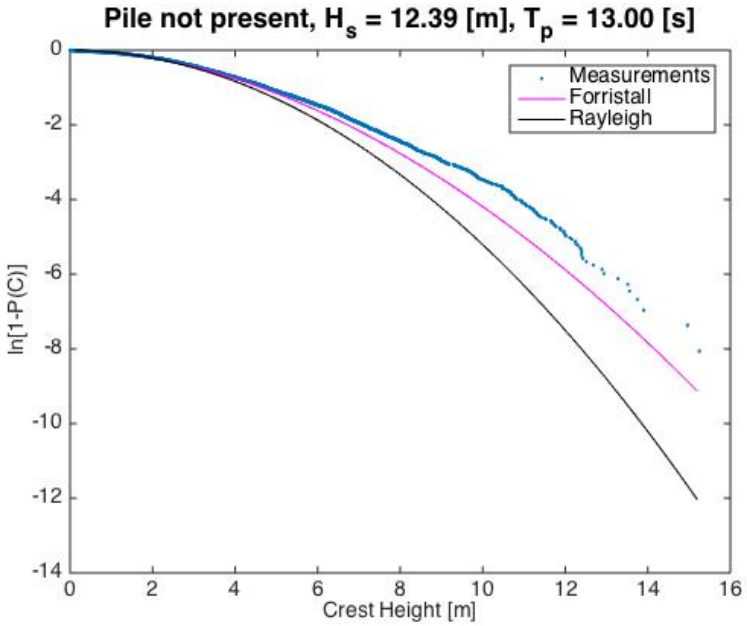

Figure D.86: Distribution of wave crests for all tests smeared together of sea state 9 without the pile present.

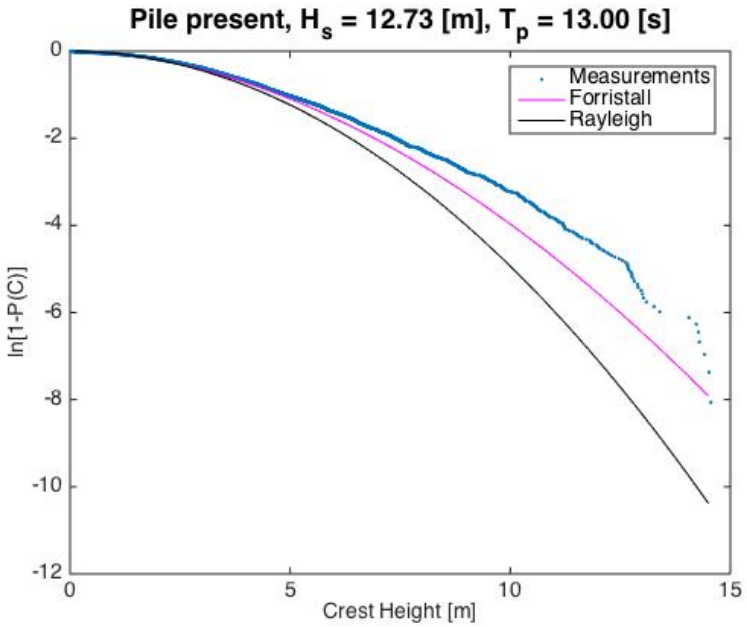

Figure D.87: Distribution of wave crests for all tests smeared together of sea state 9 with the pile present.

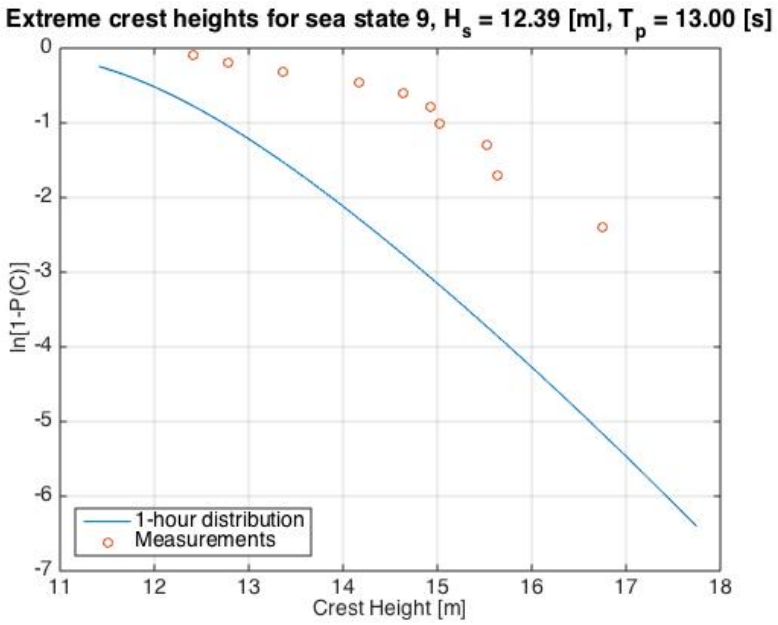

Figure D.88: Distribution of extreme wave crests in sea state 9.

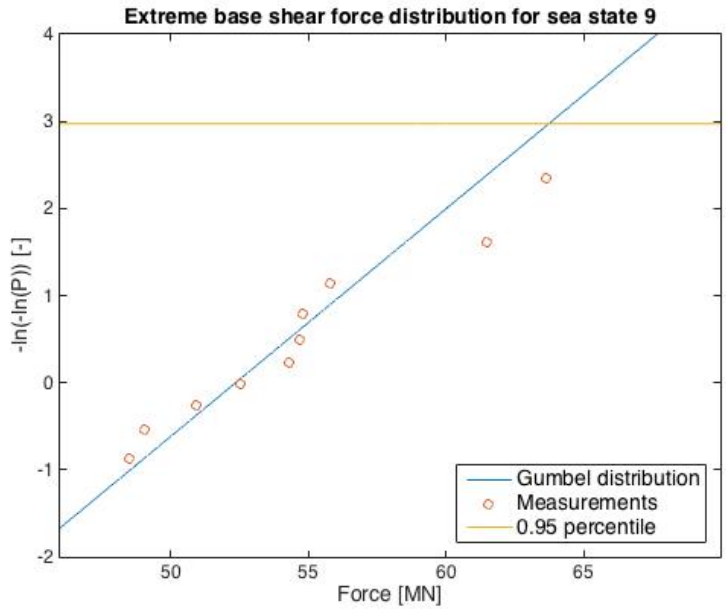

Figure D.89: Distribution of extreme base shear forces in sea state 9.

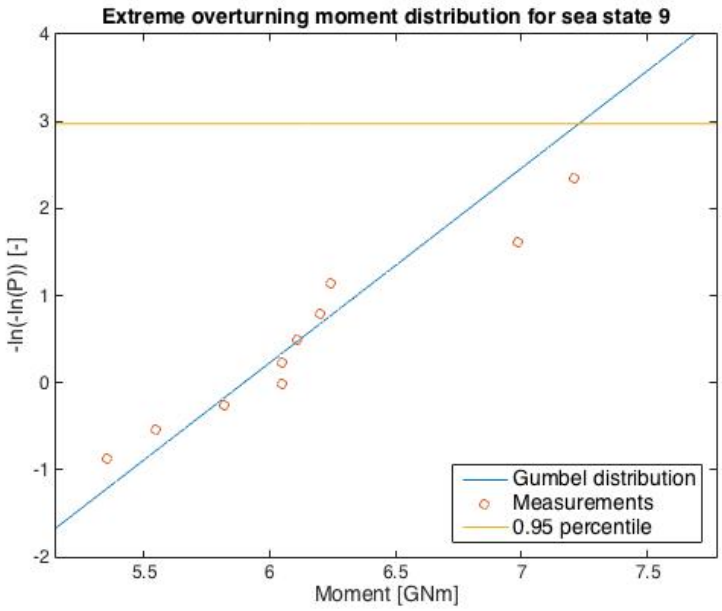

Figure D.90: Distribution of extreme overturning moments in sea state 9.

D.10 Sea state 10

Table D.37: Input information of sea state 10.

Significant wave height	H_S	15.00	[m]
Spectral peak period	T_P	14.00	[s]
Water depth	h	96.9	[m]
Number of tests	#	10	[-]
Duration of each test	d	1	[h]

Table D.38: Variances and significant wave heights for all 10 tests of sea state 10.

	Without pile		With pile	
Test	σ^2 [m^2]	H_S [m]	σ^2 [m^2]	H_S [m]
1	9.92	12.60	10.66	13.06
2	12.07	13.90	12.20	13.97
3	11.65	13.65	12.68	14.25
4	10.88	13.19	11.52	13.58
5	10.96	13.24	11.75	13.71
6	10.63	13.04	11.05	13.30
7	10.74	13.11	11.14	13.35
8	11.12	13.34	11.63	13.64
9	10.17	12.76	11.05	13.30
10	12.18	13.96	12.52	14.15
avg	11.03	13.28	11.62	13.63

Table D.39: Largest measured crest heights, overturning moment and base shear force for all 10 tests of sea state 10.

Test	C_{max} [m]	$C_{max,pile}$ [m]	F_{max} [MN]	M_{max} [GNm]
1	14.60	14.53	50.58	5.73
2	12.64	13.87	53.73	5.81
3	14.75	16.43	58.70	6.29
4	14.70	16.08	60.16	6.50
5	15.03	15.99	54.55	5.82
6	12.25	12.58	50.86	5.72
7	14.39	13.52	55.72	6.15
8	15.36	17.42	57.90	6.53
9	13.00	13.57	44.01	4.98
10	18.59	21.01	73.11	7.74

Table D.40: Output information of sea state 10.

Variance	σ^2_{out}	11.03	[m^2]	σ^2_{pile}	11.62	[m^2]
Standard deviation	σ_{out}	3.32	[m]	σ_{pile}	3.41	[m]
Significant wave height	$H_{S,out}$	13.28	[m]	$H_{S,pile}$	13.63	[m]
Sea state steepness	ε_{out}	0.0448	[-]	ε_{pile}	0.0460	[-]
Range $\frac{H_{S,min}-H_{S,max}}{H_{S,mean}} \cdot 100$	$\Delta H_{S,out}$	10.24	[%]	$\Delta H_{S,pile}$	8.73	[%]
Deviation from $H_{S,in}$	$\frac{H_{S,out}}{H_{S,in}}$	0.8863	[-]	$\frac{H_{S,pile}}{H_{S,in}}$	0.9087	[-]

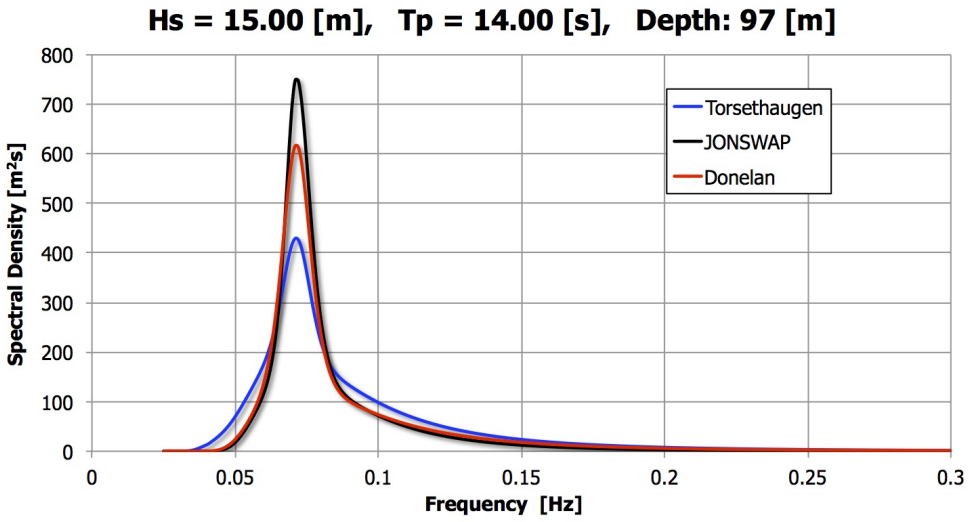

Figure D.91: Comparison of the JONSWAP, Torsethaugen and Donelan spectrum for sea state 10.

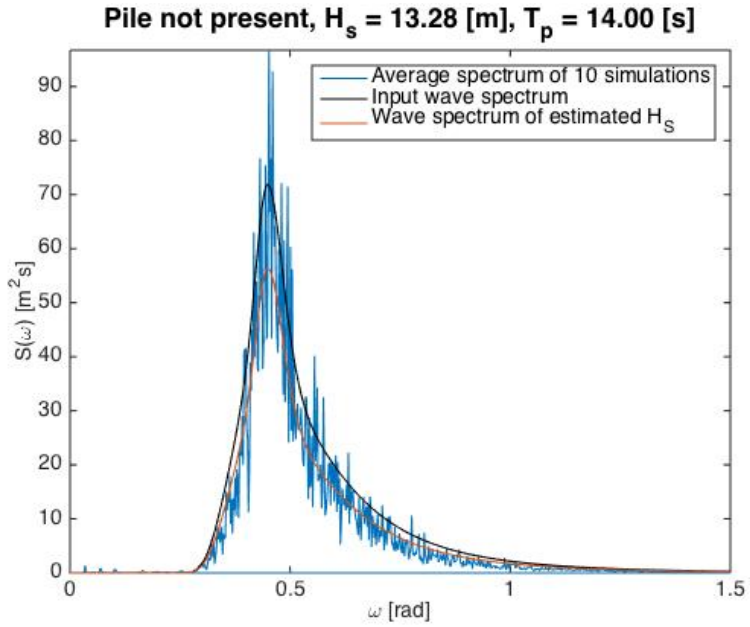

Figure D.92: Averaged estimated wave spectrum for all ten tests of sea state 10 without the pile present.

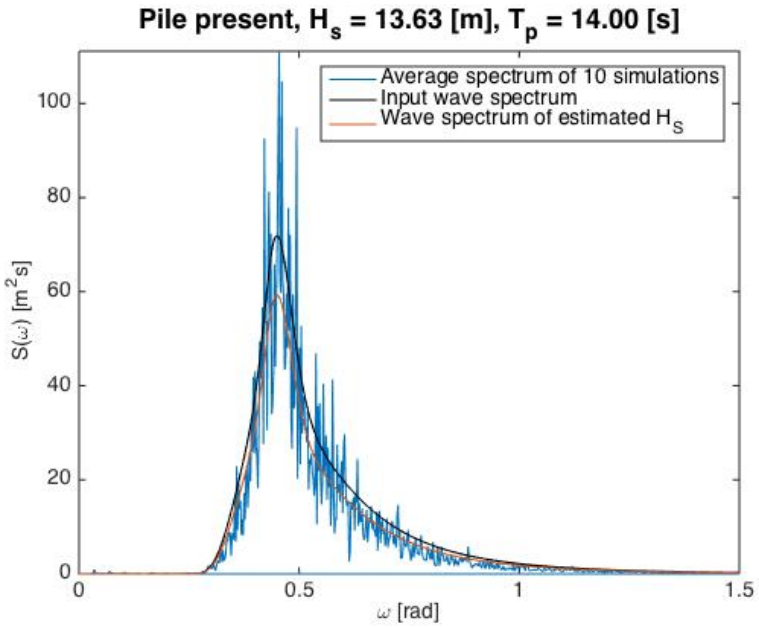

Figure D.93: Averaged estimated wave spectrum for all ten tests of sea state 10 with the pile present.

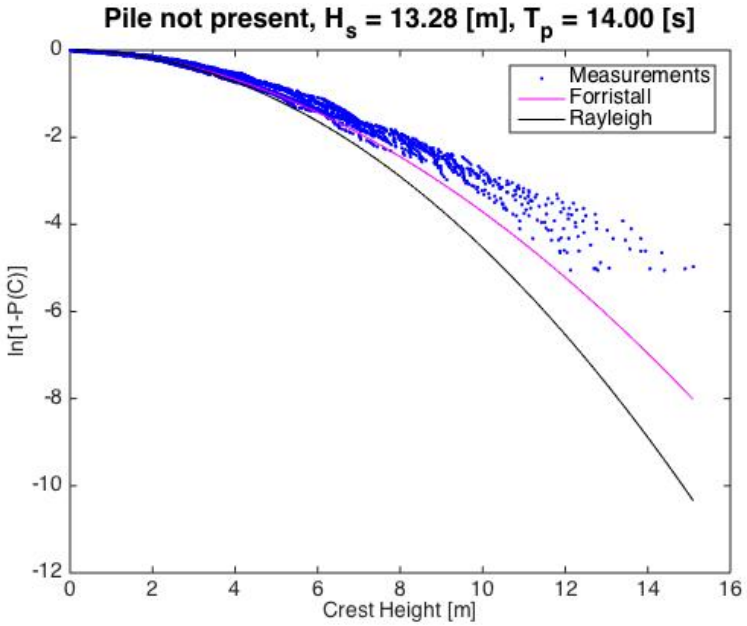

Figure D.94: Distribution of wave crests for all the ten tests of sea state 10 without the pile present.

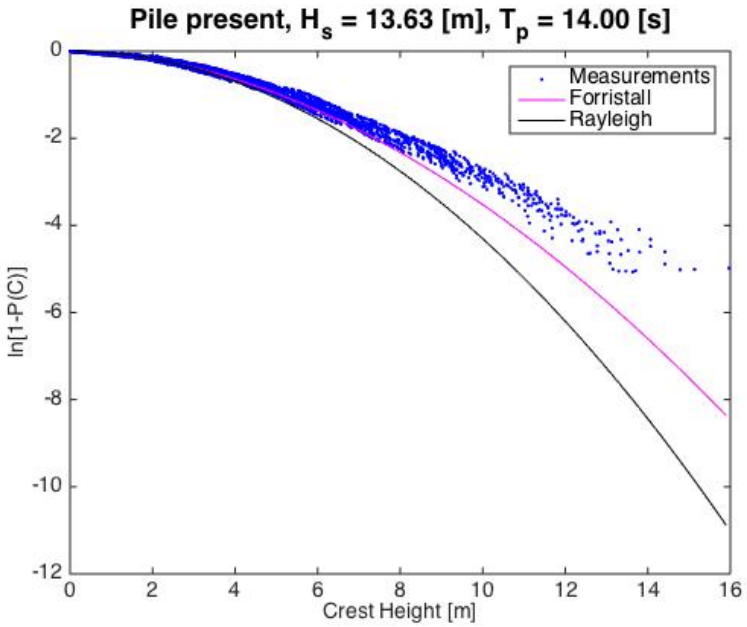

Figure D.95: Distribution of wave crests for all the ten tests of sea state 10 with the pile present.

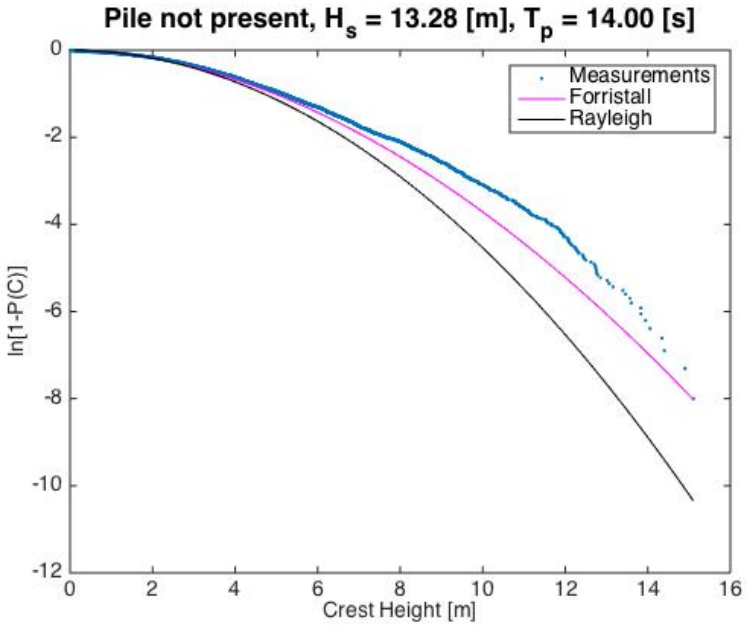

Figure D.96: Distribution of wave crests for all tests smeared together of sea state 10 without the pile present.

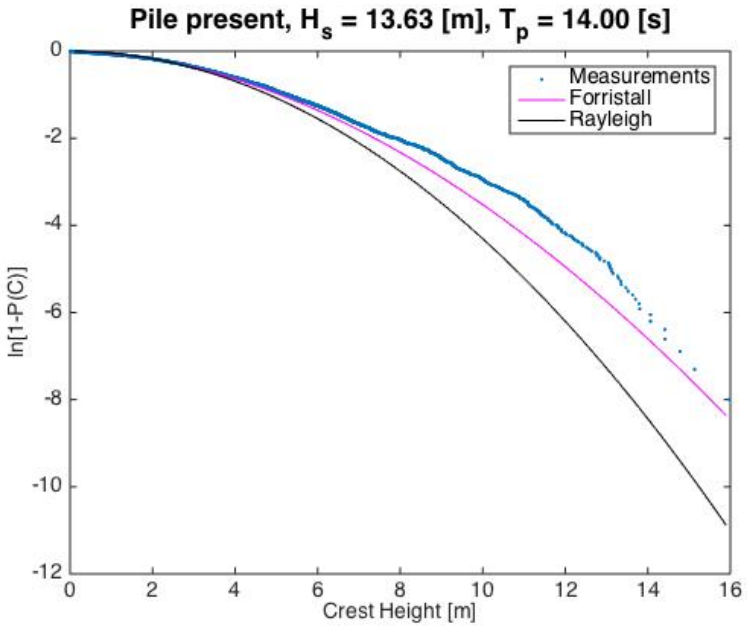

Figure D.97: Distribution of wave crests for all tests smeared together of sea state 10 with the pile present.

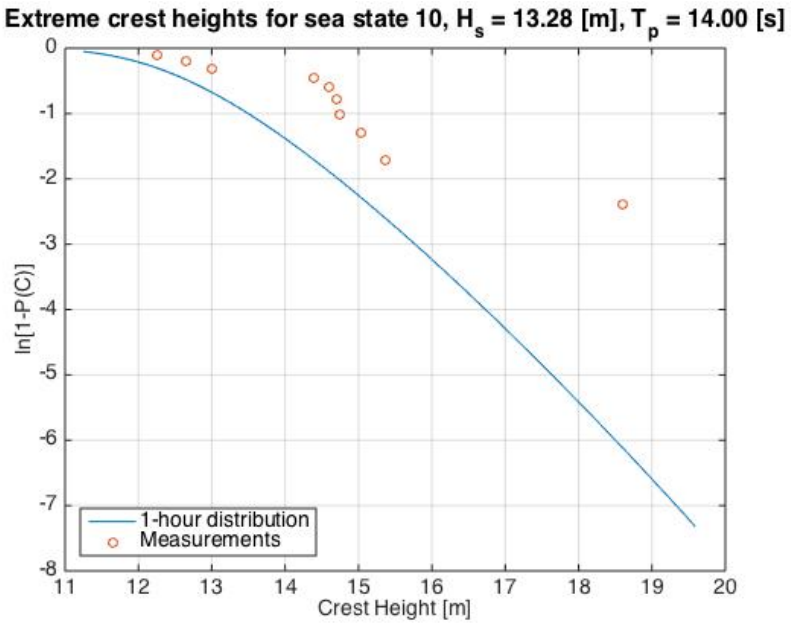

Figure D.98: Distribution of extreme wave crests in sea state 10.

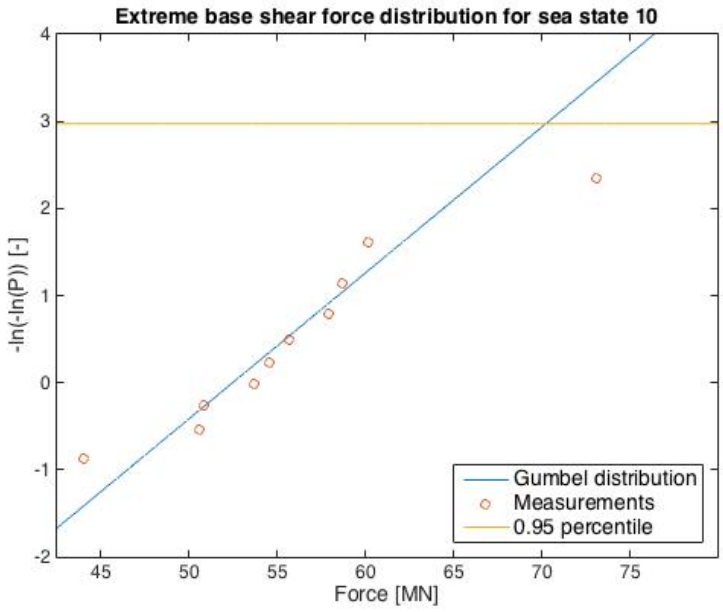

Figure D.99: Distribution of extreme base shear forces in sea state 10.

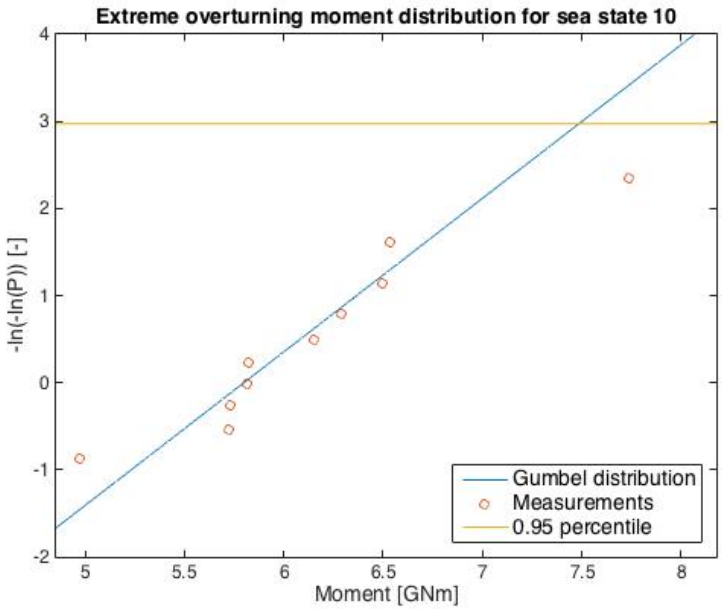

Figure D.100: Distribution of extreme overturning moments in sea state 10.

D.11 Sea state 11

Table D.41: Input information of sea state 11.

Significant wave height	H_S	16.00	[m]
Spectral peak period	T_P	15.20	[s]
Water depth	h	96.8	[m]
Number of tests	#	10	[-]
Duration of each test	d	1	[h]

Table D.42: Variances and significant wave heights for all 10 tests of sea state 11.

	Without pile		With pile	
Test	σ^2 [m^2]	H_S [m]	σ^2 [m^2]	H_S [m]
1	10.24	12.80	10.84	13.17
2	12.56	14.17	13.42	14.65
3	12.30	14.03	13.03	14.44
4	12.26	14.00	13.00	14.42
5	11.54	13.59	11.90	13.80
6	11.93	13.81	12.50	14.14
7	11.19	13.38	11.67	13.67
8	11.27	13.43	11.97	13.84
9	11.92	13.81	12.49	14.13
10	13.16	14.51	14.23	15.09
avg	11.84	13.75	12.50	14.14

Table D.43: Largest measured crest heights, overturning moment and base shear force for all 10 tests of sea state 11.

Test	C_{max} [m]	$C_{max,pile}$ [m]	F_{max} [MN]	M_{max} [GNm]
1	11.83	14.65	45.92	4.76
2	18.23	19.74	71.51	7.25
3	16.26	15.15	61.21	6.49
4	14.82	16.41	57.73	6.32
5	15.29	16.76	56.85	6.64
6	14.51	18.28	53.23	5.67
7	12.63	15.99	55.43	5.79
8	17.82	20.22	73.26	7.91
9	14.40	14.43	56.02	5.97
10	14.51	14.28	58.94	6.41

Table D.44: Output information of sea state 11.

Variance	σ^2_{out}	11.84	[m^2]	σ^2_{pile}	12.50	[m^2]
Standard deviation	σ_{out}	3.44	[m]	σ_{pile}	3.54	[m]
Significant wave height	$H_{S,out}$	13.75	[m]	$H_{S,pile}$	14.14	[m]
Sea state steepness	ε_{out}	0.0403	[-]	ε_{pile}	0.0415	[-]
Range $\frac{H_{S,min}-H_{S,max}}{H_{S,mean}} \cdot 100$	$\Delta H_{S,out}$	12.44	[%]	$\Delta H_{S,pile}$	13.58	[%]
Deviation from $H_{S,in}$	$\frac{H_{S,out}}{H_{S,in}}$	0.8594	[-]	$\frac{H_{S,pile}}{H_{S,in}}$	0.8838	[-]

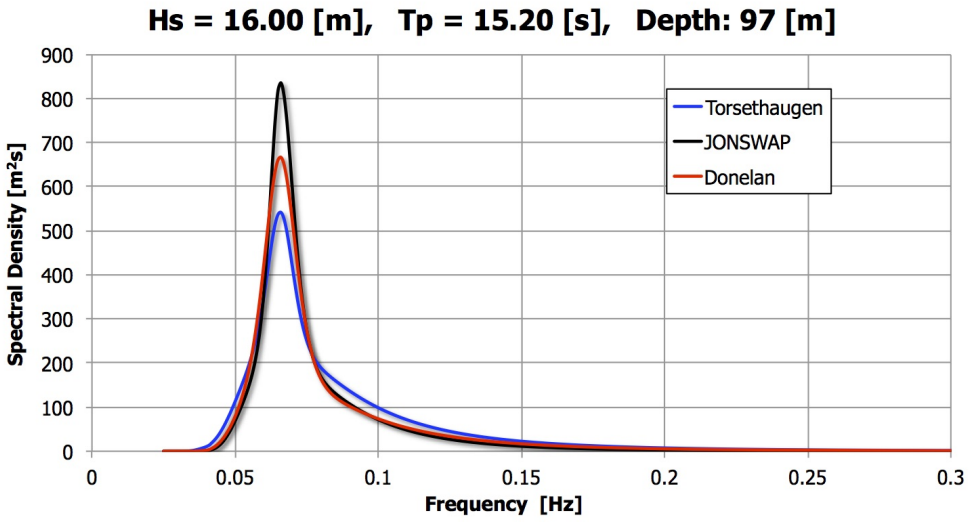

Figure D.101: Comparison of the JONSWAP, Torsethaugen and Donelan spectrum for sea state 11.

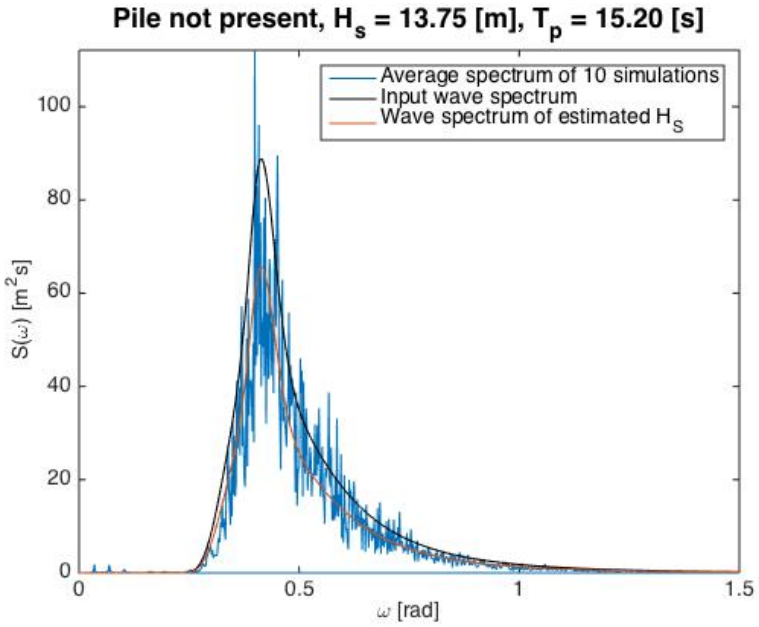

Figure D.102: Averaged estimated wave spectrum for all ten tests of sea state 11 without the pile present.

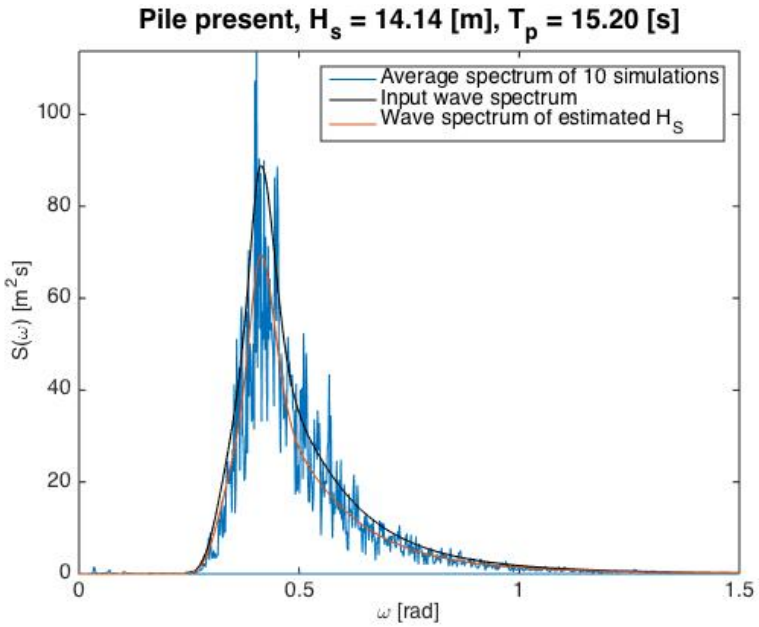

Figure D.103: Averaged estimated wave spectrum for all ten tests of sea state 11 with the pile present.

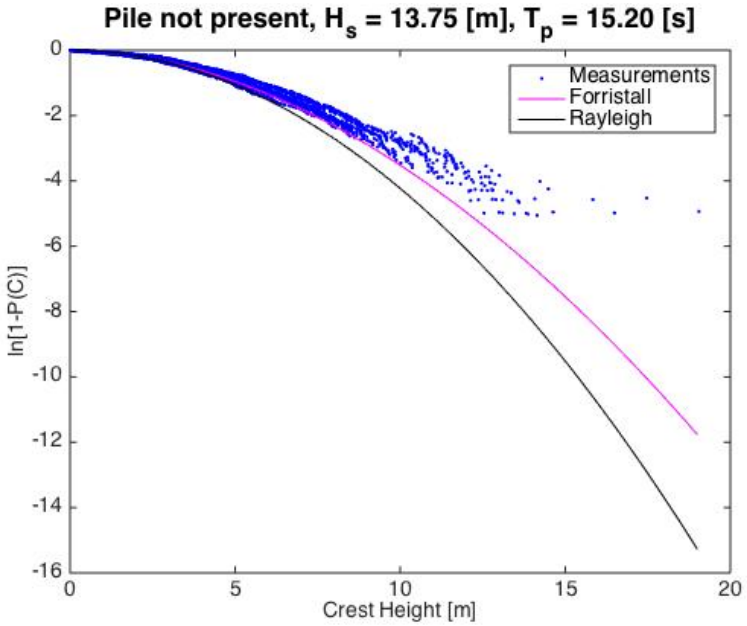

Figure D.104: Distribution of wave crests for all the ten tests of sea state 11 without the pile present.

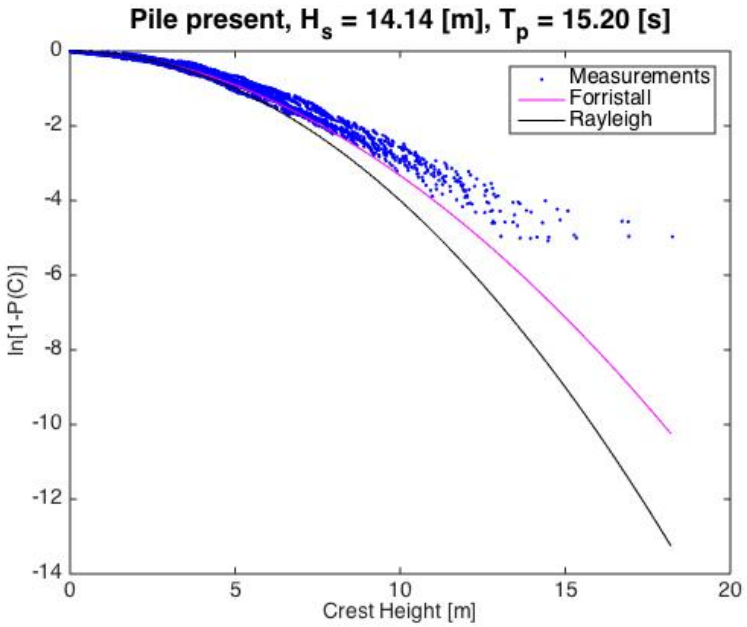

Figure D.105: Distribution of wave crests for all the ten tests of sea state 11 with the pile present.

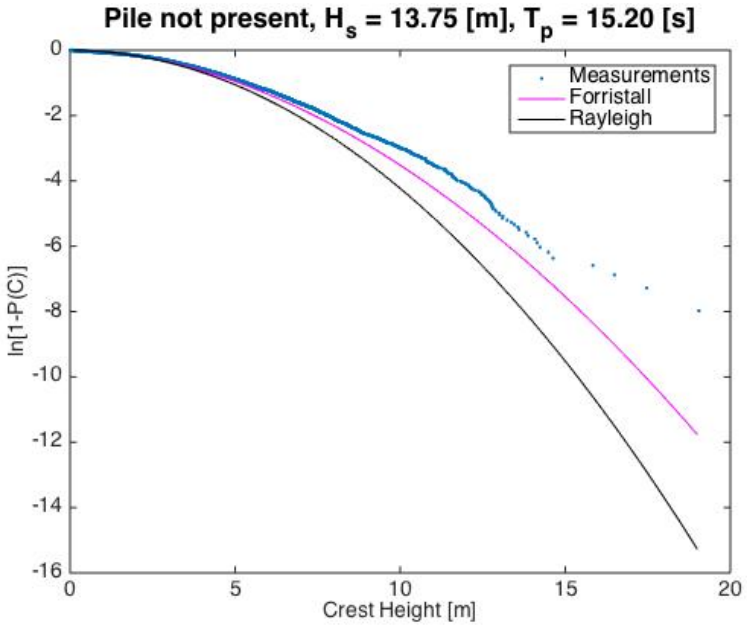

Figure D.106: Distribution of wave crests for all tests smeared together of sea state 11 without the pile present.

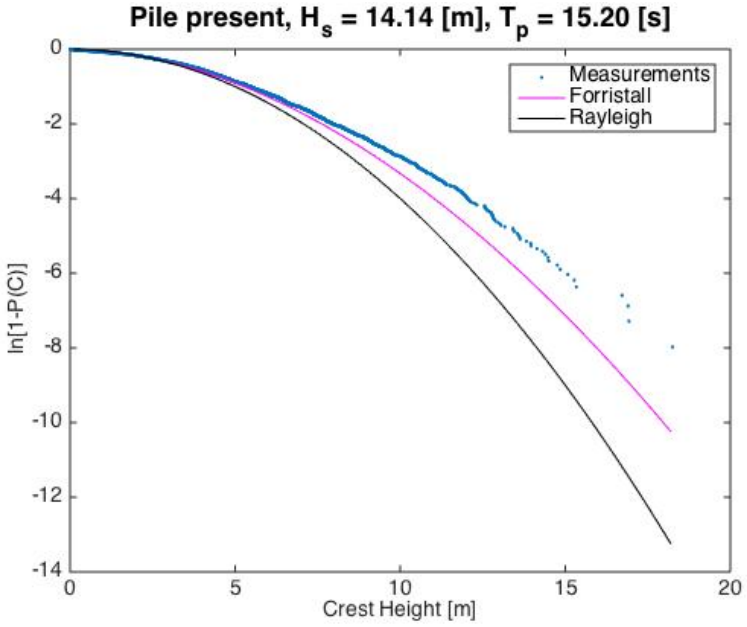

Figure D.107: Distribution of wave crests for all tests smeared together of sea state 11 with the pile present.

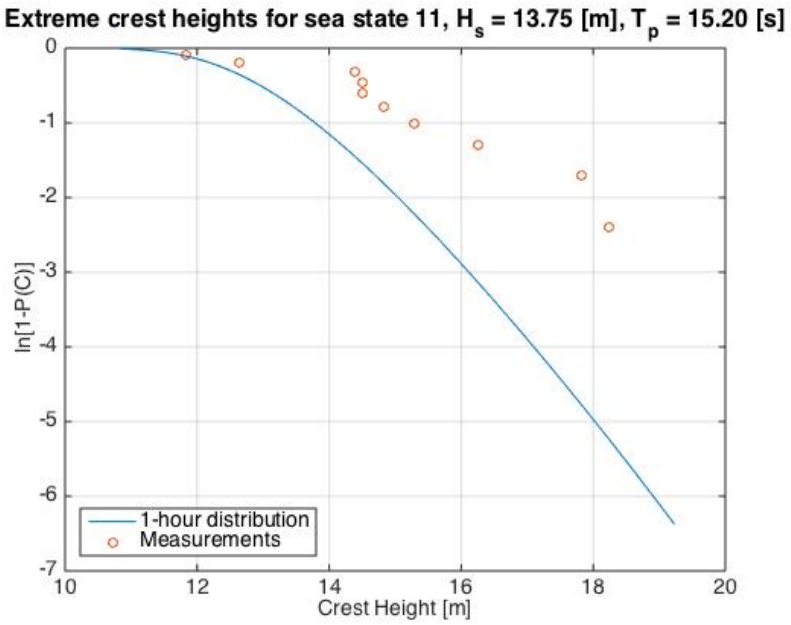

Figure D.108: Distribution of extreme wave crests in sea state 11.

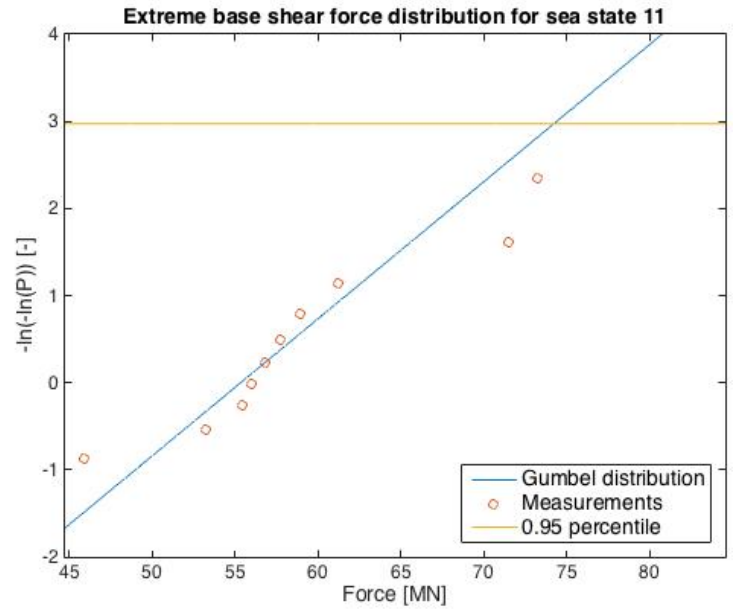

Figure D.109: Distribution of extreme base shear forces in sea state 11.

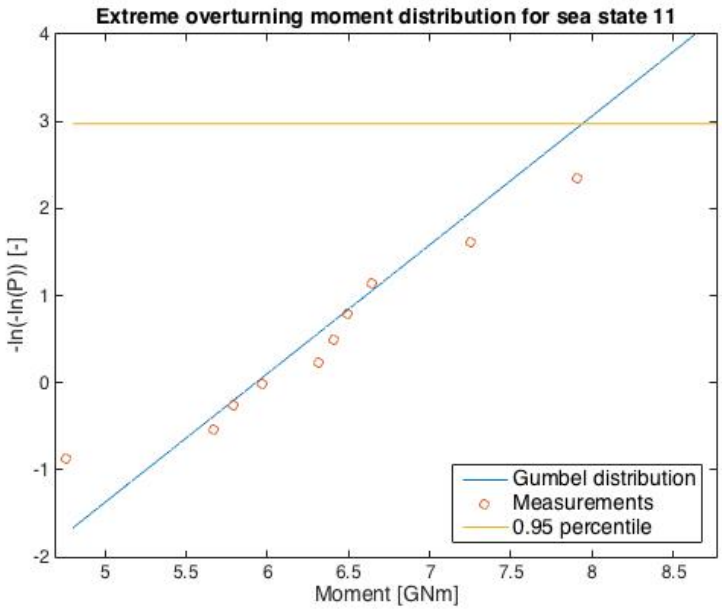

Figure D.110: Distribution of extreme overturning moments in sea state 11.

D.12 Sea state 12

Table D.45: Input information of sea state 12.

Significant wave height	H_S	17.00	[m]
Spectral peak period	T_P	16.00	[s]
Water depth	h	96.8	[m]
Number of tests	#	10	[-]
Duration of each test	d	1	[h]

Table D.46: Variances and significant wave heights for all 10 tests of sea state 12.

	Without pile		With pile	
Test	σ^2 [m^2]	H_S [m]	σ^2 [m^2]	H_S [m]
1	14.47	15.22	15.31	15.65
2	14.25	15.10	14.63	15.30
3	12.72	14.27	13.12	14.49
4	13.79	14.86	14.81	15.39
5	14.11	15.03	15.18	15.58
6	14.55	15.26	15.56	15.78
7	13.26	14.57	14.28	15.12
8	13.72	14.81	14.58	15.28
9	15.26	15.63	16.02	16.01
10	13.76	14.84	14.74	15.36
avg	13.99	14.96	14.82	15.40

Table D.47: Largest measured crest heights, overturning moment and base shear force for all 10 tests of sea state 12.

Test	C_{max} [m]	$C_{max,pile}$ [m]	F_{max} [MN]	M_{max} [GNm]
1	16.07	17.99	55.18	5.98
2	17.11	19.82	67.51	6.92
3	14.89	15.85	50.59	5.75
4	16.78	18.10	54.78	5.58
5	15.99	17.09	59.49	6.41
6	15.57	16.42	61.17	6.45
7	14.60	13.49	56.24	5.77
8	16.04	17.97	81.66	8.91
9	17.64	18.77	60.09	6.23
10	16.71	18.62	71.07	7.44

Table D.48: Output information of sea state 12.

Variance	σ^2_{out}	13.99	[m^2]	σ^2_{pile}	14.82	[m^2]
Standard deviation	σ_{out}	3.74	[m]	σ_{pile}	3.85	[m]
Significant wave height	$H_{S,out}$	14.96	[m]	$H_{S,pile}$	15.40	[m]
Sea state steepness	ε_{out}	0.0404	[-]	ε_{pile}	0.0415	[-]
Range $\frac{H_{S,min}-H_{S,max}}{H_{S,mean}} \cdot 100$	$\Delta H_{S,out}$	9.09	[%]	$\Delta H_{S,pile}$	9.87	[%]
Deviation from $H_{S,in}$	$\frac{H_{S,out}}{H_{S,in}}$	0.8800	[-]	$\frac{H_{S,pile}}{H_{S,in}}$	0.9059	[-]

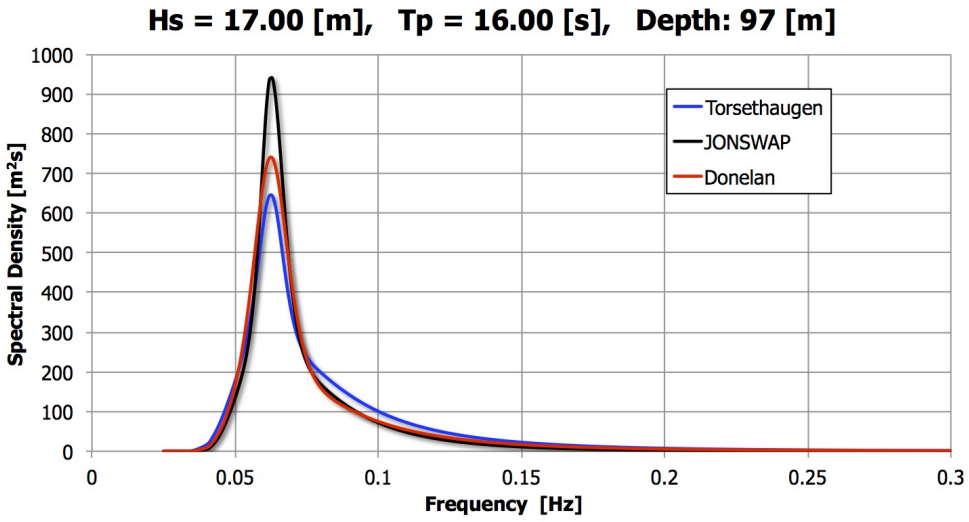

Figure D.111: Comparison of the JONSWAP, Torsethaugen and Donelan spectrum for sea state 12.

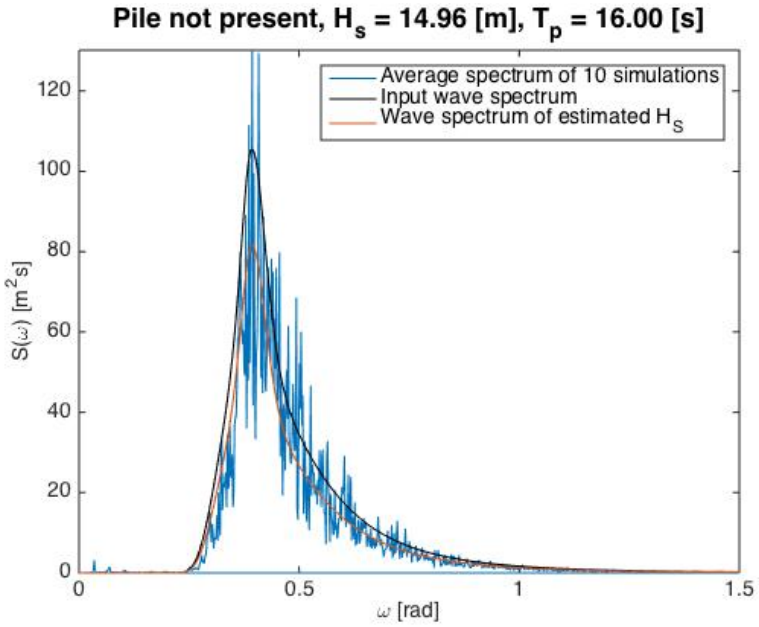

Figure D.112: Averaged estimated wave spectrum for all ten tests of sea state 12 without the pile present.

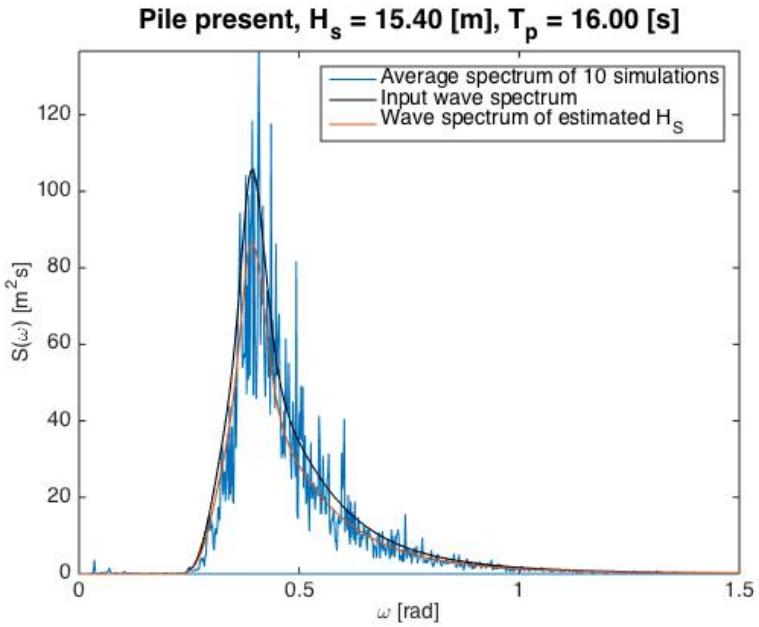

Figure D.113: Averaged estimated wave spectrum for all ten tests of sea state 12 with the pile present.

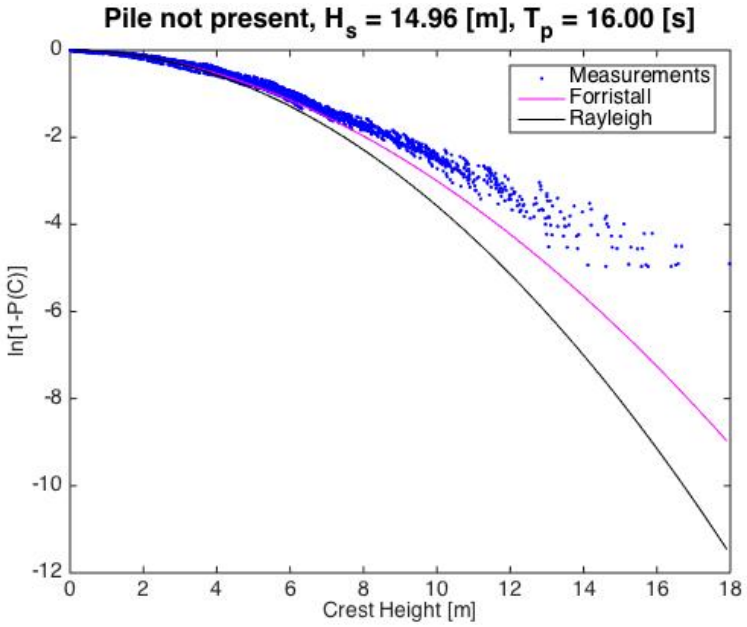

Figure D.114: Distribution of wave crests for all the ten tests of sea state 12 without the pile present.

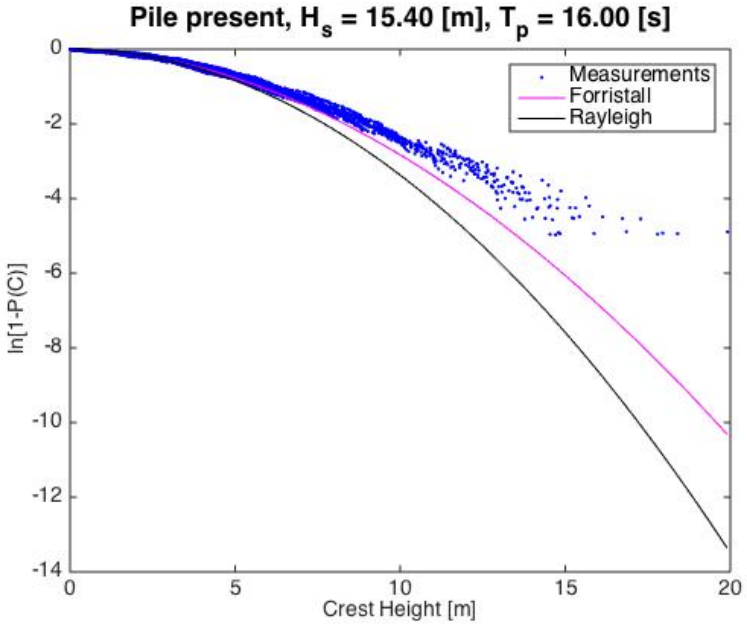

Figure D.115: Distribution of wave crests for all the ten tests of sea state 12 with the pile present.

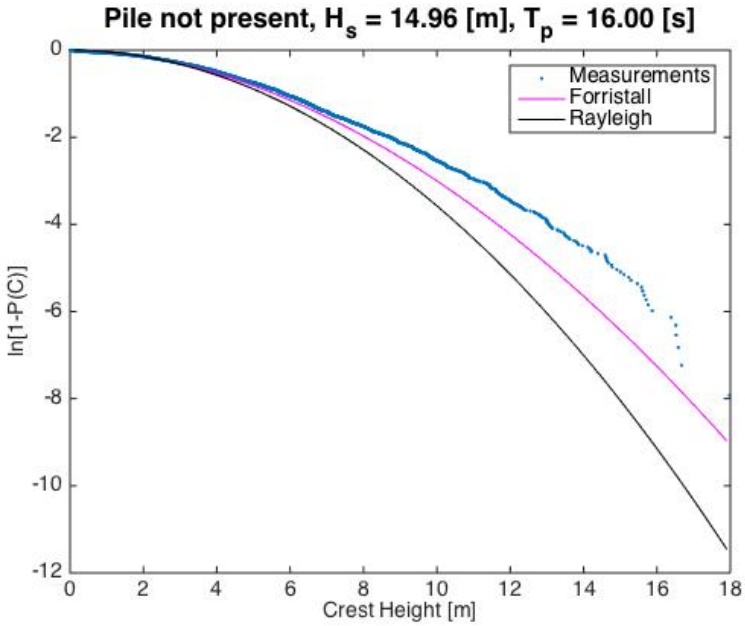

Figure D.116: Distribution of wave crests for all tests smeared together of sea state 12 without the pile present.

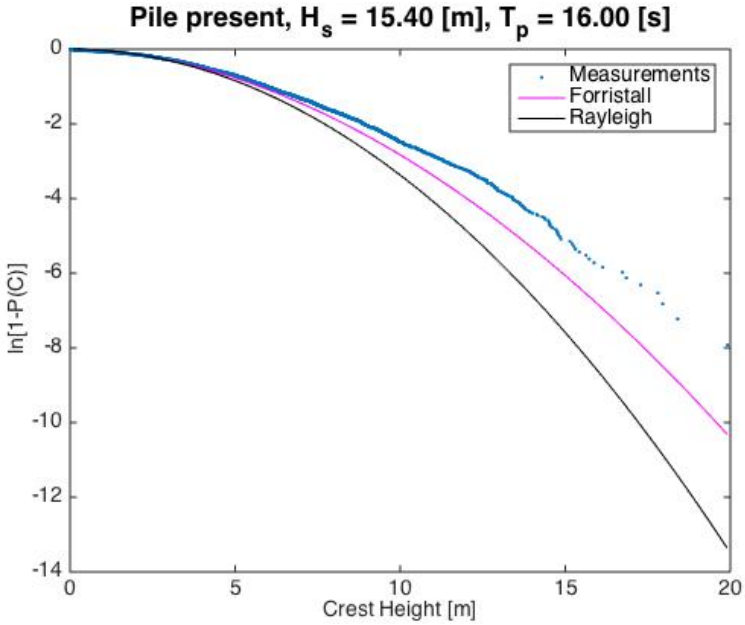

Figure D.117: Distribution of wave crests for all tests smeared together of sea state 12 with the pile present.

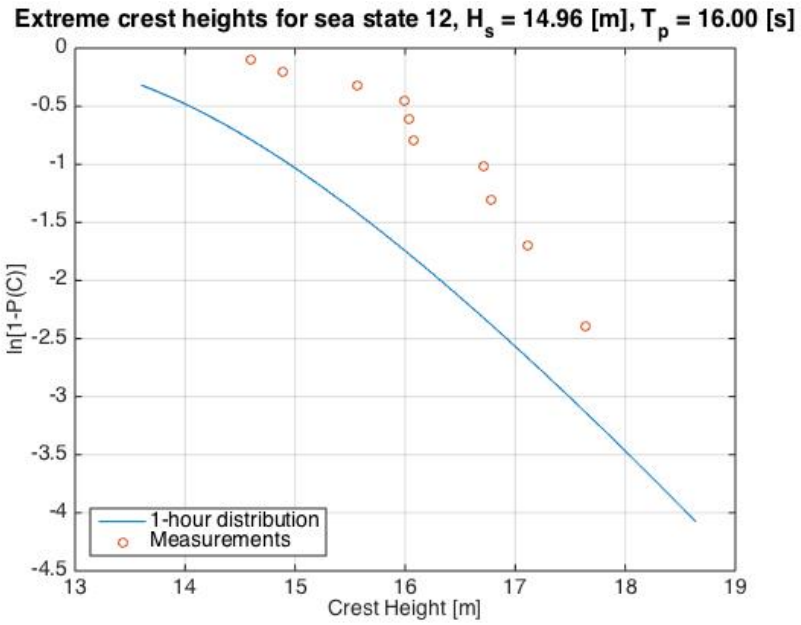

Figure D.118: Distribution of extreme wave crests in sea state 12.

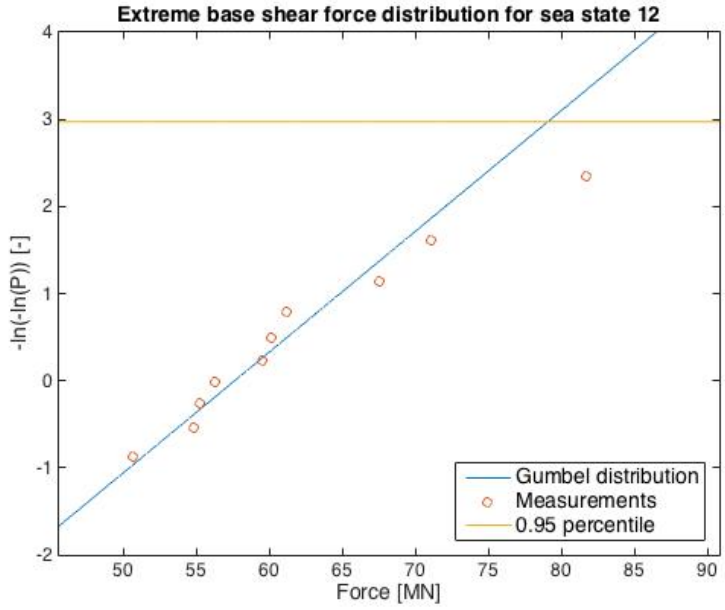

Figure D.119: Distribution of extreme base shear forces in sea state 12.

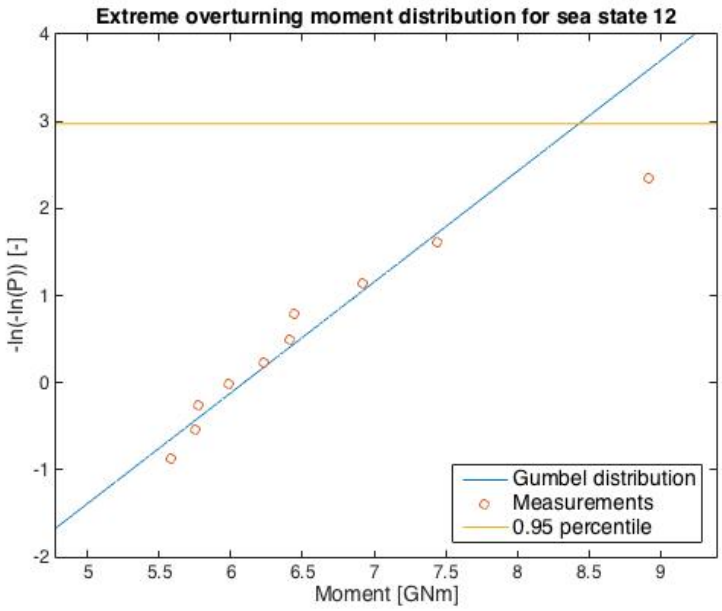

Figure D.120: Distribution of extreme overturning moments in sea state 12.

D.13 Sea state 13

Table D.49: Input information of sea state 13.

Significant wave height	H_S	18.00	[m]
Spectral peak period	T_P	16.90	[s]
Water depth	h	97	[m]
Number of tests	#	10	[-]
Duration of each test	d	1	[h]

Table D.50: Variances and significant wave heights for all 10 tests of sea state 13.

	Without pile		With pile	
Test	σ^2 [m^2]	H_S [m]	σ^2 [m^2]	H_S [m]
1	13.55	14.73	15.53	15.76
2	14.50	15.23	16.19	16.09
3	14.25	15.10	15.46	15.73
4	13.91	14.92	15.34	15.67
5	14.32	15.14	17.86	16.90
6	14.12	15.03	16.97	16.48
7	12.22	13.98	12.04	13.88
8	13.71	14.81	16.18	16.09
9	15.03	15.51	16.78	16.39
10	13.63	14.77	17.37	16.67
avg	13.92	14.92	15.97	15.97

Table D.51: Largest measured crest heights, overturning moment and base shear force for all 10 tests of sea state 13.

Test	C_{max} [m]	$C_{max,pile}$ [m]	F_{max} [MN]	M_{max} [GNm]
1	19.70	19.30	70.46	7.47
2	15.97	16.48	52.07	5.40
3	16.64	16.30	58.13	5.87
4	16.50	14.59	60.13	5.97
5	17.19	16.32	71.26	7.46
6	18.40	19.63	56.94	6.13
7	12.43	14.41	49.87	5.14
8	21.25	21.53	68.92	7.17
9	18.12	17.82	67.20	6.87
10	20.68	19.67	83.03	8.95

Table D.52: Output information of sea state 13.

Variance	σ^2_{out}	13.92	[m^2]	σ^2_{pile}	15.97	[m^2]
Standard deviation	σ_{out}	3.73	[m]	σ_{pile}	4.00	[m]
Significant wave height	$H_{S,out}$	14.92	[m]	$H_{S,pile}$	15.97	[m]
Sea state steepness	ε_{out}	0.0369	[-]	ε_{pile}	0.0395	[-]
Range $\frac{H_{S,min}-H_{S,max}}{H_{S,mean}} \cdot 100$	$\Delta H_{S,out}$	10.25	[%]	$\Delta H_{S,pile}$	18.91	[%]
Deviation from $H_{S,in}$	$\frac{H_{S,out}}{H_{S,in}}$	0.8289	[-]	$\frac{H_{S,pile}}{H_{S,in}}$	0.8872	[-]

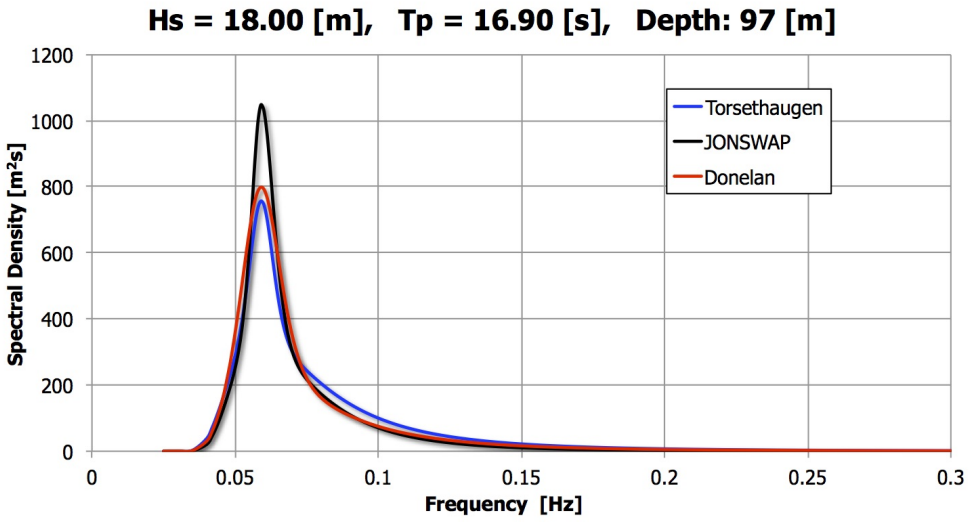

Figure D.121: Comparison of the JONSWAP, Torsethaugen and Donelan spectrum for sea state 13.

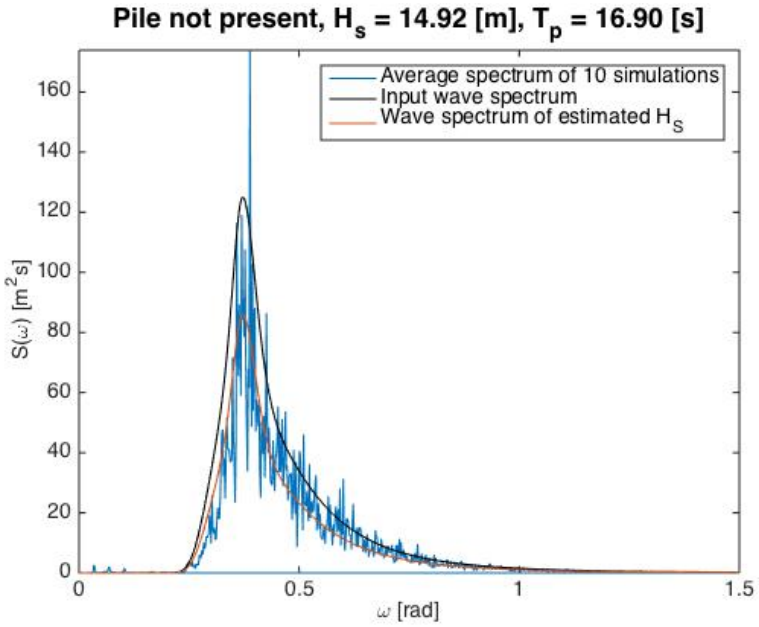

Figure D.122: Averaged estimated wave spectrum for all ten tests of sea state 13 without the pile present.

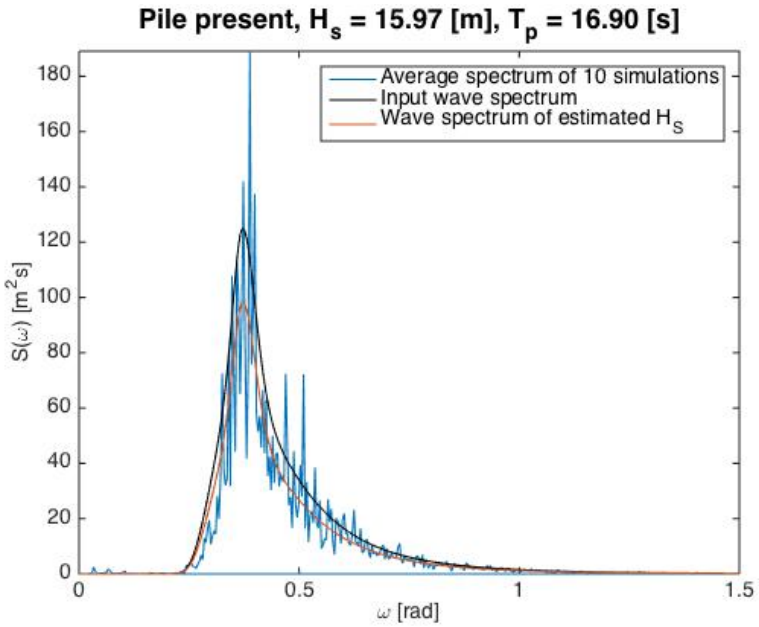

Figure D.123: Averaged estimated wave spectrum for all ten tests of sea state 13 with the pile present.

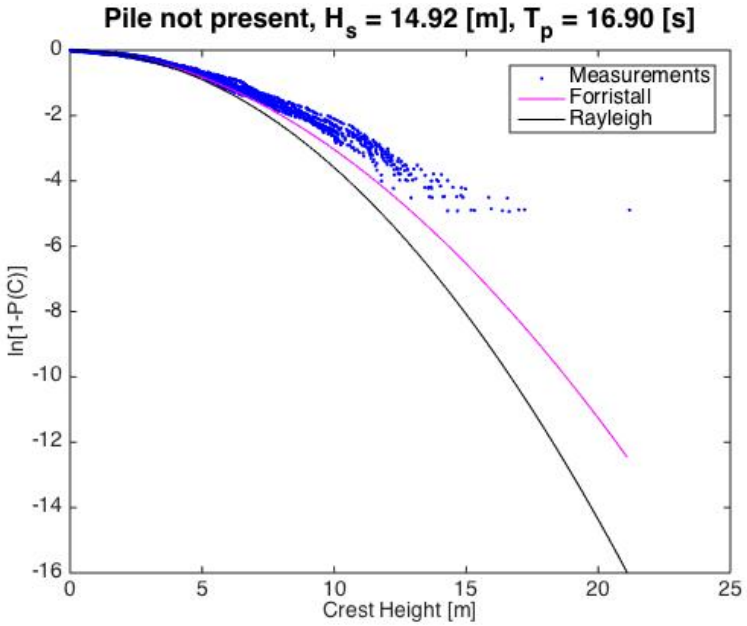

Figure D.124: Distribution of wave crests for all the ten tests of sea state 13 without the pile present.

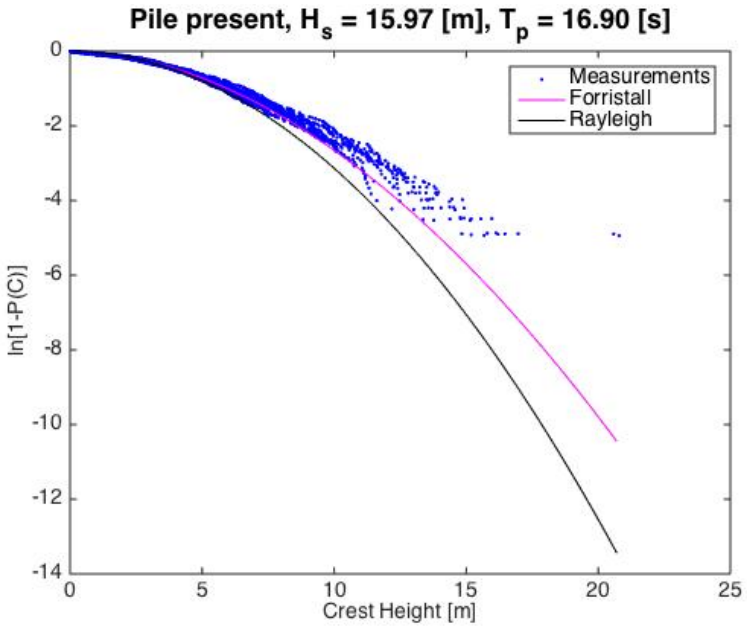

Figure D.125: Distribution of wave crests for all the ten tests of sea state 13 with the pile present.

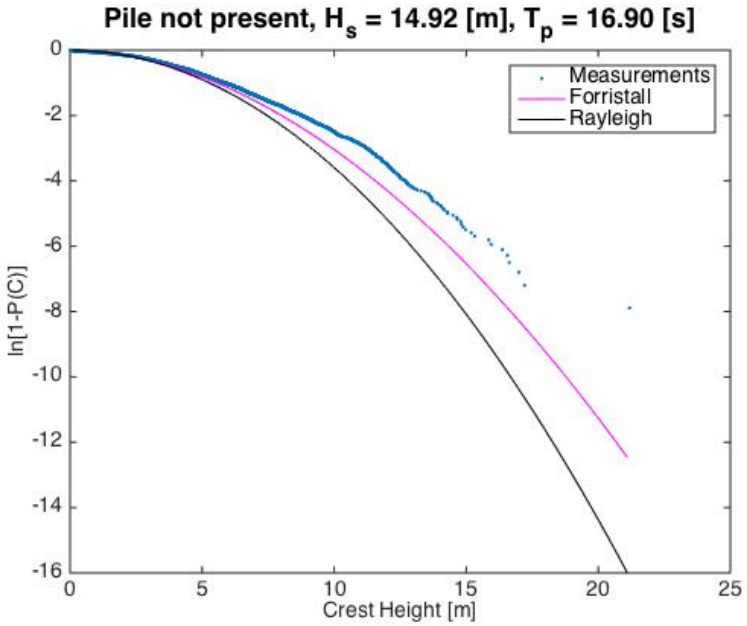

Figure D.126: Distribution of wave crests for all tests smeared together of sea state 13 without the pile present.

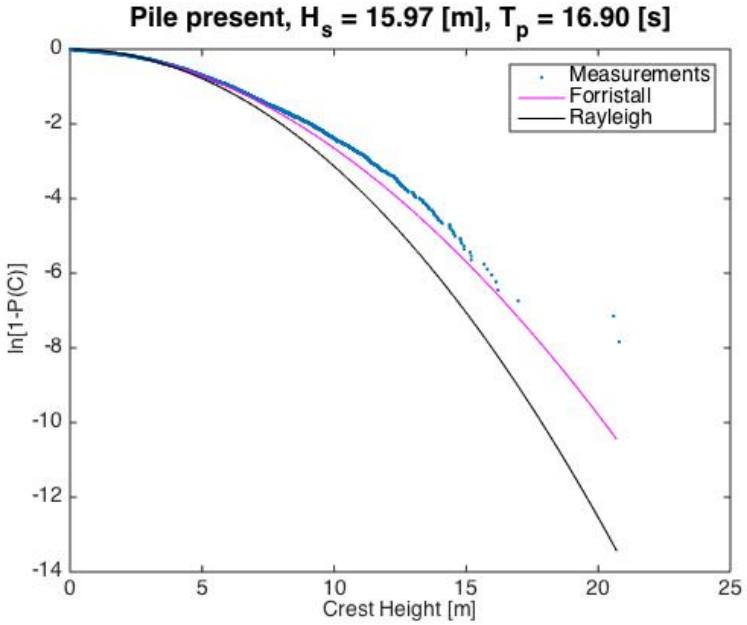

Figure D.127: Distribution of wave crests for all tests smeared together of sea state 13 with the pile present.

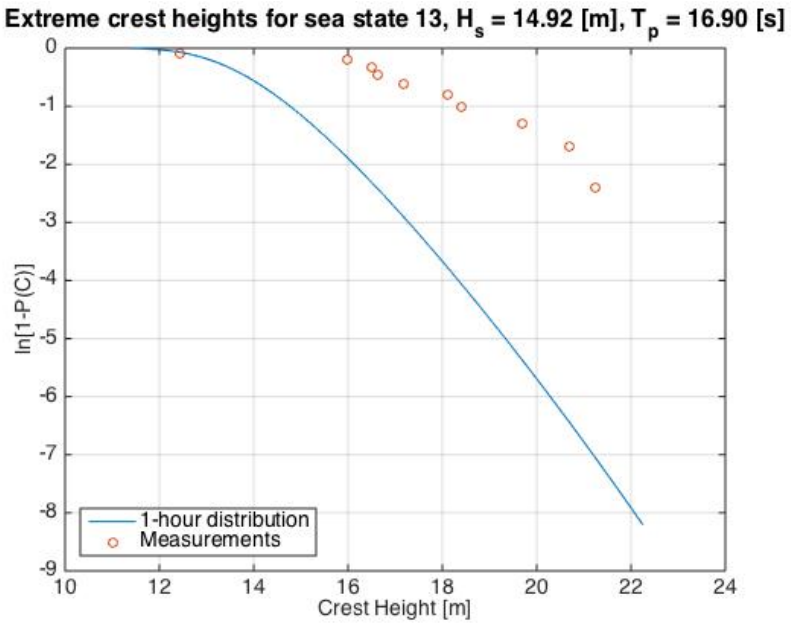

Figure D.128: Distribution of extreme wave crests in sea state 13.

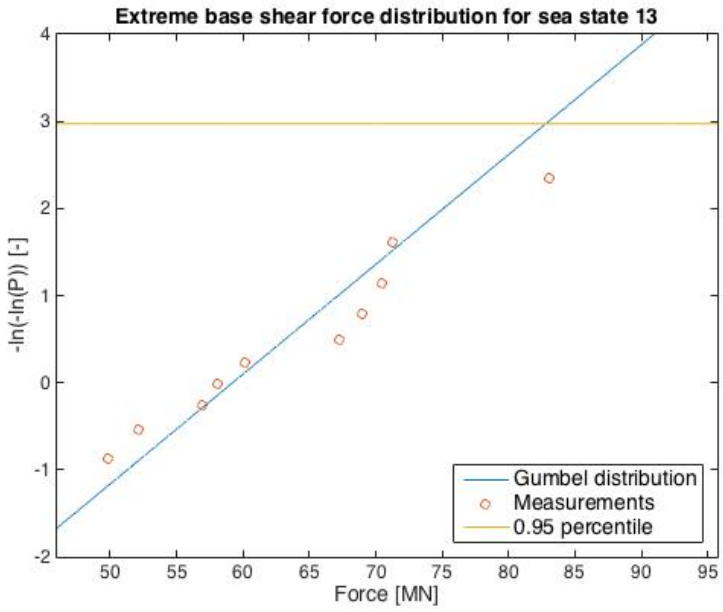

Figure D.129: Distribution of extreme base shear forces in sea state 13.

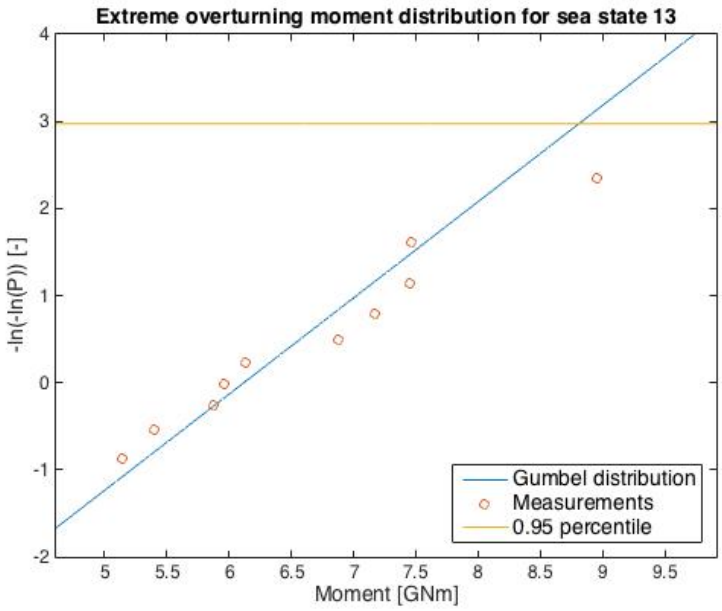

Figure D.130: Distribution of extreme overturning moments in sea state 13.

D.14 Sea state 14

Table D.53: Input information of sea state 14.

Significant wave height	H_S	19.00	[m]
Spectral peak period	T_P	18.00	[s]
Water depth	h	96.9	[m]
Number of tests	#	10	[-]
Duration of each test	d	1	[h]

Table D.54: Variances and significant wave heights for all 10 tests of sea state 14.

	Without pile		With pile	
Test	σ^2 [m^2]	H_S [m]	σ^2 [m^2]	H_S [m]
1	14.52	15.24	15.55	15.77
2	16.32	16.16	17.35	16.66
3	13.98	14.96	15.18	15.58
4	16.36	16.18	18.40	17.16
5	15.61	15.81	16.65	16.32
6	14.00	14.97	15.57	15.78
7	14.09	15.02	14.68	15.33
8	16.50	16.25	17.30	16.64
9	16.24	16.12	16.56	16.28
10	15.20	15.59	15.58	15.79
avg	15.28	15.63	16.28	16.13

Table D.55: Largest measured crest heights, overturning moment and base shear force for all 10 tests of sea state 14.

Test	C_{max} [m]	$C_{max,pile}$ [m]	F_{max} [MN]	M_{max} [GNm]
1	17.79	16.26	58.74	6.31
2	16.18	17.52	54.93	5.78
3	17.81	18.12	68.53	7.34
4	17.05	15.62	64.53	6.70
5	17.83	17.86	57.54	5.65
6	14.27	15.88	54.57	5.56
7	14.01	14.14	52.34	5.29
8	17.54	18.45	65.13	6.72
9	16.30	17.47	59.45	6.17
10	16.04	15.87	63.21	6.66

Table D.56: Output information of sea state 14.

Variance	σ^2_{out}	15.28	[m^2]	σ^2_{pile}	16.28	[m^2]
Standard deviation	σ_{out}	3.91	[m]	σ_{pile}	4.03	[m]
Significant wave height	$H_{S,out}$	15.63	[m]	$H_{S,pile}$	16.13	[m]
Sea state steepness	ε_{out}	0.0352	[-]	ε_{pile}	0.0363	[-]
Range $\frac{H_{S,min}-H_{S,max}}{H_{S,mean}} \cdot 100$	$\Delta H_{S,out}$	8.25	[%]	$\Delta H_{S,pile}$	11.35	[%]
Deviation from $H_{S,in}$	$\frac{H_{S,out}}{H_{S,in}}$	0.8226	[-]	$\frac{H_{S,pile}}{H_{S,in}}$	0.8489	[-]

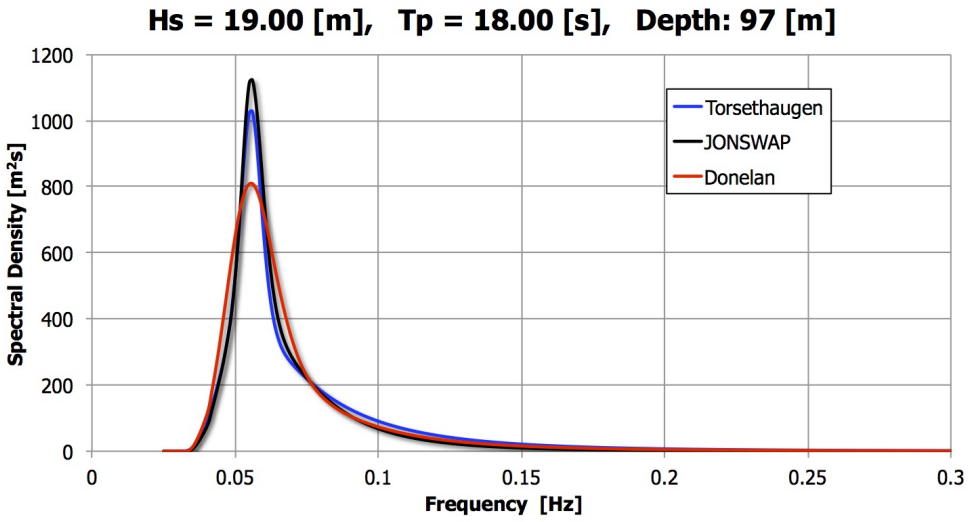

Figure D.131: Comparison of the JONSWAP, Torsethaugen and Donelan spectrum for sea state 14.

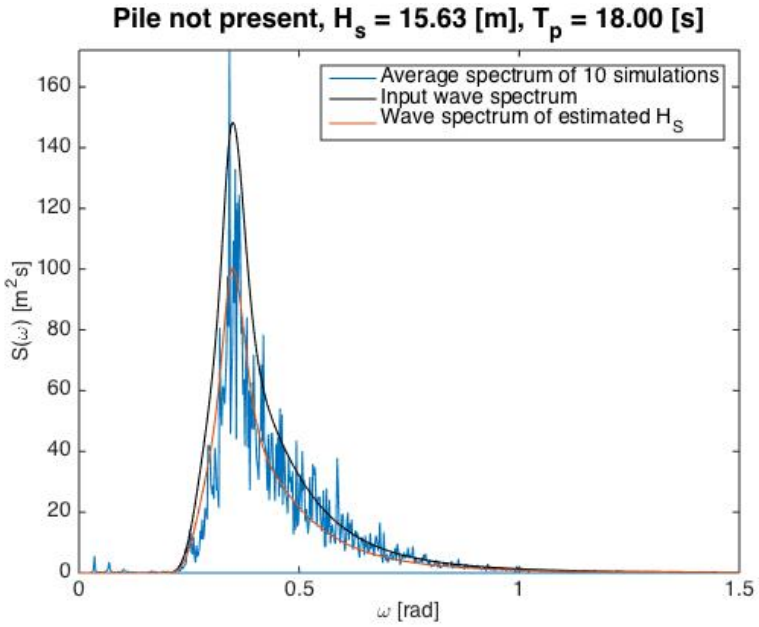

Figure D.132: Averaged estimated wave spectrum for all ten tests of sea state 14 without the pile present.

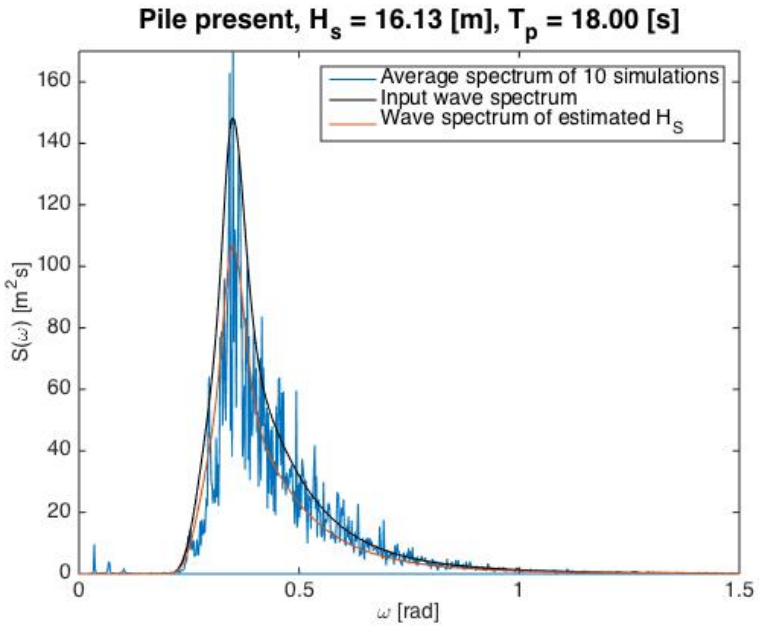

Figure D.133: Averaged estimated wave spectrum for all ten tests of sea state 14 with the pile present.

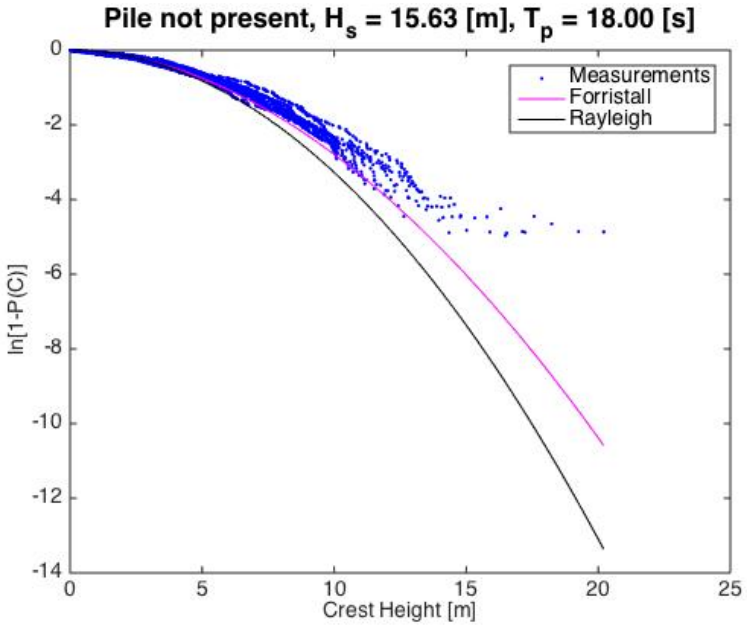

Figure D.134: Distribution of wave crests for all the ten tests of sea state 14 without the pile present.

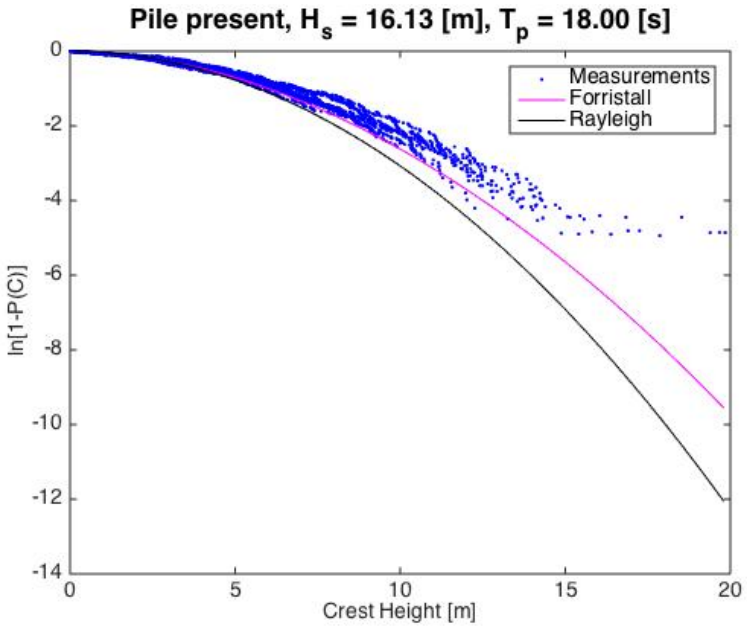

Figure D.135: Distribution of wave crests for all the ten tests of sea state 14 with the pile present.

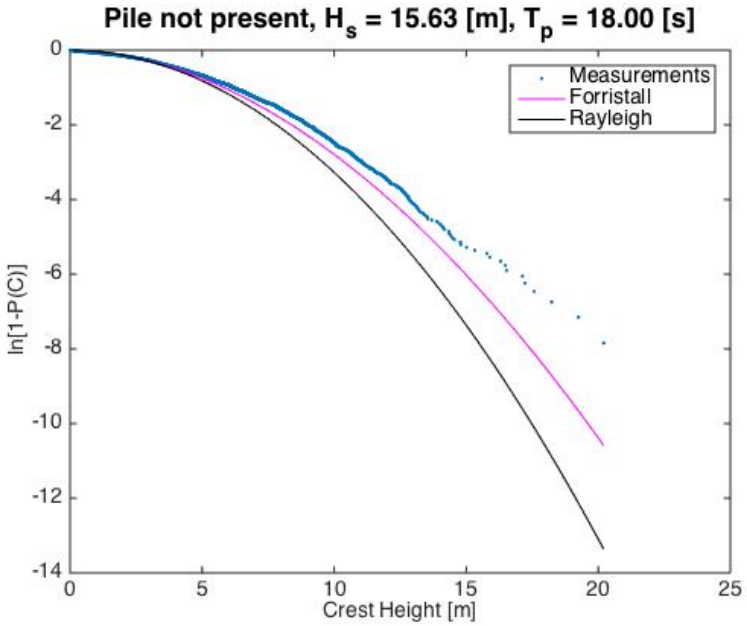

Figure D.136: Distribution of wave crests for all tests smeared together of sea state 14 without the pile present.

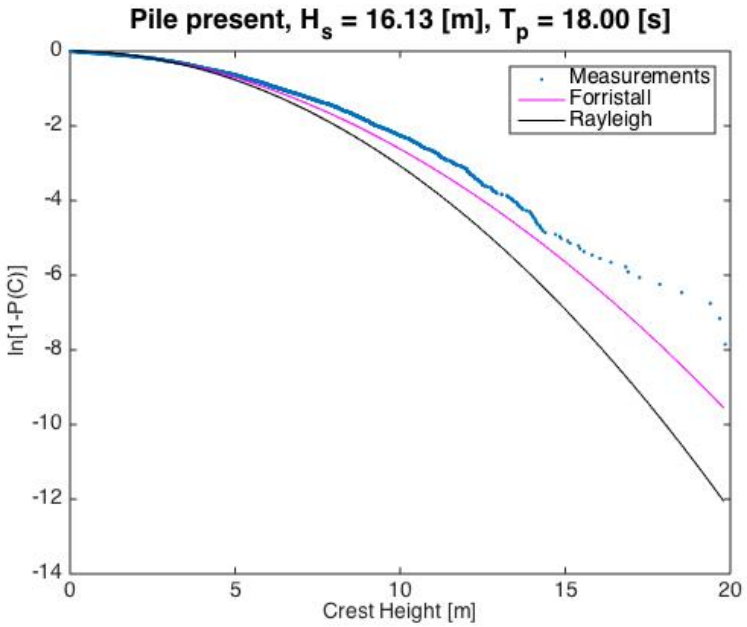

Figure D.137: Distribution of wave crests for all tests smeared together of sea state 14 with the pile present.

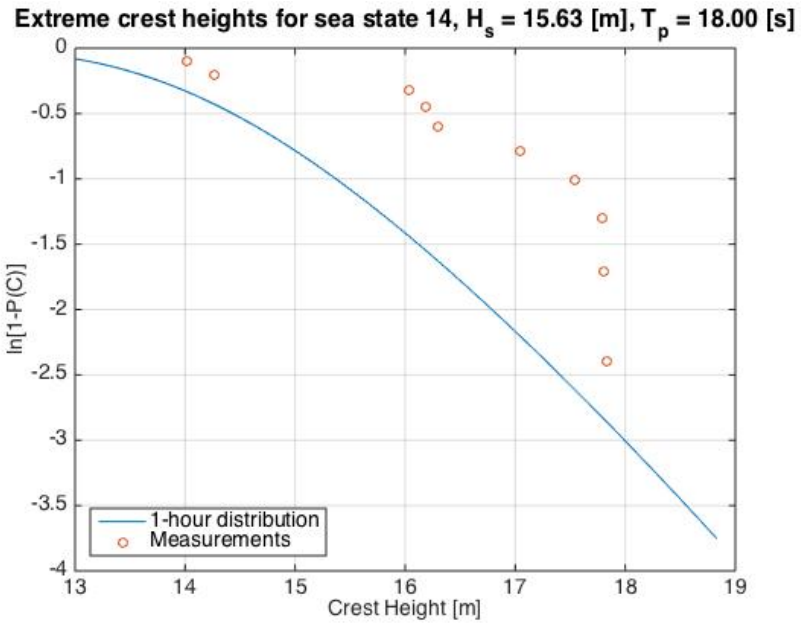

Figure D.138: Distribution of extreme wave crests in sea state 14.

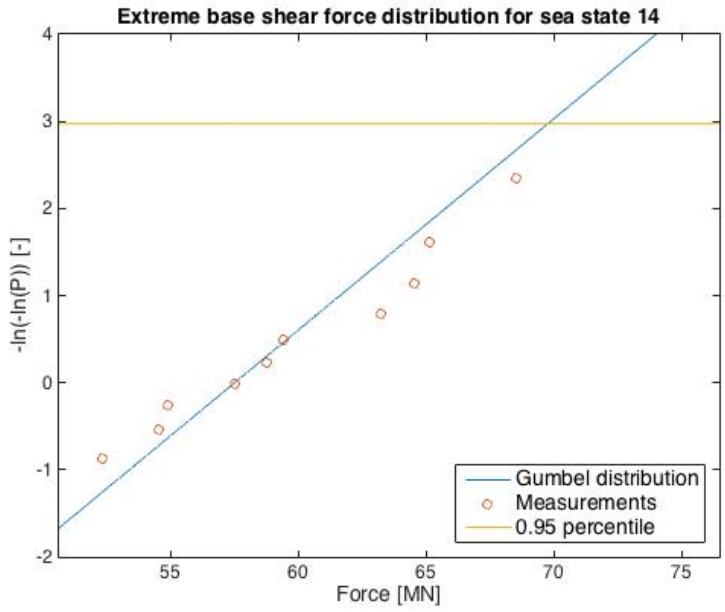

Figure D.139: Distribution of extreme base shear forces in sea state 14.

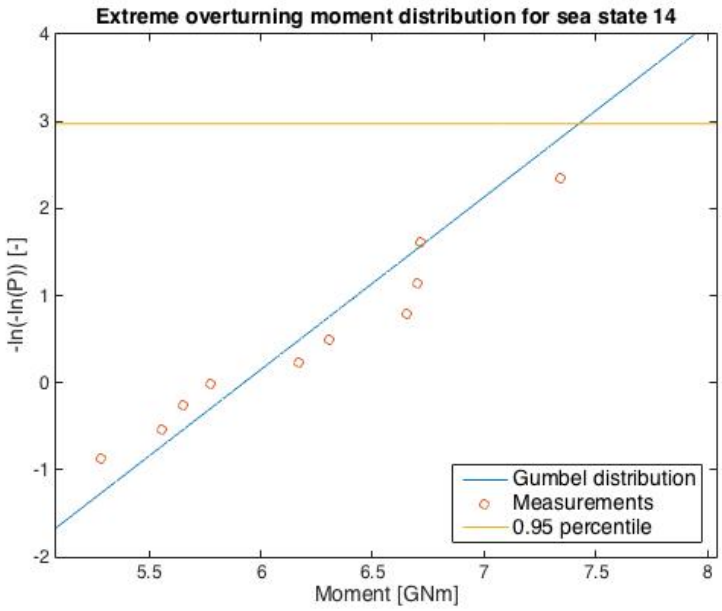

Figure D.140: Distribution of extreme overturning moments in sea state 14.

D.15 Sea state 15

Table D.57: Input information of sea state 15.

Significant wave height	H_S	19.60	[m]
Spectral peak period	T_P	19.00	[s]
Water depth	h	96.9	[m]
Number of tests	#	10	[-]
Duration of each test	d	1	[h]

Table D.58: Variances and significant wave heights for all 10 tests of sea state 15.

	Without pile		With pile	
Test	σ^2 [m^2]	H_S [m]	σ^2 [m^2]	H_S [m]
1	15.50	15.75	16.52	16.26
2	15.97	15.98	16.77	16.38
3	16.21	16.10	17.09	16.54
4	18.24	17.08	19.09	17.48
5	14.75	15.36	15.78	15.89
6	16.11	16.05	16.77	16.38
7	15.11	15.55	16.14	16.07
8	14.54	15.25	15.50	15.75
9	17.03	16.51	18.44	17.18
10	15.48	15.74	16.82	16.40
avg	15.89	15.94	16.89	16.43

Table D.59: Largest measured crest heights, overturning moment and base shear force for all 10 tests of sea state 15.

Test	C_{max} [m]	$C_{max,pile}$ [m]	F_{max} [MN]	M_{max} [GNm]
1	17.09	19.40	69.78	6.98
2	18.84	18.49	67.47	6.54
3	17.44	17.22	54.92	6.17
4	17.45	17.42	54.63	6.16
5	14.63	16.63	54.79	5.28
6	16.89	17.44	51.74	5.05
7	18.85	19.59	59.99	6.14
8	18.13	19.13	56.61	6.14
9	17.34	19.41	72.07	7.28
10	15.22	17.03	65.88	7.26

Table D.60: Output information of sea state 15.

Variance	σ^2_{out}	15.89	[m^2]	σ^2_{pile}	16.89	[m^2]
Standard deviation	σ_{out}	3.99	[m]	σ_{pile}	4.11	[m]
Significant wave height	$H_{S,out}$	15.94	[m]	$H_{S,pile}$	16.43	[m]
Sea state steepness	ε_{out}	0.0332	[-]	ε_{pile}	0.0342	[-]
Range $\frac{H_{S,min}-H_{S,max}}{H_{S,mean}} \cdot 100$	$\Delta H_{S,out}$	11.48	[%]	$\Delta H_{S,pile}$	10.53	[%]
Deviation from $H_{S,in}$	$\frac{H_{S,out}}{H_{S,in}}$	0.8133	[-]	$\frac{H_{S,pile}}{H_{S,in}}$	0.8383	[-]

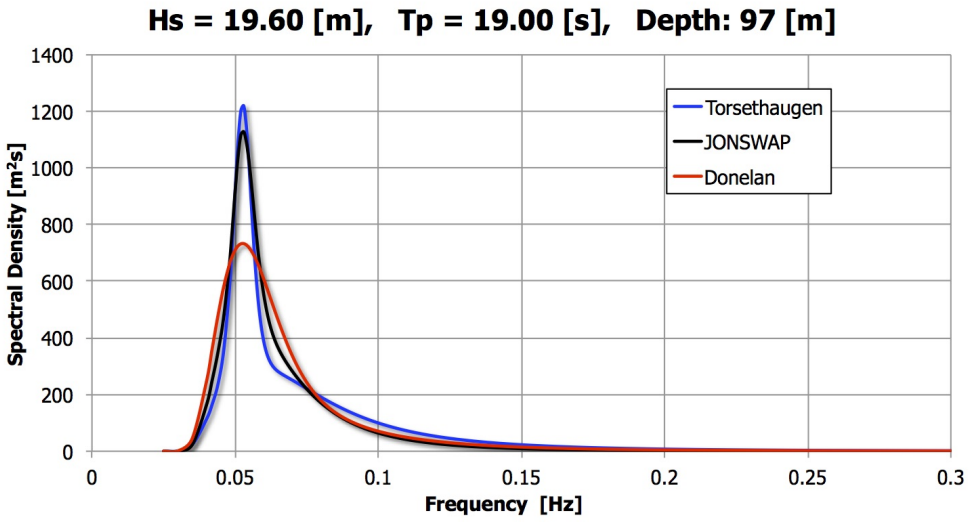

Figure D.141: Comparison of the JONSWAP, Torsethaugen and Donelan spectrum for sea state 15.

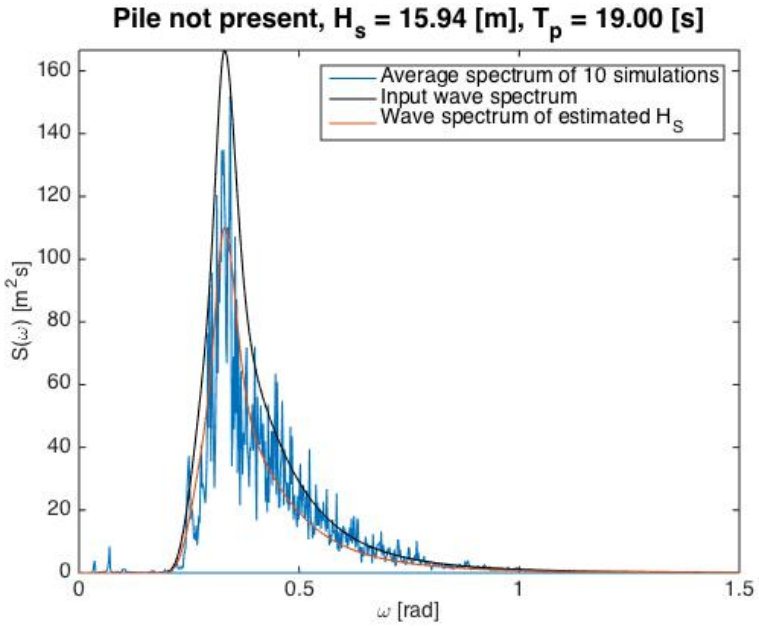

Figure D.142: Averaged estimated wave spectrum for all ten tests of sea state 14 without the pile present.

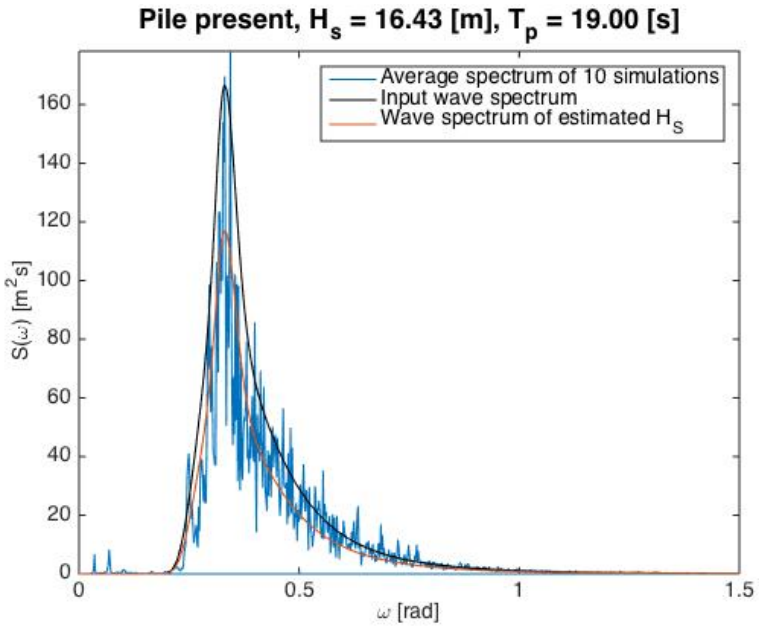

Figure D.143: Averaged estimated wave spectrum for all ten tests of sea state 14 with the pile present.

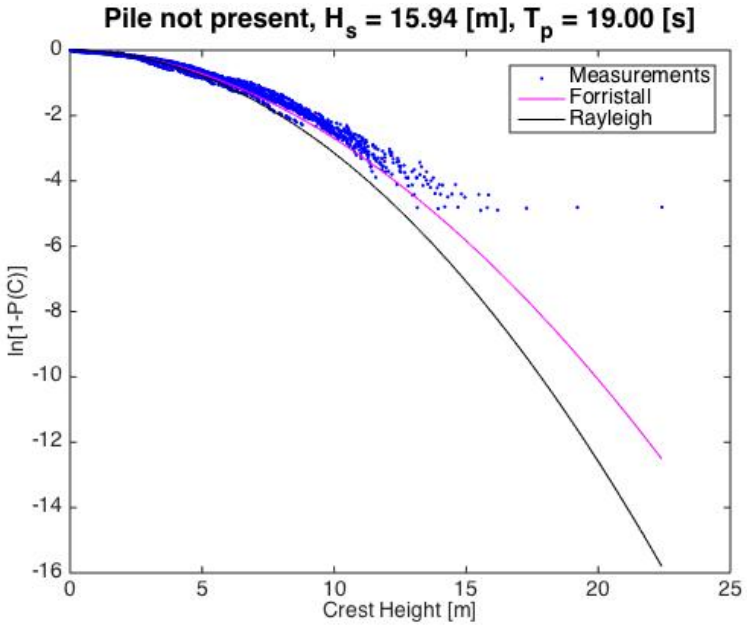

Figure D.144: Distribution of wave crests for all the ten tests of sea state 14 without the pile present.

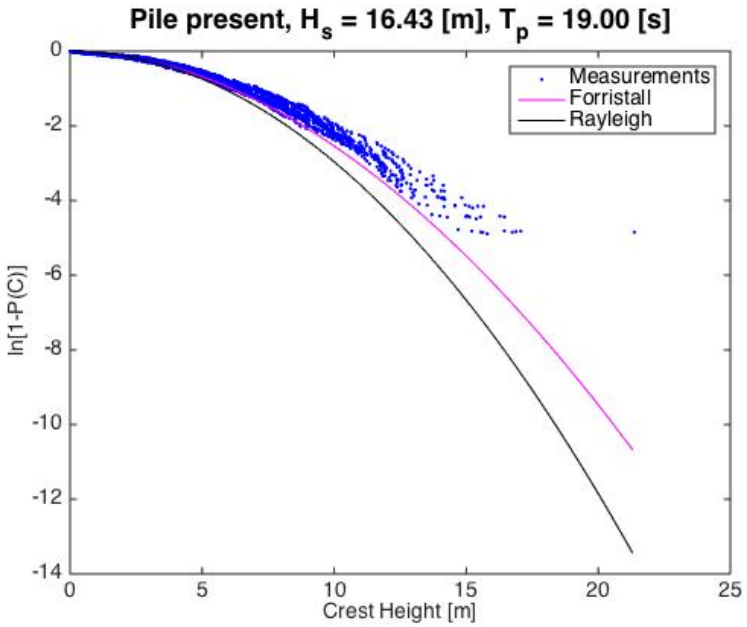

Figure D.145: Distribution of wave crests for all the ten tests of sea state 14 with the pile present.

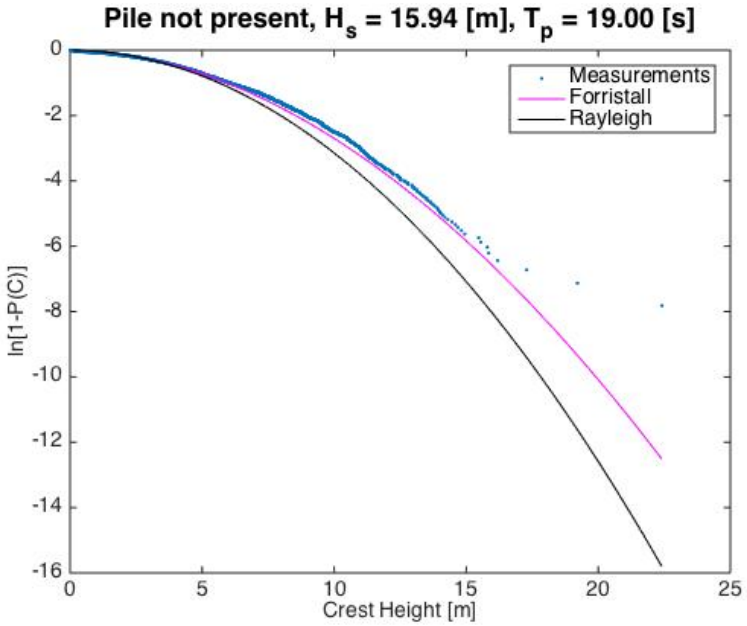

Figure D.146: Distribution of wave crests for all tests smeared together of sea state 14 without the pile present.

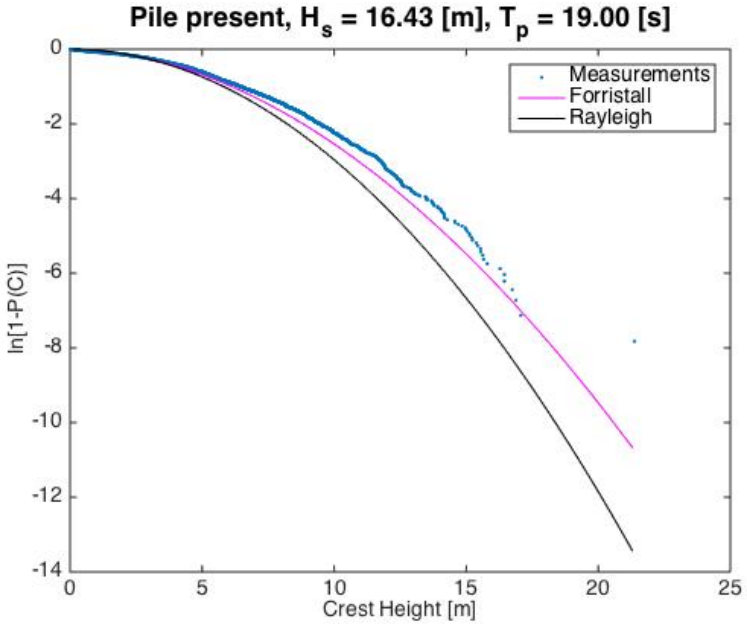

Figure D.147: Distribution of wave crests for all tests smeared together of sea state 14 with the pile present.

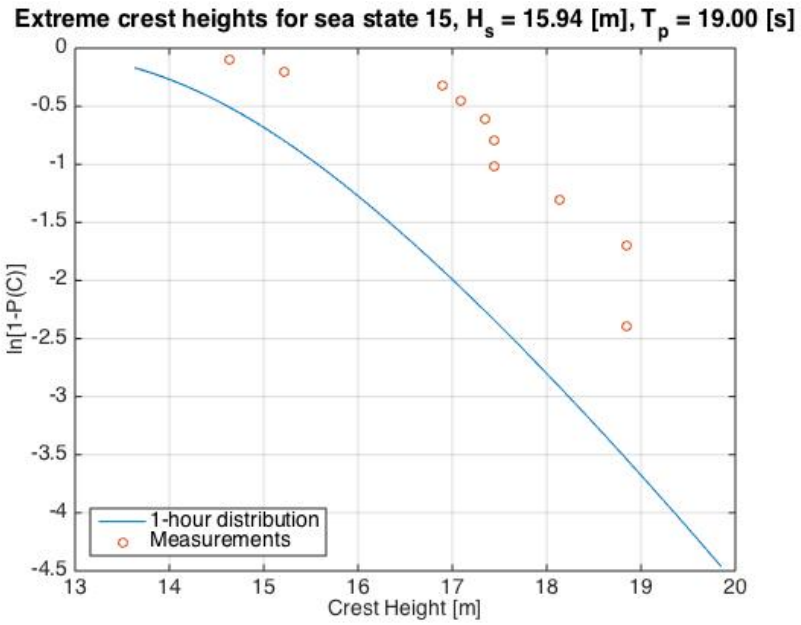

Figure D.148: Distribution of extreme wave crests in sea state 15.

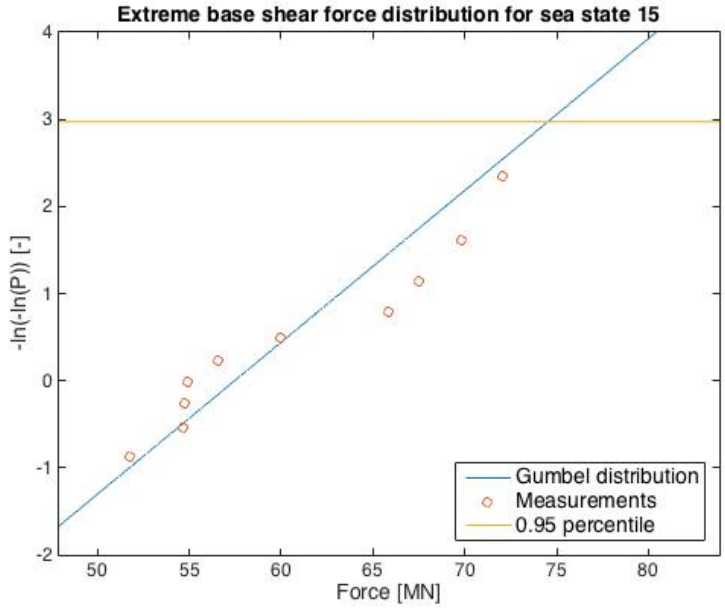

Figure D.149: Distribution of extreme base shear forces in sea state 15.

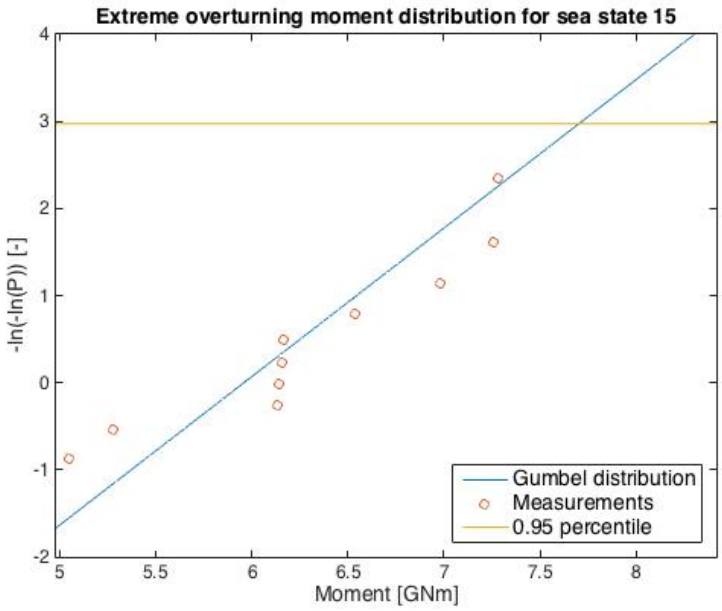

Figure D.150: Distribution of extreme overturning moments in sea state 15.

Appendix E

Donelan

E.1 Theoretical spectrum for different H_S values

E.1.1 Sea state 1

Table E.1: Input and output H_S values using Donelan wave spectrum for $T_P = 10.55$ [s].

$H_{S,in}$ [m]	$\varepsilon_{ss,in}$ [-]	$H_{S,D}$ [m]	$\frac{H_{S,D}}{H_{S,in}}$
5.00	0.0288	3.41	0.6820
6.00	0.0346	6.05	1.0083
7.00	0.0404	7.13	1.0186
8.00	0.0461	8.00	1.0000
9.00	0.0519	8.96	0.9956
10.00	0.0576	9.99	0.9990
11.00	0.0634	11.03	1.0027
12.00	0.0692	12.08	1.0067
13.00	0.0749	13.13	1.0100
14.00	0.0807	14.18	1.0129
15.00	0.0865	15.21	1.0140
16.00	0.0922	16.24	1.0150
17.00	0.0980	17.26	1.0153
18.00	0.1038	18.28	1.0156
19.00	0.1095	19.29	1.0153

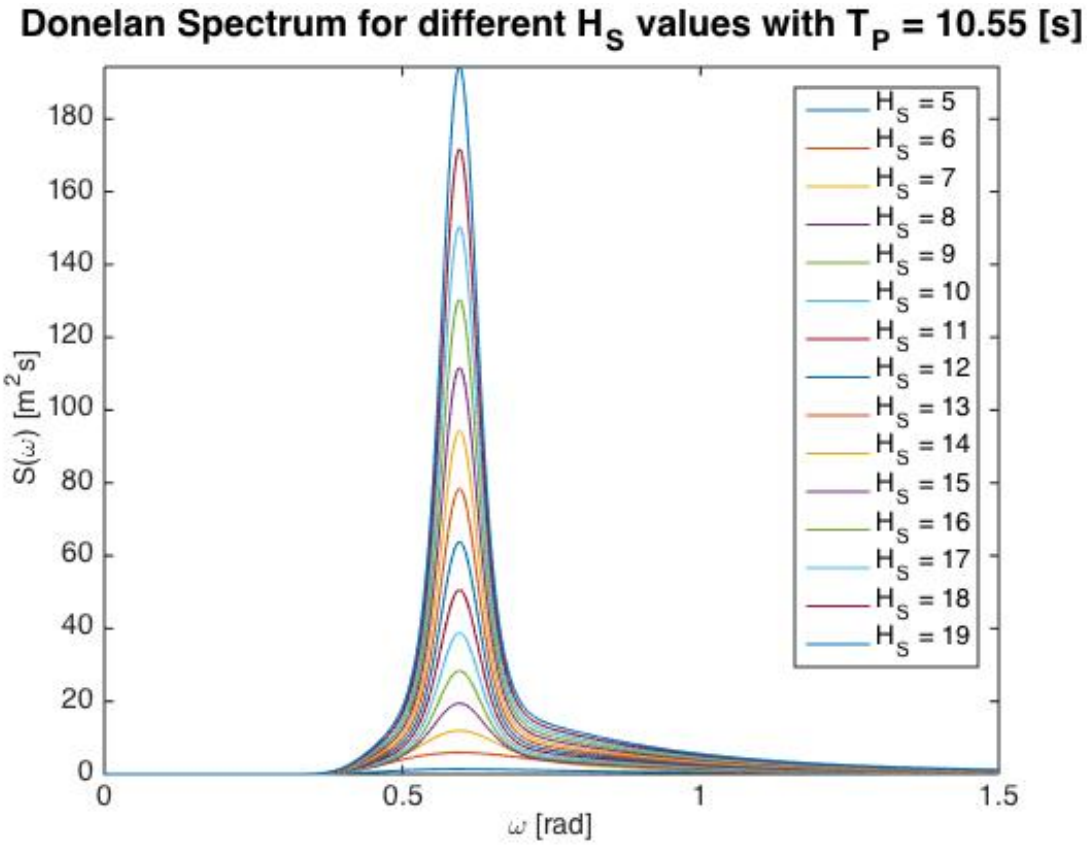

Figure E.1: Theoretical Donelan wave spectrum for different H_S values with $T_P = 10.55$ [s].

E.1.2 Sea state 6

Table E.2: Input and output H_S values using Donelan wave spectrum with $T_P = 16.76$ [s].

$H_{S,in}$ [m]	$\varepsilon_{ss,in}$ [-]	$H_{S,D}$ [m]	$\frac{H_{S,D}}{H_{S,in}}$
12.00	0.0301	5.20	0.4333
13.00	0.0326	10.03	0.7715
14.00	0.0351	13.00	0.9286
15.00	0.0376	14.98	0.9987
16.00	0.0401	16.33	1.0206
17.00	0.0426	17.34	1.0200
18.00	0.0451	18.20	1.0111
19.00	0.0476	19.05	1.0026
20.00	0.0501	19.94	0.9970
21.00	0.0526	20.86	0.9933
22.00	0.0551	21.83	0.9923
23.00	0.0576	22.82	0.9922
24.00	0.0601	23.83	0.9929

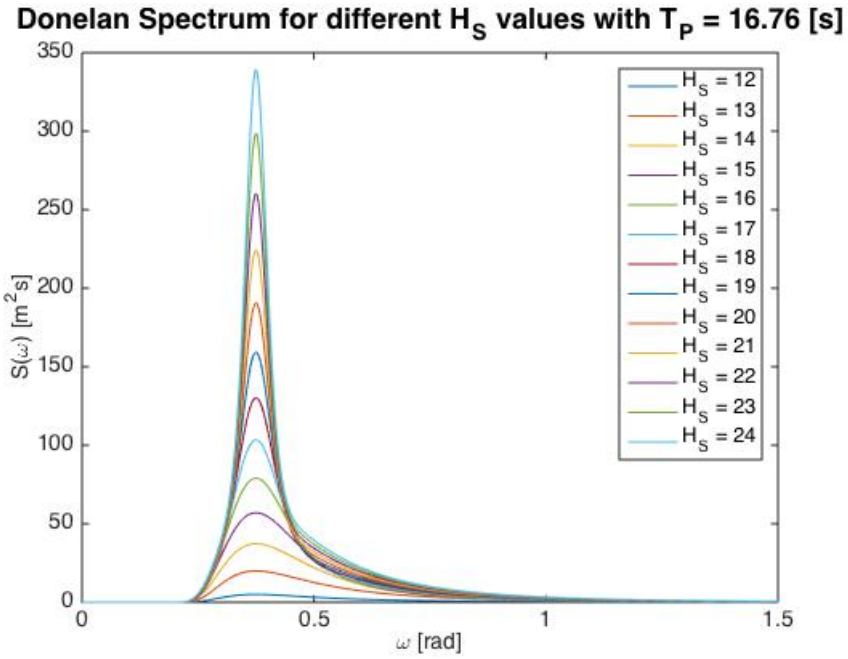

Figure E.2: Theoretical Donelan wave spectrum for different H_S values with $T_P = 16.76$ [s].

E.1.3 Sea state 7

Table E.3: Input and output H_S values using Donelan wave spectrum with $T_P = 11.30$ [s].

$H_{S,in}$ [m]	$\varepsilon_{ss,in}$ [-]	$H_{S,D}$ [m]	$\frac{H_{S,D}}{H_{S,in}}$
6.00	0.0302	4.91	0.8183
7.00	0.0353	7.11	1.0157
8.00	0.0403	8.16	1.0200
9.00	0.0453	9.02	1.0022
10.00	0.0504	9.96	0.9960
11.00	0.0554	10.97	0.9973
12.00	0.0605	12.01	1.0008
13.00	0.0655	13.06	1.0046
14.00	0.0705	14.11	1.0079
15.00	0.0756	15.16	1.0107
16.00	0.0806	16.20	1.0125
17.00	0.0856	17.24	1.0141
18.00	0.0907	18.27	1.0150
19.00	0.0957	19.29	1.0153
20.00	0.1008	20.31	1.0155

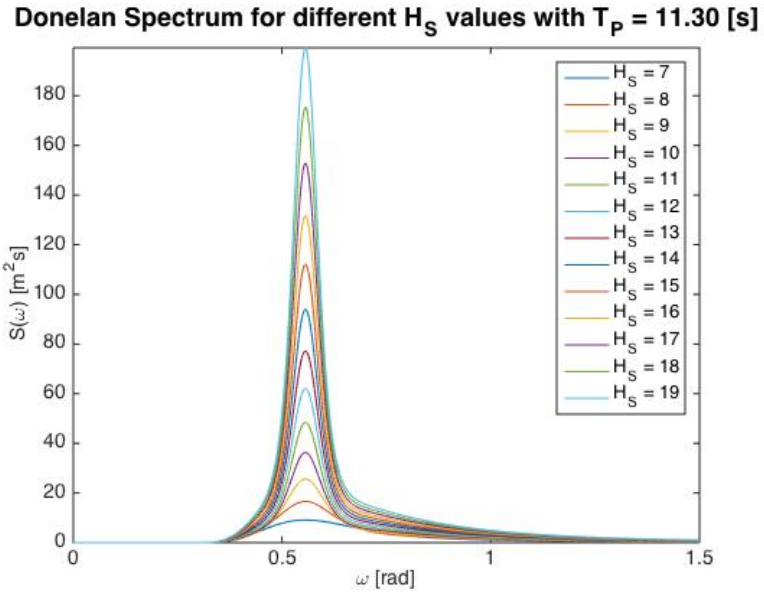

Figure E.3: Theoretical Donelan wave spectrum for different H_S values with $T_P = 11.30$ [s].

E.1.4 Sea state 15

Table E.4: Input and output H_S values using Donelan wave spectrum with $T_P = 19.00$ [s].

$H_{S,in}$ [m]	$\varepsilon_{ss,in}$ [-]	$H_{S,D}$ [m]	$\frac{H_{S,D}}{H_{S,in}}$
15.00	0.0312	2.77	0.1847
16.00	0.0333	10.11	0.6319
17.00	0.0354	14.03	0.8253
18.00	0.0374	16.84	0.9356
19.00	0.0395	18.89	0.9942
20.00	0.0416	20.41	1.0205
21.00	0.0437	21.58	1.0276
22.00	0.0458	22.53	1.0241
23.00	0.0478	23.40	1.0174
24.00	0.0499	24.25	1.0104
25.00	0.0520	25.12	1.0048
26.00	0.0541	26.02	1.0008
27.00	0.0562	26.96	0.9985

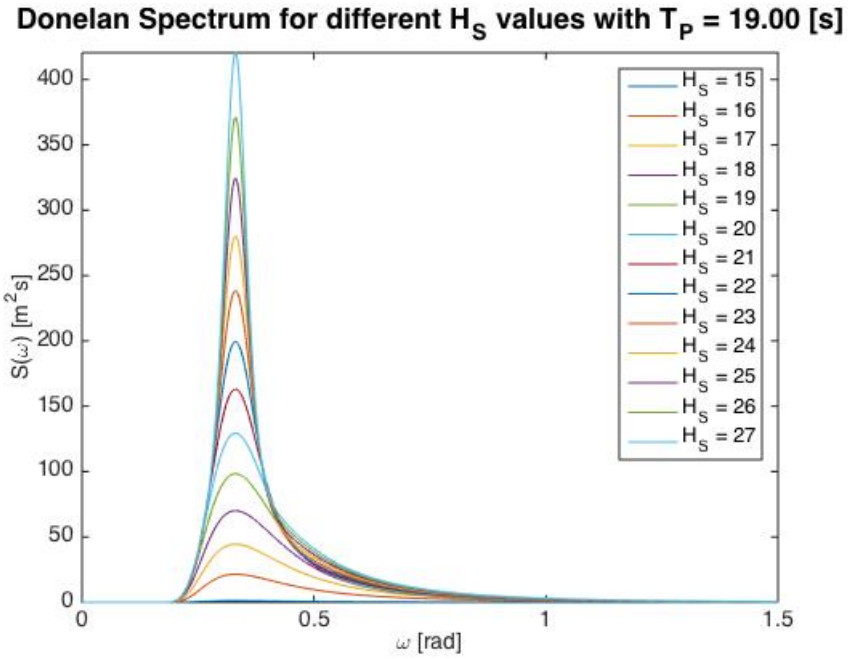

Figure E.4: Theoretical Donelan wave spectrum for different H_S values with $T_P = 19.00$ [s].

E.2 Measured values

E.2.1 Sea state 1

Table E.5: Variance and H_S values for all 10 tests of sea state 1 using the Donelan wave spectrum.

	Without pile			**With pile**				
Test	σ^2 [m^2]	H_S [m]	C_{max} [m]	σ^2 [m^2]	H_S [m]	C_{max} [m]	F_{max} [MN]	M_{max} [GNm]
1	4.75	8.72	9.16	4.94	8.89	9.88	50.26	5.31
2	5.38	9.28	10.09	5.29	9.20	9.62	62.79	6.79
3	5.02	8.96	9.43	5.17	9.10	10.06	51.11	5.79
4	5.27	9.18	9.52	5.43	9.32	9.50	58.22	6.55
5	5.24	9.16	10.77	5.22	9.14	11.03	64.17	7.16
6	5.03	8.97	9.28	5.01	8.95	8.66	50.73	5.47
7	5.55	9.41	10.56	5.62	9.49	10.75	55.75	6.24
8	4.93	8.88	9.39	5.03	8.97	9.26	46.98	5.18
9	5.50	9.38	10.80	5.46	9.35	11.92	57.52	6.14
10	5.46	9.35	9.99	5.40	9.30	9.21	49.01	5.60
avg	5.21	9.13		5.26	9.17			

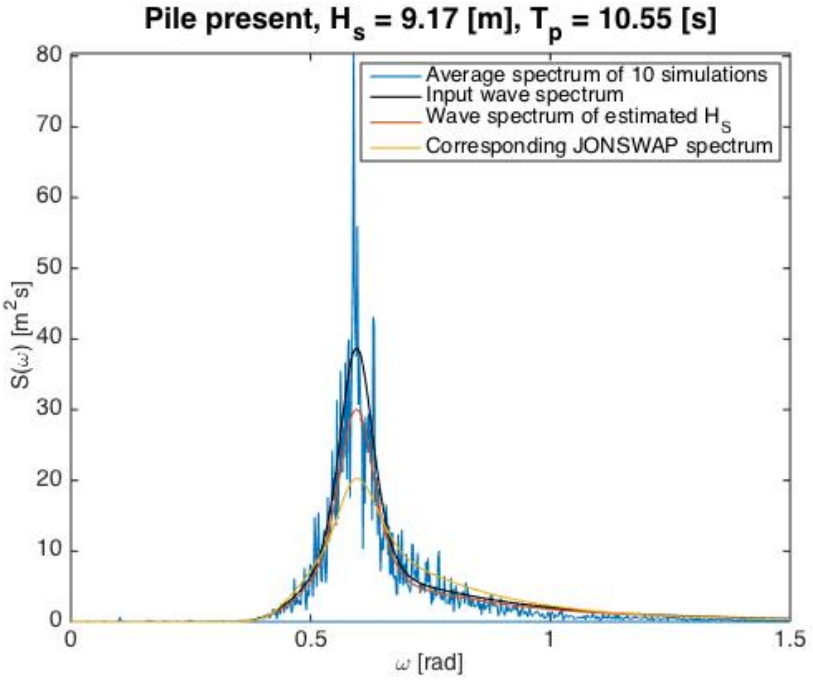

Figure E.5: Measured wave spectrum of sea state 1 using the Donelan wave spectrum.

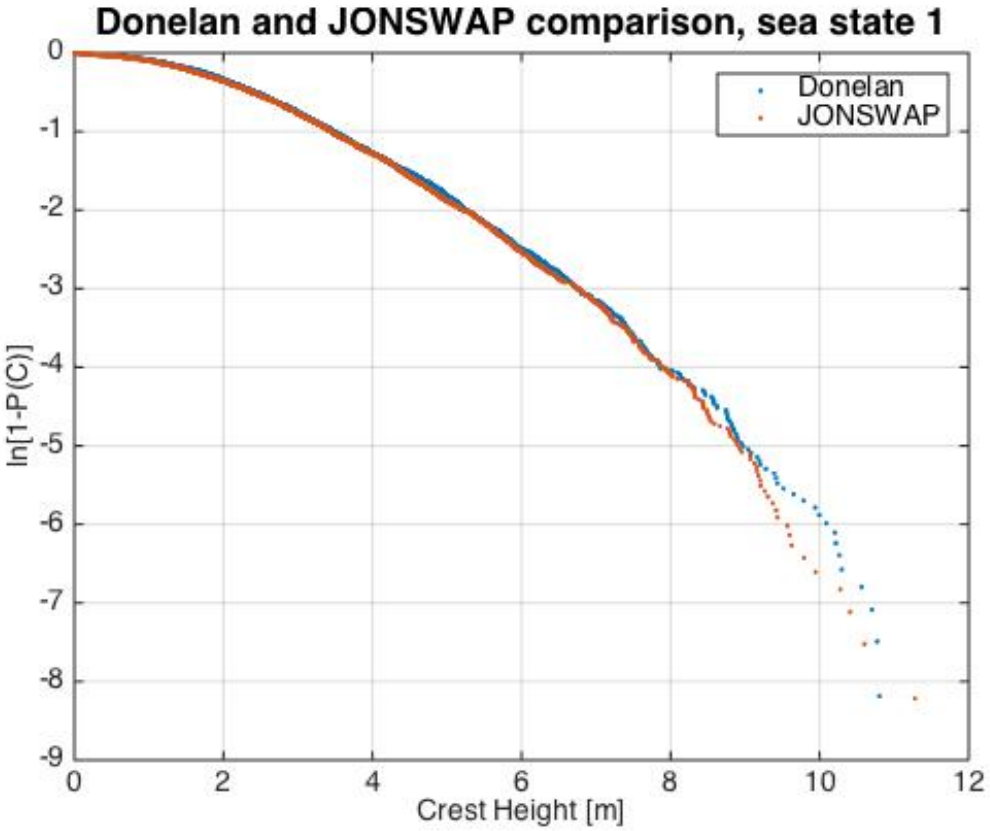

Figure E.6: Distribution of wave crests of sea state 1 using both the Donelan wave spectrum and the JONSWAP wave spectrum.

E.2.2 Sea state 6

Table E.6: Variance and H_S values for all 10 tests of sea state 6 using the Donelan wave spectrum.

	Without pile			**With pile**				
Test	σ^2 [m^2]	H_S [m]	C_{max} [m]	σ^2 [m^2]	H_S [m]	C_{max} [m]	F_{max} [MN]	M_{max} [GNm]
1	10.01	12.66	12.47	10.34	12.86	12.80	52.31	5.32
2	9.86	12.56	11.92	10.15	12.75	12.62	49.08	5.34
3	9.74	12.48	13.70	10.07	12.69	12.84	54.88	5.89
4	9.81	12.53	14.83	9.71	12.47	14.56	60.39	6.74
5	10.19	12.77	12.32	10.49	12.96	13.48	53.62	5.88
6	10.70	13.08	13.74	10.87	13.19	12.67	53.62	5.61
7	10.52	12.97	14.18	10.70	13.08	14.47	46.68	5.12
8	9.55	12.36	10.68	9.39	12.26	11.52	45.29	5.05
9	10.36	12.88	11.39	10.34	12.86	12.10	50.13	5.29
10	9.60	12.40	13.39	9.56	12.37	12.35	60.13	6.40
avg	10.03	12.67		10.16	12.75			

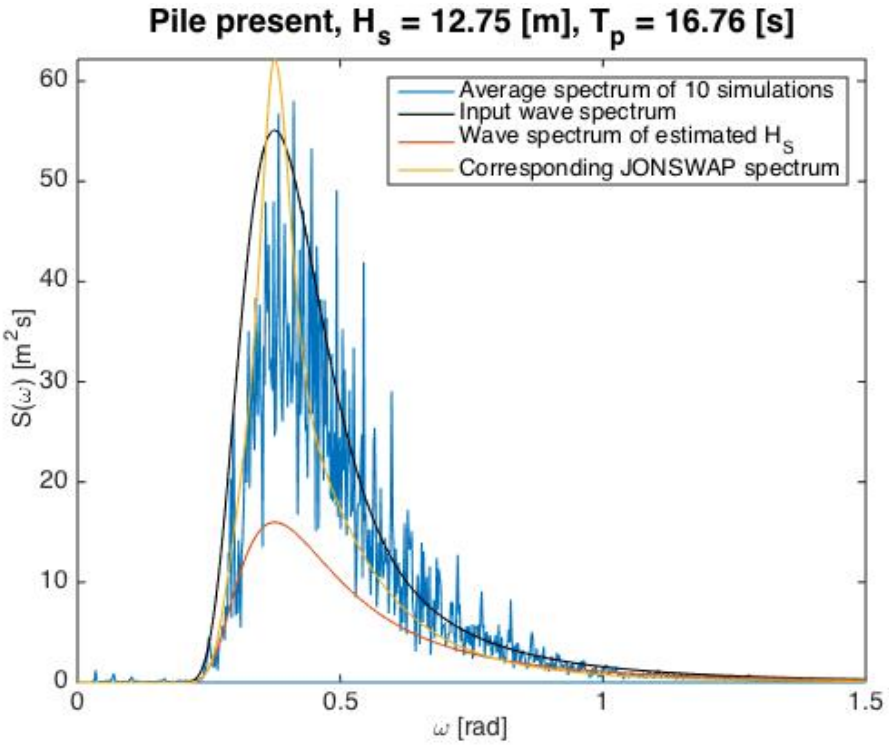

Figure E.7: Measured wave spectrum of sea state 6 using the Donelan wave spectrum.

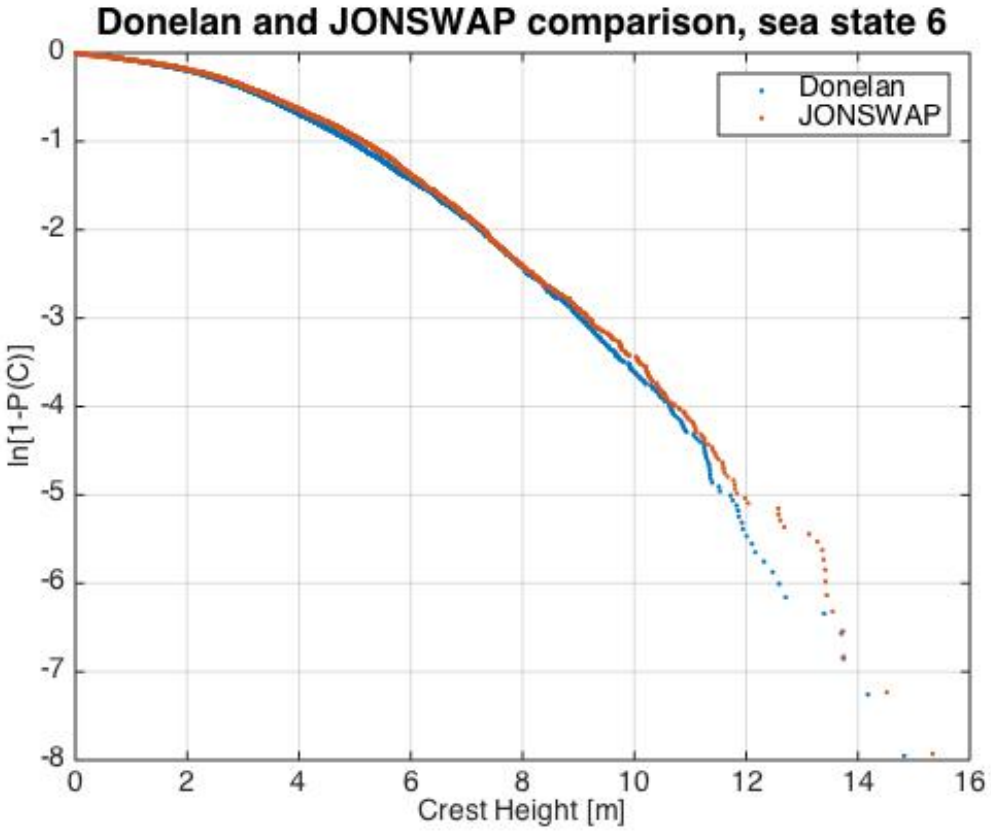

Figure E.8: Distribution of wave crests of sea state 6 using both the Donelan wave spectrum and the JONSWAP wave spectrum.

E.2.3 Sea state 7

Table E.7: Variance and H_S values for all 10 tests of sea state 7 using the Donelan wave spectrum.

	Without pile			**With pile**				
Test	σ^2 [m^2]	H_S [m]	C_{max} [m]	σ^2 [m^2]	H_S [m]	C_{max} [m]	F_{max} [MN]	M_{max} [GNm]
1	8.30	11.53	13.29	8.38	11.58	12.80	55.51	6.18
2	7.91	11.25	13.29	7.26	10.78	12.46	57.21	6.12
3	8.43	11.61	12.24	8.59	11.72	12.34	64.67	6.99
4	7.11	10.66	11.67	7.20	10.73	12.58	61.53	6.60
5	8.71	11.81	13.61	8.84	11.90	12.72	60.81	6.30
6	7.46	10.93	11.00	7.42	10.90	11.46	54.97	6.24
7	8.11	11.39	12.65	8.54	11.69	13.53	61.60	6.82
8	8.80	11.86	12.05	8.83	11.88	12.89	58.35	6.32
9	6.58	10.26	9.66	6.78	10.41	9.97	51.80	5.82
10	6.56	10.24	11.04	6.88	10.49	10.67	59.89	6.66
avg	7.80	11.15		7.87	11.21			

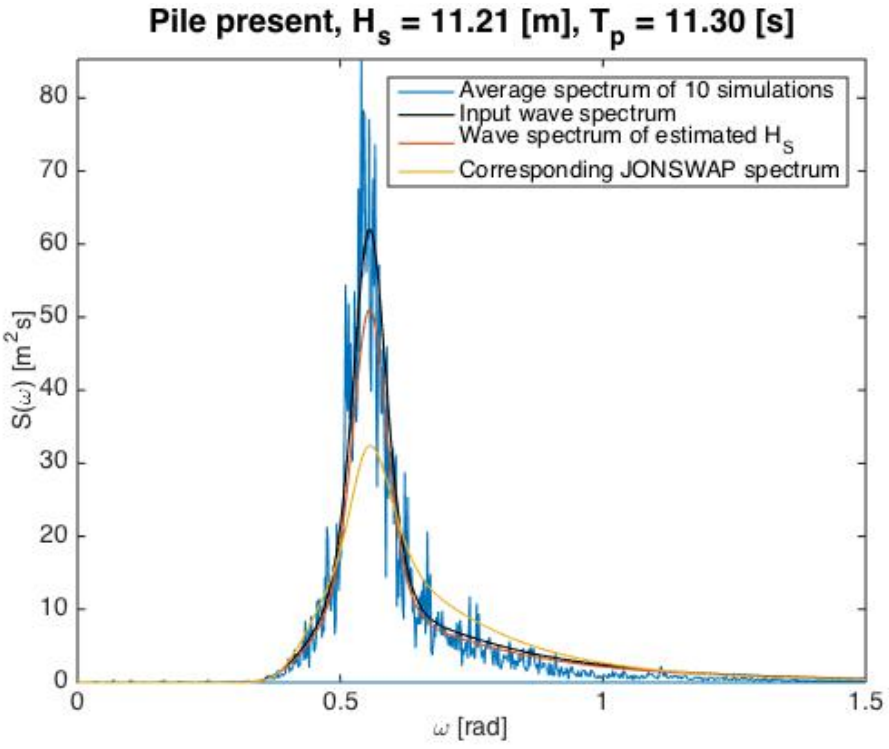

Figure E.9: Measured wave spectrum of sea state 7 using the Donelan wave spectrum.

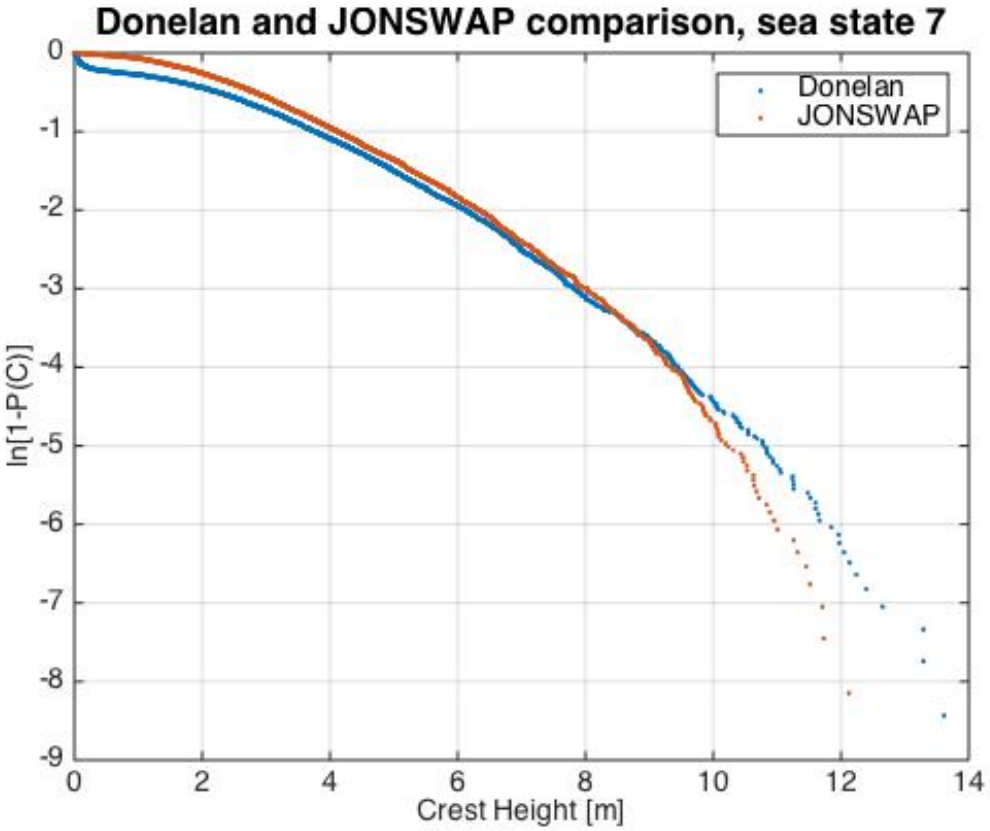

Figure E.10: Distribution of wave crests of sea state 7 using both the Donelan wave spectrum and the JONSWAP wave spectrum.

E.2.4 Sea state 15

Table E.8: Variance and H_S values for all 10 tests of sea state 15 using the Donelan wave spectrum.

	Without pile			**With pile**				
Test	σ^2 [m^2]	H_S [m]	C_{max} [m]	σ^2 [m^2]	H_S [m]	C_{max} [m]	F_{max} [MN]	M_{max} [GNm]
1	14.25	15.10	14.47	15.35	15.67	15.23	51.24	5.10
2	15.11	15.55	15.11	16.32	16.16	16.99	62.13	6.29
3	15.31	15.65	15.92	16.54	16.27	17.54	62.97	6.41
4	14.43	15.19	15.06	15.77	15.89	15.58	59.75	6.44
5	15.28	15.63	13.86	16.36	16.18	15.49	51.56	5.50
6	15.03	15.51	16.45	16.07	16.03	18.62	61.36	6.16
7	15.85	15.93	17.47	17.29	16.63	17.30	58.17	5.77
8	18.08	17.01	17.32	19.48	17.65	20.40	66.12	6.66
9	16.95	16.47	16.66	18.27	17.10	17.17	66.79	6.81
10	14.74	15.36	15.17	16.01	16.00	16.64	53.13	5.32
avg	15.50	15.74		16.75	16.36			

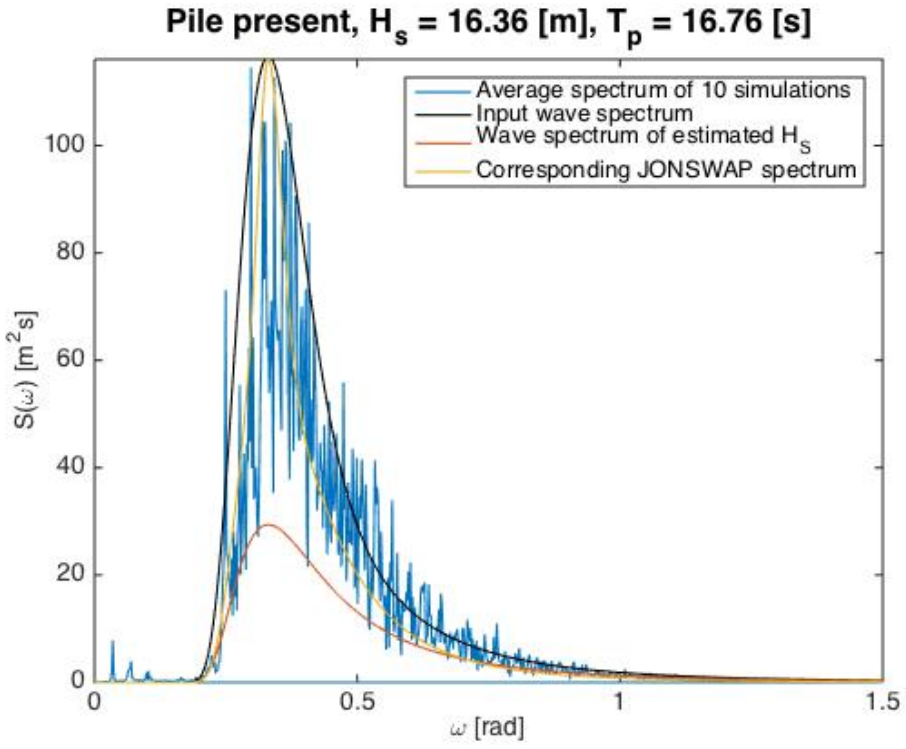

Figure E.11: Measured wave spectrum of sea state 15 using the Donelan wave spectrum.

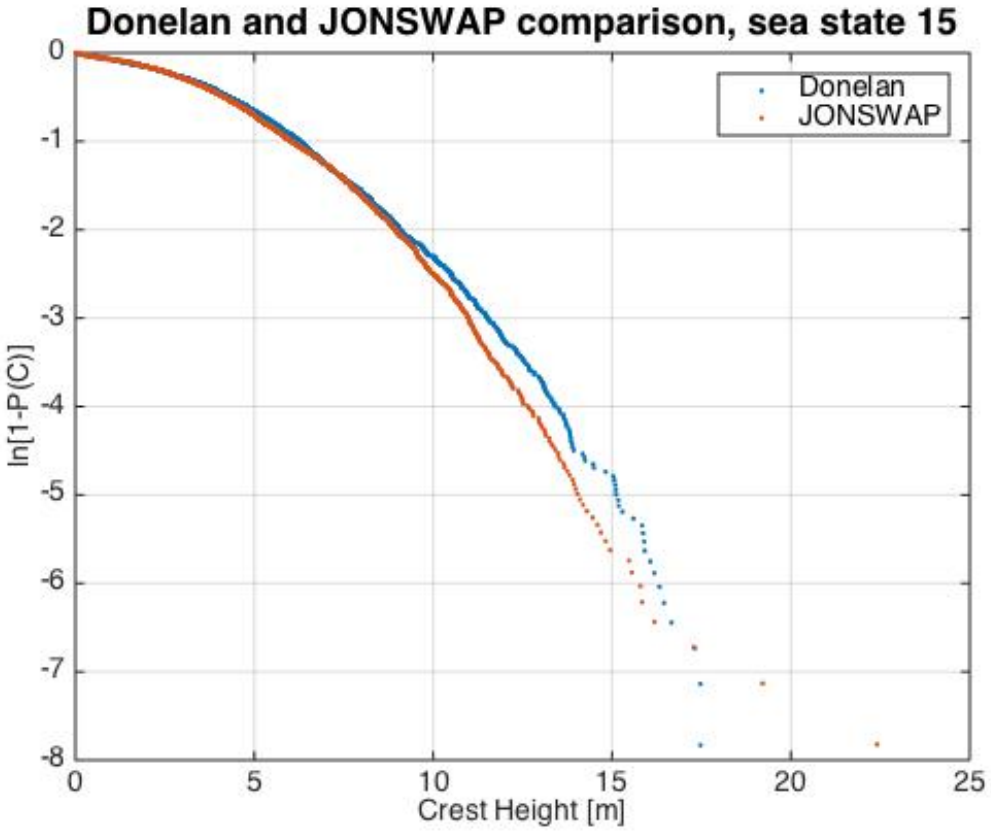

Figure E.12: Distribution of wave crests of sea state 15 using both the Donelan wave spectrum and the JONSWAP wave spectrum.

Appendix F

Stokes 5^{th} perturbation

Truncated after fifth order, the expansion for the free surface profile is given as shown in equation F.1 [58].

$$\begin{aligned} k\eta\left(x\right) = kh + \varepsilon\cos kx + \varepsilon^2 B_{22}\cos 2kx + \varepsilon^3 B_{31}\left(\cos kx - \cos 3kx\right) \\ + \varepsilon^4\left(B_{42}\cos 2kx - B_{44}\cos 4kx\right) + \varepsilon^5(-(B_{53}+B_{55})\cos kx \\ + B_{53}\cos 3kx - B_{55}\cos 5kx) + 0(\varepsilon^6) \end{aligned} \tag{F.1}$$

The dimensionless coefficients in this expansion can be calculated as follows [58]:

$$B_{22} = \frac{\coth kh(1+2S)}{2(1-S)} \tag{F.2}$$

$$B_{31} = \frac{-3(1+3S+3S^2+2S^3)}{8(1-S)^3} \tag{F.3}$$

$$B_{42} = \frac{\coth kh(6-26S-182S^2-204S^3-25S^4+26S^5)}{6(3+2S)(1-S)^4} \tag{F.4}$$

$$B_{44} = \frac{\coth kh(24+92S+122S^2+66S^3+67S^4+34S^5)}{24(3+2S)(1-S)^4} \tag{F.5}$$

$$B_{53} = \frac{9(132+17S-2.216S^2-5.897S^3-6.292S^4-2.687S^5+194S^6+467S^7+82S^8)}{384(3+2S)(4+S)(1-S)^6} \tag{F.6}$$

$$B_{55} = \frac{5(300+1.579S+3.176S^2-2.949S^3+1.188S^4+675S^5+1.326S^6+827S^7+130S^8)}{384(3+2S)(4+S)(1-S)^6} \tag{F.7}$$

where

$$S = sech\ 2kh \equiv \frac{1}{\cosh 2kd} \tag{F.8}$$

Truncated after fifth order, the expansion for the velocity potential shown in equation F.9 is obtained, where $\bar{u}$ is the mean horizontal fluid speed given in F.10.

$$\phi(x,y) = -\bar{u}x + C_0\left(\frac{g}{k^3}\right)^{\frac{1}{2}}(\varepsilon A_{11}\cosh ky\sin kx + \varepsilon^2 A_{22}\cosh 2ky\sin 2kx + \varepsilon^3(A_{31}\cosh ky\sin kx + A_{33}\cosh 3ky\sin 3kx) + \varepsilon^4(A_{42}\cosh 2ky\sin 2kx + A_{44}\cosh 4ky\sin 4kx) + \varepsilon^5(A_{51}\cosh ky\sin kx + A_{53}\cosh 3ky\sin 3kx + A_{55}\cosh 5ky\sin 5kx)) + 0(\varepsilon^6) \quad \text{(F.9)}$$

$$\bar{u}\left(\frac{k}{g}\right)^{\frac{1}{2}} = C_0 + \varepsilon^2 C_2 + \varepsilon^4 C_4 + 0(\varepsilon^6) \quad \text{(F.10)}$$

The dimensionless coefficients in the perturbation expansion for the velocity potential and the mean horizontal fluid speed can be calculated based on the equations below, with S as given in equation F.8 [58].

$$A_{11} = \frac{1}{\sinh kh} \quad \text{(F.11)}$$

$$A_{22} = \frac{3S^2}{2(1-S)^2} \quad \text{(F.12)}$$

$$A_{31} = \frac{-4-20S+10S^2-13S^3}{8\sinh kh(1-S)^3} \quad \text{(F.13)}$$

$$A_{33} = \frac{-2S^2+11S^3}{8\sinh kh(1-S)^3} \quad \text{(F.14)}$$

$$A_{42} = \frac{12S-14S^2-264S^3-45S^4-13S^5}{24(1-S)^5} \quad \text{(F.15)}$$

$$A_{44} = \frac{10S^3-174S^4+291S^5+278S^6}{48(3+2S)(1-S)^5} \quad \text{(F.16)}$$

$$A_{51} = \frac{-1.184+32S+13.232S^2+21.712S^3+20.940S^4+12.554S^5-500S^6-3.341S^7-670S^8}{64\sinh kh(3+2S)(4+S)(1-S)^6} \quad \text{(F.17)}$$

$$A_{53} = \frac{4S+105S^2+198S^3-1.376S^4-1.302S^5-117S^6+58S^7}{32\sinh kh(3+2S)(1-S)^6} \quad \text{(F.18)}$$

$$A_{55} = \frac{-6S^3+272S^4-1.552S^5+852S^6+2.029S^7+430S^8}{64\sinh kh(3+2S)(4+S)(1-S)^6} \quad \text{(F.19)}$$

$$C_0 = \sqrt{\tanh kh} \quad \text{(F.20)}$$

$$C_2 = \frac{\sqrt{\tanh kh}(2+7S^2)}{4(1-S)^2} \quad \text{(F.21)}$$

$$C_4 = \frac{\sqrt{\tanh kh}(4+32S-116S^2-400S^3-71S^4+146S^5)}{32(1-S)^5} \quad \text{(F.22)}$$

Appendix G

Plunging Breaker

G.1 Measurements

Table G.1: Measured values from waveprobe 2 for the two wavetrains in full scale.

Wavetrain	Pile	H [m]	C [m]	T [s]	λ [m]	ε [-]
1	No	33.00	20.10	14.4	311.13	0.1060
	Yes	34.04	20.92	14.9	329.83	0.1032
	Yes	34.07	20.68	14.8	326.09	0.1045
	Yes	35.50	22.13	14.9	329.83	0.1076
	Yes	36.73	22.98	14.7	322.35	0.1139
	Yes	35.60	21.64	14.8	326.09	0.1092
	Yes	34.61	21.30	15.0	333.57	0.1038
2	No	37.07	22.66	14.2	303.65	0.1221
	Yes	34.08	20.94	14.7	322.35	0.1057
	Yes	33.47	19.76	14.9	329.83	0.1015
	Yes	34.60	21.36	14.7	322.35	0.1073
	Yes	33.79	20.26	14.8	326.09	0.1036
	Yes	32.98	19.36	14.9	329.83	0.1000
	Yes	33.15	19.46	14.7	322.35	0.1028

Table G.2: Measured values from waveprobe 3 for the two wavetrains in full scale.

Wavetrain	Pile	H [m]	C [m]	T [s]	λ [m]	ε [-]	F [MN]	M [GNm]
1	No	29.09	15.61	14.3	307.39	0.0946	-	-
	Yes	33.96	19.58	14.9	329.83	0.1030	60.90	7.31
	Yes	33.61	19.26	14.9	329.83	0.1019	60.07	7.18
	Yes	33.92	19.41	14.8	326.09	0.1040	60.06	7.21
	Yes	36.44	22.45	14.8	326.09	0.1117	60.30	7.30
	Yes	37.19	22.82	14.8	326.09	0.1140	56.63	6.91
	Yes	36.17	21.67	14.8	326.09	0.1109	57.84	7.08
2	No	34.99	20.27	13.7	285.01	0.1228	-	-
	Yes	34.86	21.51	14.6	318.61	0.1094	77.13	9.23
	Yes	34.25	20.68	15.0	333.57	0.1027	71.54	8.71
	Yes	34.19	20.31	14.7	322.35	0.1061	75.14	9.25
	Yes	34.39	20.16	14.7	322.35	0.1067	72.17	8.85
	Yes	34.53	19.91	14.7	322.35	0.1071	70.91	8.72
	Yes	34.79	21.11	14.9	329.83	0.1055	72.31	8.67

Table G.3: Measured values from waveprobe 4 for the two wavetrains in full scale.

Wavetrain	Pile	H [m]	C [m]	T [s]	λ [m]	ε [-]
1	No	28.75	14.06	13.2	266.49	0.1079
	Yes	28.36	15.25	14.0	296.19	0.0957
	Yes	27.58	14.18	14.0	296.19	0.0957
	Yes	27.50	14.53	14.2	303.65	0.0906
	Yes	28.92	15.99	14.2	303.65	0.0952
	Yes	27.80	14.32	14.1	299.92	0.0927
	Yes	28.34	15.48	14.1	299.92	0.0945
2	No	29.43	15.15	15.2	341.05	0.0863
	Yes	28.33	14.60	15.1	337.31	0.0831
	Yes	27.88	14.85	15.1	337.31	0.0817
	Yes	29.35	16.03	15.2	341.05	0.0861
	Yes	31.04	16.22	15.1	337.31	0.0910
	Yes	28.72	15.11	15.2	341.05	0.0842
	Yes	27.97	14.16	15.1	337.31	0.0820

G.2 Time histories

G.2.1 Wavetrain 1

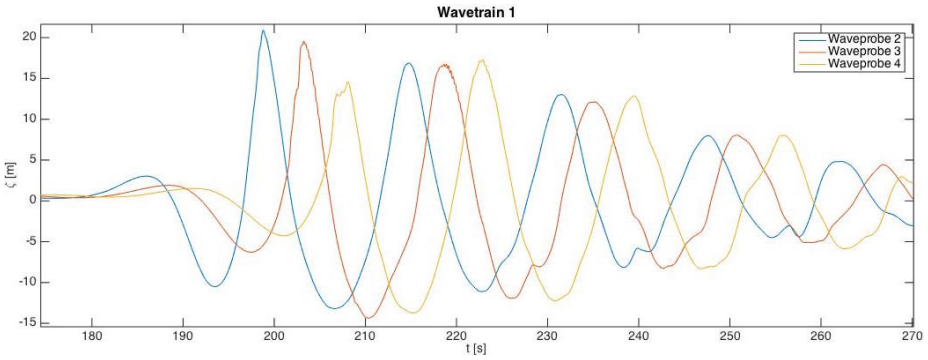

Figure G.1: Time history of first test of wavetrain 1 with the pile present.

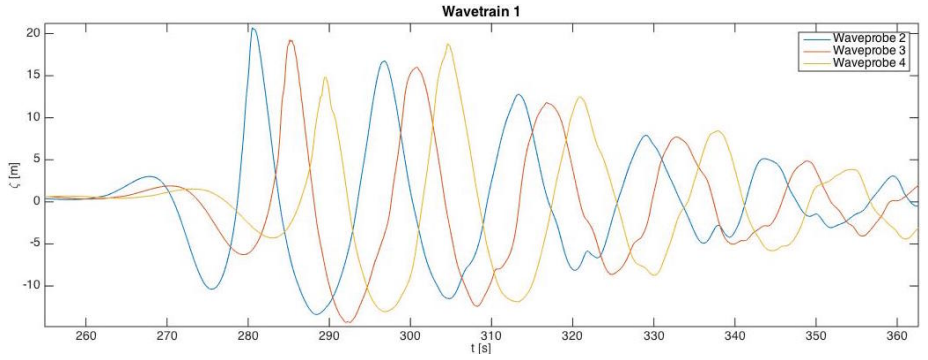

Figure G.2: Time history of second test of wavetrain 1 with the pile present.

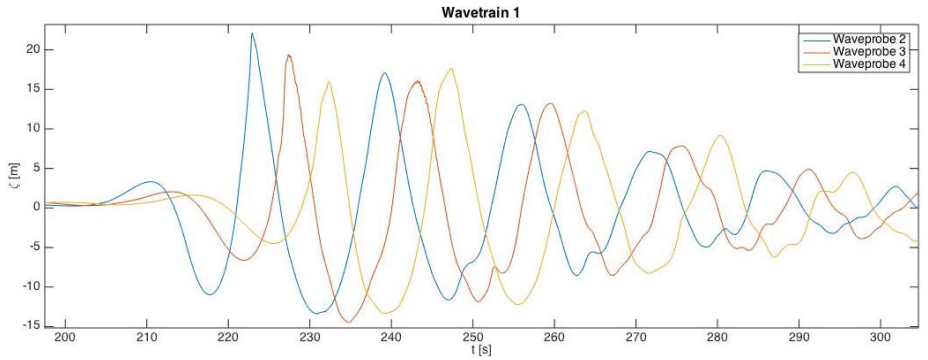

Figure G.3: Time history of third test of wavetrain 1 with the pile present.

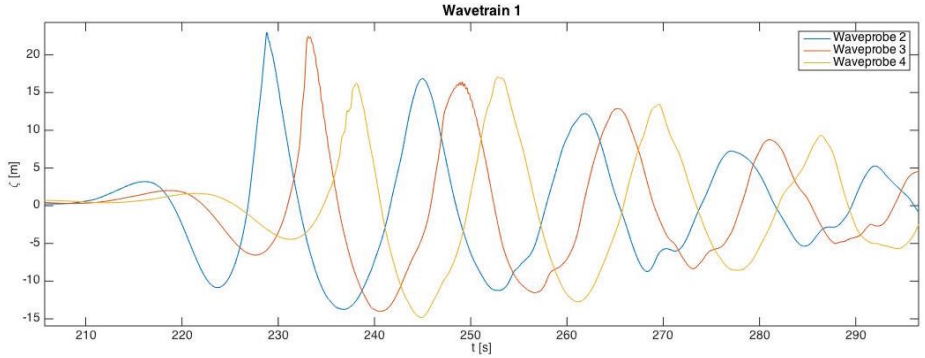

Figure G.4: Time history of fourth test of wavetrain 1 with the pile present.

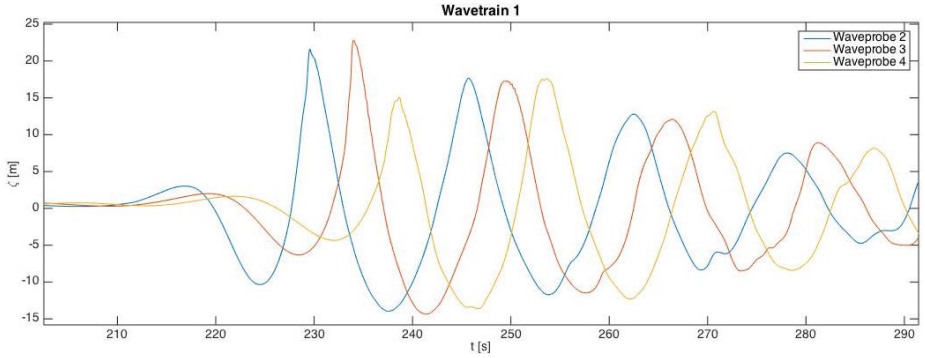

Figure G.5: Time history of fifth test of wavetrain 1 with the pile present.

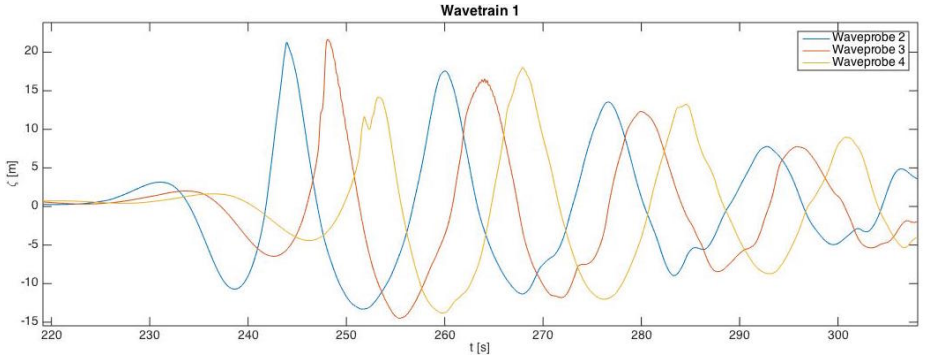

Figure G.6: Time history of sixth test of wavetrain 1 with the pile present.

G.2.2 Wavetrain 2

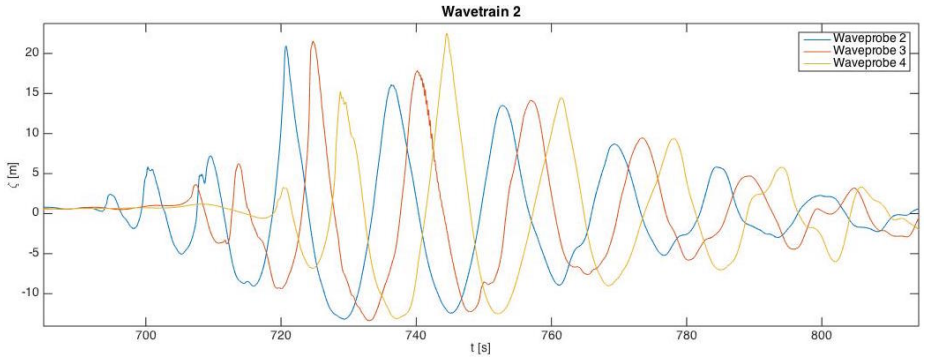

Figure G.7: Time history of first test of wavetrain 2 with the pile present.

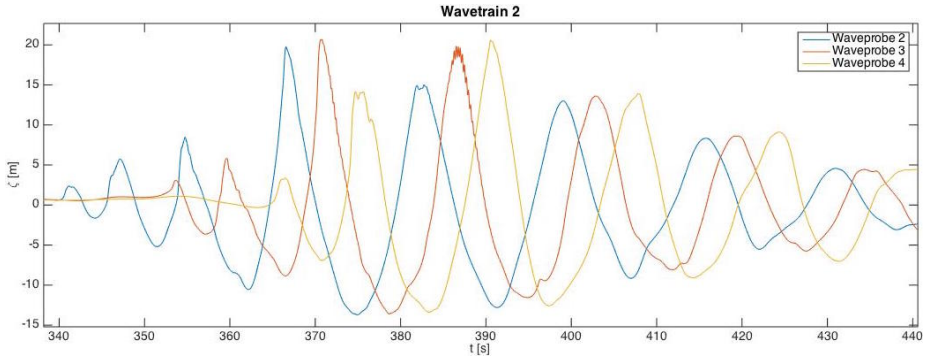

Figure G.8: Time history of second test of wavetrain 2 with the pile present.

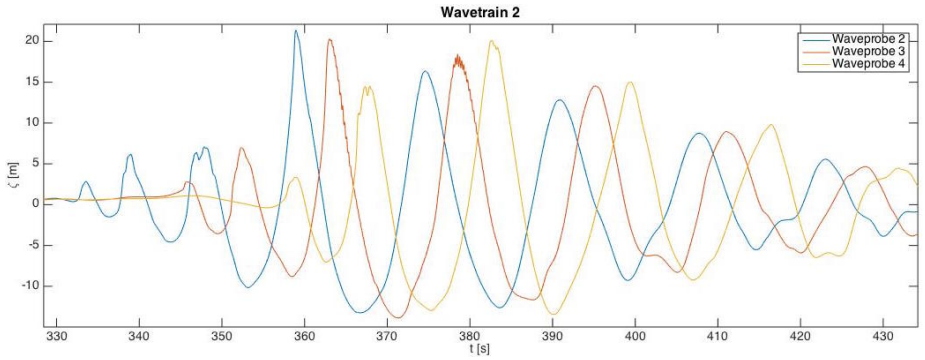

Figure G.9: Time history of third test of wavetrain 2 with the pile present.

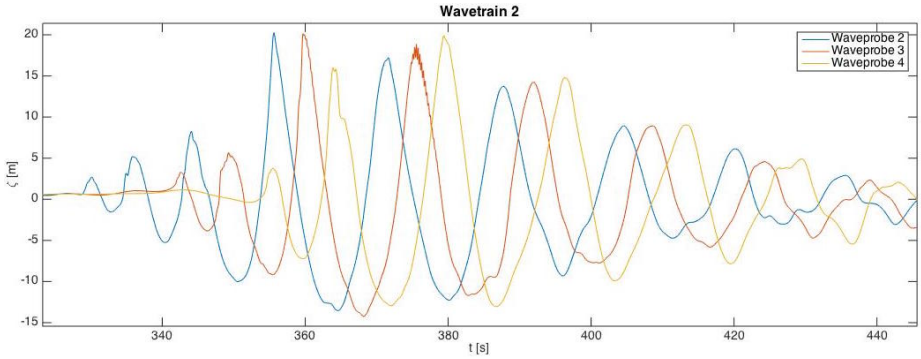

Figure G.10: Time history of fourth test of wavetrain 2 with the pile present.

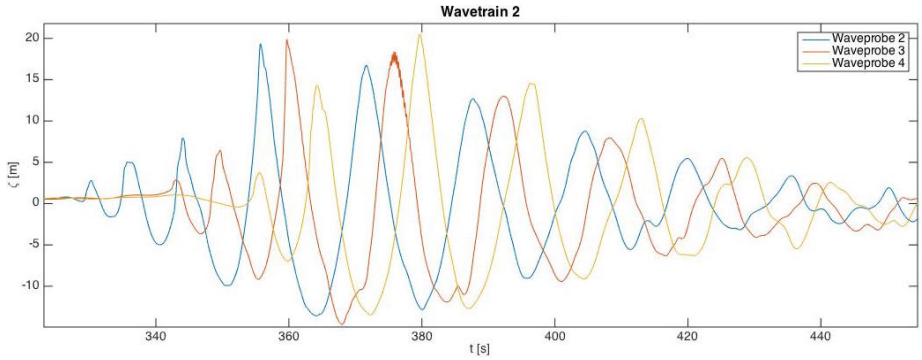

Figure G.11: Time history of fifth test of wavetrain 2 with the pile present.

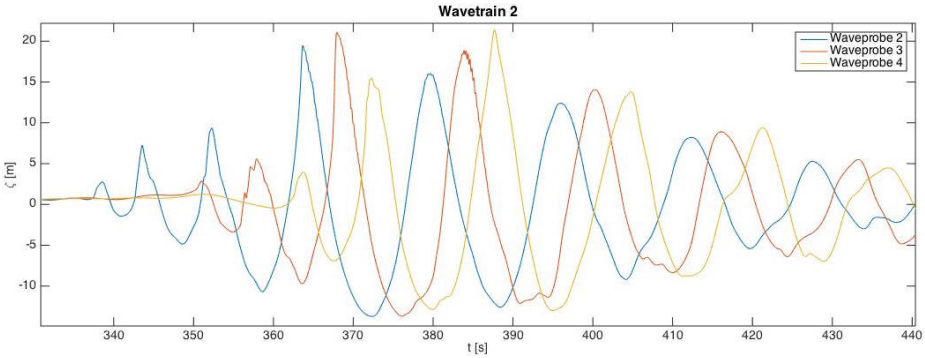

Figure G.12: Time history of sixth test of wavetrain 2 with the pile present.

Appendix H

Improved static calculation method

The improved static calculation method for predicting loads exerted by the annual q-probability waves is based on figure H.1, where rotation angle θ and displacement y can be expressed as shown in equation H.1 and H.2.

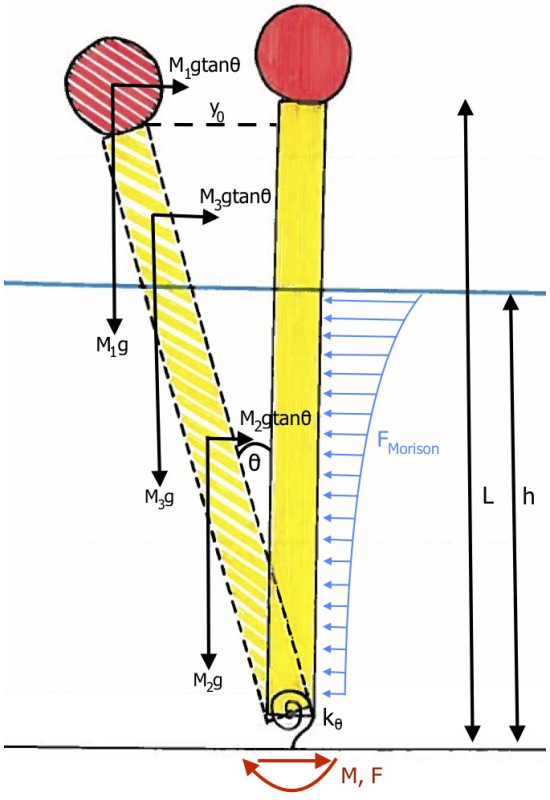

Figure H.1: Illustration of the pile model used in the improved static calculation method.

$$\theta = \frac{M_{imp}}{k_\theta} \tag{H.1}$$

$$y(z) = \theta z \Rightarrow y_0 = \theta L \tag{H.2}$$

Assuming the pile to be in static equlibrium and inserting the expressions for θ and y, the improved overturning moments M_{imp} and base shear forces F_{imp} can be calculated by solving equation H.3 and H.4, respectively. Note that the masses termed M_1, M_2 and M_3 are concentrated, whereas the masses termed $M_1(z)$ and $M_2(z)$ are uniformly distributed.

$$\begin{aligned}\sum \vec{M} = 0 \Rightarrow M_{imp} = M_{mor} &- M_3 g L \left[\tan(\theta) + \theta\right] \\ &- \left[2\int_h^L M_2(z) g z \tan\theta dz + 2\int_h^L M_2(z) g \theta z dz\right] \\ &- \left[\int_0^h M_1(z) g z \tan\theta dz + \int_0^h M_1(z) g \theta z dz\right]\end{aligned} \tag{H.3}$$

$$\sum F_x = 0 \Rightarrow F_{imp} = F_{mor} - M_1 g \tan\theta - M_2 g \tan\theta - M_3 g \tan\theta \tag{H.4}$$